



ASTM INTERNATIONAL
Selected Technical Papers

Evaluation of Existing and New Sensor Technologies for Fatigue, Fracture and Mechanical Testing

STP 1584

Editors

Jidong Kang

David Jablonski

David Dudzinski



ASTM INTERNATIONAL

SELECTED TECHNICAL PAPERS
STP1584

Editors: Jidong Kang, David Jablonski, David Dudzinski

Evaluation of Existing and New Sensor Technologies for Fatigue, Fracture and Mechanical Testing

ASTM Stock #STP1584

Library of Congress Cataloging-in-Publication Data

Evaluation of existing and new sensor technologies for fatigue, fracture and mechanical testing / editors, Jidong Kang, David Jablonski, and David Dudzinski.

pages cm. -- (Astm stock ; #STP1584)

Includes bibliographical references and index.

ISBN 978-0-8031-7613-3 (alk. paper)

1. Materials--Testing--Equipment and supplies--Evaluation. 2. Detectors--Industrial applications. 3. Fatigue testing machines--Evaluation. 4. Fracture mechanics. 5. Mechanical wear. I. Kang, Jidong. II. Jablonski, David. III. Dudzinski, David.

TA413.E854 2015

620.1'1260284--dc23

2015013071

Copyright © 2015 ASTM INTERNATIONAL, West Conshohocken, PA. All rights reserved. This material may not be reproduced or copied, in whole or in part, in any printed, mechanical, electronic, film, or other distribution and storage media, without the written consent of the publisher.

Photocopy Rights

Authorization to photocopy items for internal, personal, or educational classroom use, or the internal, personal, or educational classroom use of specific clients, is granted by ASTM International provided that the appropriate fee is paid to the Copyright Clearance Center, 222 Rosewood Drive, Danvers, MA 01923, Tel: (978) 646-2600; <http://www.copyright.com/>

The Society is not responsible, as a body, for the statements and opinions expressed in this publication. ASTM International does not endorse any products represented in this publication.

Peer Review Policy

Each paper published in this volume was evaluated by two peer reviewers and at least one editor. The authors addressed all of the reviewers' comments to the satisfaction of both the technical editor(s) and the ASTM International Committee on Publications.

The quality of the papers in this publication reflects not only the obvious efforts of the authors and the technical editor(s), but also the work of the peer reviewers. In keeping with long-standing publication practices, ASTM International maintains the anonymity of the peer reviewers. The ASTM International Committee on Publications acknowledges with appreciation their dedication and contribution of time and effort on behalf of ASTM International.

Citation of Papers

When citing papers from this publication, the appropriate citation includes the paper authors, "paper title", STP title, STP number, book editor(s), page range, Paper doi, ASTM International, West Conshohocken, PA, year listed in the footnote of the paper. A citation is provided on page one of each paper.

Printed in Bay Shore, NY

April, 2015

Overview

New sensor technologies are used in fatigue, fracture, and mechanical testing to determine a variety of properties that are subject to ASTM standards. As these standards are used in practical applications, issues with existing and new sensors specified in the standards need to be resolved.

The *4th Symposium on the Evaluation of Existing and New Sensor Technologies* is intended to provide a forum to disseminate state-of-the-art advances in sensor technology, as well as to identify the limitations of existing sensor technology as it applies to fatigue, fracture, and mechanical testing. This symposium is the fourth in a series of symposia addressing issues with existing sensors and development in new sensor technologies for fatigue, fracture, and mechanical testing.

In the last decade, digital image correlation (DIC) has been seen as a rapidly growing noncontact strain-measuring technique and has been used extensively in many applications. The first four papers reflect this trend. Bruhis et al. demonstrate how to use DIC to measure mechanical properties of fillet arc T-welded aluminum alloy AA7xxx extrusions. Kang and Gong show the use of DIC to determine fracture behavior of AA6060 aluminum alloy extrusion in specimens with a wide range of stress triaxiality. Williams et al. present an application of DIC in assessing yield and forming limit criteria for sheet material deformation and forming. The final paper in this section by Barhli et al. reviews recent work on the analysis of 2D and 3D damage in engineering materials, and describes developments in quantitative analysis of defects by 2D and 3D image correlation.

The next three papers address new developments in potential drop techniques for crack-length monitoring in fracture-toughness testing. Tarnowski et al. present an experimental investigation that quantifies the apparent crack extension, purely as a result of plasticity, in the absence of physical crack growth in a variety of specimen geometries when using potential drop techniques. Chen et al. show results of applying direct current potential drop techniques to derive the J-integral versus a crack-growth-resistance curve (J-R curve) for fracture-toughness characterization of structural materials. The third paper in this section by Glasser et al. presents an experimental technique using surface strain gauges to determine a calibration curve in terms of strain range versus crack length as a function of loading cycles. By using multiple strain gauges across the width of the specimen, it is possible to map out the crack front and its change in position as a function of loading cycles.

There have been continuous efforts in exploring new applications using various sensors. Cuadra et al. present a hybrid optico-acoustic approach combining DIC and acoustic emission (AE) to account for both surface and volume effects and to provide cross-validation when using in situ nondestructive evaluation (NDE) methods. Sebastian et al. describe an optical sensor that utilizes an extrinsic Fabry–Perot interferometer to measure thermal and mechanical strain on a variety of substrates at temperatures up to 870°C.

The last two papers discuss sensors for use in elevated-temperature applications. Bailey discusses the use of infrared thermography for the measurement of temperature during fatigue testing and a method to adjust the test frequency using an adaptive frequency control algorithm to keep the specimen temperature constant. In the last paper, Jones et al. demonstrate the use of infrared thermography as a noninvasive temperature-measurement technique, and use it in cyclic high-temperature loading. They demonstrate that it is important to coat the specimens with a thin layer of material that has a stable emissivity to obtain accurate temperature measurements.

It is interesting to note that some existing technologies, for example, the potential drop technique, have been in practice for a long time but yet need standardization. In the meantime, some new sensor technologies, for example, DIC, need guidance in practice; thus, the interpretation of results could be fairly compared and understood well. It is the intent of the Sensor Technologies Task Group (E08.03.03) within ASTM E08.03 to revisit the existing corresponding standards and work together with their peers within ASTM to develop new ASTM standards in suitable areas to better serve the fatigue, fracture, and mechanical testing community. This symposium has, no doubt, provided a timely opportunity to stimulate critical thinking and planning.

The editors express their gratitude to all of the authors and co-authors responsible for the papers included in this STP and the presentations made during the symposium. We also thank all of the reviewers for their great efforts and professionalism ensuring the high quality of this STP. Finally, the editors are grateful for the ASTM planning and to the editorial staff for their tireless assistance in making this symposium and STP a great success.

Jidong Kang
David Jablonski
David Dudzinski

Foreword

This compilation of *Selected Technical Papers*, STP1584, *Evaluation of Existing and New Sensor Technologies for Fatigue, Fracture and Mechanical Testing*, contains 11 peer-reviewed papers presented at a symposium held May 7–8, 2014 in Toronto, Ontario, Canada. The symposium was sponsored by ASTM International Committee E08 on Fatigue and Fracture and Subcommittee E08.03 on Advanced Apparatus and Techniques.

The Symposium Chairpersons and STP Editors are Jidong Kang, Canmet MATERIALS, Hamilton, Ontario, Canada, David Jablonski, Thermo Fisher Scientific, Tewksbury, Massachusetts, USA, and David Dudzinski, Derivation Research Laboratory, Inc., Ottawa, Ontario, Canada.

Contents

Digital Image Correlation and Its Applications

Measuring Mechanical Properties of Fillet Arc T-Welded Aluminum Alloy AA7xxx Extrusions Using Digital Image Correlation	3
M. Bruhis, J. Dabrowski, and J. R. Kish	

Determination of Fracture Behavior of AA6060 Aluminum Alloy Extrusion Using Digital Image Correlation	13
Jidong Kang and Kevin Gong	

Advanced Characterization of Sheet Metal Deformation and Forming using Digital Image Correlation	32
B. W. Williams, K. P. Boyle, L. Blaga, and J. McKinley	

Advanced 2D and 3D Digital Image Correlation of the Full-Field Displacements of Cracks and Defects	56
S. M. Barhli, D. Hollis, B. Wieneke, M. Mostafavi, and T. J. Marrow	

Crack Length Monitoring Techniques

The Influence of Plasticity on Crack Length Measurements using the Potential Drop Technique	73
K. M. Tarnowski, C. M. Davies, D. W. Dean, and K. M. Nikbin	

Application of Direct Current Potential Drop for the J-integral vs. Crack Growth Resistance Curve Characterization	97
Xiang (Frank) Chen, Randy K. Nanstad, and Mikhail A. Sokolov	

Determination of Calibration Function for Fatigue-Crack Propagation by Measurement Surface Deformation	113
B. Glaser, N. Gubeljak, and J. Predan	

Various Sensors

A Hybrid Optico-Acoustic NDE Approach for Deformation and Damage Monitoring 135

Jefferson Cuadra, Prashanth A. Vanniamparambil, Kavan Hazeli,
I. Bartoli, and Antonios Kotsos

Static and Dynamic Strain Measurement at Ambient and Elevated Temperatures Using an Extrinsic Fabry-Perot Interferometer (EFPI) Optical Strain Sensor 147

James Sebastian, William Boles, and James Taylor

Sensors for Elevated Temperature Applications

Use of IR Temperature Measurement and Thermography for Control and Monitoring of Fatigue Tests 169

P. B. S. Bailey

Assessment of Infrared Thermography for Cyclic High-Temperature Measurement and Control 186

J. P. Jones, S. P. Brookes, M. T. Whittaker, R. J. Lancaster, and B. Ward

DIGITAL IMAGE CORRELATION AND ITS APPLICATIONS

STP 1584, 2015 / available online at www.astm.org / doi: 10.1520/STP158420140050

M. Bruhis,¹ J. Dabrowski,¹ and J. R. Kish¹

Measuring Mechanical Properties of Fillet Arc T-Welded Aluminum Alloy AA7xxx Extrusions Using Digital Image Correlation

Reference

Bruhis, M., Dabrowski, J., and Kish, J. R., "Measuring Mechanical Properties of Fillet Arc T-Welded Aluminum Alloy AA7xxx Extrusions Using Digital Image Correlation," *Evaluation of Existing and New Sensor Technologies for Fatigue, Fracture and Mechanical Testing*, STP 1584, Jidong Kang, David Jablonski, and David Dudzinski, Eds., pp. 3-12, doi:10.1520/STP158420140050, ASTM International, West Conshohocken, PA 2015.²

ABSTRACT

There has been an increasing interest in fabricating automotive components from copper (Cu)-lean 7xxx-series aluminum (Al) alloys because of their relatively high strength, toughness, energy absorption, weldability, and formability. Fusion arc welding is a preferred process to join these alloys to other Al alloys during assembly. A study was undertaken to characterize the mechanical (tensile-shear) response of single-sided fillet arc T-welded joints between Cu-lean AA7xxx extrusions and AA6063 sheet made using the gas metal arc-welding (GMAW) process and ER5356 filler wire. Strain measurements were made using an ARAMIS system based on digital image correlation (DIC). An upper-bound analysis (UBA) was conducted to derive an empirical model of the upper-bound strength of the arc-welded joints. The good agreement between the predicted and experimental results shows that the empirical model can be used to evaluate the tensile-shear response of the dissimilar Al alloy arc-welded joint.

Manuscript received April 30, 2014; accepted for publication December 17, 2014; published online January 30, 2015.

¹GM Centre for Automotive Materials and Corrosion, McMaster Univ., Hamilton, ON L8S 4L7, Canada.

²ASTM Fourth Symposium on the *Evaluation of Existing and New Sensor Technologies for Fatigue, Fracture and Mechanical Testing* on May 7-8, 2014 in Toronto, Canada.

Keywords

Al alloys, fillet weld, tensile-shear, digital image correlation, upper-bound analysis

Introduction

In response to more stringent global emission standards, automotive manufactures are turning to lightweight alloys to reduce emission and improve fuel efficiency. There has been an increasing interest in fabricating automotive components from copper (Cu)-lean 7xxx-series aluminum (Al) alloys because of their relatively high strength, toughness, energy absorption, weldability, and formability [1]. Fusion arc welding is a preferred process to join these alloys to other Al alloys during assembly. A well-characterized performance of such welds is critical to safety design and life prediction efforts [2–4].

Fusion arc welding of Cu-lean AA7xxx (Al-Zn-Mg) alloys (which is typically done using ER5356 filler wire) is a complex process. The fluctuation in temperature during arc welding causes a decrease in the mechanical properties of both the base material and fillet weld. The ultimate strength of fillet weld loaded in shear depends on the strength of the fillet weld material and the direction of loading. It is well known that Al-Mg alloys (to which ER5356 belongs) often fail by localization of flow into shear bands [5,6]. The mechanical properties of the fillet weld measured perpendicular to the direction of loading (transverse fillet) at large strain is of considerable interest in the effort to design and model fusion arc fillet-welded joints. The tensile-shear test method to evaluate the tensile properties of the arc-welded joints has been successfully used in this regard [7]. The digital image correlation (DIC) method has been widely used to measure strain evolution (deformation and damage mechanisms) during uniaxial tension testing [8,9]. However, an effort has not been made hitherto to combine the DIC method with tensile-shear testing at large strains to study the deformation and damage mechanisms of fusion arc fillet-welded joints.

The purpose of this study was to characterize the tensile-shear properties of single-sided fillet-welded T joints between Cu-lean AA7xxx extrusions and AA6063 sheet made using the gas metal arc-welding (GMAW) process and ER5356 filler wire. A novel instrumented testing approach using an ARAMIS strain measurement system based on digital image correlation (DIC) was developed to measure the tensile-shear properties of fillet-welded T-joint coupons. An upper-bound analysis (UBA) was also conducted to derive an empirical model of the upper-bound strength of the welded joints. This paper presents and discusses the result of this effort.

Experimental

The materials used to fabricate the single-sided, fillet-welded T-joint coupons are [Table 1](#) along with the nominal chemical composition of each. The two

TABLE 1 Chemical compositions (wt. %) for aluminum alloys.

Alloy	Si	Fe	Cu	Mn	Mg	Cr	Zn	Zr
AA7003-T6	0.30	0.35	0.20	0.30	0.50-1.0	0.20	5.0-6.5	0.05-0.25
AA7018-T6	0.10	0.10	0.05	0.05	0.7-1.4	-	4.5-5.5	0.12-0.25
AA6063-T6	0.2-0.6	0.35	0.10	0.10	0.45-0.90	0.10	0.10	-
ER5356	0.25	0.40	0.10	0.05-0.20	4.5-5.5	0.05-0.20	0.10	-

Cu-lean AA7xxx alloys were provided as extrusion profiles heat-treated to the T6 temper. The AA6063 was provided as sheet product heat treated to the T6 temper. Arc welding was conducted using the GMAW process according to the procedures specified in the GM Global Weld Design Standard GWS-1C, Section C; specific details were not provided. The single-sided fillet weld was applied in a direction parallel to the extrusion direction of the AA7xxx flange component and perpendicular to the rolling direction of the AA6063 web component. A post-weld heat treatment was not applied. A schematic drawing of the as-received welded T-joint coupon complete with nominal dimensions is shown in Fig. 1(a). The modified “dog bone” coupon geometry used in the tensile-shear tests is shown in Fig. 1(b). This modification was deemed necessary to minimize the so-called “prying forces” that arise during the outward deflection of a relatively thin flange [10] and the tendency for the web to bend when tensile testing single-sided fillet-welded coupons.

Figure 2 shows both a schematic drawing and corresponding photograph of the custom designed and fabricated clamping device deemed necessary to enhance the test-to-test reliability of tensile-shear measurements. The upper and lower grips were independent units that were coupled to the tensile frame material testing

FIG. 1 Schematic drawing complete with nominal dimensions in mm of (a) the as-received welded T-joint coupon, and (b) modified “dog bone” geometry used in the tensile-shear test.

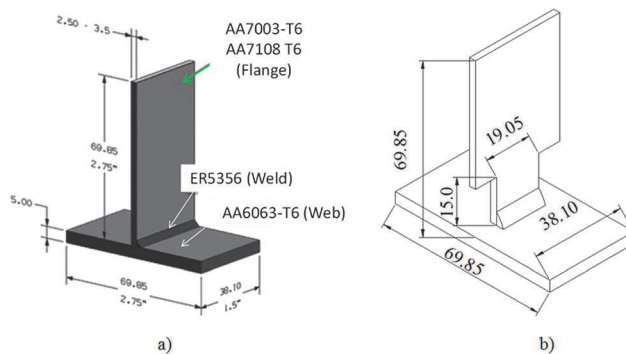
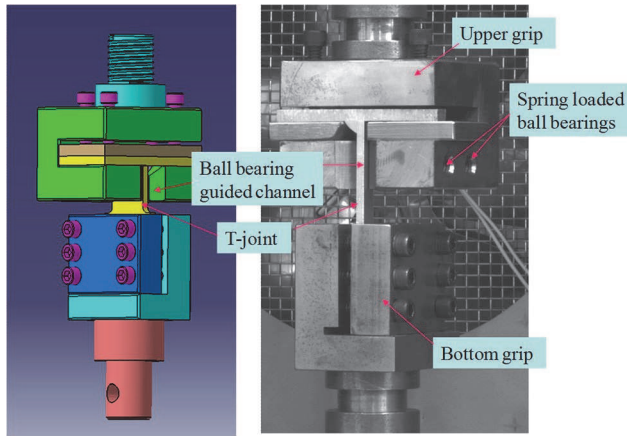


FIG. 2 Schematic drawing and corresponding photograph of the custom designed and fabricated clamping device.



system (MTS). The upper grip was fixed to the tensile frame, whereas the lower pair of grips was able to slide along with the moving actuator. A spring-loaded ball-bearing mounting mechanism was used to facilitate linear axial motion while minimizing the bending of the web component during tensile-shear testing.

Tensile-shear testing was carried out using a 250-kN MTS tensile machine at a cross-head speed of 1 mm/min (equivalent to a nominal strain rate of $8 \times 10^{-4} \text{ s}^{-1}$). The openness of the clamping device was intentional to allow the use of the DIC method for strain measurement. A random ink speckle pattern was deposited on the modified welded T-joint coupons prior to tensile-shear testing. The fillet weld itself was continuously monitored using a charge-coupled device (CCD) camera to measure the shear angles in situ. The error associated with the strain measurement was calibrated to be randomly distributed with a maximum absolute error of less than 0.25 % regardless of the measured strain [9].

Additional uniaxial tensile and compression testing of the ER5356 material was also conducted; the data from which was required to validate the upper-bound stress model derived below. Both uniaxial loading experiments were conducted using an Instron 5566 Electro-Mechanical testing machine with a 10-kN load cell at a cross-head speed of 1.0 mm/min (equivalent to a nominal strain rate of $1.3 \times 10^{-3} \text{ s}^{-1}$). The uniaxial tensile test was conducted using a 127-mm-long cylindrical sample with a 2.38-mm gauge diameter and 12.5-mm gauge length that was prepared from an ER5356 filler wire with a 3.175 diameter. The uniaxial compression test was conducted using a rectangular ($8.8 \times 3.6 \times 3.2 \text{ mm}$) sample that was cut out of an arc fillet weld using one of the welded T-joint coupons. A set of three

configurations, ER5356 filler wire, and ER5356 weld zone. The force versus displacement curve in each test was continuously recorded. The DIC method for strain measurement described above was used in both cases. The ER5356 filler wire was heat treated at 450°C for 1 h to reduce the Vickers microhardness (50-g load with 10-s dwell time) from a value of 114 (in the as-received condition) to 74, which agreed well with the Vickers microhardness value of 73 measured in the as-welded material. A reasonable agreement between the ER5356 filler wire and weld zone material was necessary to permit a meaningful validation of the empirically derived upper-bound stress model.

Upper-Bound Analysis

A simulations concept for the testing of the single-sided fillet-welded T-joint coupons loaded in shear was developed using the upper-bound analysis (UBA). This analysis of the limit load was derived on the basis of a simplified deformation field constructed by the UBA. This approach involving kinematic admissible velocity fields is an effective method of solving forming process problems [10,11]. The plastic instability was expected to occur along a single shear plane. The shear displacement and bending moment were expected based on the expected eccentricity of the applied forces resulting from the discontinuity in the welded T joint. Therefore, the deformation in the weld material was assumed to be a non-steady-state process. An upper-bound solution of this flow problem was derived by considering only the most critical point in time: the initiation of fracture, as proposed by Avitzur [11].

The dimensionless relationship for the critical average deformation stress at the point of fracture initiation is given as:

$$(1) \quad \frac{p^*}{k} = \frac{\sin \beta}{\cos \alpha \cdot \cos(\beta - \alpha)}$$

where:

p^* = the critical average deforming stress,

k = the applied shear stress, and

α and β = the angles as defined in Fig. 3(a).

According to the von Mises yield condition for an isotropic material, k is given as:

$$(2) \quad k = \frac{\sigma_e}{\sqrt{3}}$$

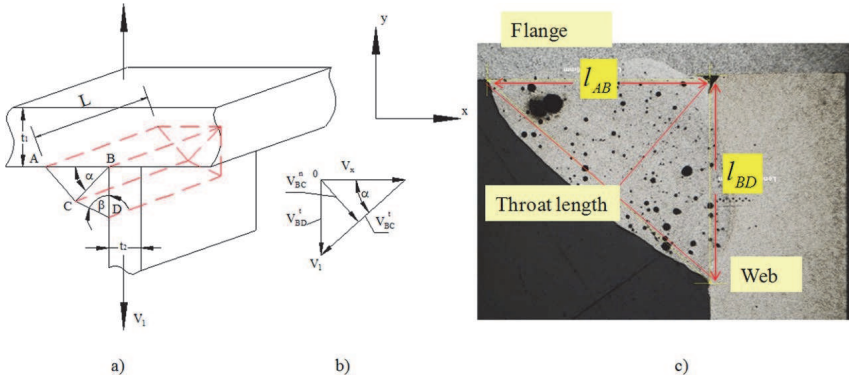
where:

σ_e = the effective stress in tension.

If the angles α and β are assumed to be 45° ($\pi/4$), then the relationship for the dimensionless critical average deformation stress (Eq 1) reduces to:

$$(3) \quad \frac{p^*}{k} = 1.0$$

FIG. 3 (a) Schematic drawing of the single shear plan expected during tension-shear testing of the welded T-joint coupon, (b) corresponding hodograph, and (c) light optical microscopy image of the welded T joint observed in cross-section.



Combining Eqs 2 and 3 yields the following relationship:

$$(4) \quad p^* = k = \frac{\sigma_e}{\sqrt{3}} \approx 0.577 \cdot \sigma_e$$

It follows that the critical collapse load, F^* , for a single-sided fillet-welded T-joint coupon can be determined from the following relationship:

$$(5) \quad F^* = A_0 \cdot p^* = 0.577 \cdot L \cdot l_{BC} \cdot \sigma_e$$

where:

- A_0 = the shear plane area,
- L = the weld length, and
- l_{BC} = the effective throat length.

The latter is given by the following relationship:

$$(6) \quad l_{BC} = l_{AB} \cdot \cos \left[\arctan \left(\frac{l_{AB}}{l_{BD}} \right) \right]$$

where:

l_{AB} and l_{BD} = the leg lengths of the weld (as defined in Fig. 3(a)).

Rearranging Eq 5 yields the following relationship:

$$(7) \quad \sigma_e = \frac{F^*}{0.577 \cdot L \cdot l_{BC}}$$

It follows that an effective stress (σ_e) can be calculated for a given applied load (F) if L and l_{BC} are known. Thus, Eq 7 represents the

empirically derived upper-bound stress model. A similar expression for a welded joint has been derived by Kamtekar [12].

Results and Discussion

A visual examination of the welded T-joint coupons after tensile-shear testing revealed that the failure occurred by shearing at the minimum section: at the throat of the weld. **Figure 4** shows a set of three DIC strain maps approaching the collapse (maximum) load for both welded T-joint coupons tested. It was evident that in both welded T-joint coupons, the shear failure mode of the weld propagated along the throat shear plane. Furthermore, the strain maps revealed that shear bands did not develop prior to the collapse load being applied.

FIG. 4 DIC shear strain distribution maps acquired prior to the collapse (max) load being applied during tensile-shear testing of the (a) welded AA7003/AA6063 T-joint coupon, and (b) welded AA7108/AA6063 T-joint coupon.

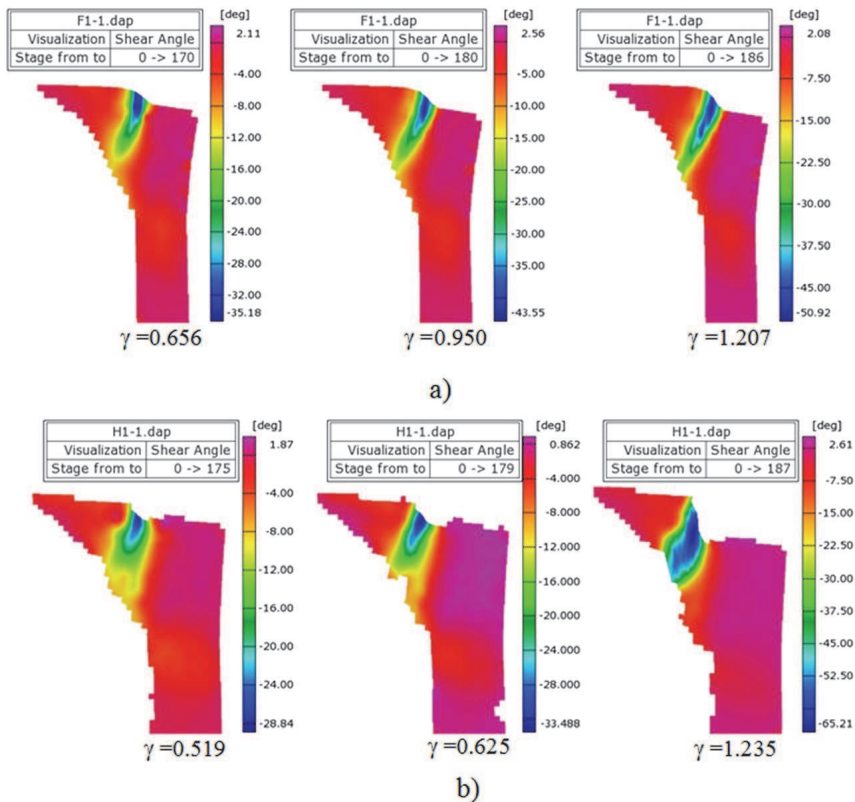
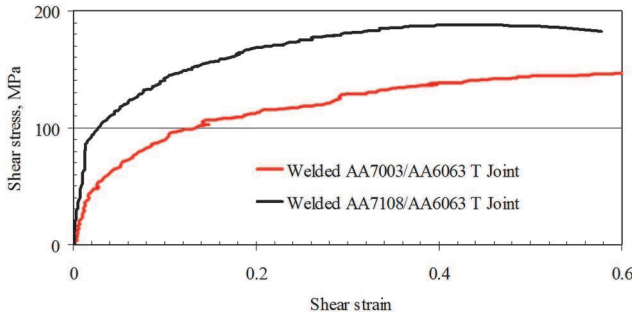


FIG. 5 Calculated shear strain–shear stress curves for the welded T-joint coupons corresponding to the applied load–measured shear angle data.



The corresponding shear stress–shear strain curve for both welded T-joint coupons was calculated based on the load–displacement curves recorded during the tensile–shear test. The shear strain values (in term of the shear angles) were obtained from the DIC strain maps. The shear angle calculations were based on six to eight selected points along the throat shear plane. The measured shear angles (α) were averaged over the entire shear zone and then converted to shear strain (γ) using $\gamma = \tan(\alpha)$ for each load step recorded (as shown in Fig. 4). The shear stress–shear strain curve calculated for both welded T joints is plotted in Fig. 5. Ideally, these two curves should overlap. The observed difference between the two curves is likely a consequence of the various weld defects present. As an example, Fig. 3(c) shows two types of defects present: porosity and lack of penetration.

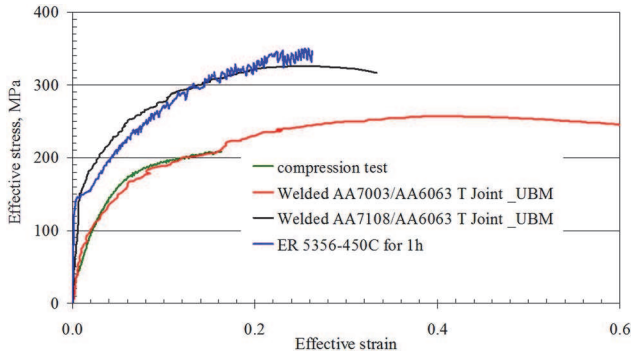
The microstructure of the fusion zone (Fig. 3(c)) was a typical cast structure, in which in-plane isotropy is usually reached [13]. Assuming this to be true, the von Mises yield criterion was used to convert the shear stress and shear strain to effective stress and effective strain using the following relationships:

$$(8) \quad \sigma_e = \sqrt{3} \cdot \tau$$

$$(9) \quad \varepsilon_e = \frac{\gamma}{\sqrt{3}}$$

Such calculations were necessary to help validate the empirically derived upper-bound stress model (Eq 7). The validation involved comparing the calculated effective stress of the ER5356 weld material with the effective stress–effective strain curve obtained during the uniaxial tensile test of the heat-treated cylindrical ER5356 weld wire and the uniaxial compression test of the rectangular ER5356 sample. This comparison is shown in Fig. 6. Ideally, these curves should overlap. Again, the observed difference between the set of curves is likely a consequence of

FIG. 6 Comparison of the calculated effective stress–effective strain curves of the isolated ER5356 weld materials and the welded T-joint coupons.



response of the uniaxial tensile sample lies above the remaining curves. The behavior is expected because the weld wire is essentially free of weld-induced macro- and micro-scale defects. It is noted that the effective stress–effective strain curve of the uniaxial compression sample followed the curve measured for the AA7003/AA6063 T-joint coupon very closely. It is this good agreement, albeit restricted to an effective strain up to about 0.16, that gives a level of confidence that the experimental approach derived is valid.

Conclusions

1. A novel technique for tension-shear testing of single-sided fillet arc-welded T-joint coupons was developed using an empirically derived upper-bound stress model coupled with DIC strain measurements and the use of modified welded T-joint coupon geometry.
2. The experimental results of single-sided fillet arc-welded AA7xxx/AA6063 T-joint coupons were successfully validated against the effective stress–effective strain behavior exhibited by uniaxial tensile and compression testing of the ER5356 material.
3. Tension-shear testing of single-sided arc-welded fillet AA7xxx/AA6063 T-joint coupons showed that failure occurred along the ER5356 weld throat shear plane. The variation in the effective tensile strengths of the ER5356 welds observed was likely a consequence of the various macro- and micro-defects present.

ACKNOWLEDGMENTS

The financial support of both the Initiative for Automotive Innovation (ORF Research Excellence) and General Motors of Canada Ltd. is greatly appreciated. Thanks to General Motors of Canada Limited for providing the welded T-joint configurations

for testing. Thanks also to D. Culley (Department of Materials Science and Engineering), D. Edmison (General Motors of Canada Ltd.), and K. Wong (Alcan Automotive Structures & Design) for their technical guidance with the experimental design of the tensile-shear measurements.

References

- [1] Staley, J. T. and Lege, D. J., "Advances in Aluminium Alloy Products for Structural Applications in Transportation," *J. Phys. IV*, Vol. 3, 1993, pp. 179–190.
- [2] Luijendijk, T., "Welding of Dissimilar Aluminum Alloys," *J. Mater. Proc. Technol.*, Vol. 103, No. 1, 2000, pp. 29–35.
- [3] Mossman, M. M. and Lippold, J. C., "Weldability Testing of Dissimilar Combinations of 5000- and 6000Series Aluminum Alloy," *Welding J.*, Vol. 81, 2002, pp. 188s–194s.
- [4] Gomez de Salazar, J. M. and Barrena, M. I., "Dissimilar Fusion Welding of AA7020/MMC Reinforced with Al₂O₃ Particles. Microstructure and Mechanical Properties," *Mater. Sci. Eng. A*, Vol. 352, Nos. 1–2, 2003, pp. 162–168.
- [5] Korbel, A., Embury, J. D., Hatherly, M., Martin, P. L., and Erbsloh, H. W., "Microstructural Aspects of Strain Localization in Al-Mg Alloys," *Acta Metall.*, Vol. 34, No. 10, 1986, pp. 1999–2009.
- [6] Sarkar, J., Kutty, T. R. G., Conlon, K. T., Wilkinson, D. S., Embury, J. D., and Lloyd, D. J., "Tensile and Bending Properties of AA5754 Aluminum Alloys," *Mater. Sci. Eng. A*, Vol. 316, Nos. 1–2, 2001, pp. 52–59.
- [7] *Welding Handbook*, 9th ed., Vol. 1, American Welding Society, Miami, 2001, pp. 247–256.
- [8] Kang, J., Wilkinson, D. S., Bruhis, M., Jain, M., Wu, P. D., Embury, J. D., Mishra, R. K., and Sachdev, A. K., "Shear Localization and Damage in AA5754 Aluminum Alloy Sheets," *J. Mater. Eng. Perform.*, Vol. 17, No. 3, 2008, pp. 395–401.
- [9] *ARAMIS—Deformation Measurement Using the Grating Method; User's Manual V4.7.4-2*, GOM GmbH, Braunschweig, Germany, 2001.
- [10] *Design of Fully Restrained Moment Connections per AISC LRFD*, 3rd ed., 2001, www.pdonline.org/courses/s154/s154content.pdf.
- [11] Avitzur, B., "Metal Forming: The Application of Limit Analysis," *Annu. Rev. Mater. Sci.*, Vol. 7, 1977, pp. 261–300.
- [12] Kamtekar, A. G., "A New Analysis of the Strength of Some Simple Fillet Welded Connections," *J. Constr. Steel Res.*, Vol. 2, No. 2, 1982, pp. 33–45.
- [13] Kang, J., McDermid, J. R., and Bruhis, M., "Determination of the Constitutive Behaviour of AA6022-T4 Aluminium Alloy Spot Welds at Large Strains," *Mater. Sci. Eng. A*, Vol. 567, 2013, pp. 95–100.

STP 1584, 2015 / available online at www.astm.org / doi: 10.1520/STP158420140058

Jidong Kang¹ and Kevin Gong²

Determination of Fracture Behavior of AA6060 Aluminum Alloy Extrusion Using Digital Image Correlation³

Reference

Kang, Jidong and Gong, Kevin, "Determination of Fracture Behavior of AA6060 Aluminum Alloy Extrusion Using Digital Image Correlation," *Evaluation of Existing and New Sensor Technologies for Fatigue, Fracture and Mechanical Testing*, STP 1584, Jidong Kang, David Jablonski, and David Dudzinski, Eds., pp. 13–31, doi:10.1520/STP158420140058, ASTM International, West Conshohocken, PA 2015.⁴

ABSTRACT

The dependence of fracture strain on stress triaxiality has been recently recognized as an important factor that controls the fracture of aluminum alloys. A number of experimental programs have been reported to determine fracture strains in a wide range of stress triaxiality using a variety of types of specimens. However, because of the lack of direct measurement of local strains near the fracture zone, indirect estimations of fracture strain are commonly used. The errors in determining fracture strain are uncertain. In this study we use the digital image correlation (DIC) method to determine the fracture strains in AA6060 aluminum extrusion material. This material is often used in automotive crash management systems. A commercially available DIC system was used to follow the deformation occurring during the tests of a set of newly designed specimens with a wide range of stress triaxiality; thus, the inception of instability and fracture can be captured and distinguished precisely. More importantly, post-experiment analysis in DIC allows strain calculations at macroscopic levels at

Manuscript received June 3, 2014; accepted for publication December 17, 2014; published online January 30, 2015.

¹CanmetMATERIALS, 183 Longwood Road South, Hamilton, Ontario, ON L8P 0A5, Canada.

²Constellium ASNA, 46555 Magellan Drive, Novi, MI 48377, United States of America.

³© Her Majesty the Queen in Right of Canada, as represented by the Minister of Natural Resources, 2015.

⁴ASTM Fourth Symposium on the *Evaluation of Existing and New Sensor Technologies for Fatigue, Fracture and Mechanical Testing* on May 7–8, 2014 in Toronto, Canada.

varying step sizes, thus, the dependence of fracture strain on gauge length has been determined in each testing condition. The fracture locus of AA6060 aluminum extrusion has been successfully determined and the concept of “scaled fracture strain” has then been proposed to ensure consistency of the fracture locus in both the experiment and in modeling.

Keywords

fracture criteria, stress triaxiality, digital image correlation, aluminum extrusion, AA6060

Introduction

Driven by the fuel economy and governmental regulations, the utilization of light-weight structural components, such as aluminum crash management systems (CMS), to replace steel ones is increasingly seen in more and more vehicle applications. However, fracture in the crash management system, e.g., a bumper beam fracture during a high-speed crash, has serious implications in meeting federal safety regulations. Unlike sheet metal forming, prediction of failure in aluminum extrusion structures has not received much attention until recently. The failure prediction of CMS in the development stage becomes so important because it will not only shorten the design and development time, but also drastically reduce the cost for full vehicle tests and often result in additional weight saving. Therefore, it is very critical to develop a reliable prediction of system failure to streamline the development process.

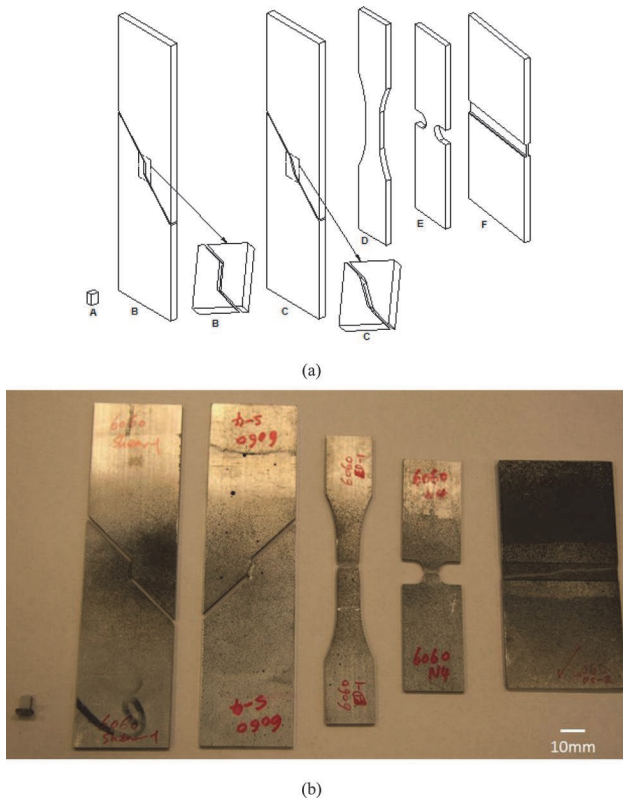
For sheet materials, the fracture forming limit diagram (FFLD) has been accepted as a standard practice to determine fracture limits under different strain paths that contain in-plane deformation modes. It is interesting to note that FFLD of metallic materials may simply fall into a straight line in the space of principle strains [1,2] where strain paths, such as uniaxial tension, plane-strain, and biaxial tension, are commonly used. Since the publication of the classical work of Bridgman on the influence of hydrostatic stress on fracture [3], a wealth of data have been reported on many aspects of ductile fracture from different points of view of researches [4–8]. More recently, in the equivalent strain–stress space, the dependence of fracture strain on stress triaxiality has been recognized as an important factor that controls the fracture of aluminum alloys [9,10]. A number of experimental programs have been reported to measure fracture strains in a wide range of triaxiality using a variety of types of specimen designs [9–14].

However, it is interesting to note that there still lacks direct measurements of fracture strains during testing, and errors in determining fracture strain are uncertain. In some specimen designs, the fracture strains are determined using the reduction of area measured by scanning electron microscopy or optical microscopy [2–4]. The measured fracture strains vary largely with the specimen geometry and size. In the other cases, the fracture strains are determined through combination of measurement and finite-element simulation, where a predetermined failure point is [9,10]. The accuracy of the determined fracture

strains is widely affected by the elements selected for the calculation because of the non-uniform distribution of stresses and strains in the fracture zone. Moreover, the size dependence of the finite-element mesh could result in even larger errors. In any of these techniques, the fracture strains are not directly measured during testing and errors in determining fracture strain are uncertain. For crash management systems made of aluminum extrusions, there is also a strong need to incorporate appropriate range of stress triaxiality that replicate the events occurring during the impact testing.

In this contribution, we focus our effort on determination of fracture strains in AA6060-T6, an aluminum extrusion material that is often used in automotive crash management systems. A set of newly designed specimens with a wide range of stress triaxiality is developed. Digital image correlation (DIC) is used to follow the deformation occurring during the tests, thus, the inception of instability and fracture can

FIG. 1 Specimen design: (a) drawings, and (b) specimens (from left to right): A, compression; B, shear; C, rotated shear; D, uniaxial tension; E, notched tension; and F, plane-strain tension.

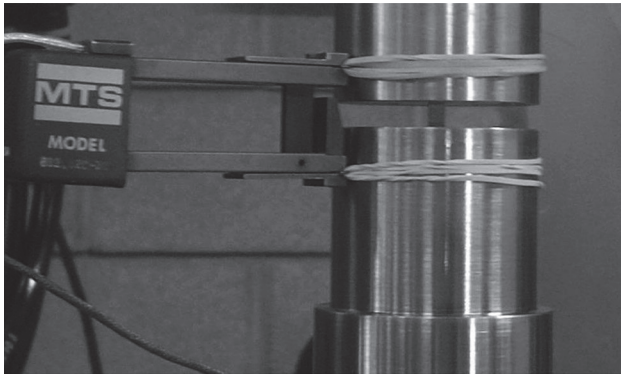


be captured and distinguished precisely. The dependence of fracture strain on gauge length will be determined in each testing condition. The concept of “scaled fracture strain” is then proposed to ensure consistency of the fracture locus in both the experiment and in modeling.

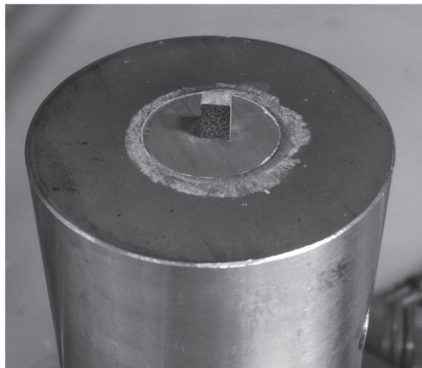
Experimental

The material used in the present study was AA6060-T6. After an intensive literature review of the existing specimen designs, a set of six types of specimens, as shown in Fig. 1, were developed in the present study, namely compression, shear, rotated shear (i.e., the axis of the shear zone is 20° with regard to the tensile axis), uniaxial tension, tensile specimen with a pair of notches in the radius of 4 mm (referred to

FIG. 2 Experimental setup of compression test: (a) actual setup, and (b) contact surface of the platen showing the circular carbide plate in the center. The compression specimen is 4 mm wide and 6 mm long.



(a)



(b)

as notched tension hereafter), and plane-strain tension. These specimen designs cover large stress triaxiality ranges occurring during the events of the impact testing in aluminum crash management systems. At least two valid tests were conducted and reported for each testing condition.

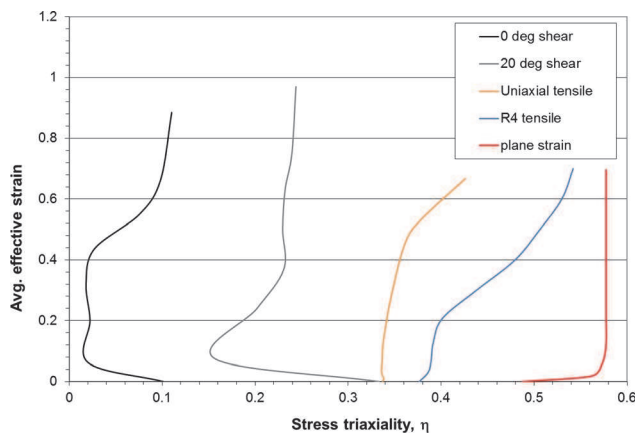
A new compression test was designed using a rectangular specimen of 6 mm long and 4 mm wide (Fig. 2). To ensure smooth and parallel surfaces of compressive platens, carbide plates were inserted into platens using adhesives (Fig. 2(b)). An extensometer was used to measure the displacement evolution during the testing. No lubricant was used in the contact areas between the specimen and the top and bottom platens.

A modified shear specimen [15,16] was used in the shear and rotated shear tests. In this new shear test specimen geometry, as in the appendix of ASTM B831-14 [16], a pair of notches 0.25 mm thick on both sides of the specimen were machined using sinker electrical discharge machining to ensure a simple shear state in the shear zone. In the meantime, as the thickness of the shear zone is reduced, the width of the shear zone is accordingly reduced from 1.6 mm, as specified in the main text of the ASTM standard, to 1.2 mm to prevent buckling of the specimen.

The notched tension specimen was used in the present study to obtain higher triaxiality than uniaxial tension. Care has been taken in specimen design to ensure that strain distribution in the minimum cross section between the notches is as uniform as possible when approaching fracture. In other words, when fracture occurs, the strains at the notch tip and in the center of the minimum cross section are sufficiently close.

The plane-strain tension specimen is similar to the one used in Ref 17, except a 4" width, is used to ensure true plan strain condition (Fig. 1(a), specimen F).

FIG. 3 Calculated stress triaxiality using finite-element analysis.



2D or 3D elastic–plastic finite-element analysis was performed to determine stress triaxiality up to large strains using LS-DANA [18]. The results are shown in Fig. 3. As reported in the earlier studies, stress triaxiality is usually not constant during the deformation processes [9–14]. An average value of the stress triaxiality was then calculated for each testing condition as follows [9],

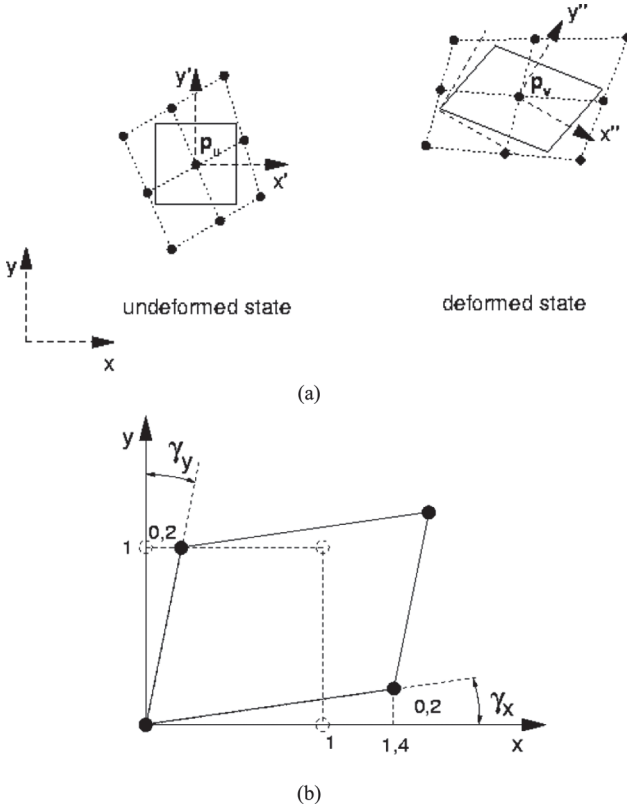
$$(1) \quad \eta = \frac{1}{\bar{\epsilon}_f} \int_0^{\bar{\epsilon}_f} \frac{\sigma_m}{\bar{\sigma}} d\bar{\epsilon}$$

where:

$\bar{\epsilon}$, $\bar{\epsilon}_f$, σ_m , and $\bar{\sigma}$ = equivalent strain, equivalent strain to fracture, hydrostatic stress, and equivalent stress, respectively.

All tests were carried out using a hydraulic test frame. A nominal strain rate of 6×10^{-6} /s was used by controlling the cross-head movement speed during the tests.

FIG. 4 Strain calculation in digital image correlation using Aramis: (a) 3×3 neighborhood for 2D strain calculation, and (b) shear strain calculation [19].



A commercially available optical strain mapping system based on DIC, was used to follow deformation occurring during each test. The principle of DIC is based on the fact that the distribution of grayscale values of a rectangular area (facet) in the initial image corresponds to the distribution of grayscale values of the same area in the destination image [19]. Prior to the testing, a black-and-white ink pattern was spray painted on the specimen surface. A cumulative strain map can be obtained by comparing each current deformed image with the initial image. The DIC measurements were made from a set of snapshots collected automatically at a frame rate of one frame per second during the tests. After the tests, the captured images were further processed to obtain the full-field strain maps using the DIC system. A calibration procedure was established, which ensured that the measuring error in strain is distributed randomly with a maximum error of 0.25 % over a range of in-plane displacement from 3 to 3 mm and out-of-plane displacement from 0.6 to 0.6 mm. In all the experiments we carried out, the parameters for DIC calculations have been carefully chosen such that the smallest step size used is equivalent to a 0.25-mm gauge length on the real specimens. The overlap of the facet size and step size is 20 %.

Strain is the measure for the deformation of a line element and can be defined as [19–21]

$$(2) \quad \lambda = \lim_{l \rightarrow 0} \left(\frac{l + \Delta l}{l} \right)$$

FIG. 5 Engineering-stress–engineering-strain curve of AA6060-T6 from the compression test. Also shown is the actual compression specimen before and after the testing.

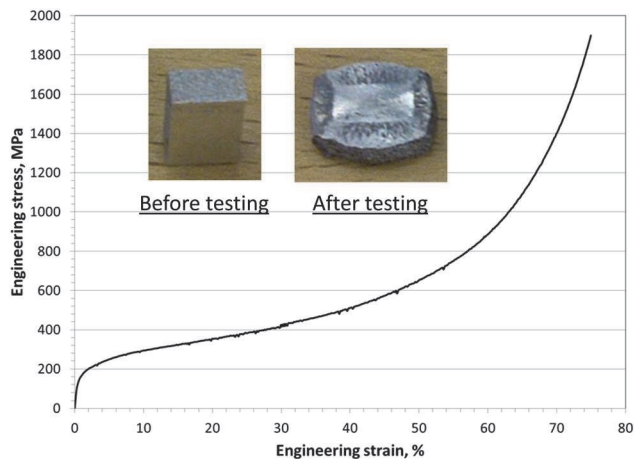
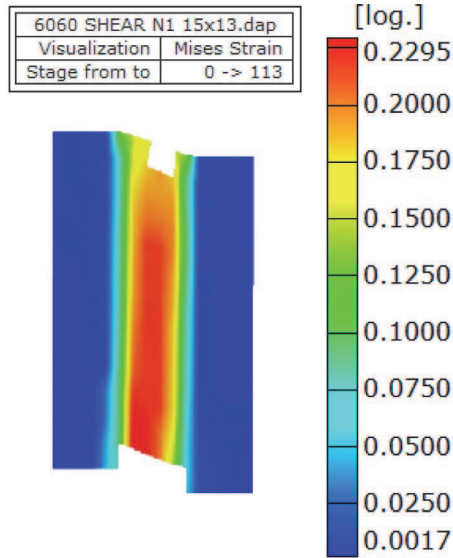
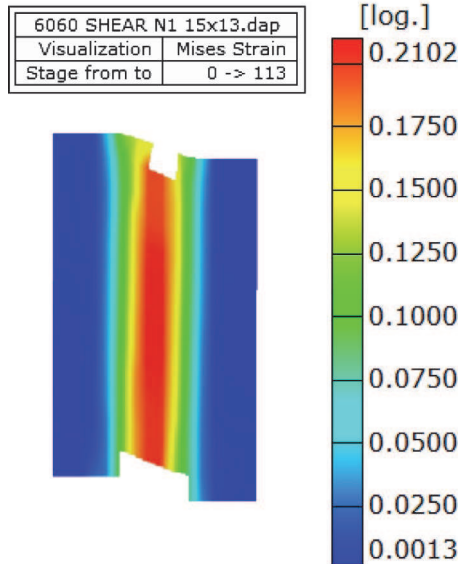


FIG. 6 Measured fracture strains in a shear specimen using different virtual gauge lengths: (a) 0.5 mm, and (b) 1.0 mm.

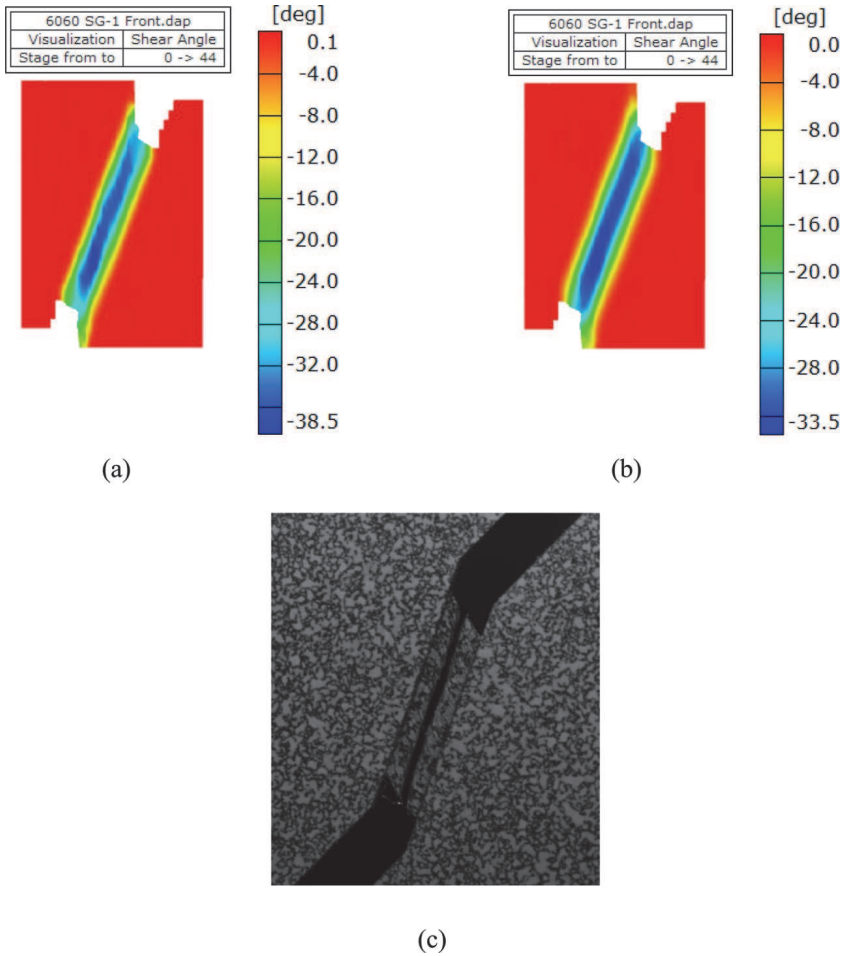


(a)



(b)

FIG. 7 Measured fracture strains in a rotated shear specimen using different virtual gauge lengths: (a) 0.5 mm, (b) 1.0 mm, and (c) actual fractured specimen showing that fracture occurs in shear mode.



where:

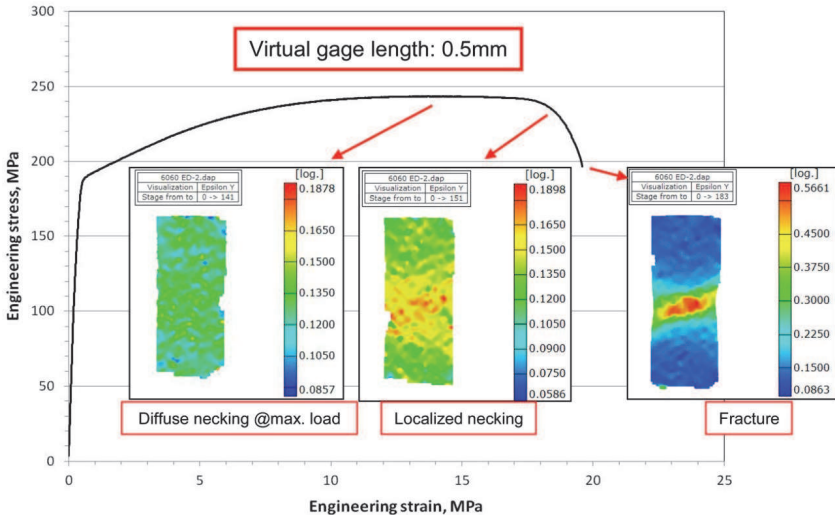
λ = the relative elongation of an infinitesimal line element, i.e., a local gauge length.

Engineering strain ε_{eng} and true strain ε_t can then defined as

$$(3) \quad \varepsilon_{\text{eng}} = \lambda - 1$$

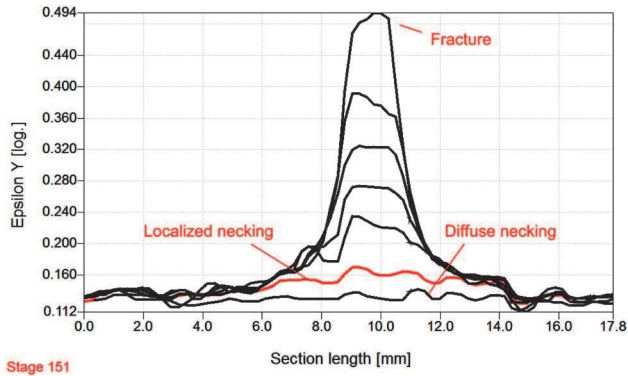
$$(4) \quad \varepsilon_t = \ln(\lambda)$$

FIG. 8 Engineering-stress-engineering-strain curve of AA6060-T6 alloy extrusion.



In DIC strain measurements, a number of neighboring points are usually used to calculate the strain field [21]. For example, a typical 3×3 neighborhood is used for the 2D strain calculation (Fig. 4(a)). As such, the local gauge length is then the spacing between the left and right points in Fig. 4(a), i.e., double of the spacing of the immediate neighboring points, or the step size, as it is referred to in Ref 21. One can simply vary the step size in the DIC calculations to vary the local gauge length; for example, to use 5×5 , 7×7 , or 9×9 neighborhood points. In the present study,

FIG. 9 Line scan of strain distribution in the middle of a uniaxial tensile specimen.



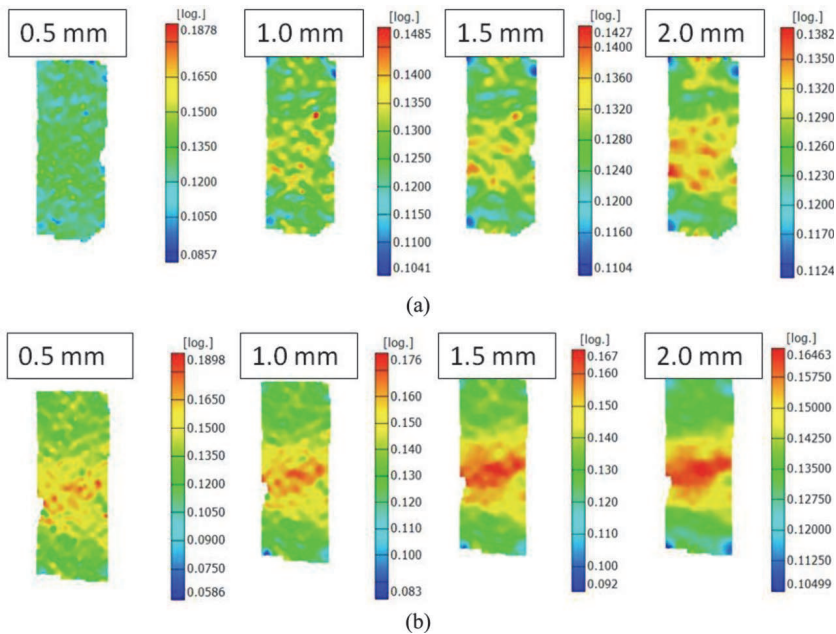
local gauge lengths of 0.5 mm, 1.0 mm, 1.5 mm, and 2.0 mm were used for all tensile tests (i.e., uniaxial tension, notched tension, and plane-strain tension), and 0.5 mm and 1.0 mm for the shear and rotated shear tests.

It is noted that the shear strains were measured through the shear angles [16,21]. The shear angle is defined as the change of an angle of 90° in the undeformed state to a new angle in the deformed state (Fig. 4(b)). Note that, in Fig. 4(b), the shear angle $\theta = \theta_x + \theta_y$. The measured shear angles, θ , were averaged over the entire shear zone and then converted to shear strain, γ , using $\gamma = \tan(\theta)$.

Results and Discussion

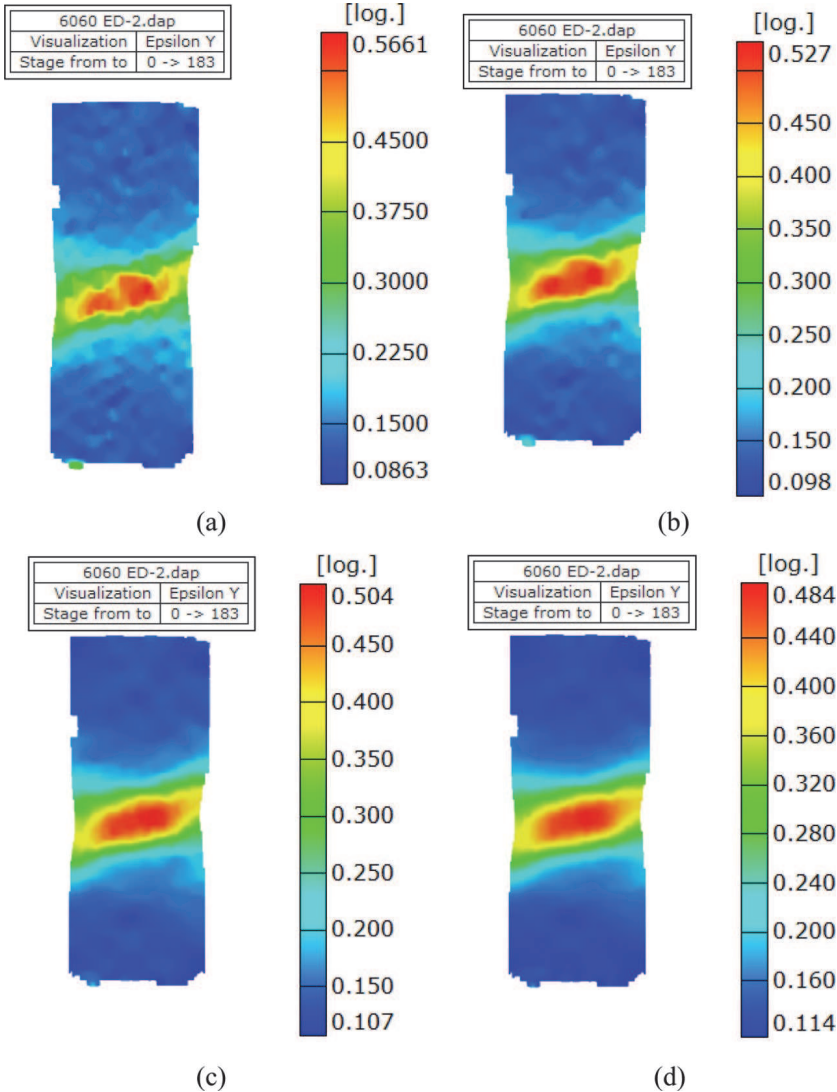
It is interesting to note that no fracture occurs in the compression tests at very large strain (Fig. 5). Note that 75 % strain, as shown in Fig. 5, was the measuring limit of the extensometer used. DIC was initially used to follow the deformation until a strain of 20 % and then the spray ink pattern cannot be tracked any more. Therefore, a triaxiality of -0.25 and a fracture strain of 0.7 was taken for the compression testing based on the strain measurement using the extensometer.

FIG. 10 Measured instability strains in a uniaxial tensile specimen using different virtual gauge length (a) strain to diffuse necking, and (b) strain to localized necking. In labels, 0.5 mm, 1.0 mm, 1.5 mm, and 2.0 mm represent the virtual gauge length used in the strain calculations.



For both the shear and rotated shear tests, fracture occurs in shear mode as shown in Figs. 6 and 7. As discussed in the previous study [15], simple shear state is realized in the shear specimen geometry used, we define fracture as the point where the shear force reaches its maximum value. Fracture strain is then reported as the effective strain converted from the measured shear strain at maximum load based

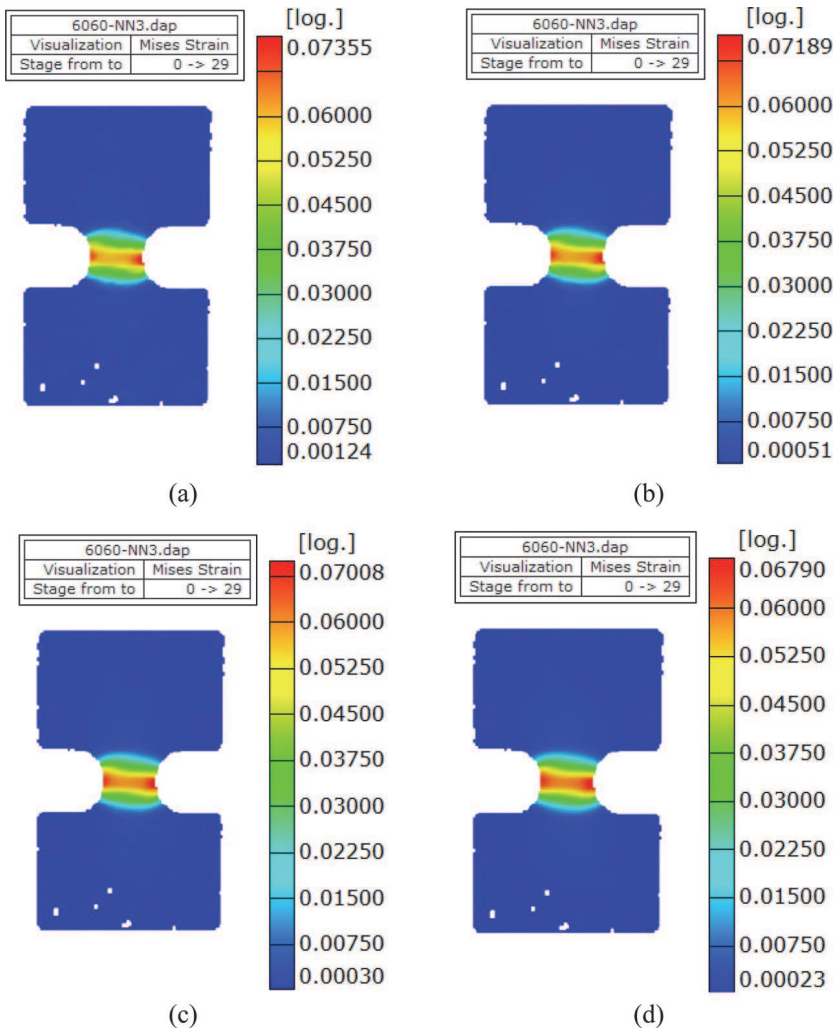
FIG. 11 Measured fracture strains in a uniaxial tensile specimen using different virtual gauge lengths: (a) 0.5 mm, (b) 1.0 mm, (c) 1.5 mm, and (d) 2 mm.



on the von Mises yield criteria. For the rotated shear specimen, i.e., the shear zone rotated 20° with regard to the loading axis, it also fractures in shear in nature. Thus, the in-plane shear strain at maximum load is used to report the fracture strain based on von Mises yield criteria as well.

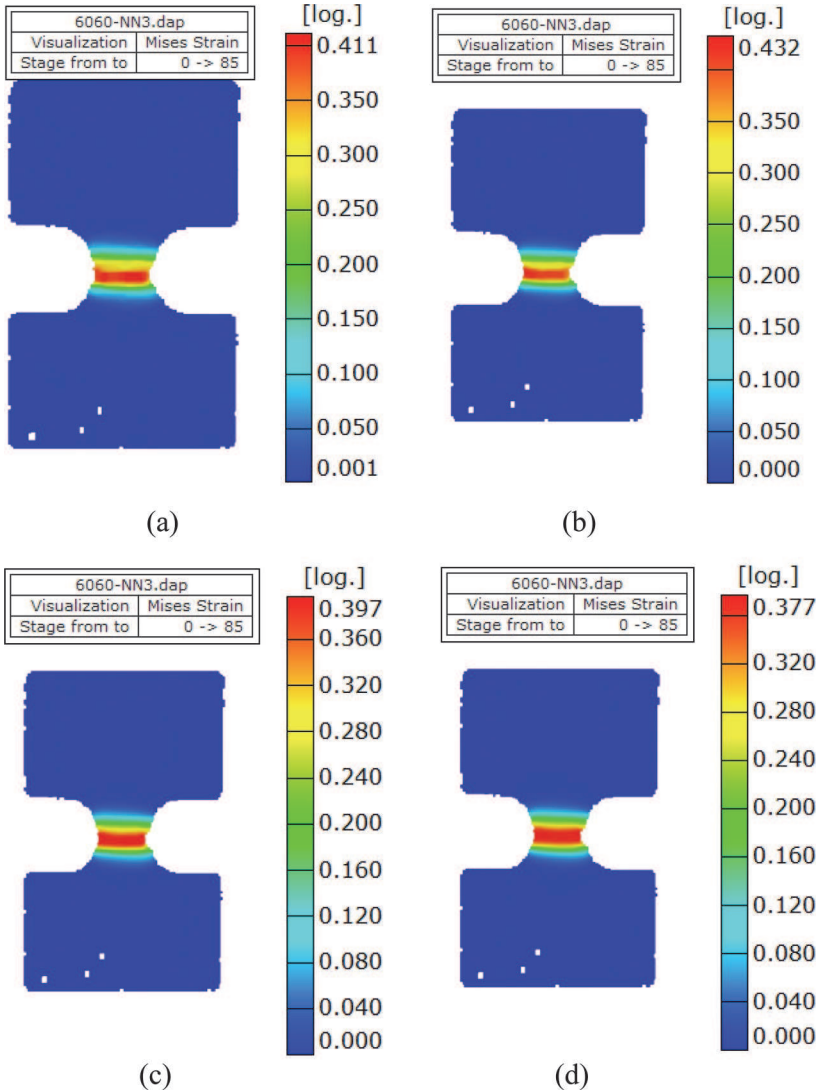
From the tensile stress–strain curve and DIC maps (Fig. 8), it is clear that the AA6060-T6 extrusion used in the present study shows progressive diffuse necking at maximum loading, localized necking, and final fracture during the test, as shown

FIG. 12 Measured instability strains in a notched tensile specimen using different virtual gauge lengths: (a) 0.5 mm, (b) 1.0 mm, (c) 1.5 mm, and (d) 2 mm.



in other aluminum alloy sheets, such as AA5754 [22]. The strain to either the diffuse necking or the localized necking is often called strain to instability. Noticeably, it is more evident to distinguish localized necking from diffuse necking when using strain distribution on line scan in the center of the specimen (Fig. 9). In other words, it is more convenient in practical applications to use strain to maximum

FIG. 13 Measured fracture strains in a notched tensile specimen using different virtual gauge lengths: (a) 0.5 mm, (b) 1.0 mm, (c) 1.5 mm, and (d) 2 mm.



loading to define strain to instability in all tensile cases. Figure 10(a) and 10(b) shows the measured strains to diffuse necking and localized necking, respectively. The fracture strain in uniaxial tension is determined as the final step prior to any visible fracture appearing on the specimen surface (Fig. 11).

When designing the notched tension specimen, it is hoped that the strain distribution is sufficiently uniform at the minimum cross section when approaching fracture. From the actual DIC strain maps, it is interesting to note that even strain at the notch tip is the highest at maximum load (Fig. 12), fracture strain becomes more uniform when approaching fracture (Fig. 13). These results confirmed that the measured fracture strain represents the location where the highest stress triaxiality exists in the notched tension specimen used in the present study.

In the plane-strain tension specimens, shear banding appears at maximum loading (Fig. 14) leading to the final fracture (Fig. 15). Fracture strain is then defined as the strain at the initiation of the fracture.

Generally speaking, for all the virtual gauge lengths (0.5 to 2.0 mm) used in the present study, instability strains vary slightly with gauge length in uniaxial, notched, and plane-strain tension cases (see Figs. 10, 12, and 14). The instability strains at a

FIG. 14 Measured instability strains in a plane-strain tensile specimen using different virtual gauge lengths: (a) 0.5 mm, (b) 1.0 mm, (c) 1.5 mm, and (d) 2 mm.

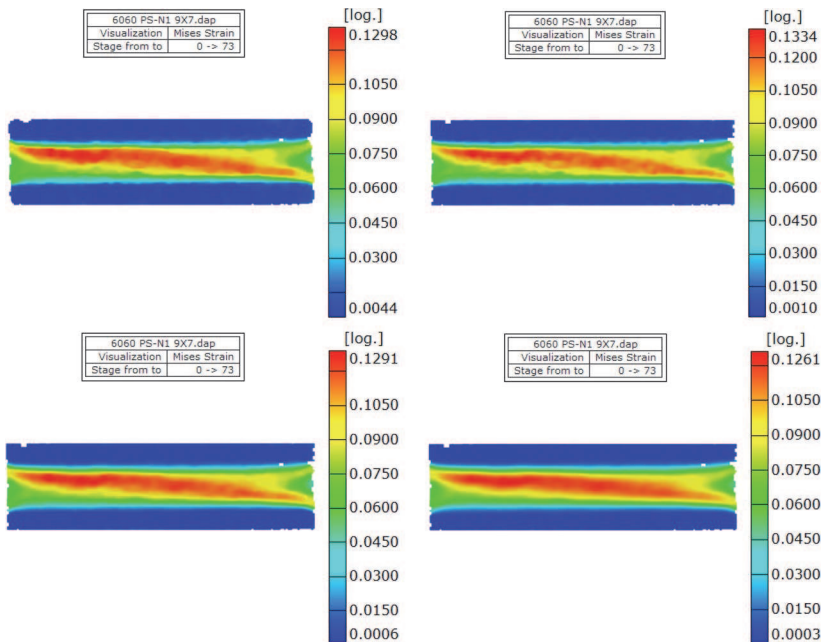
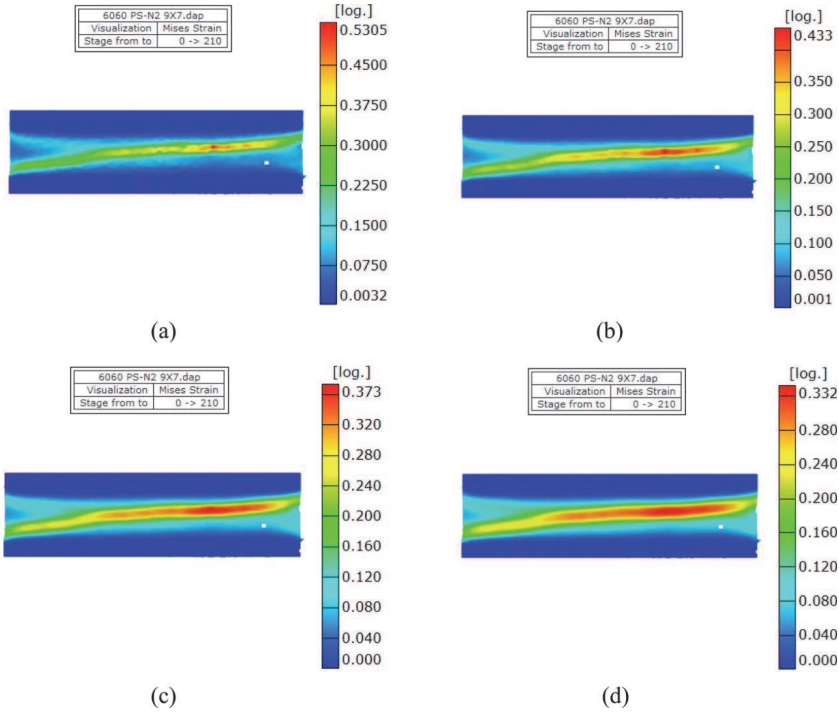


FIG. 15 Measured fracture strains in a plane-strain tensile specimen using different virtual gauge lengths: (a) 0.5 mm, (b) 1.0 mm, (c) 1.5 mm, and (d) 2 mm.



virtual gauge length of 0.50 mm are, therefore, plotted versus stress triaxiality in [Fig. 16](#).

Also shown in [Fig. 16](#) is the plot of the relationship between the experimental fracture locus versus stress triaxiality at a virtual gauge length of 0.5 mm. Following the approach used by Bao and Wierzbicki [9], and the vertical asymptote assumption at stress triaxiality of $-1/3$ [23,24], the experimental fracture locus is fitted into three equations as follows,

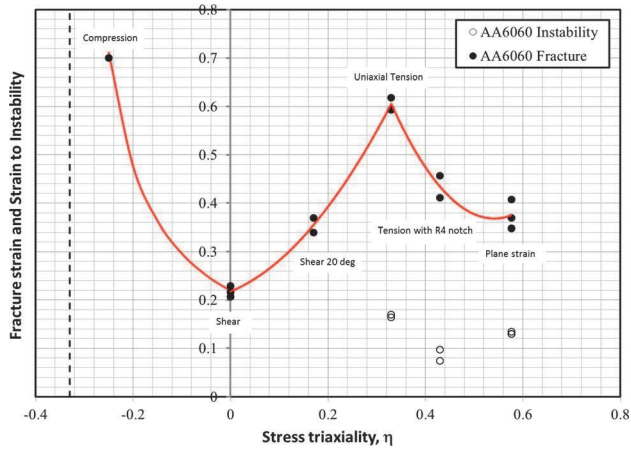
$$(5) \quad \bar{\epsilon}_f = 0.86 * \left(\eta + \frac{1}{3} \right)^{-0.85} \quad \text{for} \quad -\frac{1}{3} < \eta \leq 0$$

$$(6) \quad \bar{\epsilon}_f = 2.31\eta^2 + 0.41\eta + 0.22 \quad \text{for} \quad 0 \leq \eta \leq 0.33$$

$$(7) \quad \bar{\epsilon}_f = 5.31\eta^2 - 5.75\eta + 1.92 \quad \text{for} \quad 0.33 \leq \eta \leq 0.577$$

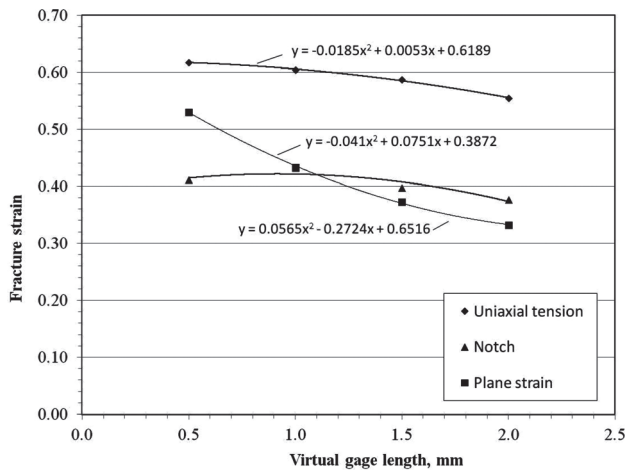
When plotting fracture strains versus gauge length for the three tensile cases, i.e.,

FIG. 16 Measured strains to instability and fracture strains versus stress triaxiality relation in AA6060.



strains vary nonlinearly with gauge length differently in each case (Fig. 17). The fitting equations shown in Fig. 17 can be used to calculate the “scaled fracture strains,” thus, fracture strain can be compared experimentally and numerically if different gauge lengths are used. This is an important but often neglected fact in practice.

FIG. 17 Influence of virtual gauge length on measured fracture strains.



Conclusions

A set of specimens with a wide range of stress triaxiality have been designed for AA6060 aluminum extrusion material to replicate the events occur during the impact testing of aluminum crash management systems. Digital image correlation has been used to determine fracture strains in the specimens; thus, the inception of instability and fracture can be captured and distinguished precisely. The fracture locus of AA6060 aluminum extrusion has been successfully determined and the concept of “scaled fracture strain” has then been proposed to ensure consistency of the fracture locus in both the experiment and modeling.

ACKNOWLEDGMENTS

The writers are grateful to the financial support from the Interdepartmental Federal Government Program on Energy R&D (PERD) and CanmetMATERIALS, Natural Resources Canada. In-kind contribution and technical support from Constellium ANSA and Kaiser Aluminum are acknowledged. The writers thank Mr. Jie Liang at CanmetMATERIALS for help on mechanical testing.

References

- [1] Lee, Y. W., 2004, “Fracture Prediction in Metal Sheets,” Ph.D. thesis, Massachusetts Institute of Technology, Cambridge, MA.
- [2] LeRoy, G. and Embury, J. D., *Formability, Analysis, Modeling, and Experimentation*, S. S. Hecker, A. K. Ghosh, and H. L. Gegel, Eds., TMS-AIME, Warrendale, PA, 1978, pp. 183–207.
- [3] Bridgman, P. W., *Studies in Large Plastic Flow and Fracture*, Harvard University Press, Cambridge, MA, 1964.
- [4] McClintock, F. A., “A Criterion of Ductile Fracture by the Growth of Holes,” *J. Appl. Mech.*, Vol. 35, No. 2, 1968, pp. 363–371.
- [5] Rice, J. R. and Tracey, D. M., “On the Ductile Enlargement of Voids in Triaxial Stress Fields,” *J. Mech. Phys. Solids*, Vol. 17, No. 3, 1969, pp. 201–217.
- [6] Hancock, J. W. and Mackenzie, A. C., “On the Mechanisms of Ductile Failure in High-Strength Steels Subjected to Multi-Axial Stress-States,” *J. Mech. Phys. Solids*, Vol. 24, No. 2–3, 1976, pp. 147–169.
- [7] Atkins, A. G., “Fracture in Forming,” *J. Mater. Proc. Technol.*, Vol. 56, Nos. 1–4, 1996, pp. 609–618.
- [8] Thomason, P. F., *Ductile Fracture of Metals*, Pergamon Press, Oxford, 1990.
- [9] Bao, Y. B. and Wierzbicki, T., “On Fracture Locus in the Equivalent Strain and Stress Triaxiality Space,” *Int. J. Mech. Sci.*, Vol. 46, No. 1, 2004, pp. 81–98.
- [10] Wierzbicki, T., Bao Y., Lee, Y.-W., and Bai, Y., “Calibration and Evaluation of Seven Fracture Models,” *Int. J. Mech. Sci.*, Vol. 47, Nos. 4–5, 2005, pp. 719–743.

- [11] Bao, Y. and Wierzbicki, T., "A Comparative Study on Various Ductile Crack Formation Criteria," *J. Eng. Mater. Technol.*, Vol. 126, No. 3, 2004, pp. 314–324.
- [12] Zadpoor, A. A., Sinke, J., and Benedictus, R., "Formability Prediction of High Strength Aluminum Sheets," *Int. J. Plasticity*, Vol. 25, No. 12, 2009, pp. 2269–2297.
- [13] Neukamm, F., Feucht, M., and Haufe, A., "Consistent Damage Modeling in the Process Chain of Forming to Crashworthiness Simulations," LS-DYNA, Livermore, CA, 2008.
- [14] Neukamm, F., Feucht, M., and Haufe, A., "Considering Damage History in Crashworthiness Simulations," LS-DYNA, Livermore, CA, 2009.
- [15] Kang, J., Wilkison, D. S., Wu, P. D., Bruhis, M., Jain, M., Embury, J. D., and Mishra, R., "Constitutive Behavior of AA5754 Sheet Materials at Large Strains," *J. Eng. Mater. Technol.*, Vol. 130, No. 3, 2008, p. 031004.
- [16] ASTM B831-14: Standard Test Method for Shear Testing of Thin Aluminum Alloy Products, *Annual Book of ASTM Standards*, West Conshohocken, PA, 2014, www.astm.org.
- [17] Spencer, K., Corbin, S. F., and Lloyd, D. J., "Notch Fracture Behavior of 5754 Automotive Aluminum Alloys," *Mater. Sci. Eng.*, Vol. A332, 2002, pp. 81–90.
- [18] *LSTC; LS-DYNA*. (2013). Livermore Software Technology Corporation, Livermore, CA.
- [19] Sutton, M., Ortu, J.-J., and Schreier, H. W., *Image Correlation for Shape, Motion and Deformation Measurements*, Springer, New York, 2009.
- [20] Malvern, L. E., *Introduction to the Mechanics of a Continuous Medium*, Prentice Hall, Englewood Cliffs, NJ, 1969.
- [21] *Aramis User's Manual; Software Version 6.3.1*. (2011). GOM mbH, Braunschweig, Germany.
- [22] Kang, J., Wilkinson, D. S., Jain, M., Embury, J. D., Beaudoin, A. J., Kim, S., Mishra, R., and Sachdev, A. K., "On the Sequence of Inhomogeneous Deformation Processes Occurring During Tensile Deformation of Strip Cast AA5754," *Acta Mater.*, Vol. 54, 2006, pp. 209–218.
- [23] Wierzbicki, T. and Werner, H., "Cockcroft and Latham Revisited," Impact & Crashworthiness Laboratory, *Report No. 16*, MIT, Cambridge, MA, 1998.
- [24] Kudo, H. and Aoi, K., "Effect of Compression Test Conditions Upon Fracturing of Medium Carbon Steel," *J. Japan. Soc. Technol. Plasticity*, Vol. 8, 1967, pp. 17–27.

STP 1584, 2015 / available online at www.astm.org / doi: 10.1520/STP158420140056

B. W. Williams,¹ K. P. Boyle,² L. Blaga,² and J. McKinley²

Advanced Characterization of Sheet Metal Deformation and Forming Using Digital Image Correlation

Reference

Williams, B. W., Boyle, K. P., Blaga, L., and McKinley, J., "Advanced Characterization of Sheet Metal Deformation and Forming Using Digital Image Correlation," *Evaluation of Existing and New Sensor Technologies for Fatigue, Fracture and Mechanical Testing*, STP 1584, Jidong Kang, David Jablonski, and David Dudzinski, Eds., pp. 32–55, doi:10.1520/STP158420140056, ASTM International, West Conshohocken, PA 2015.³

ABSTRACT

Advanced testing methods are required in order to accurately characterize the deformation and failure behaviour of anisotropic sheet metals. Full-field strain mapping techniques using digital image correlation (DIC) offer improved spatial and temporal measurement of material deformation, which allows yield and forming limit criteria to be assessed with greater fidelity. In the current work, full-field strain mapping was applied to characterize the biaxial flow response of anisotropic sheet metal. Full-field strain measurements, combined with analytical methods, allowed for the flow response to be measured for pure biaxial stress paths. It was found that the DIC strain data could be used to accurately predict the biaxial hardening response of sheet materials to high levels of effective strain, much higher than the uniform strain obtained from a tensile test. To adequately describe the hardening response of the material at these high levels of strain it was necessary to account for the anisotropy of the sheet. Full-field strain mapping techniques were also used to study forming response of

Manuscript received May 30, 2014; accepted for publication January 26, 2015; published online February 20, 2015.

¹CanmetMATERIALS, Natural Resources Canada, Hamilton, Ontario, L8P 0A5, Canada (Corresponding author), e-mail: Bruce.Williams@NRCan-RNCan.gc.ca

²CanmetMATERIALS, Natural Resources Canada, Hamilton, Ontario, L8P 0A5, Canada.

³ASTM Fourth Symposium on the *Evaluation of Existing and New Sensor Technologies for Fatigue, Fracture and Mechanical Testing* on May 7–8, 2014 in Toronto, Canada.

anisotropic sheet metal. Advantages of DIC included the capability to determine the forming response at strain-rates approaching those in stamping operations and the ability to vary the gauge length in the strain measurement for analysis after the test was performed.

Keywords

biaxial bulge, anisotropy, yield function, r value, forming

Introduction

Wrought sheet alloys that are being considered to reduce vehicle weight and fuel consumption include advanced high strength steel, aluminum, titanium, and magnesium alloys. The deformation behaviour of these alloys can be complex and there is the requirement to develop more advanced testing methodologies to calibrate and validate constitutive material models. For example, both magnesium and titanium alloys have a hexagonal closed packed (hcp) crystal structure with a pronounced anisotropic and tension/compression asymmetric behaviour that requires advanced yield functions to describe the accurate deformation behaviour [1–4].

It is often necessary to extrapolate the tensile stress versus strain behaviour to high levels of strain to describe the hardening behaviour in material models. The biaxial stress versus strain response of sheet metal was shown to describe the flow response of sheet material to higher strains than obtained in a tensile test [5]. Recently, a draft International Organization for Standardization (ISO) standard was proposed for the measurement of the biaxial stress versus strain curve measured using digital image correlation (DIC) systems [6]. One advantage to the use of full-field strain mapping DIC in the biaxial test is that the deformation of the sheet can be accurately measured to high levels of deformation, compared to most previous methodologies that relied partly on the deformation (specifically, the radius of curvature) being described by theoretical equations. One drawback of the biaxial flow test is that the stress versus strain behaviour must be adjusted to account for the anisotropy of the sheet in order to accurately describe the flow behaviour [5,7].

To characterize the anisotropy of sheet metal it is important to measure r values of the sheet during deformation. Chamanfar and Mahmudi [8,9] studied the effect of gauge length and specimen geometry on r values of interstitial free (IF) steel and Grade 2 commercially pure titanium (CP-Ti) sheet. It was found that gauge length and specimen geometry could influence the calculated r value for IF sheet with a measured range from 2.0 to 2.6. For Grade 2 CP-Ti, the r value could range from 2 to 7, depending on the gauge length, specimen geometry, and strain level [7,9]. One advantage of DIC strain measurement is that the gauge length can be modified in the strain calculations after the test is performed, to study the influence of gauge length on r value.

Another challenge in the study of lightweight sheet metals is the comparison of forming limits measured for different materials that can experience diffuse necking, localized necking, or brittle fracture [10]. In the current work, full-field strain mapping DIC techniques are used to measure the forming behaviour of anisotropic sheet metals. The advantage of DIC is that the gauge length used to compute the strain can be varied, allowing the influence of gauge length on the forming limit to be studied. Using traditional methods [11] to measure the forming limit also requires the test to be stopped upon the onset of necking, which results in forming limit curve being measured at strain-rates much lower than in stamping operations. Another advantage of DIC strain measurement is that the forming behaviour can be measured at strain-rates representative of stamping operations, which is of advantage for sheet metals that are strain-rate sensitive, such as magnesium alloys, at warm forming temperatures [12].

The objective of the current work is to measure the biaxial stress versus strain response and correctly adjust for the anisotropy of the sheet metal. Both interstitial free steel sheet and commercially pure titanium sheet are considered. The Hill48 and Cazacu-Barlat 2004 [1,4] yield functions are used to capture the anisotropic deformation behaviour of the sheet materials. Additionally, the forming behaviour under pure biaxial and near plane strain conditions are studied for anisotropic sheet metals, specifically commercially pure titanium sheet and a ZEK100 magnesium alloy sheet. The influence of varying the gauge length utilized in the strain computation on the forming behaviour is studied.

Experimental Method

MATERIALS

Three sheet materials were used in the current study, a 0.92 mm thick ASTM B265 Grade 1 commercially pure titanium (CP-Ti) sheet, a continuously annealed 0.83 mm thick interstitial-free steel sheet and a 1.65 mm thick ZEK100 magnesium alloy sheet supplied in the O temper. Tensile and biaxial bulge tests were carried out using the CP-Ti sheet. Biaxial bulge tests were also performed using the IF steel sheet. The forming behaviour response was characterized for the CP-Ti and ZEK100 sheet.

UNIAXIAL TENSILE TESTING

Room temperatures tensile tests were conducted on CP-Ti in the sheet rolling direction at an initial strain-rate of 0.001 s^{-1} , which was based on the displacement rate of the test divided by the gauge length of the sample. Testing at a strain-rate 0.001 s^{-1} was also conducted on samples machined at different orientations relative to the rolling direction of the sheet, including orientations of 22.5, 45, 67.5, and 90° . The tensile specimens had a gauge length of 40 mm and a width of 10 mm and two [13] was used to measure

the major and minor strain during the test. Strain was also measured in the loading direction using an extensometer with a 25.4 mm gauge length.

BIAXIAL BULGE TEST

Hydroforming using a 500-ton Interlaken press was used to carry out room temperature biaxial bulge tests on CP-Ti and IF sheet. To reduce the amount of bending at the pole, a 150 mm die aperture diameter was used in the design as opposed to the more commonly-used 100 mm die aperture diameter. The corner radius of the die was 6.35 mm. The sample was first clamped with a force of about 300-ton followed by hydroforming to failure. If a constant volume of water was applied during the test, then the strain-rate would vary during the test as the specimen deforms. In the current work, the volume of water was varied during the test by changing the water cylinder stroke to achieve an approximately constant strain-rate, as will be shown in the section “Biaxial Bulge Test Results for IF Steel and Commercially Pure Titanium.” The DIC system was located at a distance of about 1 m from the sample and a mirror was used to project the image at 45° (see Fig. 1). To verify that the DIC system was providing accurate displacement measurements, bulged samples (that were not failed) were also measured using a laser profilometer. A qualitative comparison of the bulge measured by the DIC system and the laser profilometer are shown in Fig. 2, indicating good agreement.

The true biaxial stress, σ_b , can be calculated according to Ref. [14]

$$(1) \quad \sigma_b = \frac{\rho P}{2t}$$

where:

ρ = the radius of curvature,

P = the applied pressure, and

FIG. 1 Depiction of biaxial bulge test setup in hydro/gas forming press.

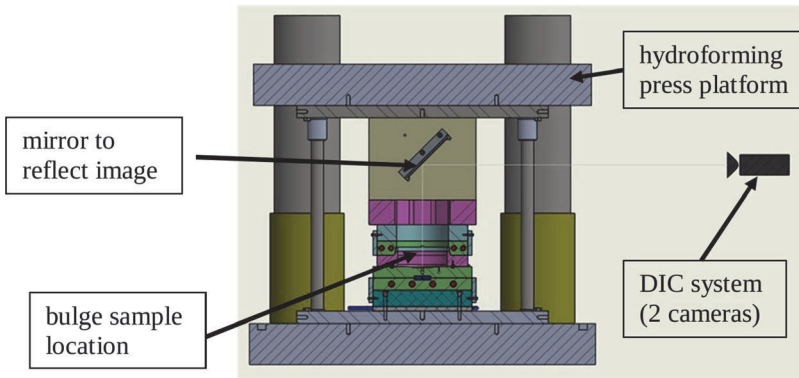
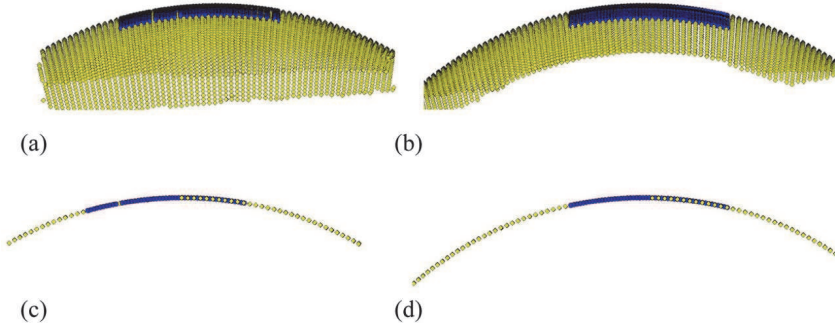


FIG. 2 Comparison of xyz measurements of the formed dome using ARAMIS (yellow) and laser profilometer (blue) (a) yz-plane, (b) xz-plane, (c) line section from centre of sample on yz-plane, and (d) line section from centre of sample on xz-plane.



t = the current thickness of the sheet, which can be determined by

$$(2) \quad t = t_0 \exp(\varepsilon_{zz})$$

where:

$\varepsilon_{zz} = -(\varepsilon_{xx} + \varepsilon_{yy})$ as the thickness strain, and

t_0 = the initial sheet thickness.

In these equations, x , y , and z correspond to the rolling, transverse, and thickness directions, respectively. The xyz coordinates measured by DIC are then used to calculate the a , b , c coefficients of an ellipsoid described by

$$(3) \quad \frac{x^2}{a^2} + \frac{y^2}{b^2} + \frac{z^2}{c^2} = 1$$

by performing a least-squares regression analysis. For pure biaxial conditions, in which the in-plane stress in the rolling direction is equal to the stress in the transverse direction (stresses due to bending are assumed negligible), the parameter $a = b$. The radius of curvature can then be determined using geometry relationships for an ellipsoid. Although the die was 150 mm in diameter, only DIC data within a diameter of 80 mm was used in the least-squares regression. Alternatively, the radius of curvature can be computed from theoretical relationships. A relationship used in the current work for comparison with the radius of curvature calculated from the DIC data is given by [14,15]

$$\rho = \frac{r_c^2 + h_d^2}{2h_d}$$

where:

r_c = the radius of the die (75 mm), and

h_d = the deformed height of the bulged sheet.

The deformed height of the sheet was based on the height of the pole of the bulged dome which was measured from DIC. Instead of calculating strain from DIC data, the effective strain can also be determined using the following equation developed by Hill [15]:

$$(5) \quad \bar{\epsilon} = 2 \ln \left(1 + \frac{h_d^2}{r_c^2} \right)$$

Equations 4 and 5 were used in the current work to provide a comparison to the stress versus strain response predicted from the DIC data.

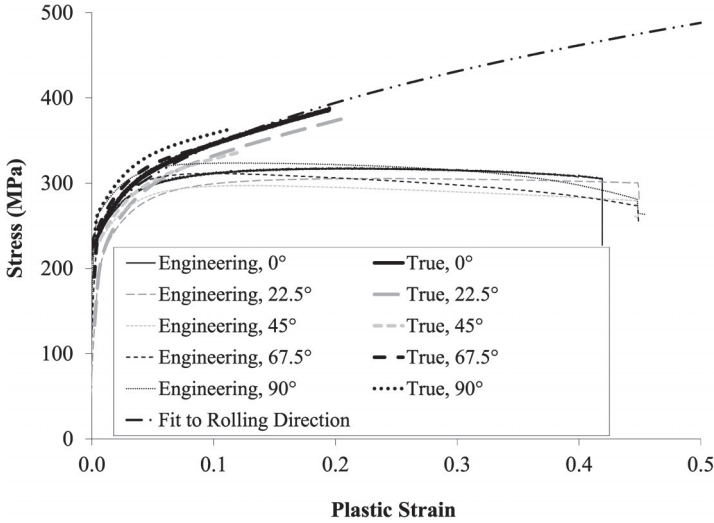
MARCINIAK TEST

The forming behaviour was obtained under pure biaxial and near plane strain conditions using the Marciniak test method [16], in which in-plane deformation is achieved through the use of a flat punch and a carrier blank. Deformation was measured in situ using full-field strain mapping. Forming limits could be obtained from DIC using the procedure outlined in the ISO 12004-2 standard, although limits are not reported using this procedure in the current work [16]. One advantage of DIC is that the gauge length can be varied in the strain computation. Consequently, the forming behaviour was studied at various gauge lengths in the current work. Another advantage of DIC is that the forming behaviour can be measured at strain-rates more representative of stamping operations, as the test does not need to be stopped upon the onset of necking, but prior to failure as is required in Ref. [11]. In the current work, the frame rate of the DIC system was specified at 50 frames per second for higher rate tests and 10 frames per second for lower rate tests. Room temperature CP-Ti tests were carried out at punch displacement rates of 0.1 and 5 mm/s. Room temperature ZEK100 tests were carried out at a displacement rate of 1 mm/s. In all cases, the samples were oriented such that the major axis corresponded to the rolling direction of the sheet.

Stress Versus Strain Response of Commercially Pure Titanium Sheet

Room temperature tensile tests were conducted at 0, 22.5, 45, 67.5, and 90° with respect to the rolling direction of the sheet at a strain-rate of 0.001 s⁻¹. **Figure 3** compares both the engineering and true stress versus plastic strain curves, where the true stress was plotted only to the maximum load measured during the test. The total elongation for each orientation was similar with failure occurring between plastic strains of about 0.42–0.45. The plastic strain at maximum load varied from about 0.2 in the rolling direction to 0.11 in the transverse direction. The true hardening response at the 67.5 and 90° orientations is slightly higher than at the 0°

FIG. 3 Room temperature stress versus plastic strain curves for Grade 1 CP titanium at various orientations with respect to the rolling direction (0°).



orientation, whereas the response at 22.5° and 45° is slightly lower than at 0° . A four-parameter Voce-type hardening law, given by Ref. [17], was used to capture the materials hardening response ($\bar{\sigma}_{\text{flow}}$) based on the true stress versus strain response in the rolling direction of the sheet

$$(6) \quad \bar{\sigma}_{\text{flow}} = [A - (A - \sigma_{YS}) \exp(-B\bar{\epsilon}^C)] \left(\frac{\dot{\bar{\epsilon}}}{\dot{\bar{\epsilon}}_0} \right)^m$$

where:

- σ_{YS} = the yield stress,
- $\bar{\epsilon}$ = the effective plastic strain,
- $\dot{\bar{\epsilon}}$ = the effective plastic strain rate,
- $\dot{\bar{\epsilon}}_0$ = a reference effective strain-rate,
- m = a strain-rate sensitivity parameter, and
- $A, B,$ and C = materials parameters.

Previously [17], the parameters for the CP-Ti sheet used in the current work were determined to be $\sigma_{YS} = 222.4$ (MPa), $A = 1550.7$ (MPa), $B = 0.32$, $C = 0.52$, $\dot{\bar{\epsilon}}_0 = 0.001$ (s^{-1}), and $m = 0.015$. The strain-rate parameter, m , was based on tests performed at strain-rates of 0.001, 0.01, and 0.1 s^{-1} . The effective stress versus plastic strain curve obtained with these parameters is also shown in Fig. 3 as “Fit to Rolling Direction.”

The major and minor strain measured from the ARAMIS DIC system were r value at the various orientations which was described by

$$(7) \quad r = -\frac{\epsilon_{\text{minor}}}{(\epsilon_{\text{major}} + \epsilon_{\text{minor}})}$$

where:

ϵ_{minor} = the true strain in the width direction, and

ϵ_{major} = the true strain in the loading direction.

Two input parameters that can be varied by the ARAMIS software in the calculation of strain are the grid spacing (GS) and gauge length (GL). The grid spacing is the spacing between xyz data points, while the gauge length is the original length (l_0) used to calculate engineering strain ($e = \Delta l/l_0$), which is then used to calculate true strain. The r value was determined over a specified length and is compared in Fig. 4 at various grid spacing (0.5, 1.3, and 1.9 mm) and gauge lengths (1.3, 1.5, 5.7, and 7.6 mm). The results show that using a small grid spacing combined with a small gauge length produces data with a lot of scatter. Increasing the grid spacing and gauge length decreases the scatter in the data. Below about 5 % strain, the r value tends to vary considerably for different combinations of grid spacing and gauge length. To reduce the scatter, it was deemed reasonable to calculate the r value with a grid spacing of about 1.3 mm and a gauge length of about 7.6 mm for the 10-mm wide, 0.92-mm thick tensile specimen.

The r values measured at the five tensile orientations are shown in Fig. 5, indicating that the r value is reasonably constant between strains of 5 and 20 %. The r values were not calculated above the maximum load (shown in Fig. 3) due to the

FIG. 4 Comparison of r values based on various grid sizes and gauge lengths from DIC for a room temperature CP-Ti tensile specimen conducted at a strain-rate of 0.001 s^{-1} in the rolling direction.

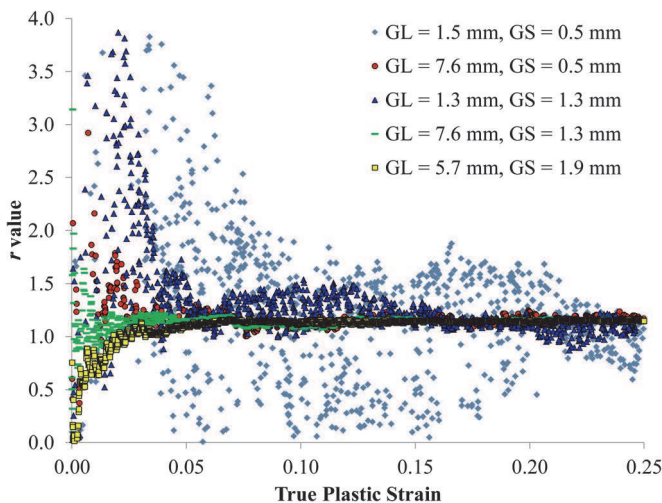
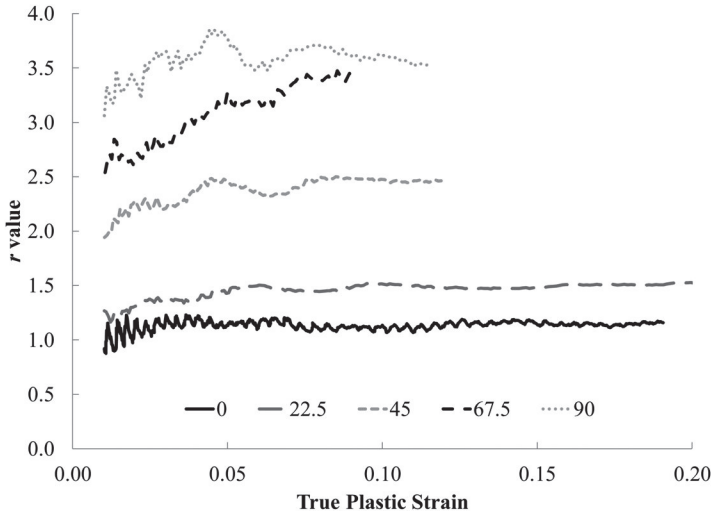


FIG. 5 Comparison of r values at various tensile orientations relative to the rolling direction (0°) of the sheet.



potential for the onset of necking. The average r value at each orientation was calculated to be 1.1, 1.5, 2.4, 3.3, and 3.6 at 0, 22.5, 45, 67.5, and 90°, respectively, which is based on the average r value from 5 % strain to maximum load.

There is considerable range of the r values reported in literature for commercially pure titanium sheet (either Grade 1 or 2), ranging from 1.5 to 5.8 at various orientations [7,9,18,19]. DIC techniques were used in some of this previous work to compute the r value and the sheet thicknesses ranged from 0.5 to 1.8 mm. In the current work, the r value of 1.2 calculated for the rolling direction is less than r values reported in literature for this direction, but the r values determined for the other directions fall within the reported ranges.

Yield Functions for Commercially Pure Titanium Sheet

As discussed above, an anisotropic yield function needs to be used to compute the pure biaxial flow stress versus strain response for CP titanium sheet. The tensile results above were used to calculate the coefficients of the Hill48 yield function, which is given by [20]

$$(8) \quad \phi = \sqrt{F(\sigma_{22} - \sigma_{33})^2 + G(\sigma_{33} - \sigma_{11})^2 + H(\sigma_{11} - \sigma_{22})^2 + L\sigma_{23}^2 + M\sigma_{31}^2 + N\sigma_{12}^2}$$

where F , G , H , L , M , and N are parameters that can be calculated from r_0 , r_{45} , and determined from the tensile data according to the following equations [20]:

$$(9) \quad r_{11} = r_{23} = r_{31} = 1; \quad r_{22} = \sqrt{\frac{r_{90}(r_0 + 1)}{r_0(1 + r_{90})}}; \quad r_{33} = \sqrt{\frac{r_{90}(r_0 + 1)}{(r_0 + r_{90})}};$$

$$r_{12} = \sqrt{\frac{3r_{90}(r_0 + 1)}{(2r_{45} + 1)(r_0 + r_{90})}}$$

with

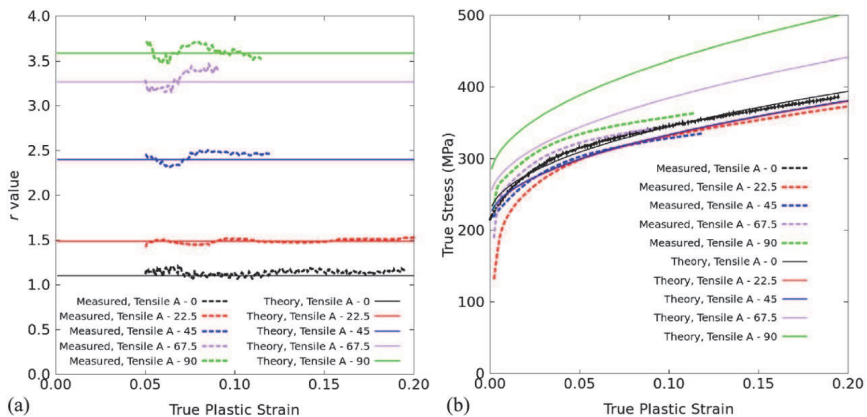
$$(10) \quad F = \frac{1}{2} \left[\frac{1}{r_{22}^2} + \frac{1}{r_{33}^2} - \frac{1}{r_{11}^2} \right]; \quad G = \frac{1}{2} \left[\frac{1}{r_{33}^2} + \frac{1}{r_{11}^2} - \frac{1}{r_{22}^2} \right]; \quad H = \frac{1}{2} \left[\frac{1}{r_{11}^2} + \frac{1}{r_{22}^2} - \frac{1}{r_{33}^2} \right]$$

$$L = \frac{3}{2r_{23}^2}; \quad M = \frac{3}{2r_{31}^2}; \quad N = \frac{3}{2r_{12}^2}$$

In these equations, r_{11} , r_{12} , and r_{22} correspond to r_0 , r_{45} , and r_{90} , respectively. The measured r values are compared to the theory in Fig. 6(a), while the measured stress versus strain curves are compared to the predicted curves in Fig. 6(b). The results show that if r values are used to calculate the coefficients in the Hill48 yield function, then the stress versus strain response is not captured, particularly at the 67.5 and 90° orientations. It could also be shown that if the stress versus strain curves were used to calculate the Hill48 coefficients, then the r values would not entirely be predicted correctly.

Cazacu and Barlat [1], proposed an asymmetric and anisotropic yield surface, which will be referred to as CB2004, to better capture the deformation behaviour of hexagonal closed packed (hcp) alloys such as CP-Ti. The CB2004 yield function was used in the current work as an alternative to the Hill48 yield function to describe the behaviour of CP-Ti. The yield function is given by [1,4]

FIG. 6 Comparison of Hill48 theory and measured (a) r values and (b) stress versus strain curves obtained at various orientations.



$$(11) \quad \phi = 3 \left[(a_2^2 + a_3^2 + a_2 a_3)^{3/2} - k(a_2 + a_3)a_2 a_3 \right]^{-1/3} \left[J_2^{3/2} - kJ_3 \right]^{1/3}$$

where:

k = the tension/compression asymmetric response, and

J_2 and J_3 = the second and third invariants of the transformed deviatoric stress tensor, $\Sigma = \mathbf{L}\sigma$, where \mathbf{L} is a fourth order linear transformation tensor.

The anisotropy coefficients, a_i (where $i = 1,6$), are used to describe \mathbf{L} . The yield function parameters calculated by Nixon et al. [4] for high purity α -Ti (99.999 %) were used in the current work to represent the CP-Ti alloy and are given in Table 1. These coefficients were determined for a 15.87 mm thick cross-rolled disc [4]. For reference, $k = 0$ with all $a_i = 1$, which is equivalent to the isotropic and symmetric von Mises response. Although the current work focuses only on tensile behaviour and not compression, the asymmetry parameter, k , is still required as it helps describe the shape of the yield surface even in the tension-tension quadrant of stress space (as is the stress state for the biaxial bulge test).

The r values and hardening responses obtained from the CB2004 model are compared to measured values in Fig. 7. The figure shows that the CB2004 parameters do not adequately describe the r value of the CP-Ti sheet, but the stress versus strain response is somewhat captured by the yield function parameters with the difference in the maximum and minimum stress for a given level of effective plastic strain being about 25 MPa in both the experimental and predicted cases.

The yield surfaces predicted from the Hill48 and CB2004 models are shown in Fig. 8 for an effective plastic strain ranging from 0 to 0.25, in increments of 0.05. The effective strain increment, $d\bar{\epsilon}$ was calculated using the principle of plastic work according to

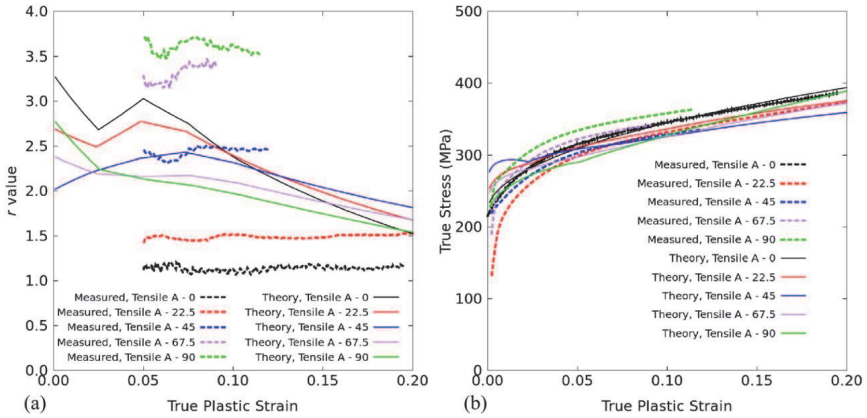
$$(12) \quad d\bar{\epsilon} = \frac{\sigma_{xx}d\epsilon_{xx} + \sigma_{yy}d\epsilon_{yy}}{\bar{\sigma}}$$

where $\bar{\sigma}$ is the effective stress obtained from the yield function. The shear stresses were zero ($\sigma_{xy} = 0$) for the yield surfaces shown in Fig. 8. Also shown in the figure are the corresponding experimental points in the rolling, transverse, and pure biaxial (calculated using Eq 1) orientations. Figure 8(a) demonstrates that the Hill48 yield function over predicts the transverse response, as was also shown in Fig. 6(b).

TABLE 1 Yield function coefficients for high purity titanium [4].

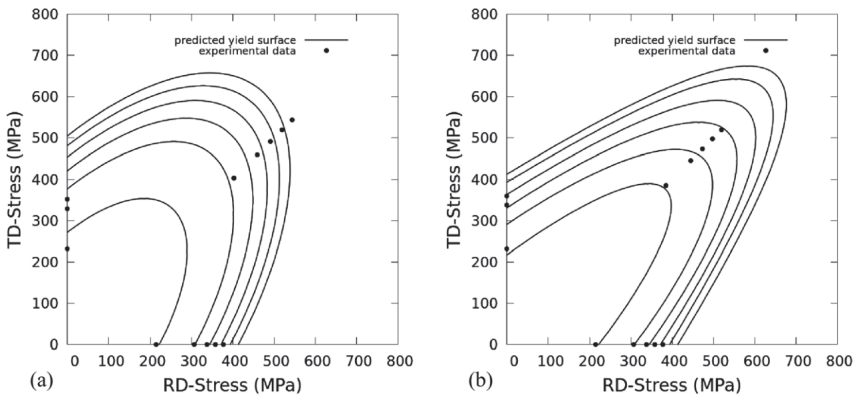
$\bar{\epsilon}$	a_2	a_3	a_4	k
0.000	0.9186	1.9985	1.3286	-0.3975
0.025	0.9071	1.7270	1.3972	-0.4202
0.050	0.8343	1.6477	1.3651	-0.3422
0.075	0.8576	1.6193	1.4135	-0.3746
0.100	0.8902	1.6062	1.4490	-0.5142
0.200	0.9443	1.4246	1.4262	-0.9685

FIG. 7 Comparison of CB2004 theory and measured (a) r values and (b) stress versus strain curves obtained at various orientations.



From the experimental biaxial bulge test, it was seen that $\epsilon_{xx} = \epsilon_{yy}$ (which will be shown in “Biaxial Bulge Test Results for IF Steel and Commercially Pure Titanium”), which indicates that Eq 1 can be used to predict the biaxial stress in the bulge test with $\sigma_{xx} = \sigma_{yy}$, which correspond to the rolling and transverse directions of the sheet. When $\epsilon_{xx} = \epsilon_{yy}$, the normal to the yield surface must be at 45° relative

FIG. 8 Comparison of Hill48 and CB2004 yield surfaces for an effective plastic strain ranging from 0 to 0.25 in increments of 0.05, $\sigma_{xy} = 0$ (experimental data points in the RD and TD directions start at an effective plastic strain of zero and increment by 0.05; experimental data points from the biaxial bulge test start at an effective plastic strain of 0.05 and increment by 0.05).



to the rolling direction. However, it can be seen in Fig. 8(a) that the normal to the yield surface is not at 45° for the pure biaxial case and it could be shown that $\varepsilon_{xx} = 2.9\varepsilon_{yy}$ for the Hill48 yield function. In other words, the major strain would be 2.9 times the minor strain during the bulge test, which is not the case from experiment. Figure 8(b) shows that the CB2004 yield function with the Nixon et al. [4] parameters significantly overpredicts the pure biaxial response.

Biaxial Bulge Test Results for IF Steel and Commercially Pure Titanium

Figure 9 shows the biaxial stress versus strain curves for CP-Ti sheet and two IF steel tests from the same batch of sheet. The effective stress and strain were calculated based on von Mises deformation. Figure 10 shows the corresponding major and minor strain versus time. The major strain was essentially equal to the minor strain for CP-Ti #1, IF Steel #1, and IF Steel #2, such that Eq 1 was applied to predict the biaxial stress. For IF Steel #1, the major strain-rate was reasonably constant at about 0.0003 s^{-1} , except at the end of the test. This strain-rate was achieved by varying the applied stroke-rate of the water cylinder during the test. Without varying the stroke-rate of the cylinder, a non-constant strain-rate would result as seen for IF Steel #2 where the strain-rate varied from about 0.0004 s^{-1} at the start of the test to 0.0015 s^{-1} at the end of the test. This strain-rate variation had only a small influence on the biaxial hardening response of the IF steel as seen in Fig. 9. For

FIG. 9 Biaxial bulge test results for IF steel and CP-Ti sheet based on von Mises deformation.

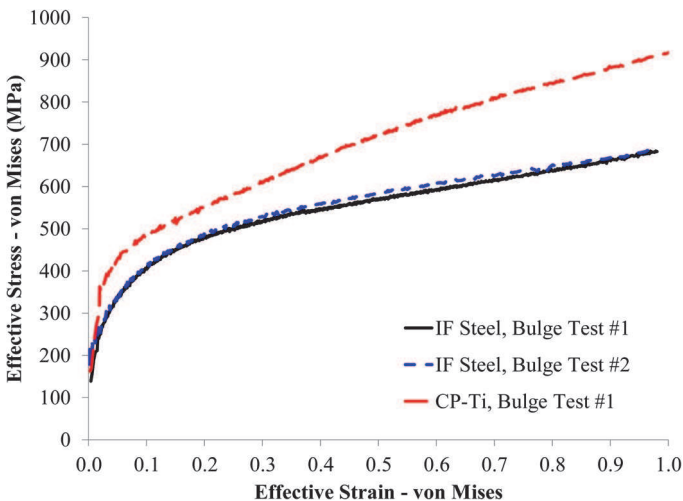
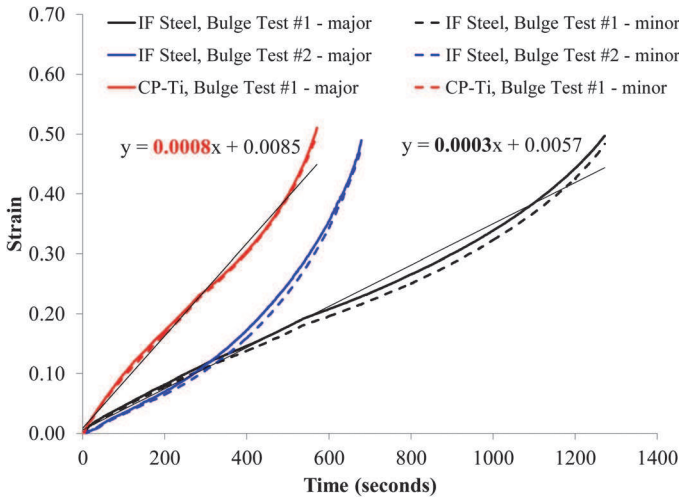


FIG. 10 Major and minor strain versus time for biaxial bulge tests IF Steel #1 and #2 and CP-Ti #1.

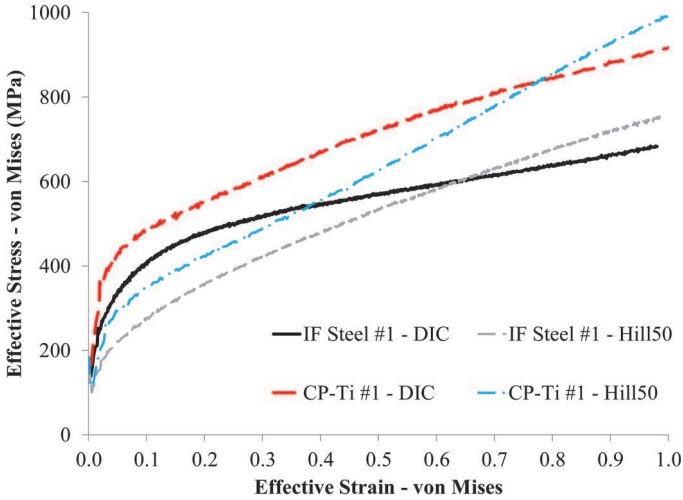


CP-Ti #1, the major strain-rate was about 0.0008 s^{-1} , which was again obtained by varying the applied stroke-rate of the water cylinder during the test.

The biaxial hardening response shown in Fig. 9 was calculated using the radius of curvature determined from the ellipsoid curve fit (Eq 3) to the DIC data. The goodness of fit of the experimental data to Eq 3 was determined by examining the R^2 coefficient (coefficient of determination), which for the CP-Ti #1 test ranged from 0.91 to 0.99, with an average of 0.97. Alternatively, the biaxial response can be obtained from the radius of curvature determined from Eq 4 and the effective strain from Eq 5. The biaxial stress versus strain curves predicted using Eqs 4 and 5, referred to as Hill50, are compared to the responses obtained from DIC data in Fig. 11 for IF Steel #1 and CP-Ti #1. The von Mises effective strain was calculated using the major and minor strain data, also from DIC. The biaxial response obtained from Hill50 (Eq 4) is significantly different from the response obtained using the DIC data (Eq 5) for which the goodness of fit average about $R^2 = 0.97$. This indicates the improved accuracy of the radius of curvature obtained through DIC measurements. Future work could consider alternative equations to better fit the DIC data for further improvement of the goodness of fit and accuracy of the radius of curvature.

Chamanfar and Mahmudi [8] measured the r values of IF steel sheet with a thickness of 1 mm and reported values ranging from 2.0 to 2.6 depending on the gauge length used in calculation. In the current work, an r value of 2.0 was used for the IF sheet in the Hill48 yield function, as r value data was not available for the specific IF steel sheet at the 0, 45, and 90°. Figure 12 compares the effective stress

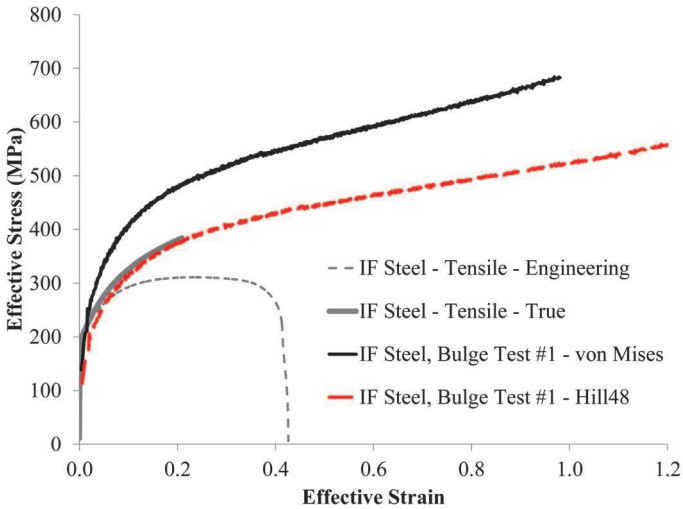
FIG. 11 Comparison of biaxial hardening response obtained from DIC and theoretical equation for IF steel and CP-Ti.



versus strain response from the biaxial test, calculated based on both the von Mises yield function and the Hill48 yield function (Eq 8) with an r value of 2.0. The yield function was used to calculate the effective stress, $\bar{\sigma}$, in Eq 12. The response from a tensile test is also shown. The tensile specimen was oriented such that the loading direction was oriented in the rolling direction of the sheet and was performed at an effective strain-rate of 0.008 s^{-1} . The effective strain-rate of the biaxial bulge test is about twice the major strain-rate of 0.0003 s^{-1} (Fig. 10). If the IF steel were isotropic, then it would be expected that strain hardening response of both the biaxial bulge test and tensile test would match. However, the results in the figure show that using an isotropic yielding response (von Mises) will result in a large over prediction of the effective stress versus strain response for IF sheet. Using Hill48 with an r value of 2.0 yields an effective flow response that matches the effective hardening response from the tensile specimen. The effective strain at maximum load for the tensile specimen was 21 %, whereas the flow behaviour in the bulge test remained stable to an effective strain of about 120 %. This indicates that the accurate radii of curvature determined from DIC can be used to describe the strain hardening response of the sheet metal to very high levels of plastic deformation. Further experimental data, such as r values at various orientations with respect to the rolling direction, would be required to verify whether the Hill48 yield function with an r value of 2.0 is best suited to describe the IF steel sheet.

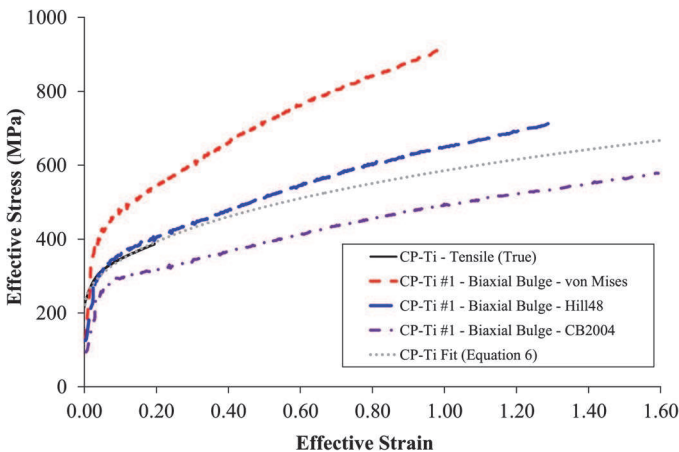
The biaxial bulge and tensile flow curves are compared for the commercially pure titanium sheet in Fig. 13. The biaxial bulge response was calculated using von

FIG. 12 Comparison of biaxial bulge and tensile stress versus strain response for IF steel.



section “Yield Functions for Commercially Pure Titanium Sheet.” The Hill48 (Eq 8) and CB2004 (Eq 11) yield functions were used to calculate the effective stress, $\bar{\sigma}$, in Eq 12. As with the IF steel bulge test, the applied volume expansion during the test was varied to achieve an effective strain-rate of approximately 0.002 s^{-1} (which is

FIG. 13 Comparison of biaxial bulge and tensile stress versus strain response for Grade 1 commercially pure titanium sheet.



approximately twice the major strain-rate of 0.0008 s^{-1} shown in Fig. 10). The effective strain rate for the rolling direction tensile test was 0.001 s^{-1} . Again, the von Mises response overpredicts the flow behaviour of the sheet. The Hill48 is in reasonable agreement with the flow behaviour obtained from the tensile specimen. Although the stress versus strain behaviour was reasonably captured using the Hill48 model, the pure biaxial strain ratio was poorly predicted ($\epsilon_{xx} = 2.9\epsilon_{yy}$) compared to the experimental case ($\epsilon_{xx} = \epsilon_{yy}$, as seen in Fig. 10), as detailed in the section “Yield Functions for Commercially Pure Titanium Sheet.”

For the CB2004 yield function, the effective stress was calculated using Eq 11 with the stress in the rolling direction equal to the stress in the transverse direction, both of which were equal to the biaxial stress calculated from Eq 1. The CB2004 predictions shown in Fig. 8(b) indicated that under pure biaxial loading ($\sigma_{RD} = \sigma_{TD}$), the stresses calculated from experiment (using Eq 1) were significantly less than the pure biaxial stresses calculated according to the CB2004 yield function. Consequently, using the lower experimental biaxial stresses (from Eq 1) leads to an effective stress versus strain response which underpredicts the flow response of the sheet, as indicated in Fig. 13. Although the effective stress versus strain response is underpredicted for the pure biaxial case, the strain ratio is correctly predicted compared to experiment (which is given in Fig. 10) with $\epsilon_{xx} = 0.97\epsilon_{yy}$.

The results show that both the Hill48 and CB2004 yield functions can capture some of the deformation behaviour of the CP-Ti sheet, but neither yield function can accurately describe the entire deformation response of the alloy. Alternative yield functions, such as the CPB06 yield function [2,3], could also be explored to better capture the deformation response of CP-Ti. As with the IF steel case, the effective strain at failure from the bulge tests is much higher than the effective strain at maximum load from a tensile test. For CP-Ti, the maximum uniform effective strain from a tensile test occurs at about 20 %, whereas the maximum effective strain from the bulge test reached about 130 % before failure in the bulge test (based on the Hill48 flow response). Also presented in Fig. 13 is flow response predicted from Eq 6, which was based on extrapolating the tensile data to higher strains [17]. The extrapolated result was similar to the strain hardening response of the material based on the biaxial bulge response with CB2004.

Influence of Gauge Length on Definition of Forming Response

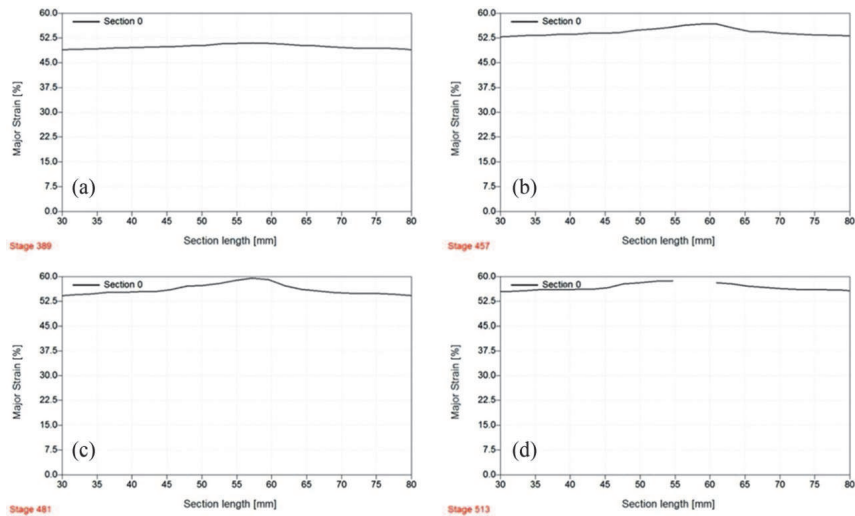
The localization behaviour of various sheet metals can vary greatly from little to no necking, localized necking, to diffuse necking before failure. As mentioned above, the gauge length used to calculate the strain components can be varied in the DIC analysis. The current section examines whether modifying the gauge length can be used to indicate changes in the localization response of sheet metal. No attempt is

necking, or failure. In addition, the analysis is mainly restricted to pure biaxial loading conditions, with some plane-strain analysis.

The major strain versus length for a section taken through the centre of the sample from a pure biaxial Marciniak test of CP-Ti sheet tested at a punch rate of 0.1 mm/s is shown in Fig. 14. The major strain was calculated based on the grid size from the DIC data, which was about 1.1 mm. Figure 14(a)–14(c) show the strain state prior to failure and Fig. 14(d) shows the strain state just after failure. The figure shows that the in-plane stretching resultant from the pure biaxial Marciniak test produces a fairly consistent strain profile, prior to strain localization. Since the strain profile obtained from in-plane stretching during the Marciniak test is reasonably consistent, it was deemed reasonable to study the effect of varying gauge length on strain for sections measured at or near the point of failure. Figure 14(b)–Fig. 14(d) show that the strain begins to localize near the centre of the sample, which would affect the strain measured from different gauge lengths, but only after the localization. Future work should consider strain paths other than pure biaxial, to determine if the strain response remains reasonably consistent across a specified section in the Marciniak test.

The influence of varying the gauge length was studied to determine whether any deviations in the strain response could indicate the onset of necking. CP-Ti and ZEK100 sheet were studied as they demonstrate various failure responses, such

FIG. 14 Major strain versus section length from Marciniak test of CP-Ti sheet tested at 0.1 mm/s in the pure biaxial condition (a) before necking, (b) close to the point of diffuse/localized necking, (c) at or near the point of the onset of localized necking, and (d) after failure.



as diffuse necking, localized necking, or fracture without necking. The effective strain (von Mises) versus time profile is shown in Fig. 15 for room temperature Marciniak tests performed at a punch displacement rate of 0.1 and 5 mm/s for CP-Ti sheet and 1 mm/s for ZEK100 magnesium sheet, for the pure biaxial condition. As opposed to the strain data in Fig. 14 which was calculated based only on the grid size from DIC, the strain data in Fig. 15 was calculated based on the gauge length. The effective strain at each time increment was calculated after the test based on the surface strain at or near the location at which the material eventually failed during the test. The strain was calculated using a gauge length (GL) of either 3.3 or 4.4 mm. The effective strain-rates obtained are about 0.004, 0.025, and 0.22 s⁻¹ for punch displacement rates of 0.1, 1.0, and 5.0 mm/s, respectively. This demonstrates that DIC can be used to obtain forming behaviour at strain-rates more representative of stamping operations which would be important for materials that demonstrate strain-rate sensitivity.

Room temperature Marciniak test results conducted at a punch displacement rate of 1 mm/s are shown in Fig. 16 for ZEK100 magnesium sheet for both pure biaxial and plane strain conditions. The effective strain (von Mises) calculated for three gauge lengths of 1.1, 3.3, and 6.6 mm is compared. Again, the effective strain was measured along a line that passed through the location of failure and the gauge length would span the failure crack such that the measured strain appears to drastically increase upon failure. The grid spacing was about 1.1 mm in all of the calculations. The results for ZEK100 indicate no deviation of the strain response with

FIG. 15 Effective strain versus time profiles obtained from Marciniak tests for the pure biaxial condition for various levels of strain-rate.

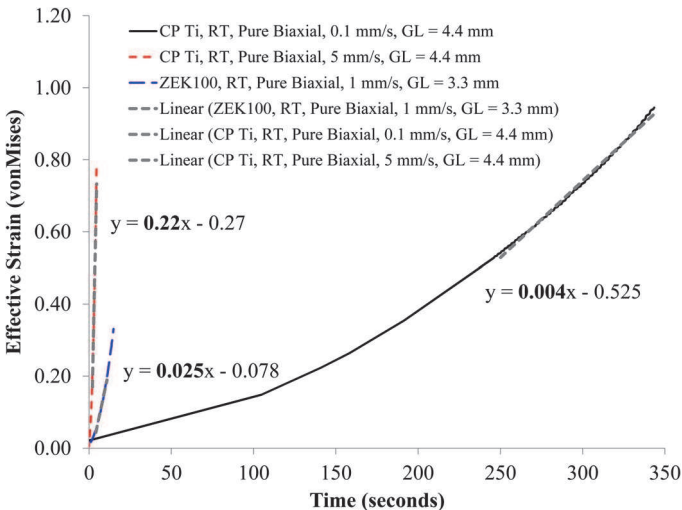


FIG. 16 Comparison of effective strain versus time determined based on different grid spacing and gauge lengths for pure biaxial and plane strain conditions for ZEK100 tested at 1 mm/s.

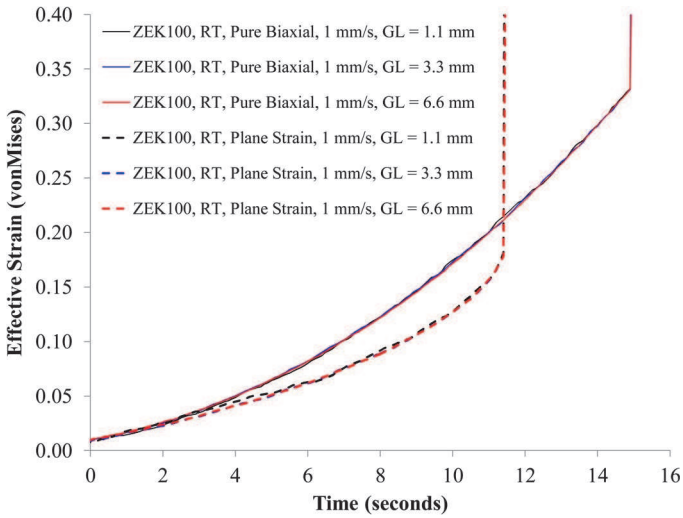


FIG. 17 Comparison of effective strain versus time determined based on different grid spacing and gauge lengths for pure biaxial and plane strain conditions for CP-Ti tested at 0.1 mm/s.

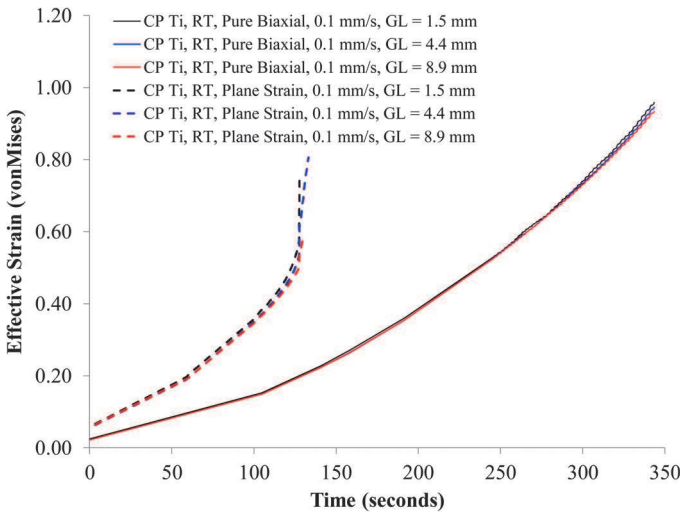
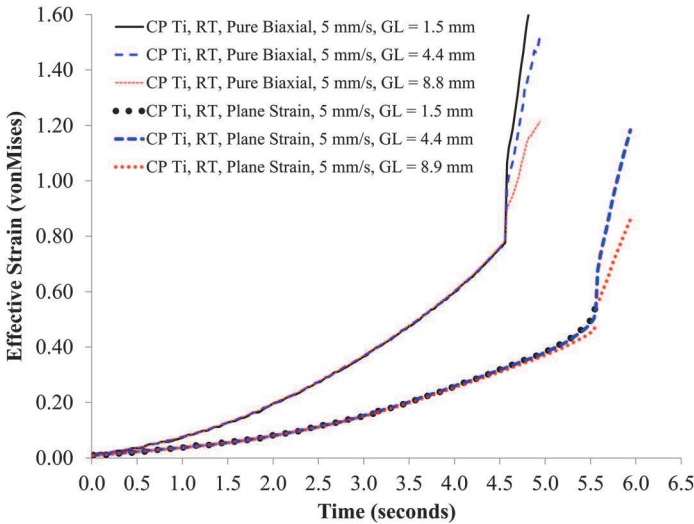


FIG. 18 Comparison of effective strain versus time determined based on different grid spacing and gauge lengths for pure biaxial and plane strain conditions for CP-Ti tested at 5 mm/s.



gauge length. Moreover, there is no localized necking observed in the data, as the strain increases vertically at the point of failure (which is an artifact of the gauge length spanning the crack). Consequently, varying the gauge length utilized in the strain calculations would not change the forming limit of room temperature ZEK100 under pure biaxial and plane strain conditions.

The pure biaxial and plane strain Marciniak test results presented in Fig. 17 and Fig. 18 are for CP-Ti sheet conducted at a punch displacement rate of 0.1 and 5 mm/s, respectively, and compared at three different gauge lengths. Figure 17 shows that the effective strain-rate for the plane strain case is greater than that for the pure biaxial case for the slower punch rate of 0.1 mm/s. However, Fig. 18 shows that the effective strain rate for the plain strain case is less than that of the biaxial case for the tests performed at 5 mm/s, indicating that strain-rate can influence strain path. The plane strain case in Fig. 17 shows a change in the strain response between the three gauge lengths that is indicative of the onset of localized necking (given by the sudden rise in effective strain, which again is an artifact of the gauge spanning the localized region that eventually failed by a crack). For the pure biaxial case, there was little difference in the strain response, which was indicative that the material underwent little to no localization prior to failure. For both the plane strain and pure biaxial tests conducted at 5 mm/s, which are shown in Fig. 18, there was a change in the strain response between the three gauge lengths, which was also in-

Conclusions

The biaxial stress versus strain response was measured for interstitial free (IF) steel and Grade 1 commercially pure titanium (CP-Ti) sheet. It was found that the effective stress versus plastic strain response from the bulge test could not be accurately predicted when considering an isotropic (von Mises) yielding response, indicating both IF steel and CP-Ti are to some degree anisotropic. For IF steel, adjusting the flow curve using the Hill48 anisotropic yield function with an r value of 2.0 was sufficient to yield a flow response in agreement with the corresponding flow response from a tensile test. Moreover, it was shown that the radius of curvature of the sheet obtained from DIC measurements was accurate to high levels of plastic deformation. The flow behaviour from the bulge test reached a high effective strain of about 120 % before failure compared to 21 % effective strain achieved at the point of instability in the tensile test. For CP-Ti sheet, the flow response was adjusted using both Hill48 and CB2004 yield functions. Coefficients for the Hill48 model were determined based on the r values from tensile tests in which DIC was used to measure the major and minor strain. The CB2004 yield function was applied using parameters from literature for a 15.87 mm thick cross-rolled pure titanium disk to represent the CP-Ti sheet. The results showed that both the Hill48 and CB2004 yield functions captured some of the deformation behaviour of the CP-Ti sheet, but neither yield function could accurately describe the entire deformation response of the alloy. As with IF steel, a high effective strain was achieved in the bulge test for CP-Ti of about 130 % before failure compared to the tensile test with an effective strain at instability of about 20 %. It can be concluded that the biaxial flow test is a valuable test to characterize the deformation of anisotropic sheet metal at high effective strains. The localization behaviour of various sheet metals was studied by varying the gauge length utilized in the DIC analysis after the test was conducted. The study was mainly limited to pure biaxial loading conditions where it was shown that for sheet metal with low ductility, varying the gauge length had no effect on the predicted strain profile. For materials with high ductility, the strain profiles could deviate near the end of the test. This deviation could be indicative of the onset of localized necking, but further work is required to determine if this deviation corresponds to a localized neck on the sheet material.

ACKNOWLEDGMENTS

Funding for this work was provided by Natural Resources Canada through the Program of Energy Research and Development. The writers would also like to acknowledge many useful discussions with Dr. Sean Agnew from the University of Virginia.

References

- [1] Cazacu, O. and Barlat, F., "A Criterion for Description of Anisotropy and Yield Differential Effects in Pressure-Insensitive Metals," *Int. J. Plast.*, Vol. 20, No. 11, 2004, pp. 2027-2045.

- [2] Cazacu, O., Plunkett, B., and Barlat, F., "Orthotropic Yield Criterion for Hexagonal Closed Packed Metals," *Int. J. Plast.*, Vol. 22, No. 7, 2006, pp. 1171–1194.
- [3] Plunkett, B., Lebensohn, R., Cazacu, O., and Barlat, F., "Anisotropic Yield Function of Hexagonal Materials Taking Into Account Texture Development and Anisotropic Hardening," *Acta Mater.*, Vol. 54, No. 16, 2006, pp. 4159–4169.
- [4] Nixon, M. E., Cazacu, O., and Lebensohn, R. A., "Anisotropic Response of High Purity α -Titanium: Experimental Characterization and Constitutive Modeling," *Int. J. Plast.*, Vol. 26, No. 4, 2010, pp. 515–532.
- [5] Rana, R., Singh, S. B., Bleck, W., and Mohanty, O. N., "Biaxial Stretching Behavior of a Copper-Alloyed Interstitial-Free Steel by Bulge Test," *Metall. Mater. Trans. A*, Vol. 41A, No. 6, 2010, pp. 1483–1492.
- [6] ISO/TC 164/SC 2: Metallic Materials— Sheet and Strip—Determination of Biaxial Stress-Strain Curve by Means of Bulge Test With Optical Measuring Systems, ISO, Geneva, Switzerland, 2012.
- [7] Demiralp, Y., 2012, "Determination of Material Properties and Prediction of Springback in Air Bending of Advance High Strength Steel (AHSS) and Commercially Pure Titanium (CP) Sheet Materials," MA.Sc. thesis, The Ohio State University, Columbus, OH.
- [8] Chamanfar, A. and Mahmudi, R., "Effect of Specimen Geometry, Gage Length, and Width Measurement Locations on Plastic Strain Ratio (R-Value) in Sheet Metals," *Metall. Mater. Trans. A*, Vol. 37A, No. 12, 2006, pp. 3477–3487.
- [9] Chamanfar, A. and Mahmudi, R., "Ti Sheet: The Effect of Gage Length and Width Measurement on Plastic Strain Ratio," *JOM*, Vol. 56, No. 2, 2004, pp. 49–52.
- [10] Aretz, H., "Numerical Analysis of Diffuse and Localized Necking in Orthotropic Sheet Metals," *Int. J. Plast.*, Vol. 23, No. 5, 2007, pp. 798–840.
- [11] ASTM E2218-14: Standard Test Method for Determining Forming Limit Curves, ASTM International, West Conshohocken, PA, 2014, www.astm.org.
- [12] Neil, C. J. and Agnew, S. R., "Crystal Plasticity-Based Forming Limit Prediction for Non-Cubic Metals: Application to Mg Alloy AZ31B," *Int. J. Plast.*, Vol. 25, No. 3, 2009, pp. 379–398.
- [13] GOM, *ARAMIS User Manual—Software v6.1*, GOM Optical Measuring Techniques, Braunschweig, Germany, 2009.
- [14] Koç, M., Billur, E., and Cora, Ö. N., "An Experimental Study on the Comparative Assessment of Hydraulic Bulge Test Analysis Methods," *Mater. Des.*, Vol. 32, No. 1, 2011, pp. 272–281.
- [15] Hill, M. R., "A Theory of Plastic Bulging of a Metal Diaphragm by Lateral Pressure," *Philos. Mag. Ser. 7*, Vol. 41, No. 322, 1950, pp. 1133–1142.
- [16] ISO 12004-2: Metallic Materials—Sheet and Strip—Determination of Forming-Limit Curves—Part 2: Determination of Forming-Limit Curves in the Laboratory, ISO, Geneva, Switzerland, 2008.
- [17] Williams, B. W. and Blaga, L., "Characterizing the Asymmetric/Anisotropic Deformation Response and Forming Behaviour of Wrought Magnesium and Titanium Alloys," *Mater. Sci. Forum*, Vol. 765, 2013, pp. 348–352.

- [18] Toussaint, F., Tabourot, L., and Vacher, P., "Experimental Study With a Digital Image Correlation (DIC) Method and Numerical Simulation of an Anisotropic Elastic-Plastic Commercially Pure Titanium," *Arch. Civ. Mech. Eng.*, Vol. 8, No. 3, 2008, pp. 131–143.
- [19] Chamos, A. N., Labeas, G. N., and Setsika, D., "Tensile Behavior and Formability Evaluation of Titanium-40 Material Based on the Forming Limit Diagram Approach," *J. Mater. Eng. Perform.*, Vol. 22, 2013, pp. 2253–2260.
- [20] Dassault Systems, *Abaqus Analysis User's Manual: Volume III: Materials, Version 6.7*, Dassault Systems, Paris, 2007.

STP 1584, 2015 / available online at www.astm.org / doi: 10.1520/STP158420140052

S. M. Barhli,¹ D. Hollis,² B. Wieneke,² M. Mostafavi,³
and T. J. Marrow^{1,4}

Advanced 2D and 3D Digital Image Correlation of the Full-Field Displacements of Cracks and Defects

Reference

Barhli, S. M., Hollis, D., Wieneke, B., Mostafavi, M., and Marrow, T. J., "Advanced 2D and 3D Digital Image Correlation of the Full-Field Displacements of Cracks and Defects," *Evaluation of Existing and New Sensor Technologies for Fatigue, Fracture and Mechanical Testing*, STP 1584, Jidong Kang, David Jablonski, and David Dudzinski, Eds., pp. 56-69, doi:10.1520/STP158420140052, ASTM International, West Conshohocken, PA 2015.⁵

ABSTRACT

Full-field mapping of displacements between successive images by digital image correlation is a powerful and well-established technique, used in fields as diverse as geo-tectonics, engineering mechanics, and materials science. Analysis of three-dimensional images, such as computed x-ray tomographs, is also becoming routine. These techniques provide new ways to study and quantify deformation and failure processes; recently, they have been applied to detect and study cracks and defects in engineering materials, for instance, by coupling the displacement analysis with finite-element codes to readily extract the crack propagation strain energy release rate (J-integral). Such analyses increase the richness of the data obtained, for example, providing information on the mode of loading and are suitable for the analysis of engineering components under complex states of stress. This work has

Manuscript received May 22, 2014; accepted for publication December 2, 2014; published online January 26, 2015.

¹Univ. of Oxford, Dept. of Materials, Oxford OX1 2JD, United Kingdom.

²LaVision UK, Ltd., DownsView House, Grove Technology Park, Grove Oxfordshire OX12 9FF, United Kingdom.

³Univ. of Sheffield, Dept. of Mechanical Engineering, Western Bank, Sheffield, South Yorkshire S10 2TN, United Kingdom.

⁴Univ. of Oxford, Dept. of Materials, Oxford OX1 2JD, United Kingdom; and Univ. of Oxford, Oxford Martin School, Oxford OX1 2JD, United Kingdom.

⁵ASTM Fourth Symposium on the *Evaluation of Existing and New Sensor Technologies for Fatigue, Fracture and Mechanical Testing* on May 7-8, 2014 in Toronto, Canada.

highlighted areas where the development of image-correlation methods that are optimized for analysis of discontinuities would be beneficial for better detection of small cracks and the early development of damage against the background displacement field, improved precision in crack-displacement field measurement by intelligent “masking” or analysis algorithms, and better integration with finite-element software packages to make use of advanced tools for 2D and 3D deformation analysis. This paper reviews some of this recent work on the analysis of 2D and 3D damage in engineering materials, and describes developments in quantitative analysis of defects by image correlation. The examples covered include brittle crack propagation in nuclear graphite, fatigue loading in magnesium alloys, and indentation damage in brittle and ductile materials.

Keywords

digital image correlation, computed tomography, digital volume correlation, fracture mechanics, damage mechanics

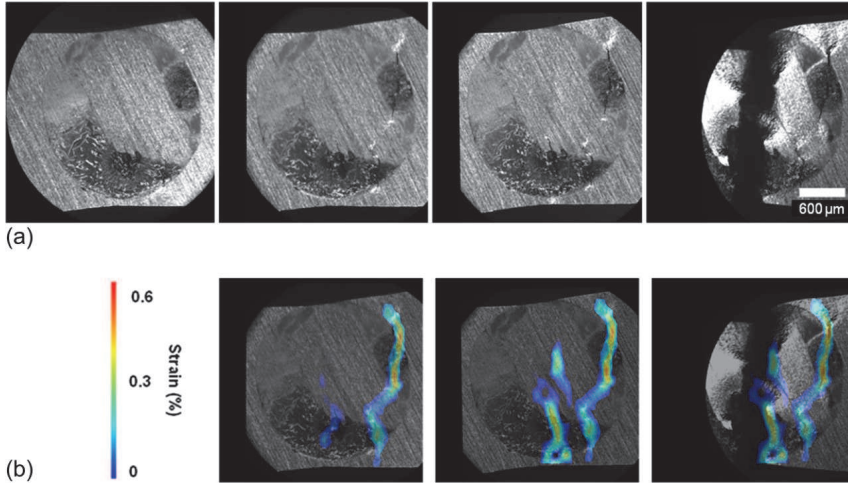
Background

Digital image correlation (DIC) is a powerful tool to measure the full-field displacement distribution on the surface of specimens. The gradients of the displacement field can be used to derive the strain field, which then may be employed for early detection of fracture nuclei [1,2]; cracks are revealed by artificially high levels of strain (i.e., significantly in excess of the elastic limit) because of their opening displacements. The effective surface lengths of observed cracks can be obtained directly from the DIC data using image segmentation of the strain map [2]; these lengths will include some contribution from the crack-tip plastic zone. The depth of the cracks also may be estimated from their opening displacements, for instance, with the assumption of elastic properties and a semi-elliptical crack geometry [1,2]. By these methods, DIC has been applied to study crack behavior in a broad range of materials (e.g., Refs 1–3).

For instance, in stress-corrosion studies, analysis in this manner of displacement fields obtained by DIC has proved very useful for the investigation of crack initiation and propagation in a range of environments in which cracks are conventionally difficult to study [4,5]. In the case of atmospheric stress corrosion of stainless steel, DIC analysis of optical images discerned crack growth beneath salt layers and adherent corrosion product deposits; crack development could be monitored over long periods of time [6] (Fig. 1). Precise measurements of crack-opening displacements have also supported the study of short fatigue crack growth [7] and stress-corrosion initiation [8] in studies of a thermally sensitized stainless steel in high-temperature, high-pressure water (Fig. 2), via DIC of optical images obtained in a windowed autoclave.

Three-dimensional in situ observation of damage within materials has become possible through high-resolution x-ray computed microtomography (μ XCT) (e.g., Refs 9–11), aided by the brilliance of synchrotron sources. Digital volume correlation (DVC) can map relative changes in displacement between tomographic datasets [12], allowing quantitative observations of the three-dimensional deformations that

FIG. 1 Stress-corrosion crack nucleation in austenitic stainless steel beneath a chloride salt deposit (under a tensile static stress): (a) Optical images at 1500 h, 1668 h, 1836 h, and 2004 h (left to right). (b) Strain map (calibrated to show relative crack-opening displacements) relative to first image (1500 h) at 168 h, 1836 h, and 2004 h (left to right). The final image includes the strain map from 1836 h overlaid on optical image of the failed specimen [6].



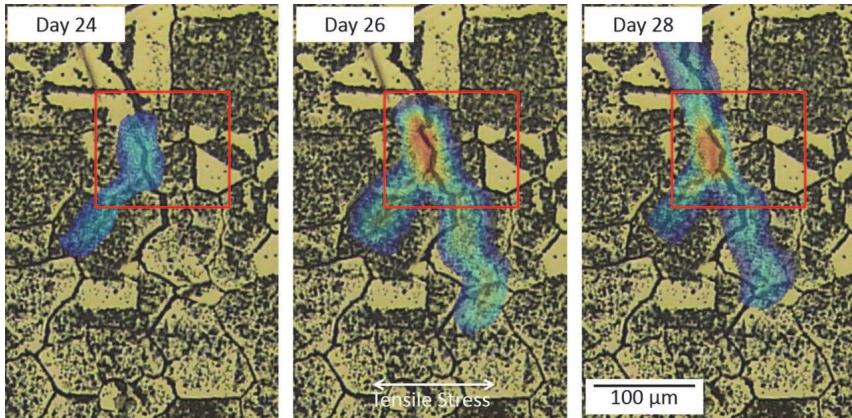
occur within materials when they respond to loads. In suitable microstructures, the displacement resolution is sub-voxel (a voxel is the three-dimensional equivalent of a pixel), and both elastic and plastic deformations can be studied [13,14].

Some recent work conducted on the joint engineering, environmental, and processing (I12 – JEEP) beam line at the diamond light source is described here, where the objective is to show how damage may be characterized by analysis of the three-dimensional displacement fields obtained from μ XCT data. The examples presented include crack propagation in a quasi-brittle porous material (polygranular graphite), sub-indentation cracking in a brittle polycrystalline ceramic (alumina), plastic deformation and damage development underneath indentations in a ductile metal (Al-SiC composite), and fatigue crack-opening behavior in a magnesium alloy, the latter using μ XCT data obtained at beamline ID19 of the European Synchrotron Radiation Facility.

Three-Dimensional Damage Analysis Using Displacement Fields

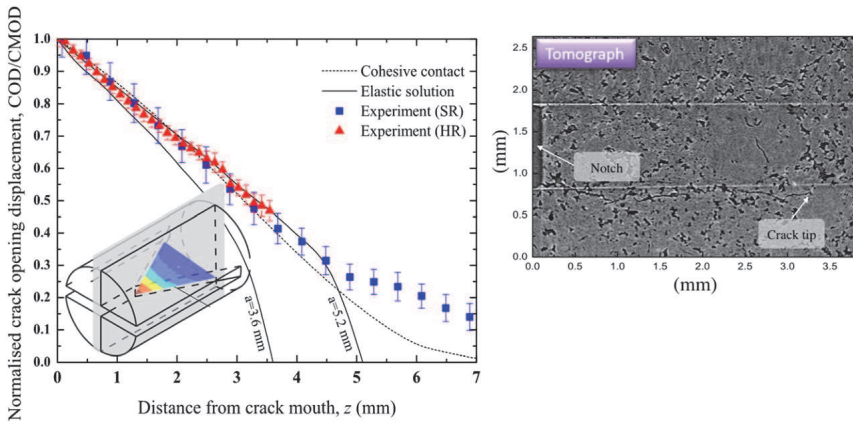
Polygranular Gilsocarbon graphite is the artificial graphite used in the United King-

FIG. 2 Visualizations at different time intervals of an intergranular stress corrosion initiated in austenitic stainless steel, observed in situ in high-temperature water. The crack openings are represented as strains calculated from the digital image correlation measured displacements. The crack initiation site is indicated by the red rectangle. The strain map is superposed on an optical observation of the sample at the end of the test. The strain scale is qualitative and indicates the magnitude of crack-opening displacement; dark blue represents low strain and red represents high strain. The maximum crack opening increased from $0.2\ \mu\text{m}$ at day 22 to $0.9\ \mu\text{m}$ at day 26 [8].



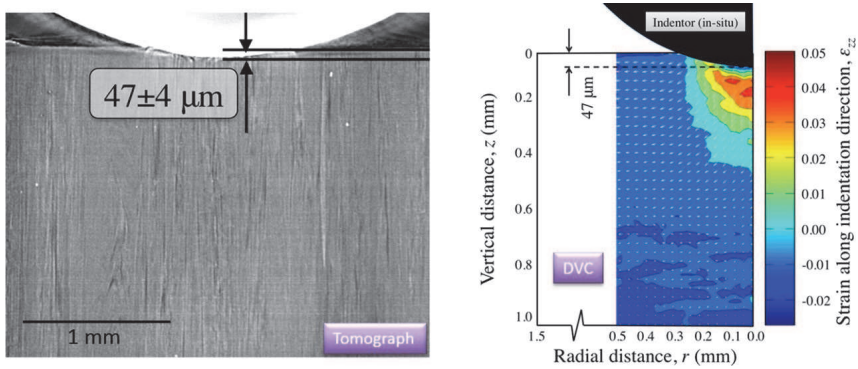
and reflector. The graphite studied was in the virgin, i.e., non-irradiated, condition, and is a model quasi-brittle material; crack propagation is accompanied by the development of a microcracked fracture process zone (FPZ) [15,16]. Through the combined use of μXCT and DVC, the deformation of the fracture process zone has been measured; full details of the experiment and analysis are provided in Ref 16, and a brief summary is given here. A short bar chevron notch specimen was used to achieve stable crack propagation (Fig. 3). X-ray tomographic images of the notched region were first obtained in the undamaged condition. A sharp wedge was then driven progressively toward the base and into the notch to initiate and propagate a crack; tomographic images were recorded at intervals as the crack propagated and then analyzed using digital volume correlation. The three-dimensional crack-opening displacement (COD) profile is obtained from the relative displacements of the faces of the crack. This shows there is a zone with a length of approximately 1.5 mm, in which the material is less stiff and displaces more than expected from linear elastic behavior. This is the fracture process zone where microcracking damage increases the strains in response to the crack-tip stresses; it can be simulated successfully using a cohesive zone finite element (FE) model (a form of strip yield model).

FIG. 3 Measurement of crack-opening displacement profile by synchrotron tomography in polygranular graphite; HR, SR denote high-resolution ($1.8\ \mu\text{m}$ voxel) and standard resolution ($3.6\ \mu\text{m}$ voxel) data. The measured profiles are compared with elastic FE and cohesive fracture FE simulations for the observed 3.6-mm crack length. The fracture process zone has the effect of increasing the crack opening, such that the crack behaves equivalent to a longer elastic crack [16].



Hardness testing has long been used to interrogate materials to understand their deformation behavior and to infer the processes of deformation that have occurred underneath the indenters (e.g., Ref 17). With appropriate assumptions or understanding of deformation processes, hardness tests on small samples can be used to evaluate the effects of changes in microstructure on the mechanical properties of engineering components. Hardness testing is a surface characterization technique and, except in transparent materials, it provides no direct observation of the assumed damage and deformation processes. Indentation in a model ductile metal, an aluminum–silicon carbide composite (Al–SiC, 15 % volume fraction reinforcement), has been studied using DVC of μXCT data to measure the subsurface displacement field in three dimensions. As with the graphite example, only brief details are presented here; full details including the parameters of the DVC analysis are provided in Ref 18. The sample was examined (1) before, and (2) in situ during indentation. The specimen was indented with a 5-mm radius ZrO_2 ball with an in situ loading rig. The reference tomograph was recorded under a small pre-load to reduce rigid body movement, with the second tomograph under the indentation load. A vertical μXCT slice shows the composite's texture (Fig. 4) and, although individual particles are not resolved, DVC operates successfully on the contrast from microstructure heterogeneity. Further post-processing to fully remove rigid

FIG. 4 Vertical section of the μ XCT data of Herzian indentation in Al-15 % SiC composite (left). The DVC-measured vertical strain is shown as a contour map (right) with vectors of the displacement field superposed [18].

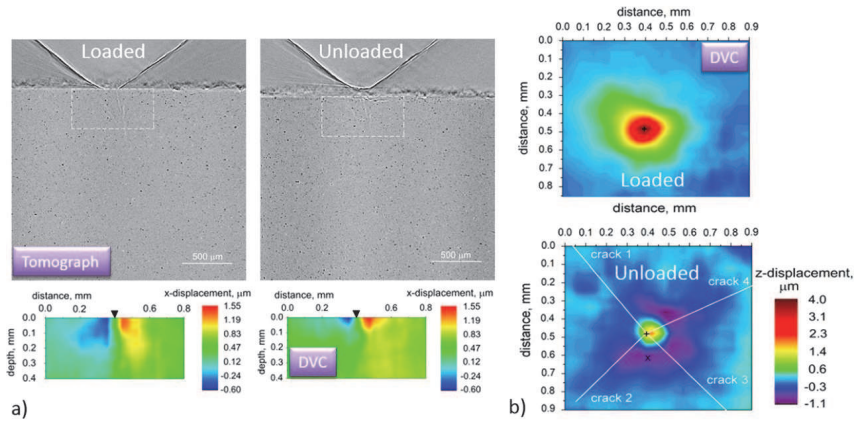


be able to consider its components with respect to the coordinate system of the indentation field, which is not necessarily aligned with that of the observations; this is particularly important in indentation experiments because of the small displacements within the sample and the high loads that can cause sample movements that are significant compared to these, even with a stiff loading rig.

Hence, following DVC analysis, fine rigid body movements and rotations of the displacement data matrix were corrected to obtain the displacement field around the indentation; a novel and efficient algorithm, reported briefly in Ref 18, and described in more detail in Ref 19 was used. In brief, using the 3D matrix of displacement vectors, the body translation is first isolated and corrected using an averaging technique. The rotation matrix is then determined by inverting the displacement matrix to find its Euler angles, which are used to apply a corrective rotation. Following correction of the rigid body movements, the displacement field has radial symmetry; hence, to simplify the displacement data presentation, they are transformed to polar coordinates, with the axis of the indentation as origin, to obtain average radial displacements. Except close to the indentation, the displacement field and the reaction force agree well with an elastic–plastic FE simulation of the indentation, using the measured indentation depth and properties from tensile tests of the same material. A reverse-modeling analysis via FE simulation can then be applied to extract material properties from such observations to investigate the elastic–plastic behavior of ductile materials [19].

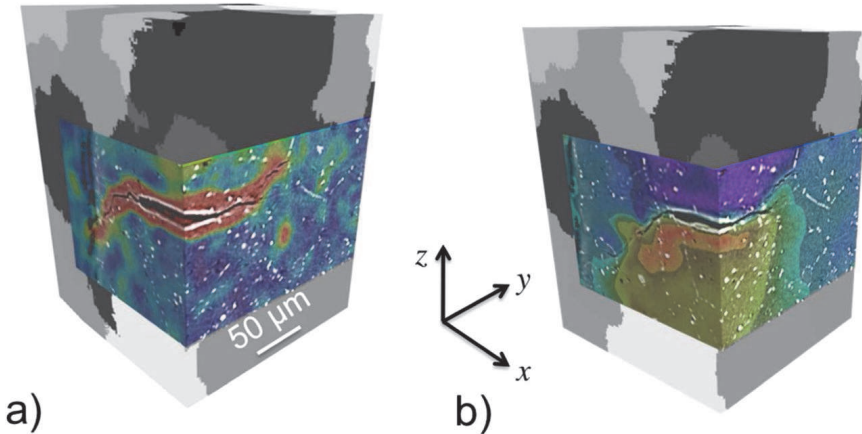
During indentation of brittle materials, a system of subsurface radial cracks is generated to accommodate the indentation strain. Lateral cracks, which are approximately parallel to the surface, arise from the residual strain field surrounding the indentation plastic zone as the sample is unloaded. Understanding indentation

FIG. 5 Vicker's indentation of Al_2O_3 ceramic: (a) Tomographic vertical cross-sections of sample under load and unloaded. The corresponding maps of the horizontal displacement in the area presented by a dashed rectangle are shown below; and (b) maps of vertical displacements in a horizontal plane under the indentation, showing the indentation deformation and the uplift from lateral cracking. The radial cracks are indicated [21].



cracking in hard, brittle materials is important, because indentation damage contributes to certain forms of wear [20]. Although it is routine to study the surfaces of indented materials to characterize surface cracking, there are very few observations of indentation cracking below the surface. Such studies are usually destructive, and may modify the residual stress state during observation. The combined $\mu\text{XCT}/\text{DVC}$ methodology has been applied recently to investigate the cracks that develop in a model brittle material, polycrystalline alumina, during indentation. Brief details are described here; further information including the parameters of the DVC analysis is provided in Ref 21. The polycrystalline Al_2O_3 sample was indented using a standard Vickers pyramidal diamond; the sample was imaged by μXCT (1) before indentation, with small pre-load to fix the sample position; (2) in situ at the maximum indentation load; and (3) after removal of the load. The μXCT images provide a limited description of the cracking; Fig. 5(a) shows a vertical section (peak load and after unloading) in which one of the four radial cracks is visible by phase contrast. The horizontal displacement component for the same section is below, showing the relative opening of the radial crack decreases on load removal. The DVC data therefore provide a means to study crack opening. Vertical displacements close to the top surface (Fig. 5(b)) reveal the uplift from the development of lateral cracking after radial cracking, such that lateral cracks are bounded by the radial cracks. The

FIG. 6 Visualisations of digital volume-correlation measurement of crack-opening behavior for a short fatigue crack in Mg alloy, observed by synchrotron x-ray tomography: (a) z-displacement; and (b) maximum principal strain. The scale is qualitative (hot colors are higher values) [24].



with the indentation's residual stress field. Such observations may support models that predict the stability and development of contact-induced cracks during wear.

Cracks interact with the three-dimensional microstructure of the material as they develop. These interactions are particularly important for microstructural short cracks, which are short relative to microstructure length scales, such as grain size; knowledge is required of crack growth rates within grains and the resistance to crack growth presented by features, such as grain boundaries. Non-destructive 3D grain mapping techniques such as synchrotron x-ray diffraction contrast tomography (DCT) can complement μ XCT by providing a description of grain shape and crystal orientation in polycrystalline materials [22]. Short fatigue crack growth behavior in a cast magnesium alloy (Elektron 21), studied using a combination of DCT and μ XCT [23], showed that crack propagation occurred most rapidly along the basal crystal plane, with crack retardation occurring at grain boundaries that required tilt and twist of this plane for continued growth. More recently, using the same tomography data, a DVC analysis measured the displacements between the original undamaged material and the opening of the crack under load. Consequently, the local modes of crack opening were determined for the first time in a short fatigue crack in 3D (full details are provided in Ref 24). Visualizations of the displacements and the maximum principal strain field in two orthogonal sections across the crack are shown in Fig. 6; the largest displacements are in the vertical z-direction, parallel to the applied load, and the strain is obtained from the gradients of the displacement field. These images, which are composites of different

data types, are not fully quantitative; hot colors indicate larger displacements and cold colors smaller displacements with the same range for each figure. Quantitative analysis of the data showed the maximum crack-opening displacements to be around $1\ \mu\text{m}$; the basal plane cracks propagated with mixed mode opening.

Advanced Analysis of Crack-Displacement Fields

The studies of cracks that were described in the previous sections have used the measurement of the crack-opening displacements only, provided by two- or three-dimensional digital image-correlation analysis. However, it has also been shown, for two-dimensional analysis so far, that the displacement fields *around* cracks can be used, in particular to calculate the stress field via direct FE solution [25]. From this, the elastic strain energy release rate (i.e., J-integral) associated with crack growth may be obtained. The J-integral describes the thermodynamic driving force for crack propagation, which is a critical parameter in any study of fracture or fatigue. The technique is based on the contour integral method, and the energy release rate is calculated by taking contours of the calculated strain field around the crack tip. DIC observation of displacement fields, therefore, has the potential to measure the parameters that control crack propagation. A key issue, however, is the need to obtain accurate displacement fields close to cracks; these interfaces and conventional DIC algorithms are prone to error under such conditions. Solutions to this are needed before three-dimensional analysis of cracks, and then the driving force for their development under complex states of stress can be studied. In addition to improved precision in crack-displacement field measurement, for instance, by intelligent “masking” or analysis algorithms, better integration with FE software packages is also needed to make use of the available tools for 2D and 3D deformation analysis. Advanced image-correlation methods may also aid in detection of small cracks and the early development of damage against the background displacement field.

To support the development of these tools, it is necessary to have a reliable method that can deform images, using the known deformation field of a crack, to assess the quality of the measurement of that deformation field by digital image correlation, and the subsequent calculation of parameters such as the J-integral that depend on this displacement field. As part of this process, a tool (ODIN) has been developed; this is a `MATLAB` code that allows one to accurately distort a 2D image in an arbitrary manner; a 3D code is under development. Using an input FE element nodal displacement field that describes the required deformation, ODIN interpolates a pixel-wise displacement field using the shape function of the elements, changing the positions of points of known intensity in the original image to new positions in the deformed image. A cubic interpolation algorithm is then used to create the final deformed image, which has a regular pixel array; a B-spline interpo-

process are not readily measurable, but an assessment using deformations with known mathematical functions (i.e., sine waves) gives an average relative error of 0.05 % in the distorted image pixel intensity values when using the cubic interpolator with a 16-bit image. The maximum relative error was 0.1 %.

Errors in the displacement field that is measured after DIC analysis of the ODIN-deformed image, relative to its original, arise from the combined effects of the ODIN deformation and the usual measurement errors that occur from the DIC algorithms; the latter may be quantified by the conventional comparison of displaced images, but not the former. An example that illustrates the magnitude of the errors and their sensitivity to the DIC parameters is presented for a mode I center-cracked plate model, which was chosen to obtain the crack's elastic strain energy release rate from a DIC analysis of the displacement field. The reference model is a 60 mm \times 60 mm plate with a center crack of 10-mm length loaded in tension; the linear elastic analysis uses the material properties of steel ($E = 270$ GPa, Poisson's ratio = 0.33) with a regular FE size of 0.20 mm (ABAQUS, CPS4 elements; four-node plane stress quadrilateral with full integration).

The FE-obtained displacement field was used, with ODIN, to deform an image (Fig. 7). This was a digitally modified picture of a concrete surface, chosen as it provides a good degree of heterogeneity over a wide range of length scales; the image size was 1800 \times 3870 pixels². The DIC analysis to obtain displacement and strain fields was performed using the LaVision StrainMaster software that was also used for the other image-correlation analyses described in this paper; a multi-pass approach was applied with final pass interrogation window or subset sizes of 128, 96, 64, 48, and 32 pixels at 75 % overlap. An arbitrary rectangular mask was applied to the crack; the mask was 20 pixels wide and extended to 5 pixels beyond the crack-tip position. Calculation of the J-integral from the DIC result was achieved by importing the obtained displacement fields into ABAQUS, using a Python code to create the required input file. To quantify the relative effects of the DIC analysis parameters, the obtained J-integrals, calculated using only contours that did not touch the image border, were then normalized by the J-integral that was obtained in the original FE simulation.

Visual comparison of the strain fields of the original FE model and those obtained by DIC of the deformed images (Fig. 8) shows good agreement; however, some periodic noise appears as the final interrogation subset size decreases. There is also data loss adjacent to interfaces, i.e., the crack tip and image borders, which is usual in DIC with conventional algorithms. The periodicity is considered, at present, to be because of effects of interference between the ODIN interpolator and the interpolation algorithms used in the DIC analysis; the effect increases as the window size decreases because the strain is evaluated on smaller subsets that reduce the effect of averaging. Nonetheless, comparison of the displacement fields found that typically the relative error in strain was less than 0.09 % for 90 % of the dataset, with errors approaching 1 % at positions close to the masked crack tip.

FIG. 7 Original image from picture of a concrete surface and ODIN-distorted image, with zoomed image of the crack shown.

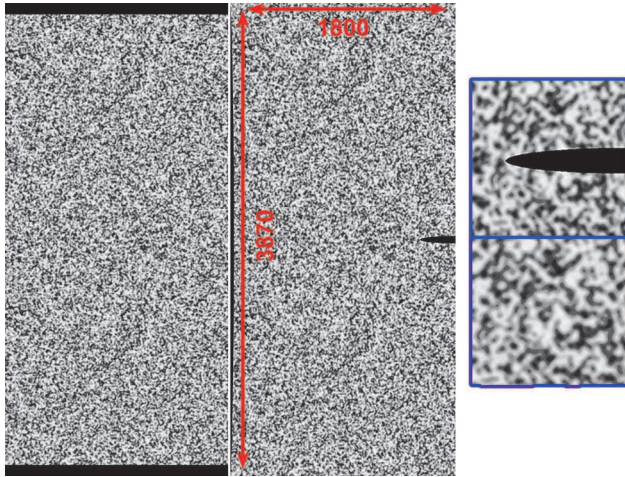


FIG. 8 Comparison between the original FE strain field, and example extraction of the field following DIC of deformed images; the strain component parallel to the applied stress is shown: (a) Original FE field; (b) DIC analysis, 96×96 pixels² interrogation subset; and (c) DIC analysis, 32×32 pixels² interrogation subset.

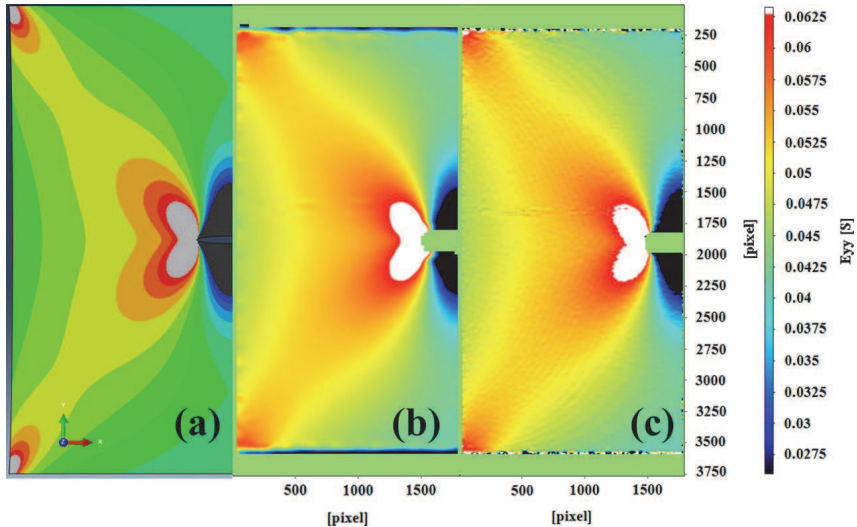


TABLE 1 Summary of J-integral values (standard deviation is given in brackets) obtained as a function of the interrogation subset size, in terms of pixels and relative size of the subset to the crack (normalized using 32 pixels).

FE Element Size (pixels)	Subset Size (pixels)	Subset Size (relative)	Normalized J-Integral
30	128	4	0.66 (0.017)
	96	3	0.96 (0.008)
	64	2	0.85 (0.006)
	48	1.5	0.80 (0.003)

The J-integrals were contour independent, with an error that depends on the interrogation subset or window size (Table 1). Some of this error can be attributed to the loss of displacement data closest to the crack tip, where the strain energy density is highest; the increasing loss of its contribution to the J-integral, thus, becomes more significant as the relative subset size increases. With decreasing window size, the error in the displacements also becomes larger, and this causes a progressive loss in accuracy. Further work is in progress to evaluate improved methods for DIC analysis, for instance, using anisotropic interrogation subsets aligned with the displacement field and subset splitting [26] to improve the displacement measurements close to the crack. The aim is to identify the required experimental and analysis conditions that reliably achieve an error of better than 10 %, which will be acceptable for engineering property measurements.

Conclusion

Digital image-correlation analysis provides a useful tool for the measurement of the displacement fields associated with cracks, which can be mapped in two or three dimensions. In principle, fracture mechanics parameters such as the J-integral can be extracted, given a sufficiently accurate, high-resolution mapping of the displacements. However, the effects of image-correlation parameters are complex; significant underestimation of the J-integral can occur if the displacements close to the crack tip are not sufficiently measured. Simulation of image deformation provides a means to evaluate the effects of image-correlation parameters, and so provides a tool to support image-correlation algorithm development and also to experiment with design. Use of these methods with DVC applied to tomographic images would allow the accurate characterization of 3D cracks as a three-dimensional object, and enable their study under complex states of loading.

ACKNOWLEDGMENTS

M.M. and T.J.M. acknowledge the support of the Oxford Martin School. The writers acknowledge the beam time awards at the Diamond Light Source (experiments

EE9036 and EE7730) and appreciate the considerable help of M. Jordan, H. Çetinel, S. Barhli, R. Atwood, C. Cooper, and R. Bradley to conduct the experiments.

References

- [1] Li, H., Duff, J., and Marrow, T. J., "In-Situ Observation of Crack Nucleation in Nuclear Graphite by Digital Image Correlation," *Proceedings of PVP2008 ASME Pressure Vessels and Piping Division Conference, Paper PVP2008-61136*, Chicago, July 27–31, 2008.
- [2] Mostafavi, M. and Marrow, T. J., "In Situ Observation of Crack Nuclei in Poly-Granular Graphite Under Ring-on-Ring Equi-Biaxial and Flexural Loading," *Eng. Fract. Mech.*, Vol. 78, 2011, pp. 1756–1770.
- [3] Aswad, M. A. and Marrow, T. J., "Intergranular Crack Nucleation in Polycrystalline Alumina," *18th European Conference on Fracture*, ECF18, Dresden, Germany, Aug 30–Sept 3, 2010.
- [4] Rahimi, S., Engelberg, D. L., Duff, J. A., and Marrow, T. J., "In Situ Observation of Intergranular Crack Nucleation in a Grain Boundary Controlled Austenitic Stainless Steel," *J. Microsc.*, Vol. 233, No. 3, 2009, pp. 423–431.
- [5] Kovac, J., Alaux, C., Marrow, T. J., Govekar, E., and Legat, A., "Correlations of Electrochemical Noise, Acoustic Emission and Complementary Monitoring Techniques during Intergranular Stress-Corrosion Cracking of Austenitic Stainless Steel," *Corrosion Sci.*, Vol. 52, No. 6, 2010, pp. 2015–2025.
- [6] Cook, A., Duff, J., Stevens, N., Lyon, S., Sherry, A., and Marrow, T. J., "Preliminary Evaluation of Digital Image Correlation for In Situ Observation of Low Temperature Atmospheric-Induced Chloride Stress Corrosion Cracking in Austenitic Stainless Steels," *216th ECS Meeting*, Vienna, Austria, Oct 4–9, 2009.
- [7] Duff, J. A. and Marrow, T. J., "In Situ Observation of Short Fatigue Crack Propagation in Oxygenated Water at Elevated Temperature and Pressure," *Corros. Sci.*, Vol. 68, 2012, pp. 34–43.
- [8] Stratulat, A., Duff, J., and Marrow, T. J., "Grain Boundary Structure and Intergranular Stress Corrosion Crack Initiation in High Temperature Water of a Thermally Sensitised Austenitic Stainless Steel, Observed In Situ," *Corros. Sci.*, Vol. 85, 2014, pp. 428–435.
- [9] Stock, S. R., "X-Ray Microtomography of Materials," *Int. Mater. Rev.*, Vol. 44, No. 4, 1999, pp. 141–164.
- [10] Maire, E., Buffière, J.-Y., Salvo, L., Blandin, J. J., Ludwig, W., and Letang, J. M., "On the Application of X-Ray Microtomography in the Field of Materials Science," *Adv. Eng. Mater.*, Vol. 3, No. 8, 2001, pp. 539–546.
- [11] Marrow, T. J., Buffière, J.-Y., Withers, P. J., Johnson, G., and Engelberg, D., "High Resolution X-Ray Tomography of Short Fatigue Crack Nucleation in Austempered Ductile Cast Iron," *Int. J. Fatigue*, Vol. 26, No. 7, 2004, pp. 717–725.
- [12] Bay, B. K., Smith, T. S., Fyhire, D. P., and Saad, M., "Digital Volume Correlation: Three-Dimensional Strain Mapping Using X-Ray Tomography," *Exp. Mech.*, Vol. 39, No. 3, 1999, pp. 217–226.

- [13] Forsberg, F. and Siviour, C. R., "3D Deformation and Strain Analysis in Compacted Sugar Using X-Ray Microtomography and Digital Volume Correlation," *Meas. Sci. Technol.*, Vol. 20, No. 9, 2009, p. 095703.
- [14] Barranger, Y., Doumalin, P., Dupre, J.-C., Germaneau, A., Hedan, S., and Valle, V., "Evaluation of Three-Dimensional and Two-Dimensional Full Displacement Fields of a Single Edge Notch Fracture Mechanics Specimen, in Light of Experimental Data Using X-Ray Tomography," *Eng. Fract. Mech.*, Vol. 76, 2009, pp. 2371–2383.
- [15] Mostafavi, M., McDonald, S. A., Mummery, P. M., and Marrow, T. J., "Observation and Quantification of Three-Dimensional Crack Propagation in Poly-Granular Graphite," *Eng. Fract. Mech.*, Vol. 110, 2013, pp. 410–420.
- [16] Mostafavi, M., Baimpas, N., Tarleton, E., Atwood, R. C., McDonald, S. A., Korsunsky, A. M., and Marrow, T. J., "Three-Dimensional Crack Observation, Quantification and Simulation in a Quasi-Brittle Material," *Acta Mater.*, Vol. 61, 2013, pp. 6276–6289.
- [17] Giannakopoulos, A. E. and Suresh, S., "Determination of Elastoplastic Properties by Instrumented Sharp Indentation," *Scripta Mater.*, Vol. 40, 1999, pp. 1191–1198.
- [18] Mostafavi, M., Vertyagina, Y., Reinhard, C., Bradley, R., Jiang, X., Galano, M., and Marrow, J., "3D Studies of Indentation by Combined X-Ray Tomography and Digital Volume Correlation," *Key Eng. Mater.*, Vols. 592–593, 2014, pp. 14–21.
- [19] Mostafavi, M., Collins, D. M., Cai, B., Bradley, R., Atwood, R. C., Reinhard, C., Jinang, X., Galano, M., Lee, P. D., and Marrow, T. J., "Yield Behavior Beneath Hardness Indentations in Ductile Metals, Measured by Three-Dimensional Computed X-Ray Tomography and Digital Volume Correlation," *Acta Mater.*, Vol. 82, 2015, pp. 468–482.
- [20] Lawn, B. R., "Indentation of Ceramics With Spheres: A Century After Hertz," *J. Am. Ceram. Soc.*, Vol. 81, 1998, pp. 1977–1994.
- [21] Vertyagina, Y., Mostafavi, M., Reinhard, C., Atwood, R., and Marrow, T. J., "In Situ Quantitative Three-Dimensional Characterisation of Sub-Indentation Cracking in Polycrystalline Alumina," *J. Eur. Ceram. Soc.*, Vol. 34, No. 12, 2014, pp. 3127–3132.
- [22] King, A., Johnson, G., Engelberg, D., Ludwig, W., and Marrow, J., "Observations of Intergranular Stress Corrosion Cracking in a Grain-Mapped Polycrystal," *Science*, Vol. 321, No. 5887, 2008, pp. 382–385.
- [23] King, A., Ludwig, W., Herbig, M., Buffière, J.-Y., Khan, A. A., Stevens, N., and Marrow, T. J., "Three-Dimensional In Situ Observations of Short Fatigue Crack Growth in Magnesium," *Acta Mater.*, Vol. 59, 2011, pp. 6761–6771.
- [24] Marrow, T. J., Mostafavi, M., Hashimoto, T., and Thompson, G. E., "A Quantitative Three-Dimensional In Situ Study of a Short Fatigue Crack in a Magnesium Alloy," *Int. J. Fatigue*, Vol. 66, 2014, pp. 183–193.
- [25] Becker, T. H., Mostafavi, M., Tait, R. B., and Marrow, T. J., "An Approach to Calculate the J-Integral by Digital Image Correlation Displacement Field Measurement," *Fatigue Fract. Eng. Mater. Struct.*, Vol. 35, 2011, pp. 971–984.
- [26] Poissant, J. and Barthelat, F., "A Novel 'Subset Splitting' Procedure for Digital Image Correlation on Discontinuous Displacement Fields," *Exp. Mech.*, Vol. 50, 2009, pp. 353–364.

CRACK LENGTH MONITORING TECHNIQUES

STP 1584, 2015 / available online at www.astm.org / doi: 10.1520/STP158420140055

K. M. Tarnowski,¹ C. M. Davies,¹ D. W. Dean,²
and K. M. Nikbin¹

The Influence of Plasticity on Crack Length Measurements Using the Potential Drop Technique

Reference

Tarnowski, K. M., Davies, C. M., Dean, D. W., and Nikbin, K. M., "The Influence of Plasticity on Crack Length Measurements Using the Potential Drop Technique," *Evaluation of Existing and New Sensor Technologies for Fatigue, Fracture and Mechanical Testing*, STP 1584, Jidong Kang, David Jablonski, and David Dudzinski, Eds., pp. 73–96, doi:10.1520/STP158420140055, ASTM International, West Conshohocken, PA 2015.³

ABSTRACT

The potential drop (PD) technique is one of the most common methods for determining crack growth; however, other factors can also change the resistance of the specimen, which may erroneously be interpreted as crack extension. In tough, ductile materials, plastic strain can cause a significant change in PD. This paper presents an experimental investigation which quantifies the apparent crack extension due to strain prior to the onset of physical crack growth and considers ways to mitigate it. Compact tension, C(T), and single edge notch tension, SEN(T), specimen geometries are considered with a range of crack lengths. The influence of probe location is also considered. The results identify apparent crack extensions of up to 1.0 mm in the absence of any physical crack extension. This can be reduced through careful selection of probe locations. Appropriate locations are suggested for the geometries considered. It is also shown that high constraint geometry can significantly reduce the influence of plasticity on PD.

Manuscript received May 30, 2014; accepted for publication December 2, 2014; published online January 27, 2015.

¹Department of Mechanical Engineering, Imperial College London, South Kensington Campus, London, SW7 2AZ, UK.

²EDF Energy, Barnett Way, Barnwood, Gloucester, GL4 3RS, UK.

³ASTM Fourth Symposium on the *Evaluation of Existing and New Sensor Technologies for Fatigue, Fracture and Mechanical Testing* on May 7–8, 2014 in Toronto, Canada.

Keywords

potential drop, strain, plasticity, ACPD, DCPD, crack length, crack extension

Nomenclature

A = crack length as defined in ASTM E1457-13 [1]

a_0 = initial crack length as defined in ASTM E1457-13 [1]

A, B, C = polynomial coefficients

B = specimen thickness as defined in ASTM E1457-13 [1]

B_n = net specimen thickness, including side-grooves, as defined in ASTM E1457-13 [1]

K_I = mode I stress intensity factor

L = specimen length, SEN(T) only, as defined in ASTM E1457-13 [1]

PD = potential drop

PD_0 = initial potential drop, corresponding to a_0

R = resistance

R_0 = initial resistance, corresponding to a_0

r_p = plastic zone size

W = specimen width as defined in ASTM E1457-13 [1]

β = constant which depends on the stress conditions at the crack tip

Δa = crack extension ($\Delta a = a - a_0$)

ΔPD = change in potential drop ($\Delta PD = PD - PD_0$)

ΔR = change in resistance ($\Delta R = R - R_0$)

σ_y = yield strength

Introduction

The potential drop (PD) method is one of the main techniques used for measuring crack growth in the laboratory. One of the key advantages of the technique is its suitability to a wide range of applications including creep [1], fatigue [2], creep-fatigue [3], and fracture toughness testing [4]. The technique works on the principle that a constant current flowing through a specimen generates an electrical field that is sensitive to changes in the geometry of the specimen, in particular crack extension. The crack extension can therefore be estimated by measuring the potential drop between two probes located either side of the crack and using a suitable calibration curve.

It is widely accepted that factors other than crack growth can also change the resistance of a test specimen. This may be erroneously interpreted as a change in crack length. Such factors include:

- Change in temperature [5,6]
- Drift in amplifier gain [5]
- Strains [7–9]

- Thermal aging [6,7]
- Electrical contact between the crack faces [6,7]
- Material texture [10]
- Residual stress relaxation [11]

Where these factors affect the resistance of the entire specimen, such as a change in ambient temperature, their influence can be minimized by normalizing the PD with respect to a reference measurement taken at a location that is not influenced by crack extension. This approach is not appropriate for factors which only cause a local change in resistance. Where such local factors have a significant influence on PD measurements, it is important to try and develop alternative ways to mitigate them.

One source of local changes in resistance in tough, ductile materials is the large strains associated with plasticity and creep, which predominately accumulate at the crack tip [7,9,12]. The aim of this paper is to quantify the apparent crack extension due to strain, in the absence of any physical crack growth, for the simple case of a monotonically loaded specimen at room temperature. An approach to minimize this strain induced change in PD to help differentiate it from actual crack extension is discussed. A review of the relevant literature is presented in the following section.

THE INFLUENCE OF STRAIN ON PD MEASUREMENTS

It is known that strain can influence the electrical behavior of materials. Indeed it is this effect which is measured in a typical strain gauge [10]. It is therefore no surprise that many authors have identified strain (elastic, plastic, or creep) as a potential source of error when estimating crack length using the PD technique.

Saxena [13] used direct current potential drop (DCPD) to monitor crack growth at elevated temperatures. Constant load line displacement rate tests were performed on compact tension (C(T)) and centre crack tension (CC(T)) specimens manufactured from ASTM grade A470 class 8 steel and a type 304 stainless steel. Discrepancies of up to 1.7 mm were identified between the crack extension estimated using PD and measured from the fracture surface. This was the equivalent to ~11 % of the actual crack extension. The discrepancy was attributed to strain effects such as specimen deformation and crack tip blunting.

Freeman and Neate [7] reviewed the use of DCPD for measuring crack extension at elevated temperatures in materials of varying ductility. They identified deformation at the crack tip, bulk specimen deformation, microstructural changes, and bridging between the crack surfaces as potential sources of PD change in addition to crack extension. In low ductility materials, where small strains produce a negligible change in PD measurements, an initial reduction in PD was identified due to microstructural changes attributed to dislocation rearrangement during primary creep and changes in precipitate size and spacing. This resulted in a minimum in the PD measurement. It was suggested that any subsequent increase in PD may indicate crack initiation and can be used to calculate crack extension using standard room temperature calibration curves, although bridging across the crack faces may cause the crack length to be underestimated.

In high ductility materials, such as type 316 stainless steel, Freeman and Neate [7] showed that the initial increase in PD due to strains can be of the same order of magnitude or larger than the reduction in PD due to microstructural changes. This can give rise to significant increases in PD prior to initiation, making it difficult to identify the onset of creep crack growth from the PD signal alone. It is also suggested that any change in PD subsequent to initiation will continue to be influenced by the time dependent nature of the creep strain field, thus precluding the use of room temperature calibration curves. For high ductility materials, any change in PD due to conduction across the crack faces is likely to be negligible even at small loads due to the relatively large displacements.

Lowes and Fearnough [9] identified that the change in PD due to plastic deformation in the absence of crack growth was directly proportional to crack opening displacement (COD). They used this relationship to identify the onset of slow crack growth in monotonically loaded 3 point bend Charpy specimens manufactured from C-M structural steels. It was suggested that initiation of crack growth occurred where a plot of DCPD against COD deviated from its linear trend. They confirmed their results by interrupting tests at various loads and inspecting the fracture surface. This approach was successfully used by other authors. A review of this work was presented by Wilkowski and Maxey [8].

Bakker [12] used DCPD to monitor crack initiation and subsequent crack growth during ductile fracture tests on mild steel ST52-3 SEN(B) specimens. Deformation, blunting, and void growth were identified as potential sources of changes in the PD signal in addition to crack growth. After the initiation of crack growth, it was suggested that for relatively small variations in crack length, the influence of these factors would be small compared to the influence of crack growth; thus the associated error in the PD measurement would remain approximately constant. By identifying the PD at the point of initiation using the method developed by Lowes and Fearnough [9] and subtracting it from all subsequent measurements, the majority of the error due to plasticity could be removed. Discrepancies of up to 0.69 mm were identified between the crack extensions estimated using PD and measured from the fracture surface. The PD method typically underestimated the crack length by less than 10 %, although errors of up to 28 % were identified. At the point of initiation, PD measurements equivalent to 0.37 mm of crack growth were recorded. Bakker [12] also commented on difficulties in identifying the point of initiation from the small change in gradient on a plot of DCPD against COD.

In summary, significant errors in crack length estimates were attributed to strains. The literature suggests that the majority of strain effects occurred prior to the initiation of crack growth and that for monotonically loaded specimens, there is a linear relationship between the change in PD and crack mouth opening displacement (CMOD) during this incubation period. Deviation from this linear trend was successfully used to identify the onset of crack extension; however, other authors

changes in gradient. Despite this, there is currently no best-practice for using the PD technique in the presence of large strains in the ASTM standards.

In this paper, the influence of strain on PD measurements in the absence of any physical crack growth is examined for incrementally loaded specimens manufactured from ex-service type 316H stainless steel. This is a tough, ductile material of particular interest to the power generation industry. A range of specimen geometries, initial crack lengths, and probe locations were considered to identify whether these factors influence the change in PD due to strain. The probe locations were selected based on finite element analysis sensitivity studies. Numerically derived calibration curves were used to convert the change in PD due to strain to an apparent crack extension to compare the susceptibility of each specimen and probe arrangement to strain induced changes in PD. The results were used to provide recommendations for using the PD technique to monitor initiation and crack extension in similar tough, ductile materials. The subsequent sections discuss different aspects of the experimental setup followed by a description of the methodology.

The PD System

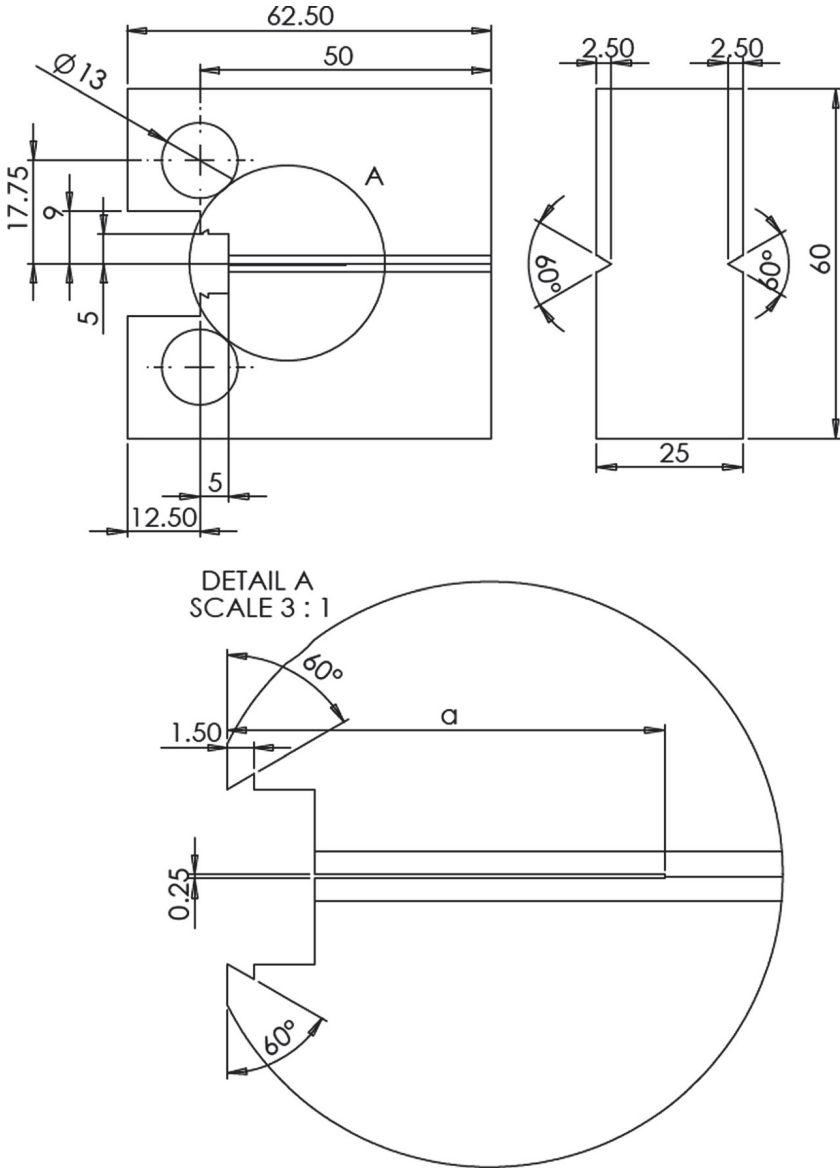
There are two main types of PD technique: DCPD and alternating current potential drop (ACPD). ACPD can be further categorized into low frequency and high frequency. In this paper, a low frequency ACPD system is used. At low frequencies, the skin depth associated with ACPD is large compared with the specimen geometry; the skin effect is thus negligible and the current distribution is the same as DCPD. The conclusions in this paper are therefore directly applicable to DCPD.

The low frequency ACPD system used implements a lock-in amplifier to significantly improve the signal-to-noise ratio compared to DCPD. This makes it ideal for monitoring small changes in PD. It also has the advantage of not being sensitive to amplifier drift or thermal electromotive force (EMF) [14], unlike DCPD. Unlike high frequency ACPD, it is not sensitive to small changes in magnetic permeability [10]; however, it is capable of monitoring any discontinuous cracking ahead of the crack tip [13,15].

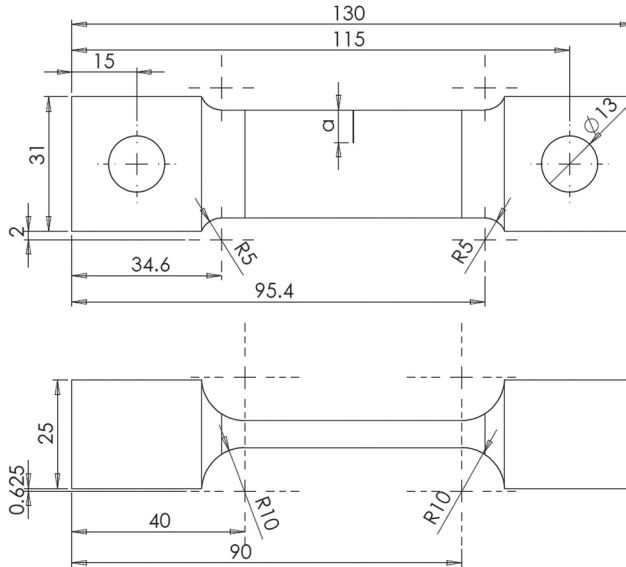
Specimen Geometry

Two specimen geometries were considered which provide different levels of constraint: a high constraint, thick, C(T) specimen with side grooves, and a lower constraint, thin, single edge notch tension (SEN(T)) specimen without side grooves. The geometry of these specimens is provided in [Figs. 1](#) and [2](#), respectively. These specimen geometries are within the guidelines provided in ASTM E1457-13 [1] with the exception of the pin hole diameters, which were increased from 12.5 to 13.0 mm to accommodate PVC insulation tape applied to the loading pins. This is discussed in more detail in the section “Experimental Setup.”

FIG. 1 C(T) specimen geometry based on guidance in ASTM E1457-13 [1].



Four SEN(T) specimens were manufactured with a/W ratios of 0.30, 0.38, 0.54, and 0.70. Two C(T) specimens were manufactured with a/W ratios of 0.45 and 0.55. The pre-crack was produced by electrical discharge machining (EDM).

FIG. 2 SEN(T) specimen geometry based on guidance in ASTM E1457-13 [1].

the C(T) and SEN(T) specimens are summarized in [Table 1](#) and [Table 2](#), respectively.

Materials

All specimens were manufactured from ex-service type 316H austenitic stainless steel. This is a tough, ductile material, which will promote significant plastic deformation at the crack tip prior to any crack extension. The relevant room temperature material properties are summarized in [Table 3](#). An engineering stress-strain plot is provided in [Fig. 3](#).

Probe Locations

A wide range of probe arrangements were initially considered for this investigation. These were reduced to a selection of preferred probe locations which were used in the experiment. An overview of the process for selecting measurement probe

TABLE 1 C(T) specimen critical dimensions.

Specimen ID	a/W	a_0 (mm)	W (mm)	B (mm)	B_n (mm)
CT45	0.45	22.5	50.0	25.0	20.0
CT55	0.55	27.5	50.0	25.0	20.0

TABLE 2 SEN(T) specimen critical dimensions.

Specimen ID	a/W (mm)	a_0 (mm)	W (mm)	B (mm)	L
SENT30	0.30	7.5	25.0	6.25	50.0
SENT38	0.38	9.5	25.0	6.25	50.0
SENT54	0.54	13.5	25.0	6.25	50.0
SENT70	0.70	17.5	25.0	6.25	50.0

locations and reference probe locations is provided in the following two sections, respectively. Finally a discussion of the preferred probe locations is provided. For brevity, the details of all locations initially considered have not been provided.

MEASUREMENT PROBE SELECTION PROCESS

Static finite element models of the two specimen geometries shown in Fig. 1 and Fig. 2 were generated using COMSOL multi-physics finite element software [16]. The C(T) model had an initial crack length, a_0 , of 25.0 mm ($a/W=0.5$) and the SEN(T) model had an initial crack length of 7.5 mm ($a/W=0.3$). The crack was then extended in increments of 0.5 mm for a total of 10 mm of crack extension. For each probe location, the change in PD, ΔPD , was recorded and a third order polynomial regression fit calibration curve was generated from the normalized crack extension, $\Delta a/a_0$, and the normalized change in PD, $\Delta PD/PD_0$, where PD_0 is the PD at the initial crack length, a_0 . The crack extension and the change in PD were normalized to generate calibration curves which are independent of material, current and specimen thickness.

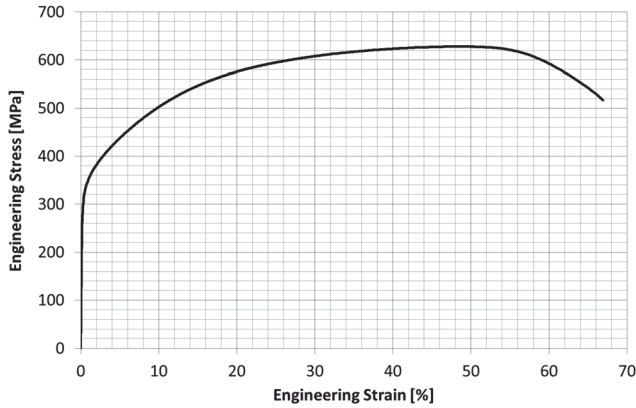
The COMSOL analyses were then repeated with the probes moved from their nominal locations by 1.0 mm to simulate probe misplacement as shown in Fig. 4(a). For each “misplaced” probe arrangement, the change in PD was recorded at each crack increment and the crack extension was estimated from the calibration curve derived from the nominal probe locations. This was compared to the actual crack extension in the model. The difference between the two values provides the error due to probe misplacement, as shown schematically in Fig. 4(b). For each nominal probe arrangement, multiple analyses were performed with probes misplaced in different directions (see Fig. 4(a)) to identify the maximum probe misplacement error.

The maximum probe misplacement error and the sensitivity to crack extension were used to select the preferred probe locations. The sensitivity to crack extension was calculated from the initial gradient of the nominal calibration curve.

TABLE 3 Room temperature material properties of ex-service type 316H stainless steel.

E (GPa)	ϵ_u	$\sigma_{0.2}$ % (MPa)	σ_{UTS} (MPa)
205	0.530	292	626

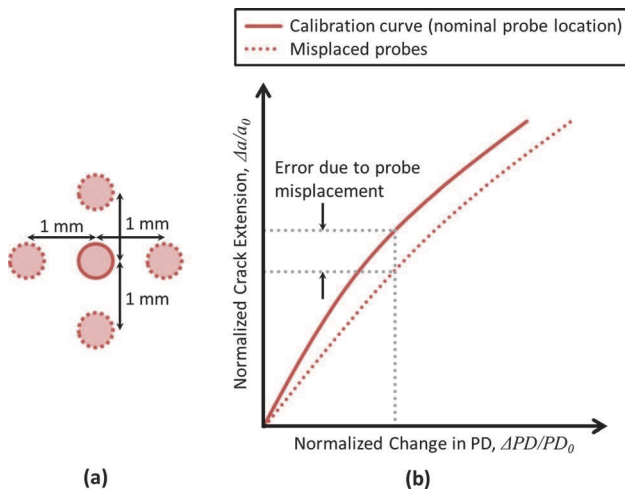
FIG. 3 Engineering stress–strain plot for ex-service type 316H stainless steel.



REFERENCE PROBE SELECTION PROCESS

As discussed in ASTM E647-13a [2], a reference measurement should be taken at a location where it is not influenced by crack extension. This is used to remove any global changes in specimen resistance from the measurement signal such as those caused by temperature fluctuations. The reference probes may be attached to the test specimen or to another specimen experiencing identical conditions to the test

FIG. 4 Schematic representation of (a) the nominal and misplaced probe locations and (b) the error due to a “misplaced” probe arrangement.



specimen. The magnitude of the reference signal should be greater than or equal to the signal measured across the crack.

When the reference probes are attached to the test specimen, it can be difficult to achieve a signal that is greater than or equal to the signal measured across the crack. When the reference probes are attached to another specimen, it is difficult to obtain identical test conditions. The requirement for the reference signal to be greater than or equal to the measured signal is to avoid the introduction of excessive noise when normalizing the measured signal with respect to the reference signal. This requirement is less significant when using the proposed low frequency ACPD due to its high signal-to-noise ratio. For this reason, the reference probes have been attached directly to the test specimen. COMSOL finite element analyses were performed to identify suitable probe locations which were not influenced by crack extension while maximizing the magnitude of the reference signal.

An alternative approach to those discussed above is to measure the PD across the crack at two different locations and divide one signal by the other. This approach was proposed by McCartney et al. [17] and was successfully implemented by Merah et al. [18]. It avoids the problem of finding a location on the specimen where a suitably large reference measurement can be obtained that is not influenced by crack extension. Moreover, both signals will be sensitive to local conditions at the crack tip so the ratio of these two signals should suppress some of the local effects at the crack tip such as crack tip strain.

The main disadvantage of this approach is that because both signals are sensitive to crack extension, the ratio of these two signals will suppress some of this sensitivity in the same way that it will reduce the sensitivity to other local effects at the crack tip such as strain. It is not obvious whether the reduction in sensitivity to crack extension or the reduction in sensitivity to other local crack effects will be more significant. The approach was proposed by McCartney et al. [17] and has therefore been considered to see if it suppresses the influence of strains on the PD measurements.

PREFERRED PROBE LOCATIONS

The preferred probe locations for the C(T) specimens are shown in Fig. 5 and summarized in Table 4. Probe labels with the prefix “I” are current injection probes. Probe labels with the prefix “C” are electrical potential sensing probes. Locations C1, C3, and C_{tip} all use injection probe I1 and are shown in Fig. 5(a). Sensing probe location C2 uses injection probe I2 as shown in Fig. 5(b). The sensing and injection reference probes, C_{ref} and I_{ref} respectively, are shown in Fig. 5(c).

The maximum probe misplacement error and the sensitivity to crack extension for the preferred probe locations are provided in Table 5. In this table, the sensitivity to crack extension was normalized with respect to the most sensitive probe location (C_{tip}) to make the results independent of applied current and material resistivity. The locations C1, C2, and C3 were the least sensitive to probe misplacement whilst

FIG. 5 C(T) specimen preferred probe locations (a) C1, C3, and C_{tip}; (b) C2; (c) C_{ref}.

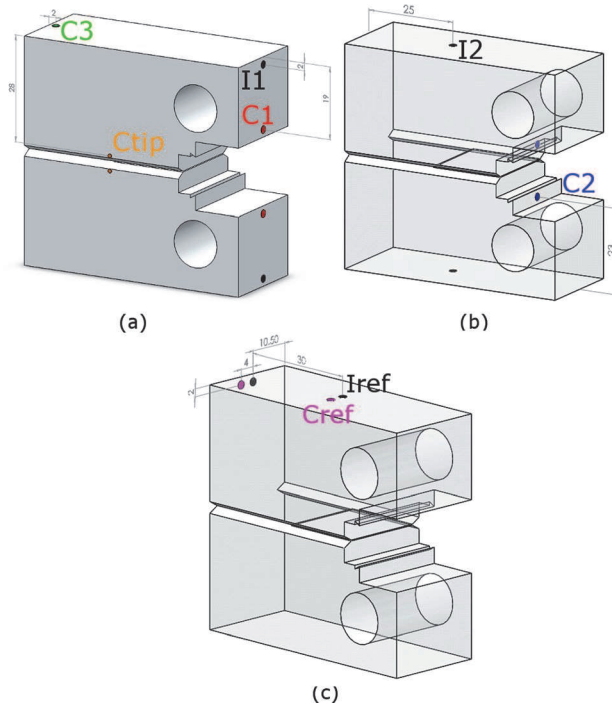


TABLE 4 Summary of preferred probe locations for C(T) specimens.

Probe Location	Description
I1	Current injection for sensing probes C1, C3 and C _{tip} .
I2	Current injection for sensing probe C2. Location from ASTM E1457-13 [1].
I _{ref}	Current injection for reference sensing probe, C _{ref} .
C1	Sensing probe with low sensitivity to probe misplacement & high sensitivity to crack extension.
C2	Sensing probe with low sensitivity to probe misplacement & high sensitivity to crack extension. Location from ASTM E1457-13 [1].
C3	Sensing probe with low sensitivity to probe misplacement & high sensitivity to crack extension.
C _{tip}	Sensing probe with highest sensitivity to crack extension, but also sensitive to probe misplacement.
C _{ref}	Reference sensing probe.
C31	(C31 = C3/C1) Sensing probe arrangement with low sensitivity to probe misplacement & high sensitivity to crack extension.

TABLE 5 C(T) probe location selection criteria for preferred locations.

Probe Location	Normalized Sensitivity to Crack Extension	Maximum Error in Crack Extension (Due to 1mm Probe Misplacement) (mm)
C1	0.63	0.16
C2	0.49	0.06
C3	0.31	0.02
C _{tip}	1.00	2.38

recommended in ASTM E1457-13 [1]. The location C_{tip} is in-line with the crack tip and therefore varies depending on the initial crack length in the specimen. This location is the most sensitive to crack extension, although the calibration curve is also very sensitive to probe misplacement.

McCartney et al. [17] used the ratio of C3 and C1 to monitor crack extension. This arrangement was also considered here. The ratio of C3 and C1 is subsequently labelled C31.

The preferred probe locations for the SEN(T) specimens are shown in Fig. 6 and summarized in Table 6. Probe labels with the prefix “I” are current injection probes. Probe labels with the prefix “S” are electrical potential sensing probes.

FIG. 6 SEN(T) specimen preferred probe locations (a) S1, S2, S3, and S_{tip}; (b) S_{ref}.

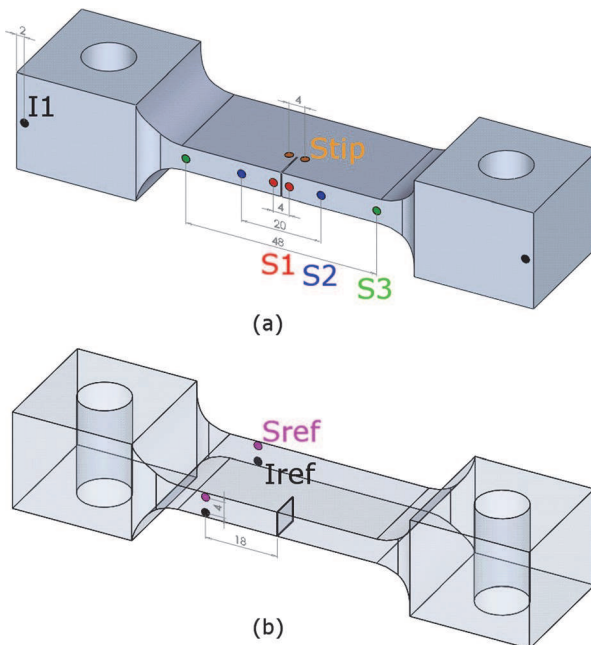


TABLE 6 Summary of preferred probe locations for SEN(T) specimens.

Probe Location	Description
I1	Current injection for sensing probes S1, S2, S3 and S _{tip} .
I _{ref}	Current injection for reference sensing probe, S _{ref} .
S1	Sensing probe with low sensitivity to probe misplacement & high sensitivity to crack extension. Location from ASTM E1457-13 [1]
S2	Sensing probe with low sensitivity to probe misplacement & high sensitivity to crack extension.
S3	Sensing probe with low sensitivity to probe misplacement & high sensitivity to crack extension.
S _{tip}	Sensing probe with highest sensitivity to crack extension, but also sensitive to probe misplacement.
S _{ref}	Reference probe.
S32	(S32 = S3/S2) Sensing probe arrangement with low sensitivity to probe misplacement & high sensitivity to crack extension. Approximately linear calibration curve.

Locations S1, S2, S3, and S_{tip} are shown in Fig. 6(a). These all use injection probe “I1.” The sensing and injection reference probes, “S_{ref}” and “I_{ref},” respectively, are shown in Fig. 6(b).

The maximum probe misplacement error and the sensitivity to crack extension for the preferred probe locations are provided in Table 7. In this table, the sensitivity to crack extension was normalized with respect to the most sensitive probe location (S_{tip}) to make the results independent of applied current and material resistivity. The location S1 is least sensitive to probe misplacement but is very sensitive to crack extension. It is also the location recommended in ASTM E1457-13 [1]. Locations S2 and S3 also have low sensitivity to probe misplacement and are sensitive to crack extension. They have been included to investigate the influence of moving the sensing probes away from the crack plane. The location S_{tip} is in-line with the crack tip and therefore varies depending on the initial crack length in the specimen. This probe location is the most sensitive to crack extension, although the calibration curve is also very sensitive to probe misplacement.

TABLE 7 SEN(T) probe location selection criteria for preferred locations.

Probe Location	Normalized Sensitivity to Crack Extension	Max. Error in Crack Extension (Due to 1mm Probe Misplacement) (mm)
S1	0.91	0.15
S2	0.65	0.30
S3	0.47	0.21
S _{tip}	1.00	1.45

TABLE 8 Calibration curve polynomial coefficients for specimens CT45 and CT55.

Probe Location	CT45			CT55		
	A	B	C	A	B	C
C1	204.6560	-7.4032	2.7683	-79.0438	1.2272	2.1216
C2	5.3168	-0.7965	0.8569	0.4858	-0.3938	0.7364
C3	2.1480	-0.8058	0.9382	-0.9128	-0.3384	0.6970
C _{tip}	0.4806	-0.1939	0.2866	0.0453	-0.0591	0.2218
C31	-3.8964	-1.0849	1.4193	-1.0785	-0.7370	1.0380

The ratio of S3 and S2 (subsequently labelled S32) was also considered. It is also of note that the calibration curve is approximately linear for a large amount of crack extension.

Calibration Curves

For each of the specimens listed in [Tables 1](#) and [2](#), calibration curves were derived using COMSOL [16]. For each specimen, the crack was extended in 0.1 mm increments for a total of 1.0 mm of crack extension. A calibration curve was generated from a third order polynomial regression fit to the normalized crack extension and normalized change in PD in the form of Eq 1. The coefficients A, B, and C of the derived calibration curves are provided in [Table 8](#), [Table 9](#), and [Table 10](#) for each of the probe arrangements and specimen geometries. It is important to note that these calibrations curves only account for crack extension and not the influence of strain. This is similar to most calibration curves available in the literature. They are also only applicable to 1.0 mm of crack extension.

$$(1) \quad \frac{\Delta a}{a_0} = A \left(\frac{\Delta PD}{PD_0} \right)^3 + B \left(\frac{\Delta PD}{PD_0} \right)^2 + C \left(\frac{\Delta PD}{PD_0} \right)$$

The probe locations selected for the SEN(T) specimens correspond to those used by Johnson [19] to derive an analytical calibration curve for a CC(T)

TABLE 9 Calibration curve polynomial coefficients for specimens SENT30 and SENT38.

Probe Location	SENT30			SENT38		
	A	B	C	A	B	C
S1	-0.6063	-0.0164	0.9975	-0.4288	-0.1251	0.9272
S2	-3.2925	-1.4545	2.2289	-0.3152	-1.0652	1.6322
S3	-64.9840	-14.9895	6.1487	3.2000	-8.2815	3.9068
S _{tip}	0.1711	-0.2168	0.4982	0.1341	-0.1695	0.3897
S23	-14.4007	-0.8513	3.4962	-3.6382	-0.3109	2.8035

TABLE 10 Calibration curve polynomial coefficients for specimens SENT54 and SENT70.

Probe Location	SENT54			SENT70		
	A	B	C	A	B	C
S1	-0.1209	-0.2797	0.7766	0.0501	-0.3739	0.5907
S2	0.1005	-0.6687	1.0407	0.1651	-0.5511	0.6907
S3	3.3497	-2.9246	1.9256	1.2715	-1.4253	1.0446
S _{tip}	0.0781	-0.1068	0.2630	0.0856	-0.1003	0.1927
S23	-3.9074	0.5665	2.2645	-11.8777	0.5048	2.0382

specimen. This is because a CC(T) specimen is geometrically equivalent to two mirrored SEN(T) specimens joined along the cracked faces [20]. To validate the use of COMSOL for deriving calibration curves, Johnson's calibration formula was compared to the polynomials presented in Table 9 and Table 10 with excellent agreement.

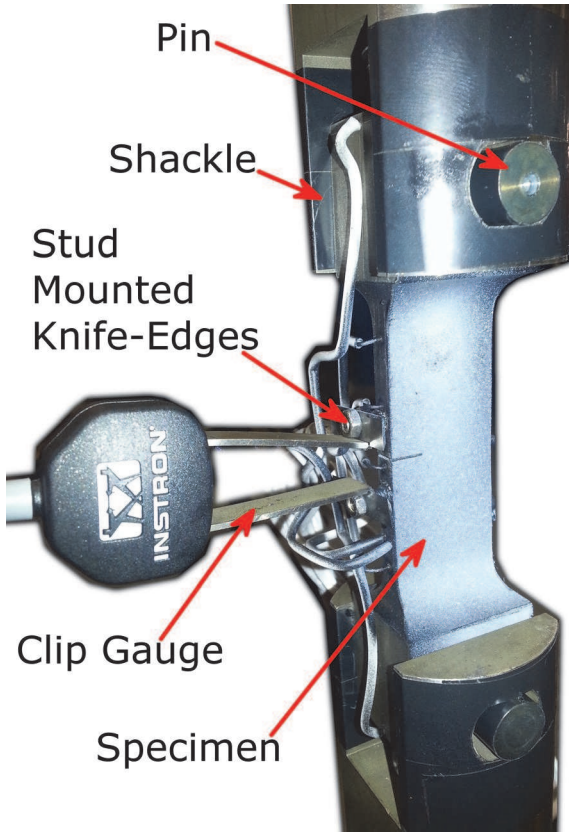
Method

The experimental setup is shown in Fig. 7 for a SEN(T) specimen. The same setup was used for all specimens. PVC insulated Chromel wires (0.81 mm diameter) were spot welded to each specimen at the probe locations shown in Fig. 5 and Fig. 6. Each pair of wires was twisted together to reduce electromagnetic interference. A clip gauge was used to monitor the CMOD. For the C(T) specimens, the knife edges for mounting the clip gauge were machined into the specimen as shown in Fig. 5. For the SEN(T) specimens, studs were spot welded onto the surface of the specimen and knife edges were firmly attached to these studs to ensure they could not move during the experiment as shown in Fig. 7. The knife edges were positioned 6 mm from the specimen surface.

Preliminary investigations on C(T) specimens demonstrated a non-linear reduction in PD with an increase in CMOD contrary to the linear increase expected. This reduction was attributed to the loading pins, which were not insulated from the specimen. As the applied load was increased, plastic deformation of the holes in the specimen increased the area of contact with the loading pins, providing an alternative path for the applied current and reducing the measured resistance. To prevent this, the loading pins and the shackles were insulated using PVC insulation tape as shown in Fig. 7. This resulted in slightly larger diameter loading pins, so the diameter of the pin holes in the specimens was increased from 12.5 (as recommended in the ASTM standards) to 13.0 mm.

A constant 3 mA AC was applied using the low frequency ACPD system and the specimen was loaded in small increments in displacement control. At each increment, with the load applied, any change in resistance was recorded and the apparent crack extension was calculated using the calibration curves provided in Tables 8-10. It is of note that the low frequency ACPD system records resistance

FIG. 7 Typical experimental setup.



rather than PD; however, the two quantities are directly proportional when using a constant current. At each increment, the specimen was partially unloaded and reloaded to identify any crack extension from the elastic unloading compliance. Each test was stopped after significant plastic deformation had occurred but before any crack extension was predicted. The specimen was heat tinted and broken open with liquid nitrogen to confirm that no crack extension had occurred. A summary of the maximum applied load, limit load, and maximum stress intensity factor applied to each specimen is provided in [Table 11](#). For the high constraint C(T) specimens, the calculation of limit load and stress intensity factor (corrected for plastic zone size) is based on plane strain conditions. For the lower constraint SEN(T) specimens, the calculations are based on plane stress conditions.

The applied frequency of the AC was 2 Hz. To ensure that this frequency was low enough to avoid any significant skin effect, the resistance at each probe location

TABLE 11 Experimental parameters for each specimen.

Specimen ID	Maximum Load (kN)	Limit Load (kN)	Maximum K_I (MPa \sqrt{m})
CT45	52.9	44.4	93.1
CT55	34.1	28.2	81.6
SENT30	33.8	23.4	66.4
SENT38	25.0	17.6	67.4
SENT54	14.0	8.6	75.1
SENT70	5.8	3.1	70.5

No frequency dependence was identified in the resistance measurements, confirming the results are directly applicable to DCPD.

Results

SEN(T) SPECIMENS

For each of the SEN(T) specimens, the fracture surface showed no visible signs of crack extension. **Figure 8** compares the change in resistance with CMOD for the different probe locations on the SENT30 and the SENT70 specimens. It confirms the linear relationship observed by Lowes and Fearnough [9] prior to the initiation of crack growth for the two extremes of crack length considered. It also demonstrates that sensing probes located closer to the crack tip (S1 and S_{tip}) tend to experience a larger change in resistance for an applied CMOD. This is possibly because the resistance measured at these locations will be dominated by the highly strained material at the crack tip, while probes further away from the crack tip will tend to measure more of an average across the entire ligament.

While resistance measurements taken close to the crack tip are more sensitive to strain, they are also more sensitive to crack extension. Selection of a probe

FIG. 8 Change in resistance against CMOD for (a) specimen SENT30 and (b) specimen SENT70.

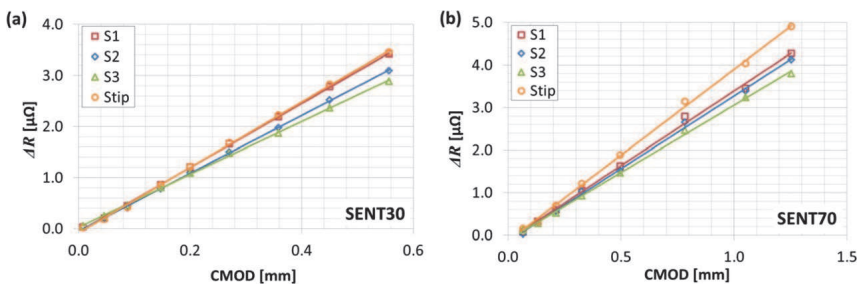
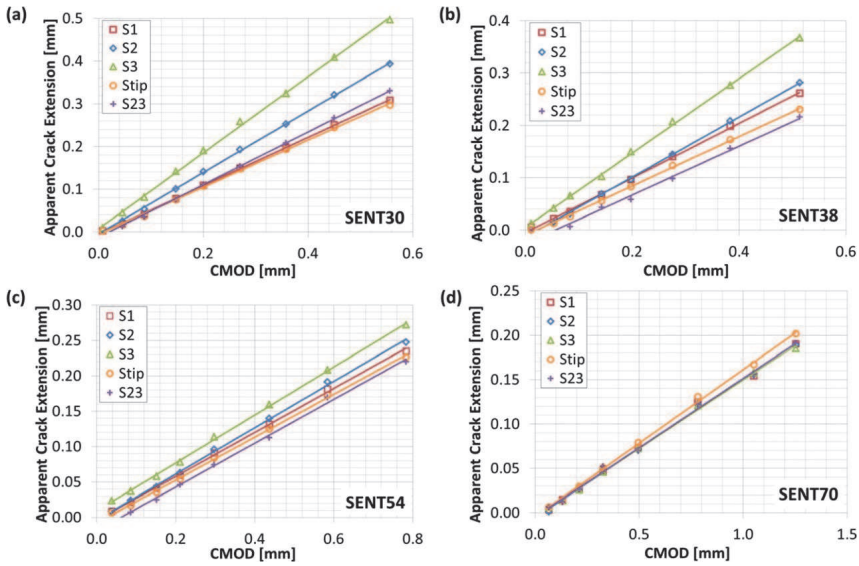


FIG. 9 Apparent crack extension against CMOD for (a) specimen SENT30, (b) specimen SENT38, (c) specimen SENT54, and (d) specimen SENT70.



location in the presence of large strains is a balance between these two factors. To identify the optimum probe location, the change in resistance was converted into an apparent crack extension using the calibration curves provided in [Table 9](#) and [Table 10](#). [Figure 9](#) shows the relationship between apparent crack extension and CMOD for all four SEN(T) specimens tested. All probe locations recorded an apparent crack extension of at least 0.18 mm prior to any actual crack growth. At the worst-case location, a change in resistance was equivalent to 0.50 mm of crack extension was recorded. This is for probe location S3 on specimen SENT30.

The influence of probe location is more significant for smaller crack lengths. For specimen SENT30, there is a wide range of apparent crack extension at a given CMOD for different probe locations. For specimen SENT70, however, the apparent crack extension at a given CMOD is very similar for all probe locations considered. The following discussion focuses on the results from specimen SENT30, where it is easier to differentiate between the different probe locations.

The apparent crack extension is smaller for a given CMOD when the probes are located close to the crack tip (S1 and S_{tip}). Any deviation from the linear trend on a plot of PD against CMOD, indicating the onset of crack extension, will therefore be easier to identify for these probe locations. Location S23 also demonstrates a relatively low apparent crack extension. This location has the advantage of a linear

estimating actual crack extension using the linear interpolation approach discussed in ASTM E1457-13 [1]. It also does not require an additional reference measurement.

Probe locations S1 and S23 demonstrate similar levels of apparent crack extension due to strain and both of these locations are suitable for estimating crack extension in ductile materials because the calibration curves are not sensitive to probe misplacement. When using a calibration curve to determine crack extension, S1 would be more suitable. When using linear interpolation to determine crack extension, S23 would be more suitable.

The calibration curve for S_{tip} is very sensitive to probe misplacement and is therefore not suitable for estimating crack extension; however, this location has slightly higher sensitivity to crack extension than S1, so it may make it slightly easier to identify the onset of crack growth using the method proposed by Lowes and Fearnough [9].

C(T) SPECIMENS

For both of the C(T) specimens, the fracture surface showed no visible signs of crack extension. Figure 10 compares the change in resistance with CMOD for the different probe locations on CT45 and CT55. Similar to the SEN(T) specimens, in the absence of crack extension, the relationship between these two quantities is approximately linear. Probe locations C1 and C_{tip} experience the largest change in resistance for an applied CMOD for both values of a/W considered, whereas C2 and C3 demonstrate the smallest change in resistance. The change in resistance at location C_{tip} is most likely for the same reason as postulated for the SEN(T) specimen: the measurement is predominately sampling the high strained material at the crack tip. The change in resistance at location C1, however, is particularly high, especially for the CT45 specimen. This is probably because it is not only influenced by plasticity at the crack tip, but also by additional plasticity in the thin section of material between the pin hole and the notch.

FIG. 10 Change in resistance against CMOD for (a) specimen CT45 and (b) specimen CT55.

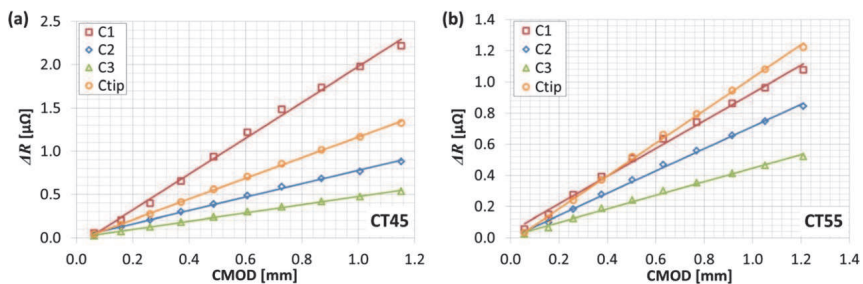
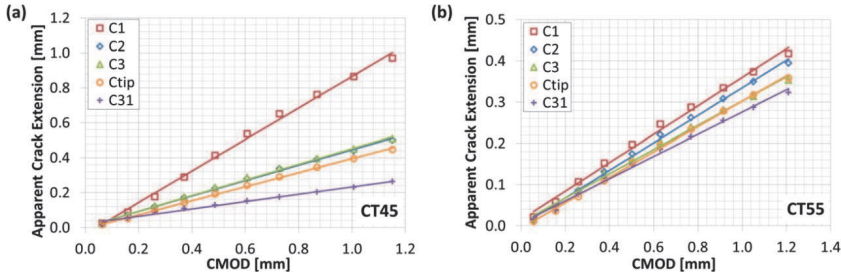


FIG. 11 Apparent crack extension against CMOD for (a) specimen CT45 and (b) specimen CT55.



To identify the optimum probe location for measuring crack extension in the presence of significant plasticity, the change in resistance was converted into an apparent crack extension using the calibration curves provided in Table 8. Figure 11 shows the relationship between apparent crack extension and CMOD for both C(T) specimens. All probe locations recorded an apparent crack extension of at least 0.25 mm prior to any actual crack growth. At the worst-case location, a change in resistance equivalent to ~ 1.0 mm of crack extension was recorded at probe location C1 on specimen CT45.

The apparent crack extension due to strain is small for a given CMOD when the probes are located at C_{tip} , although the associated calibration curve is sensitive to probe misplacement. Probe locations C2 and C3 experience slightly more apparent crack extension but the associated calibration curves are much less sensitive to probe misplacement. Any deviation from the linear trend on a plot of PD against CMOD, indicating the onset of crack extension, will therefore be easier to identify for these probe locations. Location C1 experiences relatively large apparent crack extension, particularly for $a/W = 0.45$. As discussed previously, this is probably due to plastic strain in the thin section between the pin hole and the machined notch. C1 is therefore not considered a suitable probe location for measuring crack extension in the presence of plasticity.

Location C31 (the ratio of C3 and C1) demonstrates small apparent crack extension for both values of a/W ; however, it is dependent on C1 and therefore dependent on the interaction between the loading pin and the specimen. This interaction may be variable from specimen to specimen due to small machining imperfections or contamination of the contact surfaces. For this reason, location C31 is not considered suitable for measuring crack extension in the presence of plasticity.

Locations C2 and C3 appear to be the most suitable for estimating crack extension; however, C2 is more sensitive to actual crack extension and is therefore considered the most suitable location for measuring crack extension in the presence of

The location C_{tip} demonstrates slightly less apparent crack extension than C_2 and is even more sensitive to actual crack extension. This may make this probe location suitable for identifying the onset of crack growth using the method proposed by Lowes and Fearnough [9]; however, it is not suitable for estimating subsequent crack extension due to the sensitivity of the associated calibration curve to probe misplacement.

INFLUENCE OF a/W

Figure 12 is a plot of the variation in apparent crack length with mode I stress intensity factor, K_I , for the four SEN(T) specimens with different a/W ratios. It only considers probe location S1. At low values of K_I , when the applied load is small and there is little plasticity in the specimen, the influence of a/W is small. At higher loads and higher values of K_I , when significant plasticity occurs, the apparent crack extension is larger for smaller a/W ratios. At the maximum value of K_I considered, the apparent crack extension for $a/W = 0.30$ (specimen SENT30) is approximately double that for $a/W = 0.70$ (specimen SENT70).

The plastic zone size, r_p , ahead of the crack tip can be approximated from Eq 2, where σ_y is the material yield strength and β is a constant which depends on the stress conditions at the crack tip. For plane stress conditions, β is 1, and for plane strain conditions, β is 3. The trend in Fig. 12 suggests that, for a given value of K_I , the plastic zone size is reducing as the a/W ratio increases. The value of β must therefore be increasing due to a higher level of constraint associated with larger a/W ratios.

FIG. 12 The influence of a/W on apparent crack extension for SEN(T) specimens, based on probe location S1.

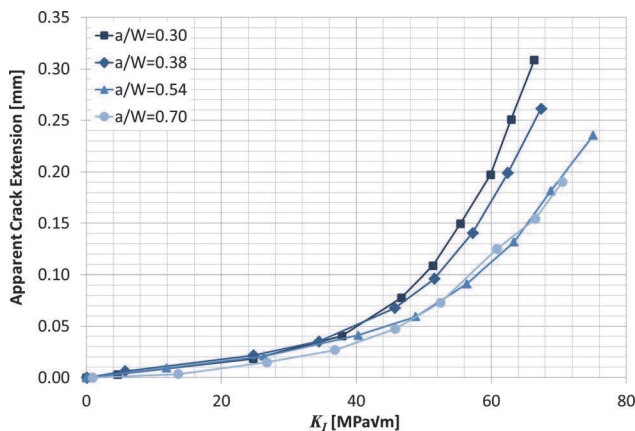
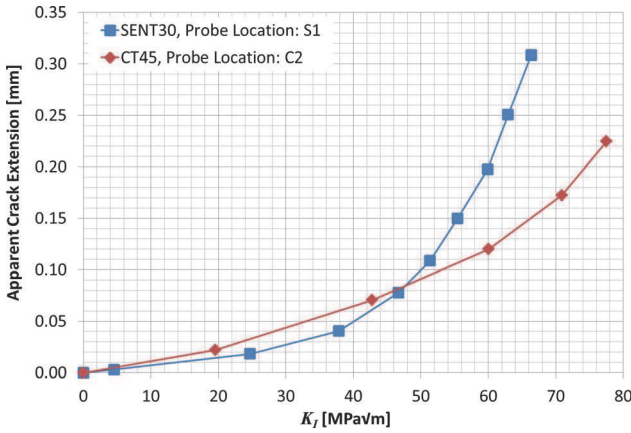


FIG. 13 The influence of specimen geometry on apparent crack extension.



(2)

$$r_p = \frac{1}{\beta\pi} \left(\frac{K_I}{\sigma_y} \right)^2$$

INFLUENCE OF SPECIMEN GEOMETRY

Figure 13 compares the apparent crack extension with K_I for the two geometries considered, C(T) and SEN(T). The comparison is for the probe locations most suitable for measuring crack extension in the presence of plasticity; these are S1 for SEN(T) specimens and C2 for C(T) specimens. Only the specimens with the smallest initial crack length are included, CT45 and SENT30.

At low values of K_I , when there is little plasticity, the influence of specimen geometry is small; however, at high values of K_I , when significant plasticity occurs, the apparent crack extension is much larger for the SEN(T) specimen than for the C(T) specimen. Similar to the effect demonstrated in Fig. 12, this is probably due to the level of constraint. The thick C(T) specimen with side grooves provides more constraint than the thin SEN(T) specimen without side grooves. This additional constraint promotes stress tri-axiality at the crack tip, reducing the size of the plastic zone and the influence of plasticity.

Conclusions

Up to 1.0 mm of apparent crack extension was recorded by the PD technique with no actual crack growth in the specimen. By careful selection of the PD probe locations, this can be significantly reduced; however, in tough ductile materials, the apparent crack extension prior to the onset of physical crack growth will remain

The most appropriate probe locations for measuring crack extension in the presence of significant plasticity are those recommended in ASTM E1457-13 [1], namely S1 for SEN(T) specimens and C2 for C(T) specimens. SEN(T) probe arrangement S23 also demonstrates reduced sensitivity to plasticity and has the additional benefit of an approximately linear calibration curve. When selecting probe locations on ductile specimens, care should be taken to avoid sources of plasticity other than the crack tip such as the loading holes on a C(T) specimen (e.g., probe location C1).

Probes attached at the crack tip may make the identification of the onset of crack growth slightly easier; however, this location should not be used for measuring crack extension because the calibration curve is extremely sensitive to small discrepancies in probe location.

The level of constraint and therefore plastic zone size influences the apparent crack growth due to strain in tough, ductile materials. The use of high constraint geometry is therefore beneficial.

As identified by Lowes and Fearnough [9], the relationship between CMOD and PD is linear prior to the initiation of crack growth. This relationship can be used to reduce the error in crack length measurements in the presence of significant plasticity. At the onset of crack growth, a plot of CMOD against PD will deviate from linear and any change in PD prior to this point can be ignored. Using high constraint geometry and the probe locations recommended above should make the identification of this point easier. While this approach will reduce the influence of plasticity, it will not remove it entirely. As the crack continues to grow, further error may be introduced to the PD signal from sources such as variations in the plastic zone size and the influence of the plastic wake behind the crack tip.

References

- [1] ASTM E1457-13: Standard Test Method for Measurement of Creep Crack Growth Times in Metals, ASTM International, West Conshohocken, PA, 2013, www.astm.org.
- [2] ASTM E647-13: Standard Test Method for Measurement of Fatigue Crack-Growth Rates, ASTM International, West Conshohocken, PA, 2013, www.astm.org.
- [3] ASTM E2760-10e2: Standard Test Method for Creep-Fatigue Crack Growth Testing, ASTM International, West Conshohocken, PA, 2010, www.astm.org.
- [4] ASTM E1820-11: Standard Test Method for Measurement of Fracture Toughness, ASTM International, West Conshohocken, PA, 2011, www.astm.org.
- [5] Venkatsubramanian, T. V. and Unvala, B. A., "An AC Potential Drop System for Monitoring Crack Length," *J. Phys. E: Sci. Instrum.*, Vol. 17, No. 9, 1984, pp. 765-771.
- [6] Hartman, G. A. and Johnson, D. A., "D-C Electric-Potential Method Applied to Thermal/Mechanical Fatigue Crack Growth," *Exp. Mech.*, Vol. 27, No. 1, 1987, pp. 106-112.

- [7] Freeman, B. and Neate, G., "The Measurement of Crack Length During Fracture at Elevated Temperatures Using the D. C. Potential Drop Technique," *The Measurement of Crack Length and Shape During Fracture and Fatigue*, C. J. Beevers, Ed., Engineering Materials Advisory Services Ltd., Worcester, UK, 1980.
- [8] Wilkowski, G. and Maxey, W., "Review and Applications of the Electronic Potential Method for Measuring Crack Growth in Specimens, Flawed Pipes and Pressure Vessels," *Fracture Mechanics: Fourteenth Symposium—Volume II: Testing and Applications*, ASTM STP 791, J. C. Lewis and G. Sines, Eds., ASTM International, West Conshohocken, PA, 1983, pp. 266–294.
- [9] Lowes, J. M. and Fearnough, G. D., "The Detection of Slow Crack Growth in Crack Opening Displacement Specimens Using an Electrical Potential Method," *Eng. Fract. Mech.*, Vol. 3, No. 2, 1971, pp. 103–104.
- [10] Madhi, E. and Nagy, P. B., "Sensitivity Analysis of a Directional Potential Drop Sensor for Creep Monitoring," *NDT & E Int.*, Vol. 44, No. 8, 2011, pp. 708–717.
- [11] Madhi, E. and Nagy, P. B., "Material Gauge Factor Of Directional Electric Potential Drop Sensors For Creep Monitoring," *AIP Conf. Proc.*, Vol. 1335, 2011, pp. 1233–1240.
- [12] Bakker, A., "A DC Potential Drop Procedure for Crack Initiation and ft-Curve Measurements During Ductile Fracture Tests," *Elastic-Plastic Fracture Test Methods: The User's Experience*, ASTM STP 856, E. T. Wessel and F. J. Loss, Eds., ASTM International, West Conshohocken, PA, 1985, pp. 394–410.
- [13] Saxena, A., "Electrical Potential Technique for Monitoring Subcritical Crack Growth at Elevated Temperatures," *Eng. Fract. Mech.*, Vol. 13, No. 4, 1980, pp. 741–750.
- [14] Wei, R. and Brazill, R., "An Assessment of AC and DC Potential Systems for Monitoring Fatigue Crack Growth," *Fatigue Crack Growth Measurement and Data Analysis*, ASTM STP 738, S. J. Hudak and R. J. Bucci, Eds., ASTM International, West Conshohocken, PA, 1981, pp. 103–119.
- [15] Merah, N., "Detecting and Measuring Flaws Using Electric Potential Techniques," *J. Qual. Main. Eng.*, Vol. 9, No. 2, 2003, pp. 160–175.
- [16] COMSOL Ltd., *COMSOL, v4.3a*, COMSOL Ltd., Cambridge, UK, 2012.
- [17] McCartney, L. N., Irving, P. E., Symm, G. T., Cooper, P. M., and Kurzfeld, A., "Measurement of Crack Lengths in Compact Tension and Single Edge Notch Specimens Using a New Electrical Potential Calibration," *National Physical Laboratory Report: DMA(B)3*, National Physical Laboratory, Middlesex, UK, 1977.
- [18] Merah, N., Bui-Quoc, T., and Bernard, M., "Calibration of DC Potential Technique Using an Optical Image Processing System in LCF Testing," *J. Test. Eval.*, Vol. 23, No. 3, 1995, pp. 160–167.
- [19] Johnson, H., "Calibrating the Electric Potential Method for Studying Slow Crack Growth," *Mater. Res. Stand.*, Vol. 5, No. 9, 1965, pp. 442–445.
- [20] Schwalbe, K.-H. and Hellmann, D., "Application of the Electrical Potential Method to Crack Length Measurements Using Johnson's Formula," *J. Test. Eval.*, Vol. 9, No. 3, 1981, pp. 218–221.

STP 1584, 2015 / available online at www.astm.org / doi: 10.1520/STP158420140057

Xiang (Frank) Chen,¹ Randy K. Nanstad,¹ and
Mikhail A. Sokolov¹

Application of Direct Current Potential Drop for the J-Integral vs. Crack Growth Resistance Curve Characterization

Reference

Chen, Xiang (Frank), Nanstad, Randy K., and Sokolov, Mikhail A., "Application of Direct Current Potential Drop for the J-Integral vs. Crack Growth Resistance Curve Characterization," *Evaluation of Existing and New Sensor Technologies for Fatigue, Fracture and Mechanical Testing*, STP 1584, Jidong Kang, David Jablonski, and David Dudzinski, Eds., pp. 97-112, doi:10.1520/STP158420140057, ASTM International, West Conshohocken, PA 2015.²

ABSTRACT

The dc potential drop (DCPD) technique has been applied to derive the J-integral versus crack growth resistance curve (J-R curve) for fracture toughness characterization of structural materials. The test matrix covered three materials including type 316LN stainless steels, Ni-based alloy 617, and one ferritic-martensitic steel, three specimen configurations including standard compact, single edge bend, and disk-shaped compact specimens, and temperatures ranging from 20 to 650°C. When compared with baseline J-R curves derived from the ASTM E1820-13 normalization method, the original J-R curves from the DCPD technique yielded much smaller J_Q values due to the influence of crack blunting, plastic deformation, etc., on potential drop. To compensate these effects, a new procedure for adjusting DCPD J-R curves was proposed. After applying the new adjustment procedure, the average difference in J_Q between the DCPD technique and the normalization method was only 5.2 % and the difference in tearing modulus was 7.4 %. These promising results demonstrate the applicability of the DCPD technique for J-R curve characterization especially in extreme

Manuscript received May 30, 2014; accepted for publication October 14, 2014; published online November 3, 2014.

¹Materials Science and Technology Division, Oak Ridge National Laboratory, Oak Ridge, TN 37831.

²ASTM Fourth Symposium on the *Evaluation of Existing and New Sensor Technologies for Fatigue, Fracture and Mechanical Testing* on May 7-8, 2014 in Toronto, Canada.

environments, such as elevated temperatures, where the conventional elastic unloading compliance method faces considerable challenges.

Keywords

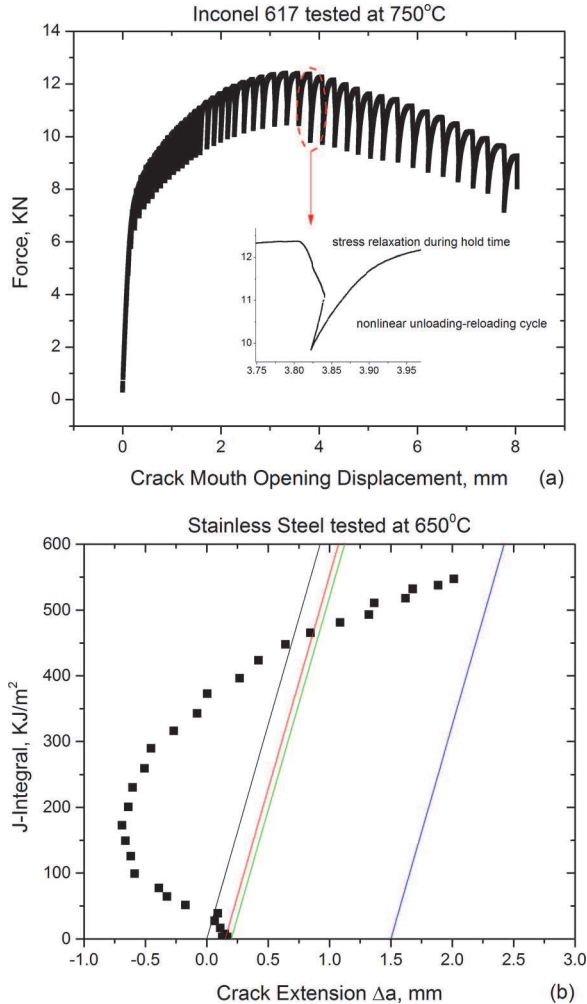
J–R curve testing, normalization method, DCPD

Introduction

To improve thermal efficiency, next generation nuclear reactors aim at operating in more severe environments, such as elevated temperatures and higher stress levels, than current reactors. Therefore, the characterization of mechanical properties of structural materials for next generation nuclear reactors in extreme environments becomes vitally important from both an engineering design and safety management point of view [1]. Among different mechanical properties of materials, the J-integral versus crack growth resistance curve (J–R curve) is a useful tool for evaluating material structural integrity in the presence of pre-existing defects. To date, extensive efforts have been devoted to the development of simplified and reliable methods for determining material J–R curves. A widely accepted practice for conducting J–R curve testing is ASTM E1820-13 [2], in which the elastic unloading compliance (EUC) method is the reference method for online crack size measurement. However, the EUC method becomes impractical for elevated temperature testing due to material stress relaxation resulting in nonlinear unloading–reloading curves (shown in Fig. 1(a)) and enhanced friction between the specimen, pins, and clevises, which results in a back-up shape of the J–R curve (shown in Fig. 1(b)). In addition, the EUC method may underpredict the crack extension for standard disk-shaped compact (DC(T)) specimens, which further limits its applications for J–R curve determination in small specimens [3].

In order to address these issues associated with J–R curve determination with the EUC method, ASTM E1820-13 Annex 15 [2] introduces the normalization method as an alternative J–R curve characterization method. The normalization method was initially developed by Herrera [4] and Landes et al. [5] and later on studied by Joyce [6] and Lee [7]. In contrast to the EUC method, the normalization method does not rely on the compliance measurement for on-line crack size measurement. Instead, the normalization method solely requires a force–displacement record together with initial and final crack size measurements from the specimen fracture surface to derive the material J–R curve. Because of the elimination of the compliance measurement, the force–displacement curve in the normalization method does not require the unloading–reloading portion as in the EUC method, which significantly simplifies the test and reduces the test time. Despite these advantages, the normalization method requires that the final physical crack extension in a J–R curve test cannot exceed the lesser of 4 mm or 15 % of the initial uncracked ligament [2]. Since the real-time crack extension is not available in a J–R curve test using the normalization method, it can be a great challenge to fulfill the

FIG. 1 Issues in elevated temperature J–R curve testing using the EUC method: (a) material stress relaxation resulting in nonlinear unloading-reloading curves; (b) a back-up shape of the J–R curve induced by friction between the specimen and loading devices.



In order to develop a J–R curve test method suitable for extreme testing conditions and with reliable online crack size measurement, the dc potential drop (DCPD) technique is investigated in this study. As another alternative J–R curve test method [8–12], the DCPD technique combines advantages of both the EUC method and the normalization method. It does not require the unloading compliance measurement, so the issues of elevated temperature testing using the EUC

method are not experienced in the DCPD technique. In addition, the DCPD technique provides experimental real-time crack size measurements in contrast to the normalization method. **Figure 2** illustrates the crack size measurement principle in the DCPD technique. As a constant dc passes through the specimen, the subsequent voltage generated across the uncracked ligament in the specimen is measured. Once a crack propagates in the specimen, less area is available for the passage of the same constant current, resulting in increases of the effective electrical resistance and the potential drop measurement. Thus, the potential drop measurement in DCPD can be used to derive the real-time crack size if the correlation between the potential drop and the crack size is known.

In this work, material fracture toughness based on the J–R curve was characterized by the DCPD technique and results were compared with J–R curves derived from the ASTM E1820-13 normalization method. The test matrix covered a wide range of materials, specimen configurations, and testing temperatures to evaluate the applicability of the DCPD technique for J–R curve characterization.

Experimental

MATERIALS AND SPECIMENS

Three different materials, covering a broad range of metallic materials including type 316LN stainless steel (MatA), Ni-based alloy 617 (MatB), and one ferritic-martensitic steel (MatC), were selected in J–R curve testing.

Specimen configurations used in J–R curve testing include 0.5T standard compact (C(T)), 5 by 10 mm and 10 by 10 mm single edge bend (SE(B)), and 0.18T DC(T) specimens. The detailed specimen designs are shown in **Fig. 3**. Each specimen was fatigue pre-cracked until the initial crack size equaled 50 % of the specimen width and then side-grooved to remove 10 % of specimen thickness from each side of the specimen.

FIG. 2 The crack size measurement principle in the DCPD technique.

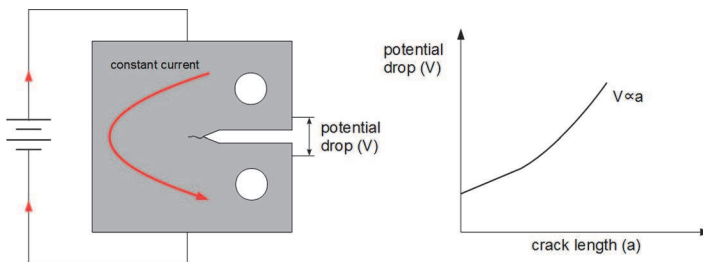


FIG. 3 Specimen configurations for (a) C(T), (b) SE(B), and (c) DC(T). The red arrows indicate the current probe locations and the green dots indicate the potential probe locations.

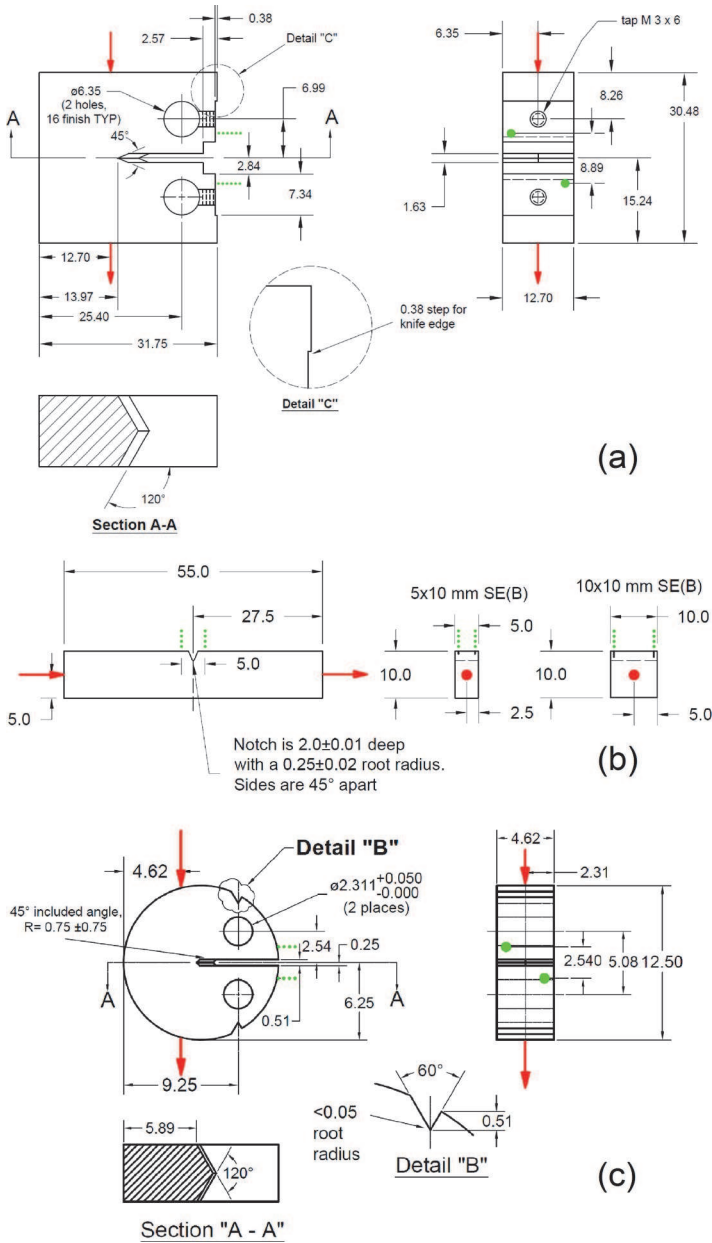


TABLE 1 Test matrix in J–R curve testing.

Material	Specimen Type	Temperature (°C)
Type 316LN stainless steel (MatA)	0.18T C(T)	24, 500
Ni-based alloy 617 (MatB)	0.5T C(T)	24, 250, 500, 650
Ferritic-martensitic steel (MatC)	0.5T C(T), 5x10 mm & 10x10 mm SE(B)	24, 114, 300, 500, 600

TEST CONDITIONS AND EXPERIMENTAL SETUP

The test matrix is summarized in [Table 1](#). All tests were performed with a quasi-static loading rate such that the rate of increase of the stress intensity factor (dK/dt) during the initial elastic portion was $2 \text{ MPa}\sqrt{\text{m/s}}$. Test temperatures cover a wide range from 20 to 650°C , representing conventional room temperature and elevated temperature J–R curve tests. For each test, force–displacement data and DCPD signals were acquired from the same specimen so that a comparison of J–R curve results between the DCPD technique and the normalization method was made on the same specimen to avoid any influence due to specimen to specimen variations.

The experimental setup for performing J–R curve testing has been described previously [[3,13](#)]. In summary, servo-hydraulic test frames were employed for loading specimens. For SE(B) and DC(T) specimens, the load-line displacement was measured, whereas, for C(T) specimens, crack mouth opening displacement (CMOD) on the specimen front face was measured (see Refs. [[14,15](#)])³. For the DCPD data acquisition, current probes and potential probes were spot welded to each specimen configuration as shown in [Fig. 3](#). The current probes were spot welded at one half of the specimen width and thickness location. The potential probes were spot welded diagonally across the starter notch to average measurements from non-uniform crack fronts if any [[16](#)].

Results and Discussion

The normalization method, described in more detail in Refs. [[2,13](#)], is applied in this study to determine the baseline J–R curves. Then results are compared with J–R curves derived from the DCPD technique to evaluate the applicability of the DCPD technique for J–R curve characterization.

J–R CURVE DETERMINATION BY THE DCPD TECHNIQUE

The DCPD technique derives experimental real-time crack sizes based on the potential drop measurement across the uncracked ligament in the specimen. A number of constitutive equations are available for converting the potential drop

measurement into crack size in the DCPD technique. Among those constitutive equations, Johnson's equation [17,18] has been widely used and is given by:

$$(1) \quad a = \frac{2W}{\pi} \cos^{-1} \frac{\cosh(\pi y/2W)}{\cosh\{(U/U_0) \cosh^{-1}[\cosh(\pi y/2W)/\cos(\pi a_0/2W)]\}}$$

where:

a = crack size corresponding to potential drop U ,

y = one half of the potential gage span (i.e., 4.445 mm for C(T), 2.5 mm for SE(B), and 1.27 mm for DC(T) per Fig. 3),

W = specimen width,

a_0 = initial crack size, and

U_0 = initial potential drop measurement.

Once the crack sizes in a J-R curve test become available, J-integral can be calculated by:

$$(2) \quad J_i = \frac{K_i^2(1-\nu^2)}{E} + J_{pli}$$

where:

K_i = stress intensity at the i th data point,

ν = Poisson's ratio,

E = Young's modulus of the material, and

J_{pli} = plastic component of J_i for the i th data point.

The equations for calculating K_i for C(T), SE(B), and DC(T) specimens, respectively, are:

$$(3a) \quad K_i = \frac{P_i}{(BB_N W)^{1/2}} \times \frac{\left(2 + \frac{a_i}{W}\right) \left[0.886 + 4.64\left(\frac{a_i}{W}\right) - 13.32\left(\frac{a_i}{W}\right)^2 + 14.72\left(\frac{a_i}{W}\right)^3 - 5.6\left(\frac{a_i}{W}\right)^4\right]}{\left(1 - \frac{a_i}{W}\right)^{3/2}}$$

$$(3b) \quad K_i = \frac{P_i S}{(BB_N)^{1/2} W^{3/2}} \times \frac{3\left(\frac{a_i}{W}\right)^{1/2} \left[1.99 - \left(\frac{a_i}{W}\right) \left(1 - \frac{a_i}{W}\right) \left(2.15 - 3.93\left(\frac{a_i}{W}\right) + 2.7\left(\frac{a_i}{W}\right)^2\right)\right]}{2\left(1 + 2\frac{a_i}{W}\right) \left(1 - \frac{a_i}{W}\right)^{3/2}}$$

$$(3c) \quad K_i = \frac{P_i}{(BB_N W)^{1/2}} \times \frac{\left(2 + \frac{a_i}{W}\right) \left[0.76 + 4.8\left(\frac{a_i}{W}\right) - 11.58\left(\frac{a_i}{W}\right)^2 + 11.43\left(\frac{a_i}{W}\right)^3 - 4.08\left(\frac{a_i}{W}\right)^4\right]}{\left(1 + \frac{a_i}{W}\right)^{3/2}}$$

where:

P_i = force at the i th data point,

B = specimen thickness,

B_N = specimen net thickness,

a_i = crack size at the i th data point, and

S = distance between specimen supports for SE(B) specimens.

The equation for calculating J_{pli} is given by:

$$(4) \quad J_{pli} = \left[J_{pli-1} + \frac{\eta_{pli-1} A_{pli} - A_{pli-1}}{b_{i-1} B_N} \right] \left[1 - \gamma_{pli-1} \frac{a_i - a_{i-1}}{b_{i-1}} \right]$$

where:

J_{pli-1} = plastic part of J-integral for the $(i-1)$ -th data point and $J_{plo} = 0$,

b_{i-1} = uncracked ligament for the $(i-1)$ -th data point and is equal to $W - a_{i-1}$.

η_{pli-1} = a dimensionless parameter that relates plastic work done on a specimen to crack growth resistance defined in terms of deformation theory J-integral [19] and equals 1.9 for SE(B) specimens and $2.0 + 0.522b_{i-1}/W$ for C(T) and DC(T) specimens, and

γ_{i-1} = a function to correct the J-integral evaluated by η_{pli-1} parameter in the crack growth situation [20] and equals 0.9 for SE(B) specimens and $1.0 + 0.76b_{i-1}/W$ for C(T) and DC(T) specimens.

The quantity $A_{pli} - A_{pli-1}$ is the increment of plastic area under the force versus plastic load-line displacement record between lines of constant plastic displacement v_{pli} and v_{pli-1} and can be calculated from the following equation:

$$(5) \quad A_{pli} - A_{pli-1} = \frac{(P_i + P_{i-1})(v_{pli} - v_{pli-1})}{2}$$

where v_{pli} is the plastic part of the i th load-line displacement data point and is given by:

$$(6) \quad v_{pli} = v_i - P_i C_{LLi}$$

where:

v_i = the load-line displacement at the i -th data point and C_{LLi} is the equivalent compliance corresponding to a_i and for C(T), SE(B), and DC(T) specimens. C_{LLi} is calculated as:

$$(7a) \quad C_{LLi} = \frac{1}{EB_e} \left(\frac{W + a_i}{W - a_i} \right)^2 \times \left[2.163 + 12.219 \left(\frac{a_i}{W} \right) - 20.065 \left(\frac{a_i}{W} \right)^2 - 0.9925 \left(\frac{a_i}{W} \right)^3 + 20.609 \left(\frac{a_i}{W} \right)^4 - 9.9314 \left(\frac{a_i}{W} \right)^5 \right]$$

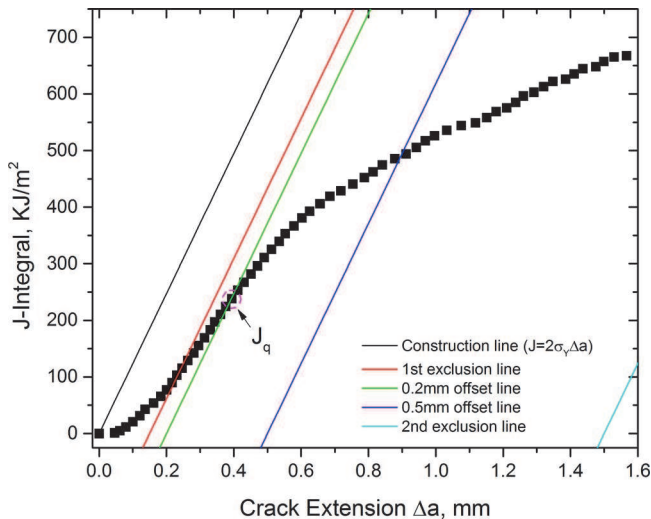
$$C_{LLi} = \frac{1}{EB_e} \left(\frac{S}{W - a_i} \right)^2 \times \left[1.193 - 1.98 \left(\frac{a_i}{W} \right) + 4.478 \left(\frac{a_i}{W} \right)^2 - 4.443 \left(\frac{a_i}{W} \right)^3 + 1.739 \left(\frac{a_i}{W} \right)^4 \right]$$

$$C_{LLi} = \frac{1}{EB_e} \left(\frac{W + a_i}{W - a_i} \right)^2 \times \left[2.0462 + 9.6496 \left(\frac{a_i}{W} \right) - 13.7346 \left(\frac{a_i}{W} \right)^2 + 6.1748 \left(\frac{a_i}{W} \right)^3 \right] \quad (7c)$$

where the effective thickness $B_e = B - (B - B_N)^2/B$.

Based on the crack size calculation in Eq 1 and the corresponding J-integral calculation in Eq 3, one example of the original DCPD J-R curve for a 0.18T DC(T) specimen made from MatA is shown in Fig. 4. The initial portion of the J-R curve in Fig. 4 indicates fast crack growth and does not follow the construction line closely, resulting in a relatively low J_Q value. Indeed, as noted in the work of Bakker [21], the material potential drop can also result from deformation, crack blunting, and void growth in the process zone ahead of the crack during J-R curve tests. If the influences of these factors are not accounted for in the crack size prediction, the DCPD technique does not predict crack size accurately and can result in much lower J_Q values. Therefore, adjustment of the original DCPD J-R curve is needed. In early DCPD adjustment methods [22,23], a slope change point, counted as the critical point distinguishing crack blunting from the onset of slow stable crack growth, is identified by visual inspection of the displacement-potential drop curve. However, the slope change point in a displacement-potential drop curve may not be clearly identified on occasion and the selection of the critical point tends to be arbitrary, resulting in poor repeatability of the analysis. In a more recent work by Chen et al. [24], new DCPD adjustment methods were developed with improved repeatability and excellent match with the EUC and normalization methods in

FIG. 4 The original DCPD J-R curve of a 0.18T DC(T) specimen from MatA. σ_Y is equal to the average of material yield and tensile strengths.

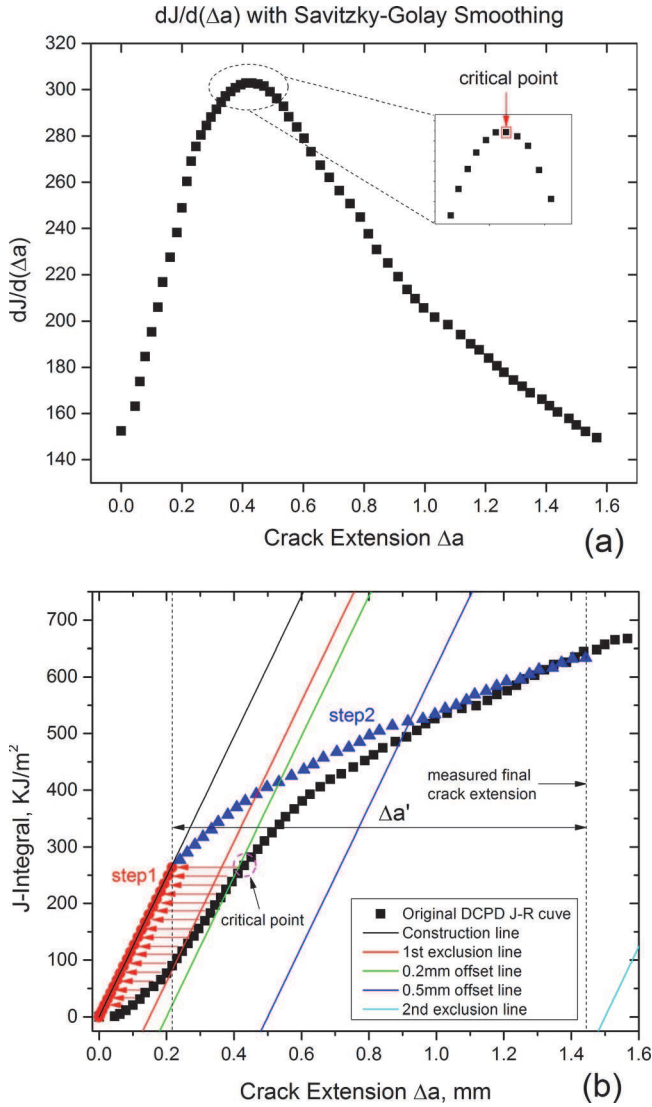


terms of J_Q values. The major drawback in that method is that the adjusted DCPD tearing modulus results show an average difference of 17 % from the EUC and normalization results. A possible explanation for that result is that, since the potential gage span in that work was relatively large, the potential drop signal was measured from a large volume of material, which enhanced the influence of plastic deformation on the DCPD measurement.

In order to address these issues, the distance between two potential probes was reduced as much as possible but was kept large enough to cover the starter notch of a specimen and not to interfere with any displacement measurement devices. In addition, a newly-developed semi-empirical DCPD adjustment procedure is proposed. The DCPD adjustment procedure is mainly composed of two steps. The first step aims at identifying the critical point distinguishing crack blunting from the onset of slow stable crack growth. To achieve this, the first order derivative of the original DCPD J–R curve coupled with Savitzky–Golay [25] second order polynomial smoothing with 19 points of window is applied as shown in Fig. 5(a). The peak point in Fig. 5(a) represents the data point from which the slope of the original DCPD J–R curve starts to decrease and is indicative of the onset of slow stable crack growth. Therefore, the peak point is selected as the critical point. The combination of first order derivative of the original DCPD J–R curve and Savitzky–Golay smoothing eliminates the ambiguity in the selection of the critical point and greatly suppress the noise, if any, in the original DCPD J–R curve data for the critical point selection. Once the critical point is identified, all data points prior to and including the critical point itself from the original DCPD J–R curve are shifted left onto the construction line since these data points correspond to the plastic deformation and crack blunting stage of the specimen (Fig. 5(b)).

After crack initiation, stable crack growth dominates the increase in the potential drop although material deformation and specimen shape change may still influence the potential drop measurement. To address the influence of those factors on DCPD-predicted crack size during the stable crack growth stage, the second step of the DCPD adjustment procedure covers data points between the crack initiation point and the last point in a J–R curve. The concept of the second step adjustment is to force the final crack size prediction from the DCPD technique to match the optically measured final crack extension so that the final crack size prediction from the DCPD technique is correct. Assuming the crack size at crack initiation is correct after the first step adjustment in the DCPD technique, data points between the crack initiation point and final crack size measurement in an adjusted DCPD J–R curve should represent the crack size of a specimen during the stable crack growth stage. To implement this concept, crack sizes for data points subsequent to the critical point in the original DCPD J–R curve are adjusted such that the final crack extension prediction from the DCPD technique matches the measured final crack extension (Fig. 5(b)). To do so, the crack size of the i th data point subsequent to the critical point in the original DCPD J–R curve is adjusted according to the following [21]:

FIG. 5 (a) Critical point selection based on the peak point of the first order derivative of the original DCPD J-R curve with Savitzky-Golay smoothing; (b) two-step adjustment of the original DCPD J-R curve.



$$\begin{aligned}
 a_{pd}' &= \Delta a_{pdcritical}' + \Delta a_{pd} - \Delta a_{pdcritical} \\
 &- \frac{v_{pdi} - v_{pdcritical}}{v_{pdfinal} - v_{pdcritical}} (\Delta a_{pdfinal} - \Delta a_{pdcritical} - \Delta a')
 \end{aligned}
 \tag{8}$$

where:

$\Delta a_{pdcritical}'$ = crack extension of the critical point after the first step adjustment,

Δa_{pdi} = original DCPD crack extension for the i th data point,

$\Delta a_{pdcritical}$ = original crack extension of the critical point,

v_{pdi} = displacement value for the i th data point,

$v_{pdcritical}$ = displacement value for the critical point,

$v_{pdfinal}$ = displacement value for the last data point in the J-R curve, and

$\Delta a_{pdfinal}$ = original DCPD crack extension for the last data point in the J-R curve.

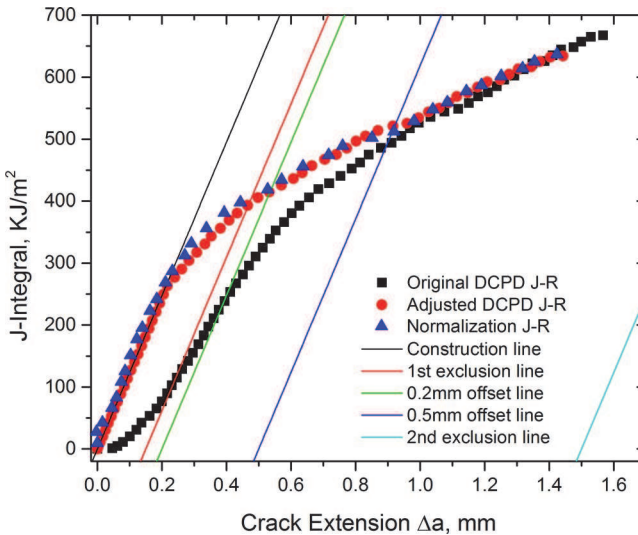
$\Delta a'$ is defined by:

$$(9) \quad \Delta a' = \Delta a_{measured} - \Delta a_{pdcritical}'$$

where $\Delta a_{measured}$ is the optically measured final crack extension.

Once the updated crack sizes from the two-step DCPD adjustment procedure become available, they are used to recalculate J-integral values since J-integral also depends on the crack size. Combining the recalculated J-integral and updated crack sizes yields the final DCPD J-R curve. One example of the comparison between the original DCPD J-R curve, the adjusted DCPD J-R curve, and the J-R curve from the normalization method is shown in Fig. 6. After adjustment, the DCPD J-R curve follows the construction line initially resulting in a much more reasonable J_Q value compared with original DCPD J-R curve. In addition, the adjusted DCPD J-R curve is almost identical to the J-R curve from the normalization method.

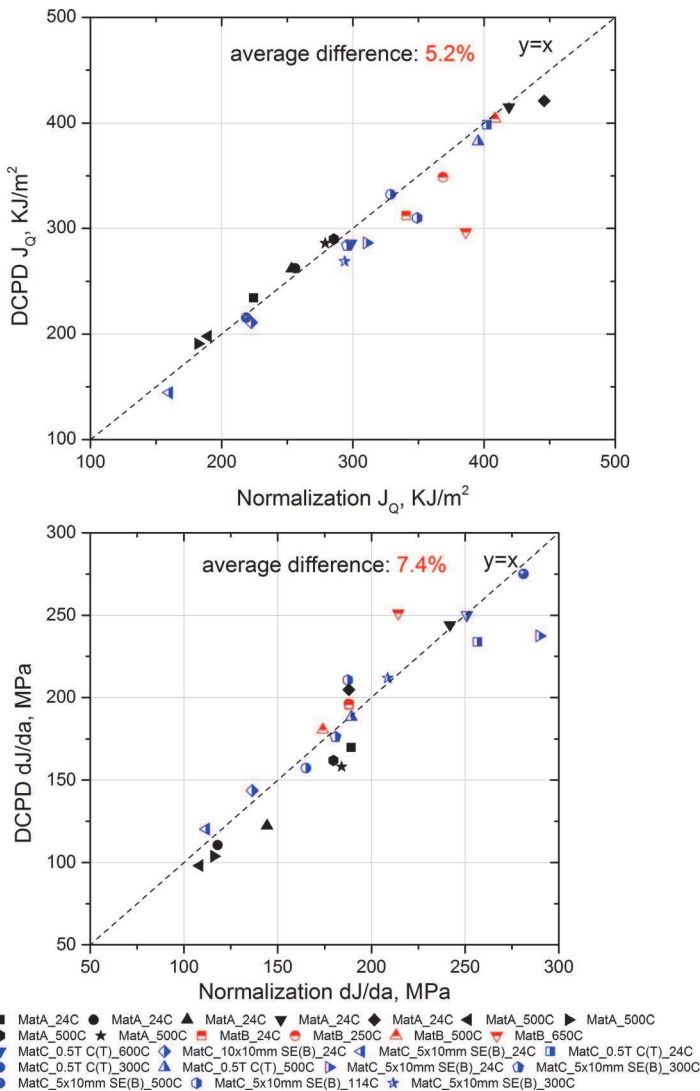
FIG. 6 Comparison of the original DCPD J-R curve, the adjusted DCPD J-R curve, and the normalization-method J-R curve of a 0.18T DC(T) specimen from MatA.



COMPARISON OF J-R CURVES DETERMINED BY THE NORMALIZATION METHOD AND THE DCPD TECHNIQUE AFTER ADJUSTMENT

The comparison of major J-R curve test results, namely the J_Q value and the J-R curve slope between the two exclusions lines, are shown in Fig. 7. Excellent agreement is observed between J-R curves from the normalization method and adjusted DCPD J-R curves in most tests. The average differences for J_Q and J-R curve slopes

FIG. 7 Comparison of J_Q and dJ/da derived from the normalization J-R curves and adjusted DCPD J-R curves.



between the normalization method and the DCPD technique after adjustment are only 5.2 and 7.4 %, respectively. Considering the variety of materials, specimen configurations, and testing temperatures investigated in this study, the DCPD technique and the newly-developed DCPD adjustment procedure show very promising results for J–R curve characterization.

Conclusions

J–R curve testing was performed on a wide range of materials, specimen configurations, and testing temperatures to evaluate the applicability of the DCPD technique for J–R curve characterization. Results are compared with baseline J–R curves derived from the ASTM E1820-13 normalization method. The original J–R curves from the DCPD technique yielded much smaller J_Q values than the normalization method due to the influence of crack blunting, plastic deformation, etc., on potential drop. To compensate these effects, a new procedure for adjusting DCPD J–R curves was proposed. After applying the new adjustment procedure, the average difference in J_Q between the DCPD technique and the normalization method was only 5.2 % and the difference in tearing modulus was 7.4 %. These promising results demonstrate the applicability of the DCPD technique for J–R curve characterization, especially in extreme environments, such as elevated temperatures, where the conventional EUC method faces considerable challenges.

ACKNOWLEDGMENTS

The writers express appreciation to Richard Wright of Idaho National Laboratory and Sam Sham of Oak Ridge National Laboratory for programmatic support. This research was sponsored by the U.S. Department of Energy, Office of Nuclear Energy, Generation IV Reactor Research Program, under contract DE-AC05-00OR22725 with UT-Battelle, LLC. The writers also would like to extend their appreciation to Eric Mannesmidt for performing part of mechanical testing, and to Gene Ice, Thak Sang Byun, and Lauren Garrison for their technical reviews.

Notice: This manuscript has been authored by UT-Battelle, LLC, under Contract No. DE-AC05-00OR22725 with the U.S. Department of Energy. The United States Government retains and the publisher, by accepting the article for publication, acknowledges that the United States Government retains a non-exclusive, paid-up, irrevocable, world-wide license to publish or reproduce the published form of this manuscript, or allow others to do so, for United States Government purposes.

References

- [1] Zhu, X. K., Lam, P. S., and Chao, Y. J., "Application of Normalization Method to Fracture Resistance Testing for Storage Tank A285 Carbon Steel," *Int. J. Pressure Vessel Piping*, Vol. 86, No. 10, 2009, pp. 669–676.

- [2] ASTM E1820-13: Standard Test Method for Measurement of Fracture Toughness, ASTM International, West Conshohocken, PA, 2013, www.astm.org.
- [3] Chen, X., Nanstad, R. K. and Sokolov, M. A., "J-R Curve Determination for Disk-Shaped Compact Specimens Based on the Normalization Method and the Direct Current Potential Drop Technique," *Proceedings of the Sixth International Symposium on Small Specimen Test Techniques*, ASTM STP 1576, M. Sokolov and E. Lucon, Eds., ASTM International, West Conshohocken, PA, 2014, pp. 1-18.
- [4] Herrera, R. and Landes, J. D., "Direct J-R Curve Analysis: A Guide to the Methodology," *Proceedings of the Fracture Mechanics: Twenty-First Symposium*, ASTM STP 1074, J. Gudas, J. Joyce, and E. Hackett, Eds., ASTM International, West Conshohocken, PA, 1990, pp. 24-43.
- [5] Landes, J., Zhou, Z., Lee, K., and Herrera, R., "Normalization Method for Developing J-R Curves with the Lmn Function," *J. Test. Eval.*, Vol. 19, No. 4, 1991, pp. 305-311.
- [6] Joyce, J., "Analysis of a High Rate Round Robin Based on Proposed Annexes to ASTM E 1820," *J. Test. Eval.*, Vol. 29, No. 4, 2001, pp. 329-351.
- [7] Lee, K., 1995, "Elastic-Plastic Fracture Toughness Determination under Some Difficult Conditions," Ph.D. thesis, University of Tennessee, Knoxville, TN.
- [8] Hicks, M. A. and Pickard, A. C., "A Comparison of Theoretical and Experimental Methods of Calibrating the Electrical Potential Drop Technique for Crack Length Determination," *Int. J. Fract.*, Vol. 20, No. 2, 1982, pp. 91-101.
- [9] Lowes, J. M. and Featnehough, G. D., "The Detection of Slow Crack Growth in Crack Opening Displacement Specimens using an Electrical Potential Method," *Eng. Fract. Mech.*, Vol. 3, No. 2, 1971, pp. 103-104.
- [10] McGowan, J. J. and Nanstad, R. K., "Direct Comparison of Unloading Compliance and Potential Drop Techniques in J-integral Testing," *Proceedings of the SEM Fall Conference, Computer-Aided Testing and Modal Analysis*, Milwaukee, WI, Nov 4-7, 1984.
- [11] Ritchie, R. O. and Bathe, K. J., "On the Calibration of the Electrical Potential Technique for Monitoring Crack Growth Using Finite Element Methods," *Int. J. Fract.*, Vol. 15, No. 1, 1979, pp. 47-55.
- [12] Tong, J., "Notes on Direct Current Potential Drop Calibration for Crack Growth in Compact Tension Specimens," *J. Test. Eval.*, Vol. 29, No. 4, 2001, pp. 402-406.
- [13] Chen, X., Nanstad, R. K., Sokolov, M. A., and Mannes Schmidt, E. T., "Determining Ductile Fracture Toughness in Metals," *Adv. Mater. Process.*, Vol. 172, 2014, pp. 19-23.
- [14] ASTM E1921-13: Standard Test Method for Determination of Reference Temperature, T_{0} , for Ferritic Steels in the Transition Range, ASTM International, West Conshohocken, PA, 2013, www.astm.org.
- [15] Landes, J. D., "J Calculation From Front Face Displacement Measurements of a Compact Specimen," *Int. J. Fract.*, Vol. 16, No. 4, 1980, pp. R183-R186.
- [16] ASTM E647-11: Standard Test Method for Measurement of Fatigue Crack Growth Rates, ASTM International, West Conshohocken, PA, 2011, www.astm.org.
- [17] Johnson, H. H., "Calibrating the Electrical Potential Method for Studying Slow Crack Growth," *Mater. Res. Stand.*, Vol. 5, 1965, pp. 442-445.

- [18] Schwalbe, K. H. and Hellmann, D., "Application of the Electrical Potential Method to Crack Length Measurements Using Johnson Formula," *J. Test. Eval.*, Vol. 9, No. 3, 1981, pp. 218–220.
- [19] Turner, C. E., "The Eta Factor," *Post Yield Fracture Mechanics*, 2nd ed., Elsevier Applied Science Publishers, London, 1984, pp. 451–459.
- [20] Chattopadhyay, J., Dutta, B. K., and Kushwaha, H. S., "New ' η_{pl} ' and ' γ ' Functions to Evaluate J-R Curve From Cracked Pipes and Elbows. Part I: Theoretical Derivation," *Eng. Fract. Mech.*, Vol. 71, No. 18, 2004, pp. 2635–2660.
- [21] Bakker, A. D., "A DC Potential Drop Procedure for Crack Initiation and R-Curve Measurements During Ductile Fracture Tests," *Elastic-Plastic Fracture Test Methods: The User's Experience*, ASTM STP 856, F. Loss and E. Wessel, Eds., ASTM International, West Conshohocken, PA, 1985, pp. 394–410.
- [22] Dufresne, J., Henry, B., and Larsson, H., "Fracture Toughness of Irradiated AISI 304 and 316L Stainless Steels," *Effects of Radiation on Structural Materials*, ASTM STP 683, J. Sprague and D. Kramer, Eds., ASTM International, West Conshohocken, PA, 1979, pp. 511–528.
- [23] Schwalbe, K.-H., Hellmann, D., Heerens, J., Knaack, J., and Müller-Roos, J., "Measurement of Stable Crack Growth Including Detection of Initiation of Growth Using the DC Potential Drop and the Partial Unloading Methods," *Elastic-Plastic Fracture Test Methods: The User's Experience*, ASTM STP 856, F.J. Loss and E.T. Wessel, Eds., ASTM International, West Conshohocken, PA, 1985, pp. 338–362.
- [24] Chen, X., Nanstad, R. K., and Sokolov, M. A., "Application of Direct Current Potential Drop for Fracture Toughness Measurement," *Proceedings of the 22nd International Conference on Structural Mechanics in Reactor Technology*, San Francisco, CA, Aug 18–23, 2013.
- [25] Savitzky, A. and Golay, M., "Smoothing + Differentiation of Data by Simplified Least Squares Procedures," *Anal. Chem.*, Vol. 36, No. 8, 1964, pp. 1627–1639.

STP 1584, 2015 / available online at www.astm.org / doi: 10.1520/STP158420140045

B. Glaser,¹ N. Gubeljak,² and J. Predan²

Determination of Calibration Function for Fatigue-Crack Propagation by Measurement Surface Deformation

Reference

Glaser, B., Gubeljak, N., and Predan, J., "Determination of Calibration Function for Fatigue-Crack Propagation by Measurement Surface Deformation," *Evaluation of Existing and New Sensor Technologies for Fatigue, Fracture and Mechanical Testing*, STP 1584, Jidong Kang, David Jablonski, and David Dudzinski, Eds., pp. 113–131, doi:10.1520/STP158420140045, ASTM International, West Conshohocken, PA 2015.³

ABSTRACT

Components and structures exposed to elastic dynamic loading respond with elastic strains on the surface of the material. Mechanical response could be monitored by deformations on the surface. The measurements and monitoring of these parameters could be performed with electronic devices for on-line measurements, controlled by computerized systems. Fatigue-induced flaw growth was monitored on a four-point specimen, loaded by cyclic dynamic bend forces. The flaw growth was monitored by strain gauges with a standard resistance of 120 Ω . After performance of fractal-graphical measurements, a flaw-growth analysis was performed to determine the shape, propagation, and cross sections of the crack. To determine the stress-intensity factor, a numerical model was developed based on measured crack shapes, material properties, and cyclic loading data of the actual tested specimen. The investigation results showed that the derived calibration curve could be used to predict surface deformations as a result of crack propagation and growth, but not crack initiation. With the determination of surface deformation, one could follow the

Manuscript received April 26, 2014; accepted for publication December 17, 2014; published online January 26, 2015.

¹Nuclear Power Plant Krško, Vrbina 12, SI-7800 Krško, Slovenia.

²University of Maribor, Faculty of Mechanical Engineering, Smetanova 17, SI-2000 Maribor, Slovenia.

³ASTM Fourth Symposium on the *Evaluation of Existing and New Sensor Technologies for Fatigue, Fracture and Mechanical Testing* on May 7–8, 2014 in Toronto, Canada.

crack transition from the semi-elliptical surface crack to the through-thickness crack. The stress-intensity factor has been determined numerically by using the finite-element method for five different fatigue-crack fronts. Results show that fatigue crack on the surface of specimens propagated under an almost constant stress-intensity factor value. Consequently, in our case, the fatigue-crack growth rate was constant during transition from a surface semi-elliptical crack to a through-thickness crack front. The aim of this paper is to describe methodology and results based on experimental and numerical modeling during crack propagation and potential use of this technique for online monitoring purposes.

Keywords

fatigue-crack growth, surface deformation measurement

Introduction

Conservatism of fatigue-crack propagation can stop further service of cracked components and, consequently, unnecessary financial losses. Continued on-line monitoring can significantly contribute to safe exploitation without risk of failure. When a short fatigue semi-elliptical surface crack has been detected during the inspection process, on-line monitoring of fatigue-crack propagation can be established, especially when service conditions are changed and standard techniques for nondestructive investigation are not possible, e.g., ultrasonic or x-ray techniques. On-line monitoring of fatigue-crack propagation is a possible solution using strain gauges, which use the strain gauge relaxation technique (SGRT), as proposed by Chappetti and Jaureguizar [1]. The fracture mechanics approach for damage tolerance based on fatigue life as the number of loading cycles consists of the fatigue initiation life of macroscopic crack size 1 mm in depth and subsequent fatigue-crack propagation until final fracture at critical crack length. The traditional approach provides the number of cycles by integration of the Paris–Erdogan crack growth relationship [2]:

$$(1) \quad \frac{da}{dN} = C\Delta K^m$$

where:

m and C = constants of the material, and

ΔK = stress-intensity factor range.

The stress-intensity factor range ΔK is given by general Eq [3]:

$$(2) \quad \Delta K = Y \cdot \Delta\sigma_n \sqrt{\pi \cdot a}$$

where:

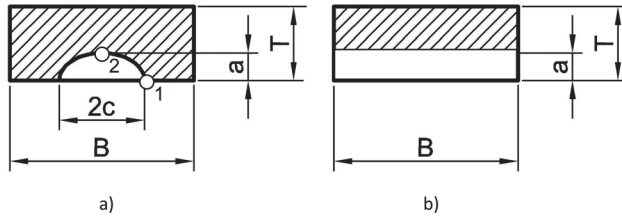
$\Delta\sigma_n$ = nominal applied stress loading range,

a = the crack length, and

Y = function of crack size and crack shape (e.g., semi-elliptical surface crack or through-thickness crack provided for semi-elliptical surface crack in the finite plate

3 (Fig. 1).

FIG. 1 (a) Semi-elliptical crack, and (b) through-thickness crack.



For engineering purposes, it is recommended to consider different stress-intensity factor (SIF) functions for K_I solutions depending on crack size and geometry. Regarding a semi-elliptical surface crack in a plate of finite dimensions for a bending load, usually two SIF values are considered: one for the deepest point, and the second for the surface point. The third SIF function was used for through-thickness crack in a plate of finite dimensions for pure (four-point) bending. All SIF functions are given in the FITNET compendia of stress-intensity factors [3].

In this paper, we have performed the finite-element method (FEM), and found the $K_{I,max}$ distributions along the perimeter of the measured semi-elliptical crack for three different crack geometries.

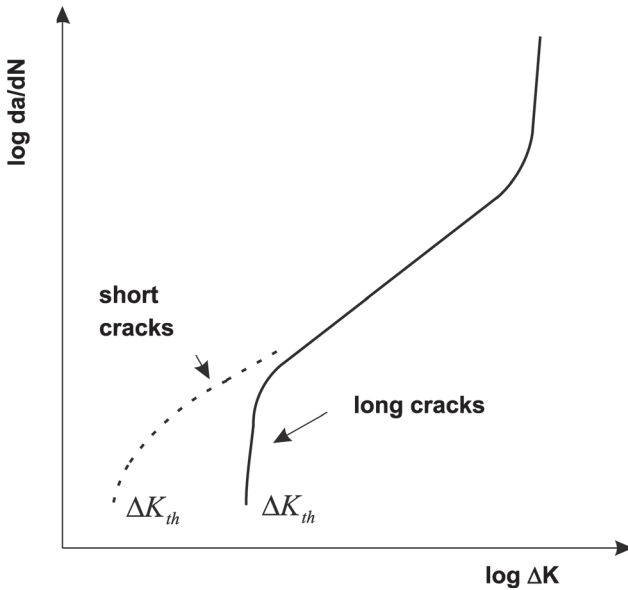
In the traditional approach, the threshold stress-intensity-factor range ΔK_{th} is considered as constant for macroscopic visible cracks, so-called long cracks. The main part of fatigue lifetime belongs to microscopic crack initiation of short fatigue cracks. The short crack effect occurs until crack length depends on the effective stress ratio, R , usually in the range from 0.5 to 1 mm for structural steels. In this range of cracks, the crack closure and other effects are not fully developed, and the threshold for fatigue-crack propagation is lower than that corresponding to long cracks for the same load ratio, R (see Fig. 2). The Kitagawa and Takahashi diagram is used for fatigue-crack initiation from surface or from a notch (Fig. 3) [4].

Figure 3 shows that threshold for crack initiation from the notch (dashed line) is higher than from a crack from the surface (solid line) in the range of micro-cracks or short cracks. The fatigue threshold stress is a function of crack length, as shown in Fig. 3.

In the case of fatigue-crack initiation from the notch, the fatigue-crack propagation becomes similar only in case of a large crack. In this case, the fatigue crack propagates only if the applied loading range is higher than the fatigue-crack-propagation threshold:

$$(3) \quad \frac{da}{dN} = C \cdot (\Delta K - \Delta K_{th})^m$$

FIG. 2 Fatigue-crack growth rate versus stress-intensity factor range for short and long cracks [4].



where:

m and C = experimentally determined material constants [5],

ΔK = stress-intensity factor range, and

ΔK_{th} = threshold stress-intensity factor.

The constants m and C ($m = 3.01$ and $C = 1,11 \times 10^{-14}$) are determined experimentally by fatigue-crack growth testing on three-point specimens of used structural steel S690, according to ASTM E647-05 [6]. The material threshold for crack propagation as a function of the long cracks is defined by an empirical equation in Ref 7 as:

$$(4) \quad \Delta K_{th-0.1} = -0.021 \cdot \sigma_u + 8.4$$

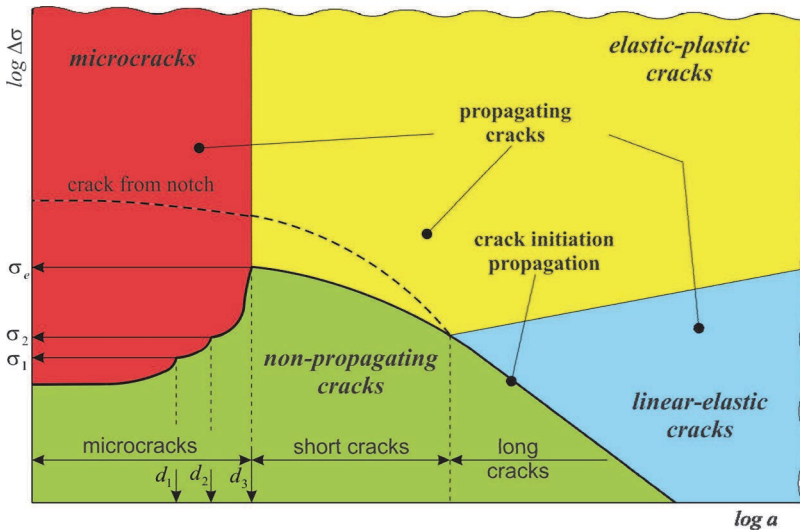
where:

σ_u = ultimate tensile strength (MPa).

Experimental Preparation

To estimate the fatigue-crack propagation from the surface notch, the experimental methodology is implemented for detection and monitoring of crack initiation and propagation by surface-strain behavior. The multi-strain-gauges technique (five

FIG. 3 Fatigue-crack propagation threshold as initiation from surface and from notch as a function of crack length [4].



initiation, as is schematically shown in Fig. 4. Figure 5 shows photography with details of a specimen, instrumented with multiple strain gauges.

The four-point bend specimens were made of S690 grade steel with a yield stress of 695 MPa and tensile strength 854 MPa. A shell-notched specimen was subjected to four-bend cyclic loading with a long span distance $S_1 = 200$ mm and a short span distance $S_2 = 90$ mm. The central notch length of 15 mm and depth of 0.5 mm was machined. Specimens were fatigue tested by using a servo-hydraulic

FIG. 4 Schematic view of the strain-gauge distribution and fatigue-crack fronts of semi-elliptical cracks.

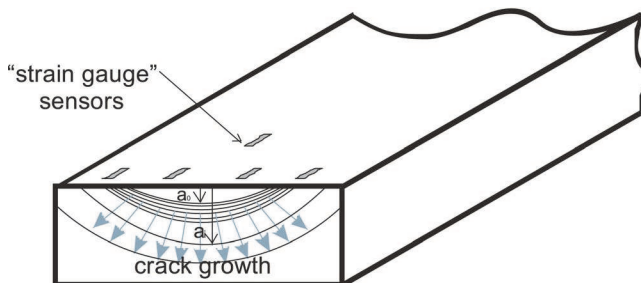
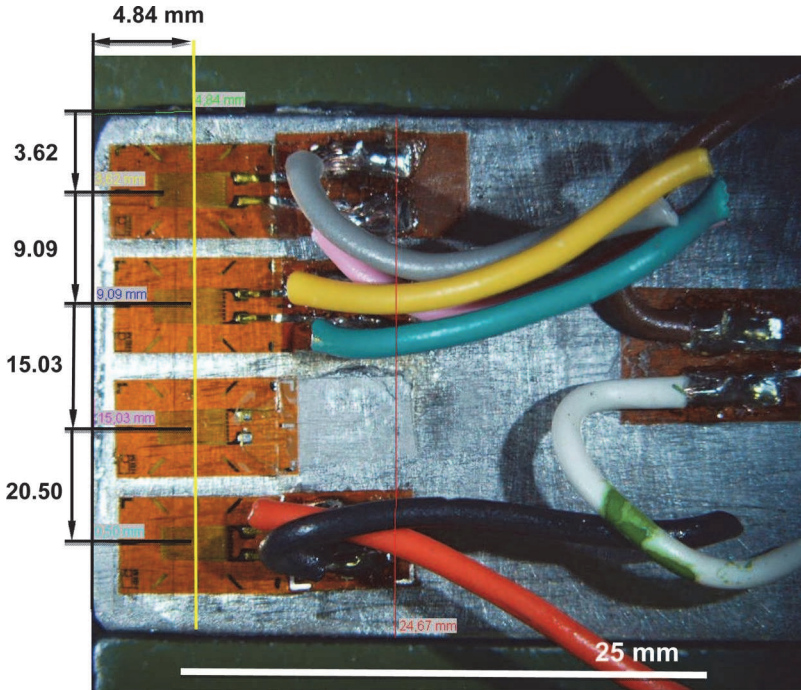


FIG. 5 Measurement on specimen with strain gauges; right strain gauge is reference strain gauge at distance 38.9 mm.



dynamic testing machine (INSTRON 1255) at a frequency of 10 Hz, as shown in Fig. 6. The position of strain-gauge sensors near the notch is essential for understanding strain behavior. Sensors near the notch are affected with crack propagation in different ways than sensors at the bulk of the specimen. Figure 7 shows the sensor's position, whereas the typical strain lines on the surface during applied bending are shown in Fig. 8. Figure 8 also shows deviations of strain lines at the surface of the specimens caused by surface notches. The electronic measurement system for strain during dynamic loading has been made as a compact independent electronic unit, supported by "Dynastrain" computer software, as shown in Fig. 6. The measurement system consists of strain-gauge sensors, a microcontroller system for sampling and data acquisition, and amplification of measured values.

Experimental Results of Fatigue Testing of a Specimen

The test procedure started with electronic device calibration. The known applied

FIG. 6 Four-point bending fatigue testing of specimen with multiple strain gauges with an electronic device.



FIG. 7 Strain-gauge measure locations.

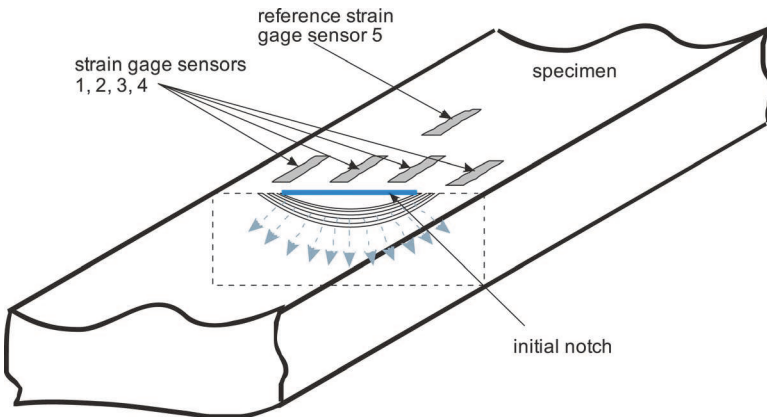
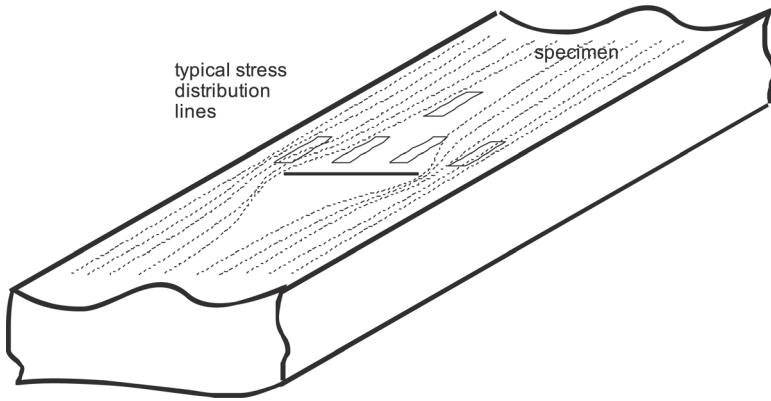


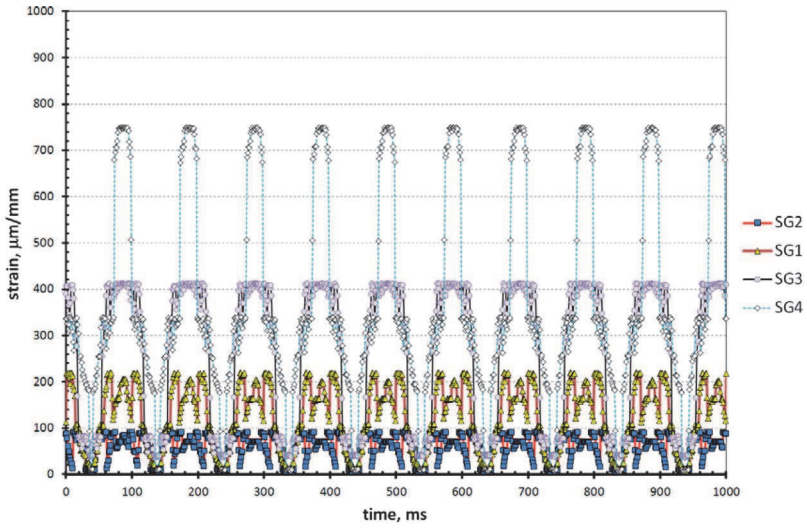
FIG. 8 Surface distribution of stress.



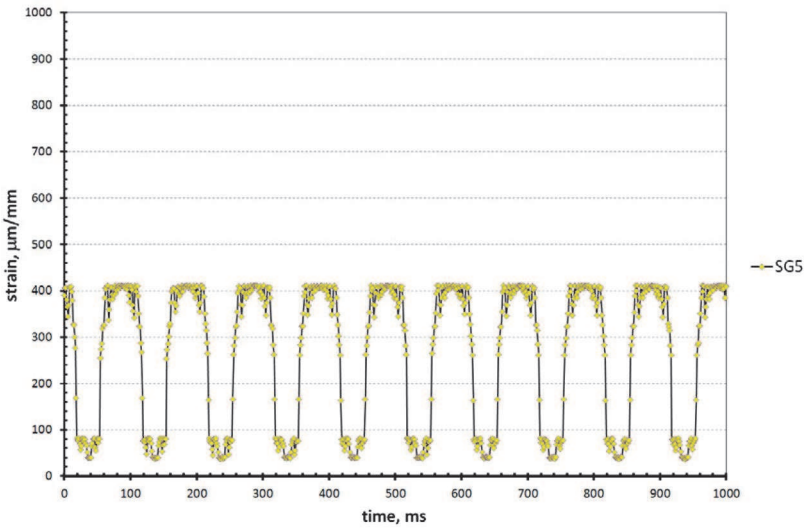
on strain-measured channels. The reference channel was calibrated for F_{\max} and F_{\min} parameters with a relative scale from 0 to 100. Based on calculated stress, the read values from Dynastain could be transferred to micro-strain units. The main calibration was done on reference strain-gauge No. 5. The typical recorded response is shown in [Fig. 9\(a\)](#) and [9\(b\)](#).

The applied dynamic load was then sequentially applied with high amplitude of force F_{\max} , $R=0.1$, for a short number of cycles and lower amplitude forces for a larger number of cycles. The amplitude of strains was collected each 1000 cycles, with an acquisition frequency of 900 samples per second. Tests were performed at ambient temperatures by frequency of dynamic loading 10 Hz for all regimes. The signals were not smooth sinusoids as applied by Instron hydraulic test device because of the dynamic effects of strain-gauge fixation on the surface and noise at the four-point fixation system. The main frequency and periodization remain as expected in line with applied loads. Each strain gauge has its own characteristics of response regarding to their position from notch or crack. In our case, we are considering strain gauges No. 2 and No. 3 as relevant for recognition of crack growth and crack-depth estimation. Because of different crack depth below SG2 and SG3, different strain amplitudes were obtained as shown in [Fig. 9\(b\)](#). [Figure 10](#) shows the performed fatigue regime with maximum forces. It is possible to recognize increasing strain during fatigue under constant maximum force, $F=6$ kN. Each maximum force area has its own strain range of loading. The strain (SG5) starts to decrease with number of cycles after more than $1.8 \cdot 10^6$ cycles. To apply uniform strain, the measured values were divided

FIG. 9 (a) and (b): Typical response signals from Dynastrain in 1 s during loading with $F_{\max} = 5$ kN.

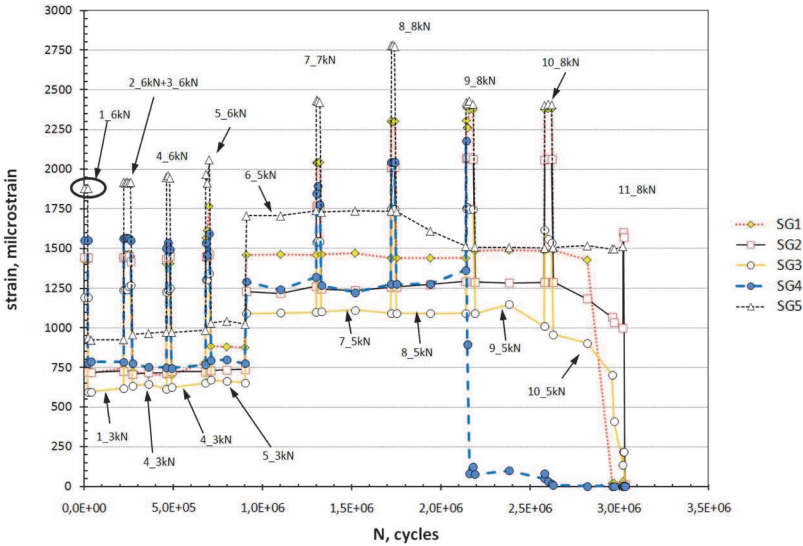


a) Outside strain gauges SG1 and SG4 and Inside strain gauges SG2 and SG3



b) reference strain gauge SG5

FIG. 10 Performed fatigue loading with strain during each sequence of loading.



Results Analysis

FRACTOGRAPHIC FATIGUE-CRACK PROPAGATION ANALYSIS

The experimental assumption was that stress distribution is likely to be equal at the position of reference sensor (SG5), and mostly affected on the position of strain gauges (SG1–SG4) behind notch. Strain gauge SG5 is the reference sensor, because its position is remote from the notch and its strain amplitude will be less affected by crack extension than strain gauges (SG1–SG4) near the notch. We were assuming that they were subjected to the highest tension load at the beginning of bending the sensors, and, consequently, their cyclic strain amplitude is higher. During the crack propagation their strain amplitude starts to decrease. The relationship between crack length and strain (amplitude and mean value) could be shown at points on the curve as the so-called calibration curve. With crack growth, the strain is going to decrease. The exact crack length/depth can be determined by fractographic investigation in post-testing analyses. The curve crack extension versus number of cycles is the so-called crack growth curve. The calibration curve provides information on crack length with regards to strain change, an essential tool for establish on-line monitoring of dynamic loading components. The dynamic loading was conducted several times until final failure of specimens occurred at the critical average crack length, $a_c = 6.96$ mm.

At the end of fatigue loading, the specimen was broken and fractographic

measured to verify fatigue-crack growth. The fractured surface of the specimen is shown in Fig. 11. To interpret fatigue-crack growth scenarios, two different fatigue-loading regimes (under the same loading ratio, $R = 0.1$) should be considered. The higher $F_{\max} = 8$ kN contributes to higher fatigue-crack growth rate with good agreement with experimentally measured parameters ($m = 3.01$ and $C = 1.11 \times 10^{-14}$) of Paris–Erdogan’s law. The fatigue-crack growth rate on specimens subjected to lower $F_{\max} = 5$ kN, because the plastic zone of higher loading becomes lower. It is evident that the C value becomes lower ($C = 3.85 \times 10^{-15}$) than experimentally measured ($C = 1.11 \times 10^{-14}$). The results shown on the log–log scale in Fig. 12 are typical linear functions of crack growth versus range of stress-intensity factor. It seems that the exponent m is almost the same, whereas the C parameter is shifted to a lower value corresponding to cyclic plastic zone size at the tip of a fatigue crack tip. The fatigue-crack growth for middle crack tip was determined by using a Paris fatigue relationship with obtained C and m parameters by using Eq 3 for whole-crack propagation but different maximum loading. The obtained curve is given in Fig. 13. The detailed microscopic review of the break recognizes few typical locations of frontal lines during elliptical crack growth. Figure 13 was created backward, starting at the last experimentally measured fatigue-crack length. Because the number of cycles and crack extensions are known, the parameters of crack growth equation C and m are used. The crack extension was obtained by integration of Eq 3 for performed number of cycles. Each step of loading with higher loading amplitude shows a steep increase of crack growth until the stage where crack increments were too small. The higher fatigue growth rate appeared under shorter number of cycles but under higher loading amplitude. One can conclude that the initiation stage for fatigue-crack propagation starts around 1.3×10^6 of cycles, but strain starts to

FIG. 11 Cross section of fractured specimen and location of strain-gauge sensors, magnification $\times 5$.

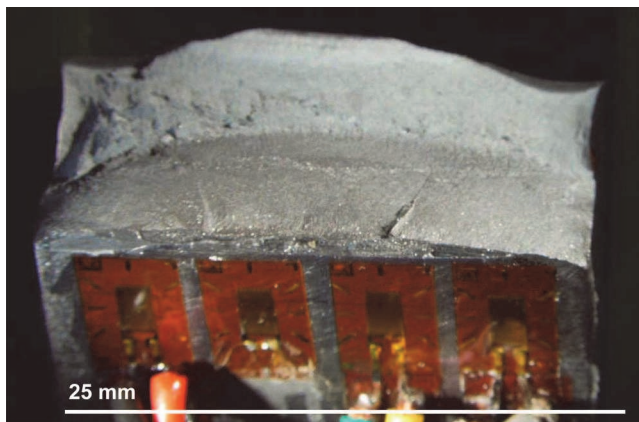


FIG. 12 Fatigue-crack growth rate versus applied range of SIF for both fatigue-loading regimes.

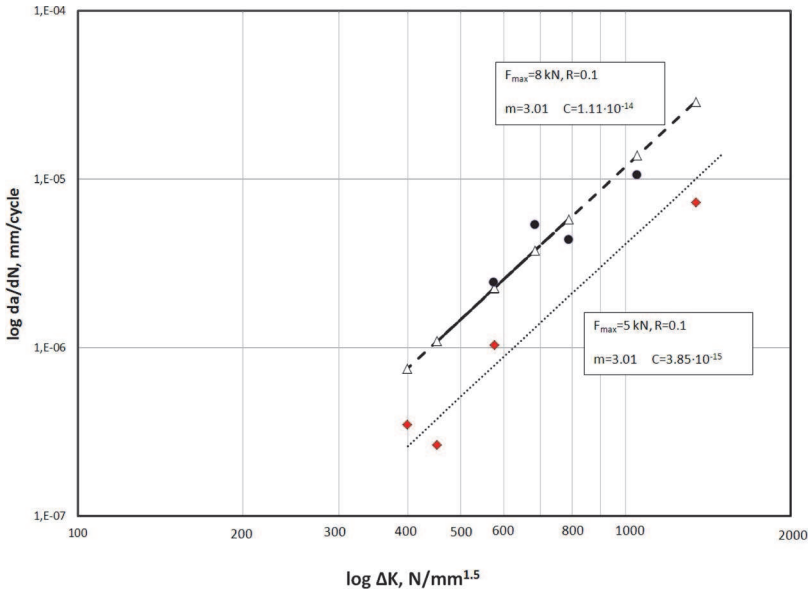
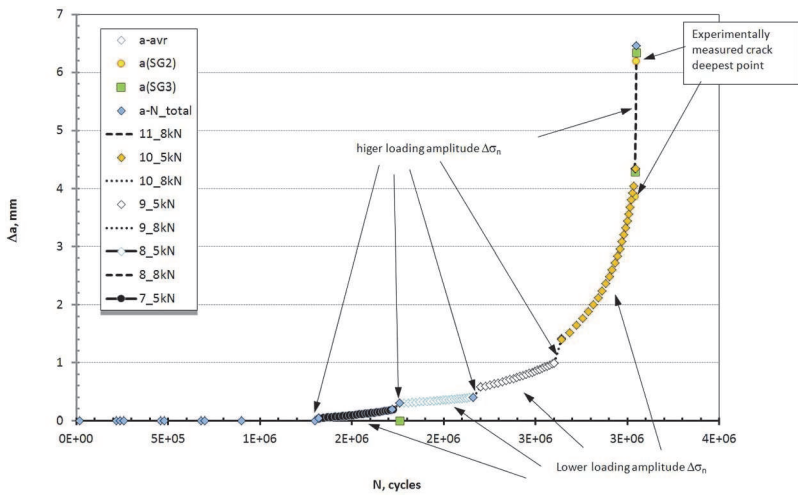


FIG. 13 Fatigue-crack growth curve for a crack tip point at the middle of the specimen.

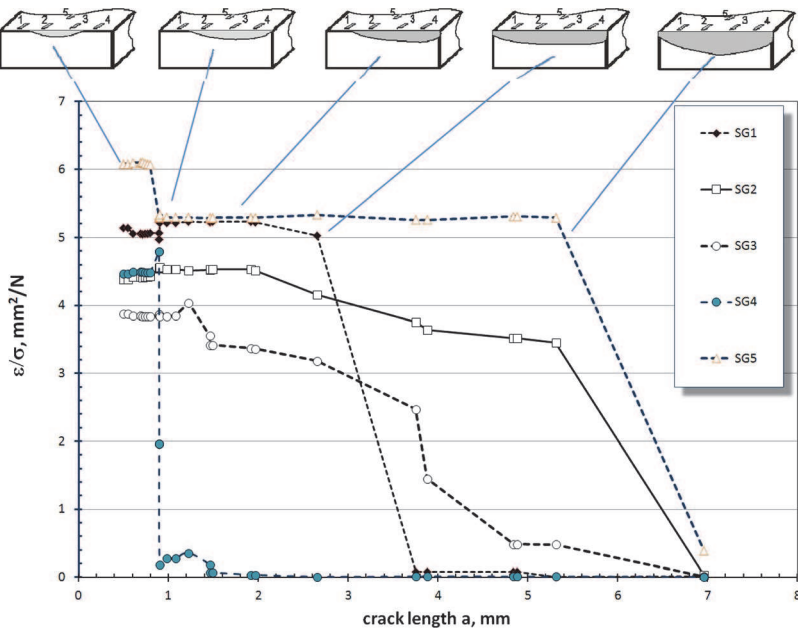


decrease after 1.8×10^6 of loading cycles. This leads to two possibilities: that fatigue crack starts to grow under a higher number of cycles, or strain gauges are not sensitive to crack initiation of short fatigue cracks because the SGs are remote for more than 4 mm from the notch.

However, during fatigue loading, the plastic zone at the crack tip appeared where the crack initiation process starts, as explained. It is important to distinguish between the crack initiation stage and macro fatigue-crack propagation textbook [7,8]. Also, it makes it difficult to distinguish the start of fatigue long-crack growth as well. The fatigue cracks can also start growing in different points along the notch. It does not fit to models where only average crack length was considered by using given Eqs 1–4. The macro fatigue-crack propagation and final failure appeared under higher fatigue loading levels. Therefore, with the presented technique, it is possible to estimate the number of cycles for the initiation stage of creating a fatigue crack.

From Fig. 10, showing number of cycles versus strain and crack extension, it is possible to create a crack length versus strain curve, the so-called calibration curve. Fatigue was performed with different amplitudes of applied forces. Because the fatigue loading is in the elastic mode of material behavior, the measured maximal strain was normalized by applied maximum stress. Figure 14 shows the change of maximum measured strain versus average fatigue-crack length. Fatigue-crack front shape is schematically shown by an additional sketch above the plot. During

FIG. 14 Calibration curve strain versus crack length.



fatigue-crack propagation, the maximum strain decreases when the crack tip passes away from the strain-measuring zone. The strain decrease rate depends on crack behavior below each strain gauge. Therefore, strain decrease is a clear signal that fatigue-crack growth and the crack itself is going to be fatal for fracture. Because the strain behaviors were recorded for known fatigue cracks, during each change of the loading regime, it is possible to connect strain magnitude and crack length in the form of the so-called “calibration curve.” SG4 at the edge of the specimen shows significant strain drop at the moment when the cracks pass the surface. There were just a few points recognized within this experiment, probably because of insufficient difference in amplitude of cyclic loading and same frequency applied at both sequences. At the same number of loading of cycles, the strain also decreased at the reference strain gauge (SG5) and slightly increased on the opposite edge for SG4 and SG2, as a consequence of redistribution of strain on the surface of the specimen. Figure 14 also shows that remote strain (measured by SG5) is not sensitive on crack extension to depth, because in the range of crack length from 1 to 5.5 mm, strain was similar. Figure 14 shows longer crack extension in points below SG3 (next to SG4) than SG2 and SG1. Therefore, we can assume that the crack was propagated asymmetrically.

Observing Fig. 13, one can conclude that fatigue-crack extension is proportional to the number of cycles in the case of lower $F_{\max} = 5$ kN loading amplitude of seventh and eighth loading proportional relationships between crack extension and number of cycles for surface point. It seems that fatigue-crack transformation from semi-elliptical crack to through-thickness crack can appear with a constant fatigue-crack growth rate. However, it is necessary to prove it by numerical analysis of the SIF along the fatigue-crack tip front. If SIF is not changed significantly along the crack profile during fatigue-crack extension, it seems that fatigue-crack growth rate is constant and, therefore, crack extension is proportional to the number of cycles.

FINITE-ELEMENT MODELING OF STRESS-INTENSITY FACTOR

Semi-elliptical and through-thickness crack has been modeled by a program for finite element modeling (FEM) combining tetrahedral and hexagonal elements in the vicinity of the crack front. The crack configuration of tested specimens was measured. Fatigue-crack profiles are created by connection of measured points. Literature review [5] shows that transition from semi-elliptical cracks in a finite plate to a single-edge surface crack in a finite plate under bending is not solved. Therefore, FEM analysis has been employed to determine the actual SIF for measured fatigue-crack fronts. FEM analysis was provided for specimens with semi-elliptical surface crack, and after fatigue-crack propagation for specimens with through-thickness fatigue crack, as shown in Fig. 15. SIF has been calculated for different fatigue-crack fronts between seventh and 11th fatigue loading with maximum load $F_{\max} = 8$ kN and loading ratio $R = 0.1$. Figure 16 shows SIF for all five fatigue-crack fronts shown in Fig. 15. Figure 16 shows also that K_{\max} and, consequently, ΔK are the almost the

FIG. 15 Fatigue-crack profiles measured for semi-elliptical surface crack and through-thickness crack between seventh and 11th fatigue loading by $F_{\max} = 8$ kN.

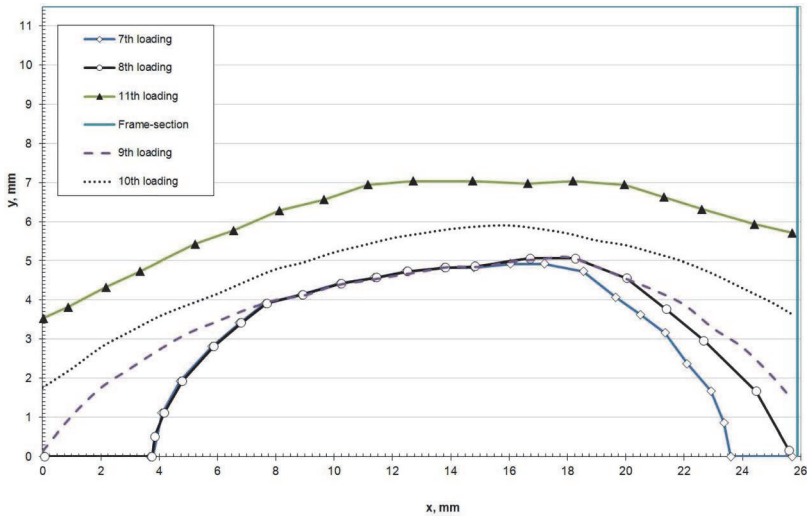
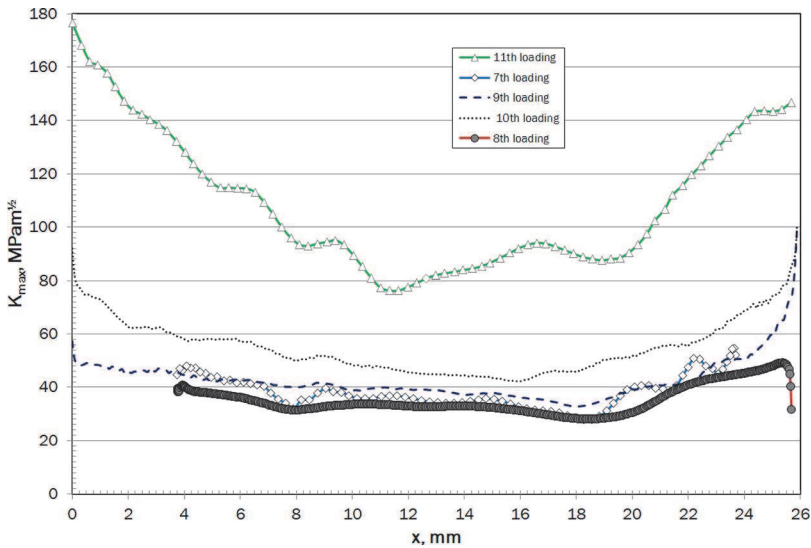


FIG. 16 Stress-intensity factor distribution along fatigue-crack profile in the four-bending specimen between seventh and 11th fatigue loading by $F_{\max} = 8$ kN.



for semi-elliptical cracks. This means that crack propagation appears under almost constant fatigue-crack growth rate da/dN until the crack achieved edge of the specimen. This corresponds to an almost linear relationship between crack extension and the number of cycles.

However, when the fatigue crack achieves the edge of the specimen, and fatigue-crack front becomes through-thickness crack, the fatigue-crack growth rate exponentially increases with the number of cycles, because ΔK is increasing as well. **Figure 15** shows that the highest values of SIF appear on the free surface of the specimen, especially when cracks propagate in full through-thickness front, as it is in the case of ninth, tenth, and final 11th front cracks. In spite of longer cracks in the middle of the specimen, the SIF values are half the value than at the edge of the specimen. This is actually an effect of plane-stress condition at the surface and plane-strain condition in the middle of the specimen. Arbitrary crack SIF corresponds to average crack length under plane-strain conditions. The standard stress-intensity solution for single-edge surface crack can be taken in account, available in standards or textbooks [8,9]. FEM analyses were used for equivalent stress analysis along actual fatigue-crack fronts. The three different fatigue-crack fronts have been analyzed, semi-elliptical surface crack (**Fig. 16**), semi-elliptic surface crack (reached one edge of specimen), and through-thickness crack. The highest von Mises stresses occurred at the crack tip at the surface (for semi-elliptical surface crack), as shown in **Fig. 17**. During continued four-bend fatigue loading with maximum load, $F_{max} = 8 \text{ kN}$, the fatigue-crack tip reaches the edge of the specimen (**Fig. 18**), where the highest plastic zone occurred, and SIF values decreased at the crack tip just before the edge (see **Fig. 16**).

FIG. 17 Elastic-plastic stress distribution in the four-bending specimen at the end of seventh fatigue loading with semi-elliptical surface crack.

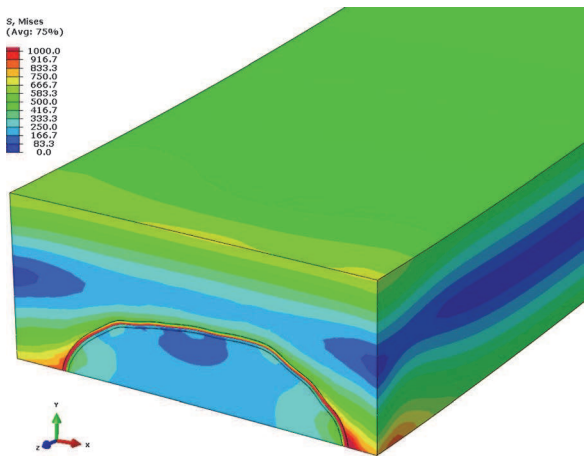


FIG. 18 Elastic-plastic stress distribution in the four-bending specimen at the end of eighth fatigue loading with crack tip at one edge.

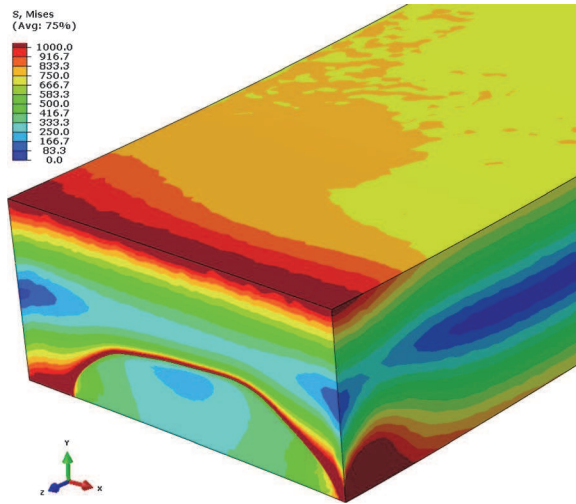
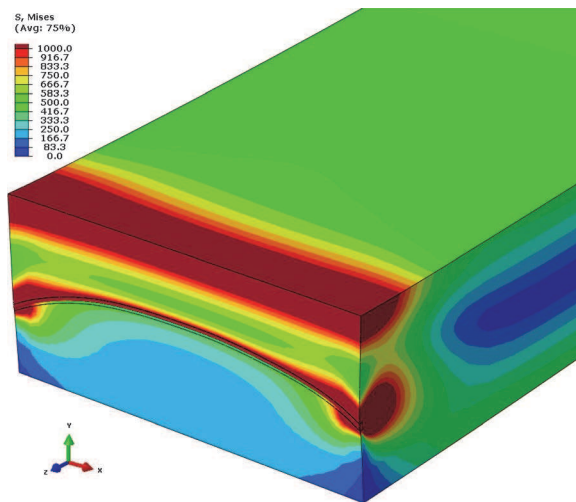


FIG. 19 Elastic-plastic stress distribution in the four-bending specimen after 11th fatigue loading at the moment of final failure of specimen.



Because the SIF are higher on the other side, one could expect that fatigue-crack growth rate under SG1 and SG2 is higher, until fatigue-crack front does not achieve another edge of specimen and fatigue-crack front spreads through the whole thickness, as shown in Fig. 19. In this case, the compressed plastic zone also occurred on the upper surface of the specimen, as shown in Fig. 19.

Conclusions

This paper presents a technique for determination of the calibration curve in terms of strain-crack length during fatigue-crack propagation on a four-point specimen. Technique is based on fatigue-crack growth law and observation of strain amplitude change versus the number of loading cycles. In the case of different loading amplitudes, the strain should be normalized by applied stress, and corresponding parameters of fatigue-crack growth rate should be taken into account. The strain redistribution occurred on the surface of the specimen during fatigue-crack propagation. Strain redistribution is recognizable as change of strain on SG, with regard to their position on the surface and crack location. The scenario of crack growth is possible to be determined in post-test analysis. The experimental results of strain monitoring show that sensitivity of strain on crack growth strongly depends on SG positions with regard to growing cracks. This makes it difficult to distinguish moments between initiation and fatigue-crack propagation number of cycles. The numerical analysis of the SIF along the fatigue-crack tip front shows that, in our case, fatigue-crack transformation from semi-elliptical crack to through-thickness crack can be treated at constant fatigue-crack growth rate. The numerical analysis shows that stress-intensity factors are not changed significantly along the crack profile during fatigue-crack extension. It seems that fatigue-crack growth rate is constant and crack extension is proportional to number of cycles. The fatigue-crack propagation of through-thickness crack appeared with exponentially increasing fatigue-crack extensions versus the number of cycles. This experimental research and investigation demonstrate the capability of continuous flaw growth measurement during the operation on critical places in the mechanical construction. In case of evident deviation from normal operating conditions, proper response is expected to prevent failure of the construction and future failure prevention.

ACKNOWLEDGMENTS

The writers acknowledge the support of Nuclear Power Plant Krško for founding this research.

References

- [1] Chapetti, M. D. and Jaureguizar, L. F., "Estimation the Fatigue Behaviour of Welded Joints," *Proc. Eng.*, Vol. 10, 2011, pp. 659–664.

- [2] Paris, P. and Erdogan, F., "A Critical Analysis of Crack Propagation Laws," *J. Fluids Eng.*, Vol. 85, No. 4, pp. 528–533.
- [3] Kocak, M., "FITNET Fitness-for-Service Procedure," *Final MK7*, GKSS Research Centre, Geesthacht, Germany, 2006.
- [4] Kitagawa, H. and Takahashi, S., "Applicability of Fracture Mechanics to Very Small Cracks or the Cracks in the Early Stage," *Proceedings of the Second International Conference on Mechanical Behavior of Materials*, Boston, Aug 16–20, 1976, pp. 627–631.
- [5] ASM International, *Atlas of Fatigue Curves*, S. D. Henry, Ed., American Society for Metals, Materials Park, OH, 1994.
- [6] ASTM E647-05: Standard Test Method for Measurement of Fatigue Crack Growth Rate, *Annual Book of ASTM Standards*, ASTM International, West Conshohocken, PA, 2005.
- [7] Chapetti, M. D., "A Simple Model to Predict the Very High Cycle Fatigue Resistance of Steels," *Int. J. Fatigue*, Vol. 33, 2011, pp. 833–841.
- [8] Gross, B. and Srawley, J. E., "Stress Intensity Factor for Single-Edge-Notch Specimens in Bending or Combined Bending and Tension by Boundary Collocation of a Stress Function," *Technical Note D2603*, NASA, Washington, D.C., 1965.
- [9] Anderson, T. L., *Fracture Mechanics—Fundamentals and Applications*, CRC, Boca Raton, FL, 1995.
- [10] *ABAQUS 6.13; Standard Code*. (2014). DS Simulia. Waltham, MA.

VARIOUS SENSORS

STP 1584, 2015 / available online at www.astm.org / doi: 10.1520/STP158420140051

Jefferson Cuadra,¹ Prashanth A. Vanniamparambil,¹
Kavan Hazeli,² I. Bartoli,³ and Antonios Kotsos⁴

A Hybrid Optico-Acoustic NDE Approach for Deformation and Damage Monitoring

Reference

Cuadra, Jefferson, Vanniamparambil, Prashanth A., Hazeli, Kavan, Bartoli, I., and Kotsos, Antonios, "A Hybrid Optico-Acoustic NDE Approach for Deformation and Damage Monitoring," *Evaluation of Existing and New Sensor Technologies for Fatigue, Fracture and Mechanical Testing*, STP 1584, Jidong Kang, David Jablonski, and David Dudzinski, Eds., pp. 135–146, doi:10.1520/STP158420140051, ASTM International, West Conshohocken, PA 2015.⁵

ABSTRACT

To account for both surface and volume effects and to provide cross-validation when using in situ nondestructive evaluation (NDE) methods, a hybrid optico-acoustic approach combining digital image correlation (DIC) and acoustic emission (AE) was developed, validated, and tested. The designed system includes hardware and software linkages between the two sensing modalities with feedback both from the mechanical testing device as well as from other complementary NDE methods including ultrasonic testing (UT) and infrared thermography (IRT). This hybrid monitoring approach targets the early identification of damage precursors which vary depending on the material tested. To corroborate the reliability of the hybrid setup, various tensile, fracture and fatigue testing procedures were implemented for different types of materials. Of interest herein was the evaluation of each individual NDE method's monitoring capabilities of deformation and damage in conjunction with their

Manuscript received May 2, 2014; accepted for publication November 17, 2014; published online January 8, 2015.

¹Mechanical Engineering & Mechanics Department, Drexel Univ., Philadelphia, PA 19104.

²Hopkins Extreme Materials Institute, John Hopkins Univ., Baltimore, MD 21218.

³Civil, Environmental and Architectural Engineering, Drexel Univ., Philadelphia, PA 19104.

⁴Mechanical Engineering & Mechanics Department, Drexel Univ., Philadelphia, PA 19104 (Corresponding author).

⁵ASTM Fourth Symposium on the *Evaluation of Existing and New Sensor Technologies for Fatigue, Fracture and Mechanical Testing* on May 7–8, 2014 in Toronto, Canada.

spatial and temporal resolutions. In carefully designed metal alloy microstructures with well-characterized mechanical properties, AE validated DIC-observed strain band formations on the sample's surface, which further enabled targeted microscopic analyses that proved the origin of the NDE findings. In the case of fracture, DIC and UT validated AE information regarding both crack initiation and growth in Mode I testing of metallic alloy samples. Finally, in fatigue loading of fiber reinforced composites, IR measurements confirmed DIC indications of early damage formation consistent with AE recordings. Post-processing of NDE datasets combined with actual loading information allowed the calculation of mechanical parameters (elastic-plastic transition stress, strain localizations, traction separation laws, energy dissipation, localized Poisson ratios) that have been used to construct physics-based computational models for multi-scale deformation and damage evolution, as well as remaining life-estimations.

Keywords

nondestructive evaluation, digital image correlation, acoustic emission, ultrasonic testing, infrared thermography, damage monitoring

Introduction

Nondestructive evaluation (NDE) techniques have successfully been implemented for higher reliability and stringent structural health monitoring (SHM) [1–12], material characterization [13–20], as well as manufacturing applications [21,22]. With technological advances, NDE techniques have become and have served as essential methods to inspect, quantify, and characterize damage for various materials and components; thus supplying the need for reliable damage monitoring and quantification. These advances in NDE techniques suggest that robust coupled NDE monitoring systems based on periodical, triggered, or continuous inspections are able to detect and identify in a multiscale whether the current condition of a material or structural component has deviated to a damage state. In addition, data post-processing and integration, also identified as data “fusion,” may be inherently constructed in the harvesting part of the system or is applied in post mortem. Data-fusion may also occur at the post-processing level in which heterogeneous sensing units provide inputs that are then classified by the data acquisition system using intelligent schemes including, e.g., machine learning [23], as well as neural/fuzzy/probabilistic networks [16,24]. Difficulties associated with classification of recorded information may be avoided by statistical pattern recognition (SPR) techniques such as novelty or anomaly detection [2,25,26], which establishes whether or not a critical structural component is unreliable due to deterioration from its normal service conditions. Such methods and techniques for SHM data and others such as the principal component analysis [27,28] have been employed for damage detection. Although NDE data are typically extracted using a single technique without real time or post mortem validation, in some structural applications, data extraction from high frequency guided ultrasonic waves (GUW) [1,8,12], acoustic emission (AE) waveforms, and low frequency vibrations [6,11] have been

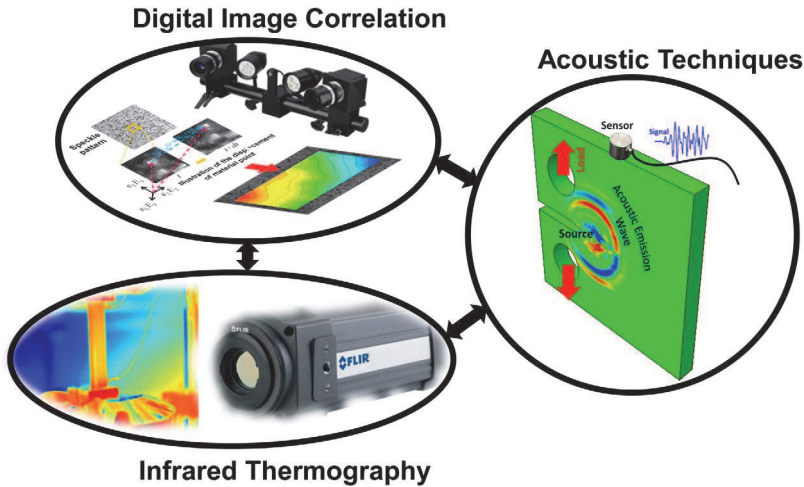
The NDE monitoring approach in this paper is based on the parallel use of two different type of techniques, i.e., optical and acoustic, which include digital image correlation (DIC), infrared thermography (IRT), ultrasonic testing (UT), and AE to quantify the damage and corroborate the modalities consistency. These techniques described for completeness provided complementary surface and volume information, and can thus be effectively used to infer the developing damage stages in three different components/materials for remaining life analysis and reliably constructing damage-specific information for a modeling framework.

Sample Preparation and Experimental Procedure

Three different type of testing setups for three different materials were performed in order to corroborate the efficacy of the hybrid NDE setup which included: uniaxial static compression of Mg alloy, compact tension mode I of Al alloy and a tension–tension fatigue of a fiber reinforced polymer composite. The compression specimens were fabricated from a soft annealed 25 mm rolled plate of a commercial magnesium alloy AZ31 (Mg- 3 % Al- 1 % Zn). Additional procedures to homogenize microstructure and remove residual stresses are provided in detail in previous work by the authors [15]. The cylindrical compression samples were machined using electrical discharged machining (EDM) with dimensions according to ASTM E9-09 [29], as shown in Fig. 2(b). Monotonic compression tests were carried out at constant strain rate of $4.5 \times 10^{-4} \text{ s}^{-1}$ at ambient temperature with a MTS hydraulic load frame. The experimental specifics of the compact tension were in detail in Ref. [9], and therefore are only briefly described herein for completeness. A compact tension (CT) specimen was prepared from an Aluminum alloy plate (Al2024) and was machined based on ASTM E1820-06 [30] (Fig. 4(a)). Before applying Mode I loading, the CT specimen was cyclically pre-cracked using a 600–6000 N loading profile at a rate of 10 Hz in accordance with ASTM E647-08 [31]. The pre-crack was continuously monitored by a digital camera and the fatigue test was terminated when the crack visible on the front surface appeared to have a length ~ 3 mm, in accordance again with the specifications described in the used testing standards. Subsequently, the CT specimen was loaded in Mode I at a constant displacement rate of 0.5 mm/min and monitored using the NDE setup shown in Fig. 1. A glass fiber reinforced epoxy laminate consisting of E-glass fibers and epoxy resin with dimensions 200 by 23 by 1.48 mm (Fig. 6(a)) was tested at 3 Hz with R values of 0.1 in accordance with ASTM D3039/D3039M-08 [32].

During the loading process, the novel optico-acoustic was recorded simultaneously. DIC in all testing setup was implemented to extract full-field displacements and strains using a 3D system ARAMIS, GOM equipped with two 5-megapixel cameras. A calibration block was used for sharply focusing the camera lenses to the field of view (FOV) and to determine the position of the cameras relative to each other, as well as their distance from the sample in the 3D space. Specifically, the

FIG. 1 Hybrid optico-acoustic NDE techniques.



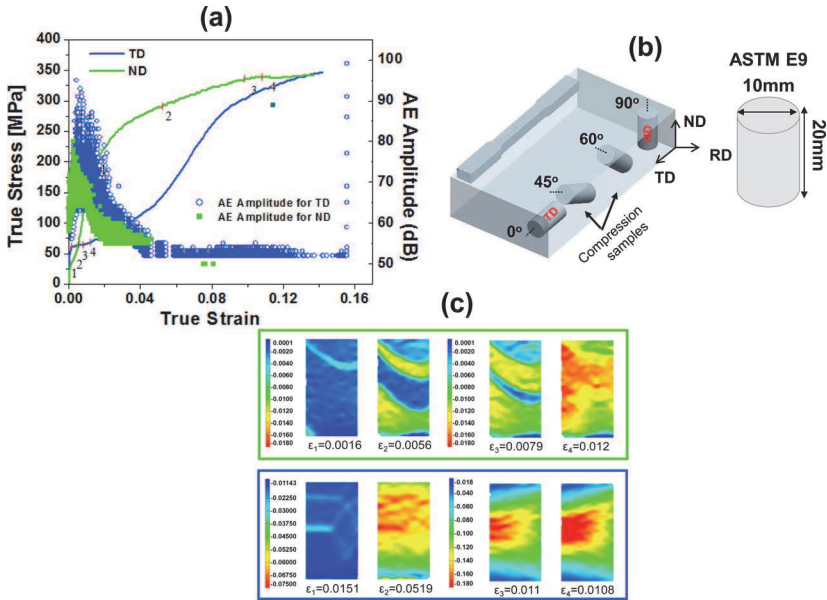
cameras with a focal length of 50 mm were positioned 485 mm from the sample and had a separation of 176 mm to achieve a FOV 65 by 55 mm² and a resulting resolution of 325 $\mu\text{m}/\text{pixel}$. A stochastic speckle pattern was placed on the surface of the specimens and a few pretest images were taken to determine the displacement and strain field sensitivities, which were calculated to be ± 2 and $\pm 150 \mu\text{m}/\text{m}$, respectively [33]. In static loading (i.e., the compression and compact tension test), the acquisition rate was 1 frame per second and for the cyclic setup was 29 frames per second with a time delay determined by the in-house AE triggering algorithm. AE was recorded using a four-channel system (AEWin DiSP, MISTRAS) and two to three piezoelectric sensors (PICO) mounted at specific locations depending on the specimen and type of testing setup [34]. All the details of the AE/UT setup were previously explained in detail for the compression test in Ref. [15], crack monitoring in Ref. [9] and fatigue test in Ref. [14]. A FLIR A325sc thermal camera with spectral range of 7.5–13 μm , 320 by 240 pixel resolution and maximum 60 Hz frame rate acquisition and a Fluke Ti55 IR FlexCam camera system operating in the 8–14 μm range were utilized to quantify full field temperature on the sample surface [35,36].

Results and Discussion

The novel optico-acoustic testing setup was essential to identify critical stages of deformation mechanism initiation at the onset of plasticity in Mg AZ31. The TD orientation sample (referring to the parallel to the rolling direction plane, shown in Fig. 2(b)) in compression sustain a characteristic stress relaxation S-type curve.

a) shows the two different strain hardened strain stress curves, i.e., three

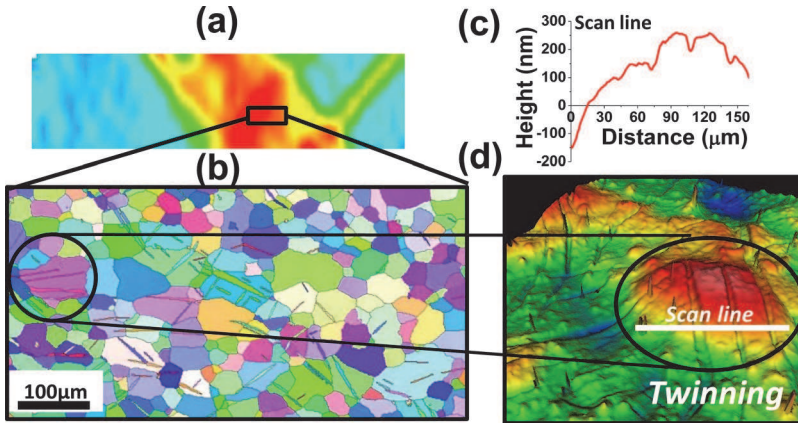
FIG. 2 (a) Stress-strain curves for ND and TD orientations correlated with corresponding AE amplitudes, (b) cylindrical compression samples extracted from alloy plate, and (c) corresponding full-field DIC strains for ND (green box) and TD (blue box) at different strain levels.



inflection points (TD) compared to one (ND), correlated with AE amplitude. It can be depicted that the TD sample AE response has higher amplitude values at the onset of plasticity (shown by marker 1 for both stress-strain curves at the knee of the starting plateau in the TD curve). Similarly, the high AE emission activity can be depicted by the full field strains (Fig. 2(c)), which show strain localization in the form of diagonal bands starting at the onset of the bulk plastic strains. These high localizations are attributed to microstructural transformations of the crystal lattice called twinning. Besides the differences between stress strain behaviors, the orientation samples show very different strain localization. For instance, TD at lower stress (including lower yield) values shows localization compared to ND, which shows localizations at high stress and is possibly attributed to final fracture.

To further analyze the strain localization, an electron backscatter diffraction (EBSD) study was implemented, as shown in Fig. 3(a). The EBSD map (Fig. 3(b)) shows intragranular defects (leave-like) effects that caused a different orientation values within the grains. This reorientation caused by twinning mechanisms in the microstructure potentially suggested that out-of-plane effects were also inherent of this crystallographic mechanism. Therefore, a surface morphological analysis was performed to quantify the surface roughness at twin locations. A scan line of the

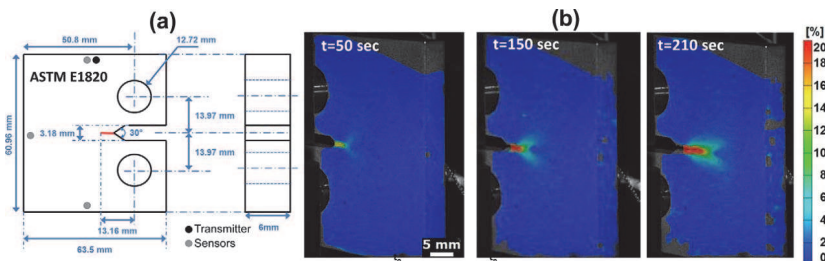
FIG. 3 (a) Full field strain map, (b) EBSD map for selected location at strain map, (c) roughness profile for scan line shown in (d) Atomic force microscopy surface morphology field.



surface roughness at this protrusion shows the out-of-plane height compared to other locations where twinning did not occur. The localizations from the DIC strain therefore showed the capability to identify, determine, and quantify the effects of microstructure evolution for the onset of plasticity.

In an attempt to corroborate the effectiveness of the coupled techniques for damage incident behavior, a crack growth mechanical testing module was performed. As a result, the specimen (Fig. 4(a)) had one main dominant damage source, i.e., crack initiation and corresponding growth. Figure 4(b) shows the evolution of the crack length and corresponding DIC strains in the Mode I loading direction as a function of time. Distinctively, the strain field shows the crack tip

FIG. 4 (a) CT sample dimensions along with sensor and transmitter locations, and (b) DIC strain full fields for the loading direction at different time instances.

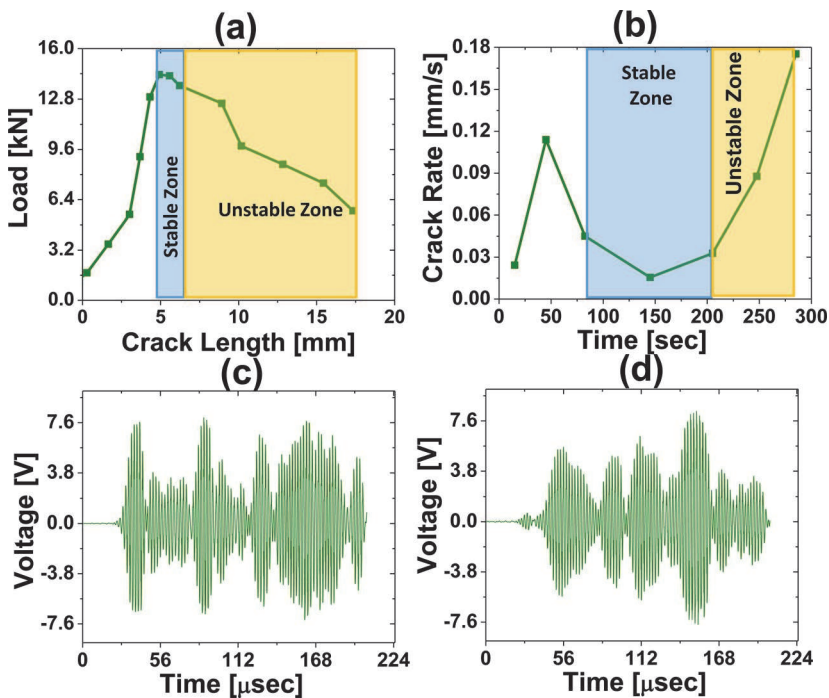


plasticity (kidney shape field) providing a location of fracture. In conjunction with these results, an acoustic technique established damage development and progress as the specimen was subjected to Mode I loading.

In addition to the DIC fields, crack length and growth rate values as a function of time were extracted, which served as a limiting parameter to identify stable and unstable crack growth, as is shown in Figs. 5(a) and 5(b). The acoustic techniques shown here were actively triggered to determine the damage state by comparison of the input and output signals. Figures 5(c) and 5(d) show two received signals and their variation as the crack grows within the stable and unstable zone. Therefore, the acoustic techniques quantify the volumetric effects and derive a description of the damage in conjunction with DIC full field data.

The hybrid NDE setup was also performed in a cyclic module to prove its reliability for complex loading conditions as well as complex mechanical behavior, which is the case for fiber reinforced composites. The multiscale failure mechanism processed in these types of composites results in damage being unready detected; thus three NDE techniques were utilized to monitor its behavior when subjected to

FIG. 5 (a) Load as a function of crack length and crack growth rate evolution depicting the stable and unstable zone. UT received transmitter waveforms for (c) no crack length and (d) an unstable crack length of 18.5 mm.



loading. The image acquisition was monitored and triggered by the acoustic techniques and recorded for each fatigue as shown in Fig. 6(b). The results from the full field strains and stresses provided elliptical shape hysteresis loops. These loops were characteristic of slope and area change (i.e., residual stiffness degradation and energy density dissipation), which are shown to be essential to determining damage stages in correlation with acoustic parameters. The full field DIC strain fields for a cycle at 99 % life fraction show localized accumulated strains and damage occurring to the surface (Fig. 6(d)). Similarly, the temperature change percentage fields depict hot spots at the fracture surface and suggest the progress of damage.

The correlation of extracted parameters of optical and acoustic techniques potentially show three fatigue life stages. The energy density dissipation and local Poisson’s ratio extracted from DIC contained three critical stages which agree upon the extracted AE cumulative energy and amplitude, respectively (Figs. 7(a) and 7(b)). The latter stage in the fatigue life of this composite shows sudden change in both mechanical and acoustic energy, which can notably be used for life remaining prediction; similarly, the local Poisson’s ratio and AE amplitude depict a comparable profile. This profile shows high amplitude emission and strain values at the beginning stage as it lowers toward the second stage, which results in sudden increases as the critical final stage is reached. The AE waveforms recorded for the second and third stage are shown in Fig. 7(c). It can be noted that the amplitude values are

FIG. 6 Polymer composite dimensions and AE sensor location. (b) Full cycle DIC image acquisition and AE triggered time delay. (c) Stress-strain hysteresis loops at different fatigue life (life fraction). Full field strain evolution at 99 % life fraction for marked stress levels in (c). Temperature percentage change fields at four levels of remaining life.

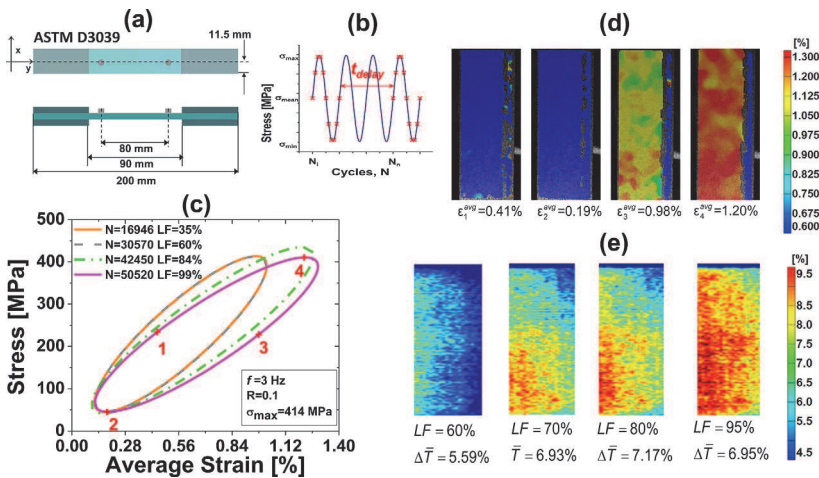
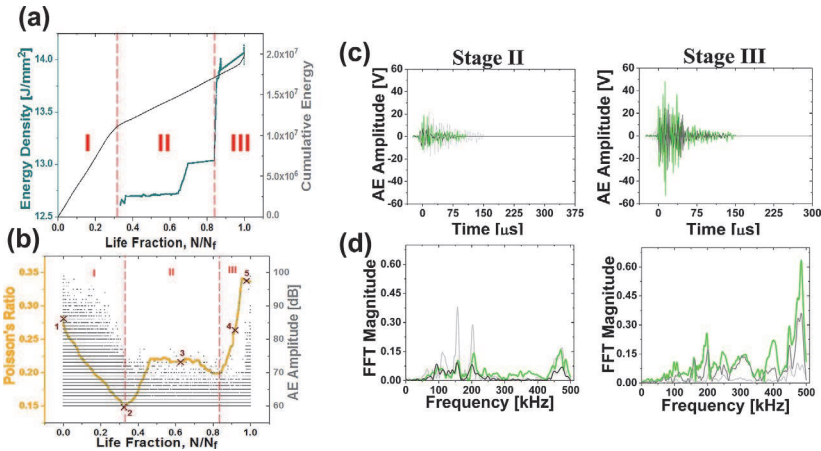


FIG. 7 (a) Energy density of hysteresis loop and AE cumulative energy as function for fatigue life. Full field averaged local Poisson's ratio at max stress level and AE amplitude evolution as life fraction increases. (c) AE waveforms with (d) corresponding frequency domain analysis for Stage II and III.



different and increase for the latter stage. In addition, these waveforms can be analyzed in the frequency domain by performing a fast Fourier transform analysis (Fig. 7(d)), which shows high frequencies at the critical third stage.

Conclusions

The integration of NDE techniques have proven to be essential for fully characterizing the failure mechanism, fracture, and occurring damage development for the three materials presented for three different loading conditions. NDE cross correlation of the independent inputs provided by separate methods allowed both the more effective interpretation of the material damage characteristics revealed by each NDE technique, while it further allowed effective cross validation, increasing the reliability of the monitoring strategy. This novel integrated NDE system demonstrated promising results that coincide in goals with SHM and other related applications, where the main intent is to detect, evaluate, and ultimately predict damage. Subsequently, it is of great importance to build a framework of damage parameters and detectors to reliably flag incipient damage on critical components and structures.

References

- [1] Bartoli, I., Salamone, S., Phillips, R., Lanza di Scalea, F., and Sikorsky, C. S., "Use of Interwire Ultrasonic Leakage to Quantify Loss of Prestress in Multiwire Tendons," *J. Eng. Mech.*, Vol. 137, No. 5, 2011, pp. 324–333.

- [2] Chandola, V., Banerjee, A., and Kumar, V., "Anomaly Detection: A Survey," *ACM Comput. Surv.*, Vol. 41, No. 15, 2009, pp. 1–58.
- [3] García-Martín, J., Gómez-Gil, J., and Vázquez-Sánchez, E., "Non-Destructive Techniques Based on Eddy Current Testing," *Sensors*, Vol. 11, No. 3, 2011, pp. 2525–2565.
- [4] Garnier, C., Pastor, M.-L., Eyma, F., and Lorrain, B., "The Detection of Aeronautical Defects In Situ on Composite Structures Using Non Destructive Testing," *Compos. Struct.*, Vol. 93, No. 5, 2011, pp. 1328–1336.
- [5] Kang, I., Shulz, M. J., Kim, J. H., and Shanov, V., "A Carbon Nanotube Strain Sensor for Structural Health Monitoring," *Smart Mater. Struct.*, Vol. 15, No. 3, 2006, pp. 737–748.
- [6] Sohn, H., Farrar, C. R., Hunter, N. F., and Worden, K., "Structural Health Monitoring Using Statistical Pattern Recognition Techniques," *J. Dyn. Syst., Meas. Control*, Vol. 123, No. 4, 2001, pp. 706–711.
- [7] Sohn, H., Farrar, C. R., Hunter, N. F., and Worden, K., "Structural Health Monitoring Using Statistical Pattern Recognition Techniques," *Trans. ASME J. Dyn. Syst., Meas. Control*, Vol. 123, No. 4, 2001, pp. 706–711.
- [8] Sultan, M. T. H., Worden, K., Pierce, S. G., Hickey, D., Staszewski, W. J., Dulieu-Barton, J. M., and Hodzic A., "On Impact Damage Detection and Quantification for CFRP Laminates Using Structural Response Data Only," *Mech. Syst. Signal Process.*, Vol. 25, No. 8, 2011, pp. 3135–3152.
- [9] Vanniamparambil, P. A., Bartoli, I., Hazeli, K., Cuadra, J., Schwartz, E., Saralaya, R., and Kontsos, A., "An Integrated Structural Health Monitoring Approach for Crack Growth Monitoring," *J. Intell. Mater. Syst. Struct.*, Vol. 23, No. 14, 2012, pp. 1563–1573.
- [10] Vanniamparambil, P. A., Khan, F., Hazeli, K., Cuadra, J., Schwartz, E., Kontsos, A., and Bartoli, I., "Novel Optico-Acoustic Nondestructive Testing for Wire Break Detection in Cables," *Struct. Control Health Monitor.*, Vol. 20, No. 11, 2013, pp. 1339–1350.
- [11] Worden, K., Manson, G., and Fieller, N. R. J., "Damage Detection Using Outlier Analysis," *J. Sound Vib.*, Vol. 229, No. 3, 2000, pp. 647–667.
- [12] Zhu, X. and Rizzo, P., "Guided Waves for the Health Monitoring of Sign Support Structures Under Varying Environmental Conditions," *Struct. Control Health Monitor.*, Vol. 20, No. 2, 2011, pp. 156–172.
- [13] Reis, P. N. B., Ferreira, J. A. M., and Richardson, M. O. W., "Fatigue Damage Characterization by NDT," *Appl. Compos. Mater.*, Vol. 18, No. 15, 2011, pp. 409–419.
- [14] Cuadra, J., Vanniamparambil, P. A., Hazeli, K., Bartoli, I., and Kontsos, A., "Damage Quantification in Polymer Composites Using a Hybrid NDT Approach," *Compos. Sci. Technol.*, Vol. 83, 2013, pp. 11–21.
- [15] Hazeli, K., Cuadra, J., Vanniamparambil, P. A., and Kontsos, A., "In Situ Identification of Twin-Related Bands Near Yielding in a Magnesium Alloy," *Scr. Mater.*, Vol. 68, No. 1, 2013, pp. 83–86.
- [16] Jiang, S.-F., Fu, C., and Zhang, C., "A Hybrid Data-Fusion System Using Modal Data and Probabilistic Neural Network for Damage Detection," *Adv. Eng. Softw.*, Vol. 42, No. 6, 2011, pp. 368–374.

- [17] Hazeli, K., Askari, H., Cuadra, J., Steller, F., Carpick, R. H., and Kontsos, A., "Microstructure-Sensitive Investigation of Magnesium Alloys Fatigue," *Int J. Plast.*, (under review).
- [18] Kontsos, A., Loutas, T., Kostopoulos, V., Hazeli, K., Anasori, B., and Barsoum, M. W., "Nanocrystalline Mg-MAX composites: Mechanical Behavior Characterization via Acoustic Emission Monitoring," *Acta Mater.*, Vol. 59, No. 14, 2011, pp. 5716–5727.
- [19] Rizzo, P., Sorrivi, E., Lanza di Scalea, F., and Viola, E., "Wavelet-Based Outlier Analysis for Guided Wave Structural Monitoring: Application to Multi-Wire Strands," *J. Sound Vib.*, Vol. 307, Nos. 1–2, 2007, pp. 52–68.
- [20] Vanniamparambil, P. A., Bolhassani, M., Carmi, R., Khan, F., Bartoli, I., Moon, F., Hamid, A., and Kontsos, A., "A Data Fusion Approach for Progressive Damage Quantification in Reinforced Concrete Masonry Walls," *Smart Mater. Struct.*, Vol. 23, No. 1, 2014, 015007.
- [21] Tyson, J., "Advanced Material Properties Measurements with Optical Metrology," *SAE Technical Paper 2011-01-0997*, SAE, Warrendale, PA, 2011.
- [22] Tyson, J., Psilopoulos, J., Schwartz, E., and Galanulis, K., "Optical Metrology, the Key to Lean Manufacturing," *SAE Technical Paper 2012-04-16*, SAE, Warrendale, PA, 2012.
- [23] Zhao, X., Wang, R., Gu, H., Song, G., and Mo, Y. L., "Hierarchical Ensemble-Based Data Fusion for Structural Health Monitoring," *Smart Mater. Struct.*, Vol. 19, 2010, pp. 1–7.
- [24] Jiang, S.-F., Zhang, C.-M., and Zhang, S., "Two-Stage Structural Damage Detection Using Fuzzy Neural Networks and Data Fusion Techniques," *Exp. Syst. Appl.*, Vol. 38, No. 1, 2011, pp. 511–519.
- [25] Markou Markos, S. S., "Novelty Detection: A Review—Part 1: Statistical Approaches," *Signal Process.*, Vol. 83, No. 12, 2003, pp. 2481–2497.
- [26] Markou Markos, S. S., "Novelty Detection: A Review—Part 2: Neural Network Based Approaches," *Signal Process.*, Vol. 83, No. 12, 2003, pp. 2499–2521.
- [27] Mustapha, F., Mason, G., Pierce, S. G., and Worden, K., "Structural Health Monitoring of an Annular Component Using a Statistical Approach," *Strain*, Vol. 41, No. 3, 2005, pp. 117–127.
- [28] Sharma, S., *Applied Multivariate Techniques*, Wiley, New York, 1996.
- [29] ASTM E9-09: Standard Test Methods of Compression Testing of Metallic Materials at Room Temperature, ASTM International, West Conshohocken, PA, 2009, www.astm.org.
- [30] ASTM E1820-06: Standard Test Method for Measurement of Fracture Toughness, ASTM International, West Conshohocken, PA, 2006, www.astm.org.
- [31] ASTM E647-08: Standard Test Method for Measurement of Fatigue Crack Growth Rates, ASTM International, West Conshohocken, PA, 2008, www.astm.org.
- [32] ASTM D3039/D3039M: Standard Test Method for Tensile Properties of Polymer Matrix Composite Materials, ASTM International, West Conshohocken, PA, 2008, www.astm.org.
- [33] ARAMIS, *ARAMIS User Manual—Software*, ARAMIS, Braunschweig, Germany, 2012.

- [34] AEwin, *AEwin SOFTWARE. Installation, Operation and User's Reference Manual*, AE, Princeton, NJ, 2004.
- [35] FLIR, *FLIR A325sc*, FLIR, Wilsonville, OR, 2013.
- [36] Fluke, *IR FlexCam Thermal Imagers—Users Manual*, Fluke, Everett, WA, 2009.

STP 1584, 2015 / available online at www.astm.org / doi: 10.1520/STP158420140053

James Sebastian,¹ William Boles,² and James Taylor³

Static and Dynamic Strain Measurement at Ambient and Elevated Temperatures Using an Extrinsic Fabry–Perot Interferometer (EFPI) Optical Strain Sensor

Reference

Sebastian, James, Boles, William, and Taylor, James, "Static and Dynamic Strain Measurement at Ambient and Elevated Temperatures Using an Extrinsic Fabry–Perot Interferometer (EFPI) Optical Strain Sensor," *Evaluation of Existing and New Sensor Technologies for Fatigue, Fracture and Mechanical Testing*, STP 1584, Jidong Kang, David Jablonski, and David Dudzinski, Eds., pp. 147–165, doi:10.1520/STP158420140053, ASTM International, West Conshohocken, PA 2015.⁴

ABSTRACT

Advances in the testing of high temperature materials for aerospace structures and propulsion components requires a thorough characterization of mechanical behavior under combined thermal, mechanical, and acoustic loading. The ability to stably measure static strain in such materials is a historically difficult challenge, especially in applications where an extensometer cannot be used. Recent research in the Aerospace Systems Directorate of the Air Force Research Laboratory is establishing a capability for the reliable measurement of mechanical strain at temperatures up to 650°C (1200°F) on metals and above 870°C (1600°F) on ceramic composite materials. Sensor testing on both coupons and structural components has been demonstrated. Quasi-static strain

Manuscript received May 29, 2014; accepted for publication February 4, 2015; published online March 12, 2015.

¹Univ. of Dayton Research Institute, Dayton, OH 45469, e-mail: james.sebastian@udri.udayton.edu

²Air Force Research Laboratory, Wright-Patterson AFB, OH 45433.

³Sierra Lobo, Fremont, OH 43420.

⁴ASTM Fourth Symposium on the *Evaluation of Existing and New Sensor Technologies for Fatigue, Fracture and Mechanical Testing* on May 7–8, 2014 in Toronto, Canada.

measurement was achieved without the metallurgical drift or high thermal sensitivity of commercially available resistive strain gages. In addition to static measurements, dynamic strain measurement at moderate strain rates was also achieved, as was static strain measurement in the presence of high level broadband acoustic excitation.

Keywords

high temperature strain, EFPI, fiber optic strain sensor, harsh environment strain

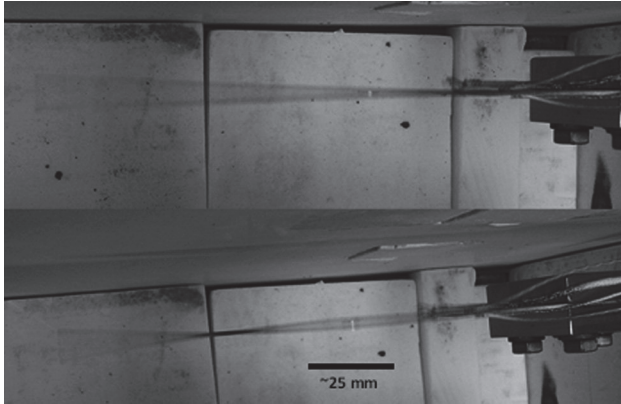
Introduction

Earlier work in harsh environment strain measurement had the goal of selecting the best sensor or combination of sensors to monitor strain in an aerospace structure exposed to turbine engine exhaust [1]. Sensors were intended to monitor static and dynamic strain on both titanium (Ti-6-4) and superalloy (ALLOY 625) structures, and would be subjected to strain from thermal excursions, as well as vibratory and acoustic loading. Expected worst-case conditions include 650°C (1200°F) temperature, acoustic excitation up to 165 dB causing 128 $\mu\epsilon$ RMS, and 14 000 $\mu\epsilon$ (1.4 %) static thermal and mechanical strain. Sensors were desired to have a useful life of at least 6 h, while maintaining a strain uncertainty of less than ± 20 % of the strain reading (± 10 % preferred). The goal was to determine what sensors would economically provide the desired data for future planned test programs.

Four strain gage technologies were initially selected for evaluation. The first was a free-filament gage consisting of a metallic alloy wire grid applied to the test article by thermal spray. The second technology was an encapsulated sensor, internally compensated for temperature, on a shim spot-welded to the test article. The third, more developmental technology, was a direct-write gage, applied by depositing an insulating layer on the test article, followed by a resistive alloy active grid and interface wires. The final technology was not a resistive technique; rather, it consisted of an extrinsic Fabry–Perot interferometer (EFPI). Gold-clad quartz optical fibers were adhered to the test object such that the gap width between an active fiber and a stationary fiber changed with strain and served as the EFPI cavity. For each technology, gage accuracy and survival were evaluated through a combination of thermal, mechanical, and acoustic testing designed to simulate several flight cycles of an exhaust-washed aerospace structure, one instance of which is shown in Fig. 1. Most of these gages showed good promise for acquiring dynamic strain data and commercial free-filament gages were selected for dynamic measurement, with some technique development required for survivability in the harsh environment.

Measuring static strain as a combination of thermal and mechanical strain at high temperatures was a more significant challenge. Gages using an FeCrAl or similar alloy all showed non-repeatable deviation in the 430°C–540°C (800°F–1000°F) range, most likely due to a phase change in the alloy. This effect has long been [2], but is downplayed in specifications and marketing materials. The

FIG. 1 First and second mode bending of a cantilever beam excited at resonance by a shaker, producing approximately $500 \mu\epsilon$ p-p at the gages at temperatures up to 650°C (1200°F).



unpredictable strain offsets that resulted led to a decision that such gages were unlikely to produce the desired static strain data. Gages using platinum alloy had a different problem: a large thermal response. Even with tungsten added to the alloy to decrease the thermal response, sensitivity on the order of $33 \mu\epsilon$ of strain per $^\circ\text{C}$ was seen, resulting in apparent strains of over $50\,000 \mu\epsilon$ (5 % strain). Efforts to thermally compensate this response found that variability between gages was substantial, leading to the conclusion that each gage would have to be individually thermally calibrated to produce useful data. In addition, gages underwent an aging effect causing some drift in output with time at temperature. The non-resistive candidate, EFPI optical technology, was therefore found to be the best candidate for the static strain requirement, although further development was needed. While the fragile optical fibers were expected to have durability issues, testing showed that handling the gages was a much bigger problem, with properly installed fiber-optic gages surviving thermal, vibratory, and acoustic excitation. Other developmental work has been more complex than originally intended, especially with regard to signal conditioning instrumentation; however, the preliminary results presented below indicate that a solution is near at hand. Secondary advantages of the optical sensors include immunity from electromagnetic interference and the ability to run long leads with very little signal degradation.

EFPI Operation

A Fabry-Perot interferometer is created when two reflections of an optical signal are returned along an optical fiber and interfere at a detector. In an extrinsic architecture, the signal leaves the input optical fiber and travels through a gap to a

FIG. 2 Basic EFPI architecture, including input fiber (1) and reflector (2) secured to a surface at attachment points (3) and a gap between the cleaved fiber ends.



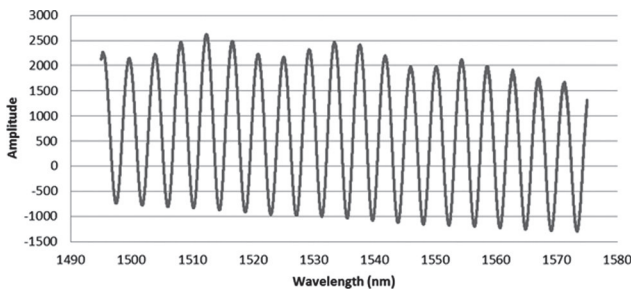
reflector. The first signal is returned by the end of the input fiber at the gap and the second is reflected back into the input fiber after twice traversing the gap, which is filled with vacuum or another medium. Unlike a single-wavelength device, such as a Michelson interferometer, the EFPI uses a broadband or frequency-scanned laser source and the interference pattern shows a regular variation of intensity as a function of wavelength, rather than distance or time at the detector. The interference pattern changes as a function of gap width, which is changed by temperature, pressure, strain, or another quantity desired to be measured. For strain measurement, the input fiber and reflector are secured to the test object and surface strain changes the distance between the attachment points and; therefore, the gap width. **Figure 2** shows a schematic of the EFPI configuration.

A typical interference pattern from an EFPI gap interrogated with a modern scanned laser source looks like the one in **Fig. 3**, with light intensity on the y -axis and wavelength on the x -axis. While this appears to be a sine curve, with some offset and amplitude variation with wavelength, the intensity of an ideal EFPI interference pattern is actually described by [3]

$$(1) \quad I(\lambda, d) = 1 + |\eta| \cos[4\pi d/\lambda + \pi - \theta(d)]$$

where intensity is a function of both wavelength (λ) and the sensor gap (d), with η defining a scale factor. Ignoring the offset and the phase term $[\pi - \theta(d)]$, which is

FIG. 3 EFPI interference spectrum, spanning roughly 70 nm.



constant at a given gap, intensity then becomes proportional to $\cos(4\pi d/\lambda)$, showing that the pattern at a given gap width is actually a swept sine wave with frequency decreasing slightly as wavelength increases. The interference pattern is unique for a given gap, but irregularities tend to cause uncertainty in evaluating the gap based on patterns which are similar to one another. A number of methods were developed to determine EFPI gap as described below [3]. One advantage to the EFPI is that errors tend to be large or do not occur at all; no data will be reported if no interference pattern is found.

PEAK TRACKING METHOD

For small gap changes, the fringes shift only slightly and the change in gap is proportional to the shift in wavelength of a given local maxima (peak) in the fringe pattern, according to

$$(2) \quad |\Delta d/d| = |\Delta\lambda_m/\lambda_m|$$

Rearranging, change in gap is thus a function of the original gap (d_0), the amount a wavelength peak moves ($\Delta\lambda$), and the original wavelength of the peak (λ_0), according to

$$(3) \quad \Delta d = (d_0 \times \Delta\lambda)/\lambda_0$$

This method works accurately for large changes as well as small ones and valleys as well as peaks. However, it cannot establish an absolute gap; only changes in a gap originally measured another way. In addition, the data rate must be sufficient to maintain tracking of the moving peak without confusion with adjacent peaks. Tracking multiple peaks, reorienting as they leave the interrogator wavelength window, and checking for dropped peaks with each data cycle make the tracking method useful, as it provides high sensitivity with low noise. Practically implemented, this method works well as long as the strain rate is not too high, including any anomalies or sudden events. It should, thus, not be relied upon as the only method of signal processing for EFPIs for strain measurement.

ADJACENT PEAK METHOD

In contrast to peak tracking, the adjacent peak method does provide an absolute gap measurement unique to a set of fringes. It operates according to

$$(4) \quad d = \lambda_1\lambda_2/2(\lambda_1 - \lambda_2)$$

where gap (d) is a function of the wavelengths of two adjacent peaks (λ_1 and λ_2). Unfortunately, implementing this method with a real fringe pattern leads to high uncertainties, as λ is near 1550 nm, so Eq 4 is essentially a large number divided by a small number, with uncertainties in the individual peak wavelengths having a disproportionate effect on the overall uncertainty due to their being implemented as a difference in the denominator. Still, this method is useful and gap uncertainty

manifested as noise in the strain signal can be reduced by averaging multiple pairs of peaks, and through averaging data in time if possible. A high data rate instrument facilitates averaging.

FULL-SPECTRUM METHODS

The above methods rely only on determining the wavelength of the peaks (or valleys) of the interference pattern in Eq 1. However, if the full spectrum is available, other methods can be implemented to take advantage of the additional data. These are based on sinusoidal curve-fitting algorithms or a Fourier transform of the data. The data rate from these methods is generally slower due to the large amount of data required to define the full interference spectrum. The instrument used in this work provided only the peak wavelengths to the user, so full-spectrum methods were not used. Note, however, that peak detection algorithms generally fit to multiple points in the peak region and, therefore, the peak data contains a significant % of the full spectrum information.

Gage Construction

In earlier work, EFPI strain sensors were installed on components using a three-pad method [4]. The input fiber and the reflector (a second cleaved fiber) are inserted into a closely fitted, but free-running, quartz capillary tube that locates and aligns the faces. The two fibers are attached to the test article along with the capillary tube with the desired starting gap between the fiber ends. For high temperature use, ceramic adhesive or flame-spray attachment is used. The gage length used in strain calculations is a function of the distance between the attachment pads; the equation

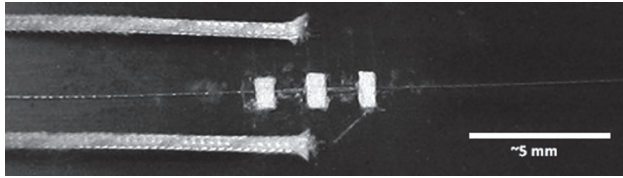
$$(5) \quad \text{Gage Length} = (2 \times IL + OL)/3$$

was historically used to account for minor disbonding at the edge of the adhesive, where IL is the distance between the inner edges of the adhesive and OL is the distance between the outer edges. Equation 5 seems to be somewhat installation-specific; for instance, the effect of the outer length measurement would be expected to decrease as the pad width increases for a given inner length.

Figure 4 shows an example of this gage construction, flanked by two thermocouples.

Several changes and improvements were tested as development progressed. One change is to reduce the number of attachment points from three to two by fusing the reflector fiber to the capillary tube. This simplifies installation and reduces errors during installation. The gage length is then taken to be IL , plus a constant that depends on the adhesive and the base material. The details of determining gage length are still being worked out; as Fig. 5 shows, definitively determining IL from a microscope image can be challenging. Another advantage of this gage design is that the gap is visible when installed, rather than hidden

FIG. 4 Three-pad EFPI strain sensor.



For installation on metal specimens, a “hardened” EFPI architecture has evolved that better protects the fragile optical fibers from accidental damage. These gages nominally consist of an input fiber, metallic reflector, and a metal cover that both protects that gage and transfers strain from the article to the gage. The reflector can now be welded to the cover and then the gage is inverted and spot-welded to the test article. The gage is further protected by running the input fiber through a metal tube in the hot zone and transitioning it to standard sheathed optical fiber. This gage architecture, shown in [Figs. 6](#) and [7](#), also greatly simplifies installation on large test articles and structures. The metal reflector tends to result in higher contrast interference fringes because it reflects or scatters all incident light, compared to the $\sim 6\%$ reflection from a cleaved quartz surface. Further improvements in hardened gages are ongoing, once again including definitive gage length determination.

EFPI Instrumentation

Instrumentation for obtaining strain data from the EFPI gages created an unexpected challenge. Initial testing was performed with fiber and instruments

FIG. 5 Two-pad EFPI installation on ceramic composite material. The end of this tube and fiber are distorted at the fusion splice to the right.

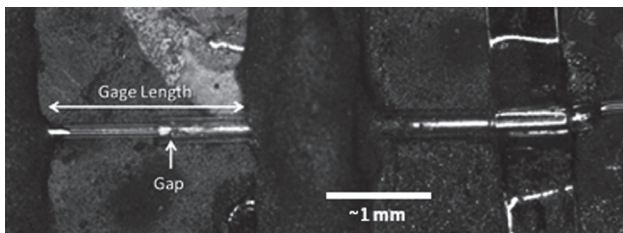
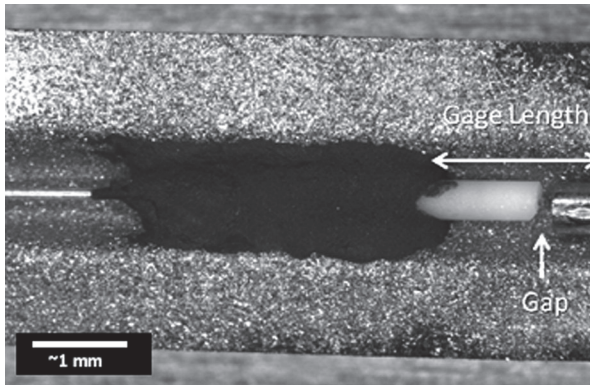
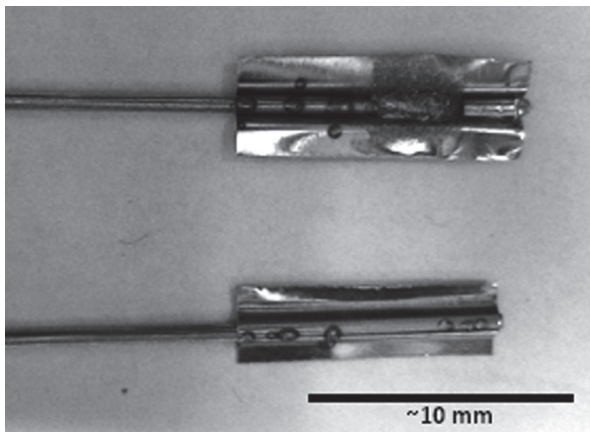


FIG. 6 Internal structure of prototype hardened gage.



from earlier work at the Air Force Research Laboratory (AFRL) [5]. The gages were constructed with $125\ \mu\text{m}$ -diameter, single-mode quartz optical fiber that was gold-clad for environmental protection. FiberPro and Fiberscan 2000 instruments from Luna Technologies were used for setting up the gages and acquiring data. Upon deciding to pursue the EFPI sensors, inquiries were made regarding the price and availability of fiber and additional instrumentation channels. News was bad on both fronts. First, the existing equipment operated at an 830 nm design wavelength; telecommunications (and thus the rest of the optical fiber world) had since moved to

FIG. 7 Hardened gages showing input tube, adhesive, reflector, and sheath.

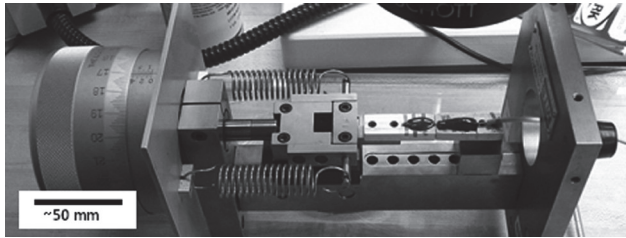


1550 nm products. Optical fiber designed for use at 830 nm could be had, but the quartz fiber needed for high-temperature operation would be prohibitively expensive as a special order. In addition, the instrumentation was no longer in production and was essentially unsupportable due to component obsolescence, meaning no additional channels could be purchased and the ten existing measurement channels could give out at any time.

Quartz optical fiber for 1550 nm is readily available and the decision then became what instrumentation to use with it. No suitable commercial instrumentation for EFPI sensors was located. While such sensors are not uncommon, they are more commonly used to measure temperature or pressure rather than strain [6], especially the large thermal strains expected during hot structure tests. Luna Innovations offered a beta version of a new product, the SPS5000, which met the requirements; this two-channel instrument was purchased along with multiplexer hardware capable of expanding it to 16 channels at a slower rate. As a beta unit, the SPS5000 required some upgrades before becoming truly useful, but now can be used in two modes, both of which support up to two channels at ~ 10 Hz or sixteen channels at ~ 1 Hz using two Luna FOS008 optical switches. Data can be streamed in real time to external data acquisition using the Modbus protocol over TCP/IP. Tracking mode provides a good signal, but can *only* be used for slow rate tests with no sudden events, including accidental events; as noted above, it looks at differences between the signal acquisitions and can only follow the signal when these differences are small. Absolute with correction (AWC) mode can recover from rapid transitions because it calculates the strain independently for each point but exhibits half-wavelength jumps in the data; these can be post-processed out of saved test data, but this mode is less desirable for real-time monitoring of a signal during a test. Analog output signals are available for two channels. The low data rate of the SPS5000 precludes its use when substantial dynamic strain is superimposed on the desired static strain measurement.

With the need to measure mean static strain in the presence of dynamic strains and the desire for data not requiring post-processing, the earlier search for appropriate instrumentation was resumed. Again, no candidate EFPI instruments were located, but we found a potential in using an instrument designed for Fiber-Bragg optical sensors. Data from such an instrument, produced first at the manufacturer and then in-house at AFRL, was evaluated and found to be promising. AFRL has now acquired several sm130 Optical Sensing Interrogators (Micron Optics, Inc.) and is developing the necessary software to use them to produce strain data in real time from the EFPI sensors. The sm130 evaluates the EFPI signal for the peak wavelengths of the interference fringe pattern at a rate of 1 kHz for four channels and this raw data is processed by in-house software into a strain reading. Both tracking and absolute modes were implemented and are undergoing refinement, along with the EFPI sensors. A multiplexer can be used to change to 8 channels at 500 Hz or 16 channels at 250 Hz.

FIG. 8 Extensometer calibrator used to apply precise gap changes to an EFPI sensor for testing.



Test Data and Discussion

A selection of data collected from various EFPI strain sensors is presented to give an idea of the capabilities of the sensors.

GAP MEASUREMENT

The optical gap length is the fundamental output from an EFPI sensor, regardless of the physical quantity being measured. While initial testing was performed with a variety of strain sensors and substrates, results were difficult to interpret with certainty due to uncertainties in gage length and system physical response. A fundamental experiment to examine gap measurement was designed using an MTS Model 650.03 extensometer calibrator. A reflector was attached to the moving slide of the calibrator and an input optical fiber was similarly attached to the stationary portion of the calibrator, forming an EFPI sensor. The calibrator was then used to adjust the gap while the sensor was monitored. [Figure 8](#) shows the EFPI on the calibrator. The gap changes applied by the calibrator were large relative to the gap changes occurring in real sensors, but this gave an opportunity to evaluate performance over a wide range and to investigate optimal sensor configurations. Test data gathered using both available instruments confirmed accurate measurement by the absolute mode of both systems and is shown in [Figs. 9](#) and [10](#). A slight difference in absolute gap measurement and slope between the two systems may have been the result of the different signal processing performed by each, but both fell well within 1 % of the calibrator displacement.

The calibrator motion was too unsteady for tracking mode signal conditioning to follow reliably, so a different experiment was devised to verify tracking mode functionality on the calibrator. The sensor in [Fig. 8](#) is mounted to aluminum pieces having a significant thermal expansion coefficient. A heat gun was used to expand these pieces, narrowing the gap, and then fan-cooled to reverse the effect. The gap

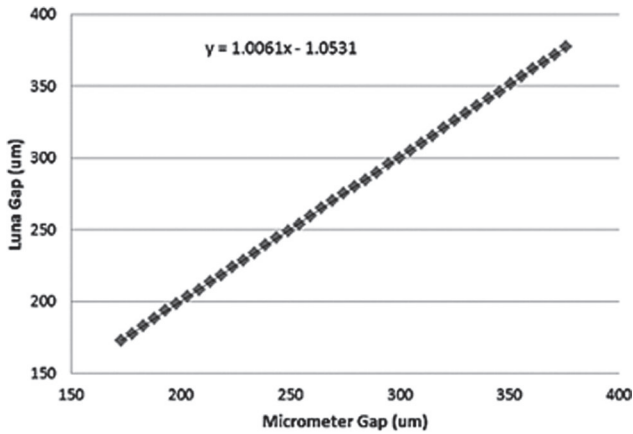
FIG. 9 Calibrator gap correlation using SPS5000.

Fig. 11. These curves clearly show the differences in the behavior of the two modes: tracking mode is much smoother, with more noise visible on the absolute mode data. As the sensor cooled, both traces converged to the same level, where they were zeroed initially prior to heating the fixture. A small ($\sim 4\%$) discrepancy in magnitude between the tracking and absolute modes is present and continued work is intended to reduce this error, which seems to occur only in sensors with higher amplitude metal reflectors.

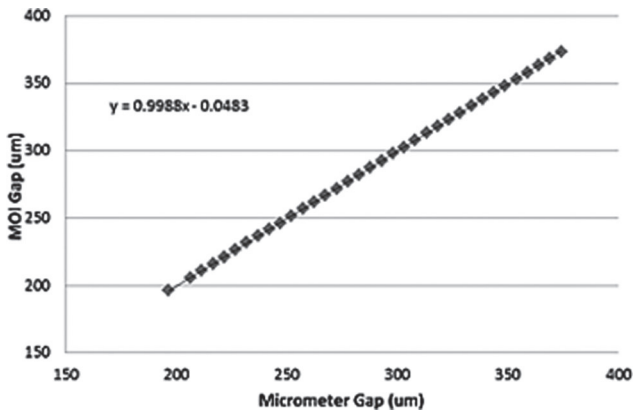
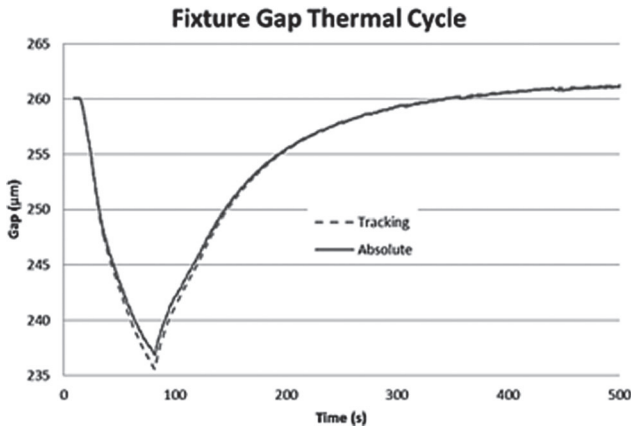
FIG. 10 Calibrator gap correlation using sm130.

FIG. 11 Multimode monitoring of gap during cooling.



THERMAL CYCLES

EFPI strain sensors were used to monitor thermal strains on several materials. Figure 12 shows the response from both signal processing modes during thermal cycling of a ceramic composite structural element from room temperature to 680°C (1250°F) and back. Note that the discrepancy above was corrected and there is very good agreement between the tracking and absolute mode data, and that the strain data follows the temperature profile very well. Reported strain values were close to

FIG. 12 Strain data during ceramic composite thermal cycle.

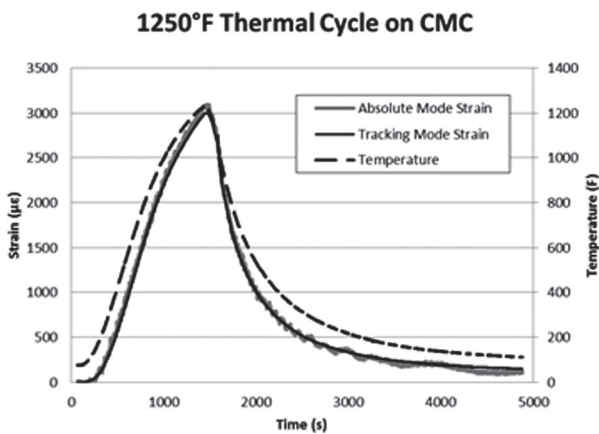
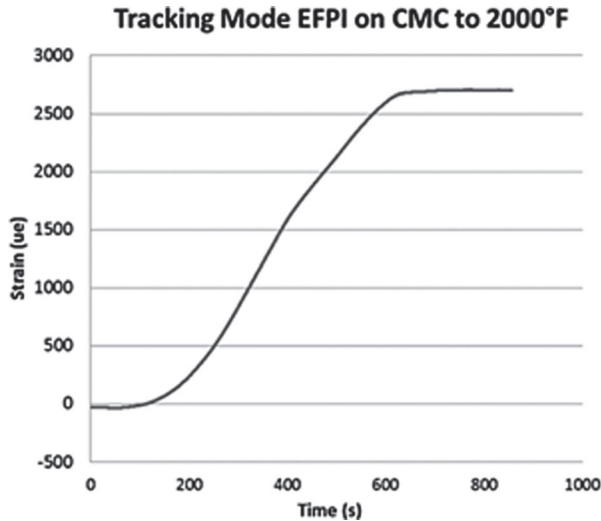


FIG. 13 Thermal strain during temperature ramp and hold. The sensor failed at the end of the displayed data, but survived long enough to demonstrate usability above the nominal 870°C (1600°F) limit for short times.



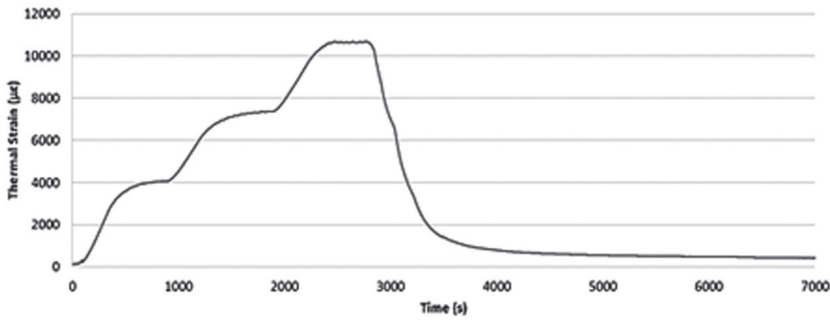
those expected for the material. A different ceramic composite was used to test the true thermal capabilities of the quartz EFPI sensors, which have a nominal limit of 870°C (1600°F). Above this temperature, dopant atoms begin to diffuse between the optical fiber core and cladding creating a graded index of refraction, rather than the sharp boundary needed for total internal reflection in the single-mode fiber. Because diffusion is not instantaneous, it was found that sensor data could be collected at or above 1090°C (2000°F) for a brief period, as shown in Fig. 13.

Similar results were obtained with hardened gages on metal samples. Figure 14 shows the output from a hardened EFPI on an INCONEL 625 sample as it was stepped from room temperature to 260, 480, and 650°C (500, 900, 1200°F), and allowed to cool. While, in this case, the data could easily be obtained with an extensometer, having a gage on the surface of the sample raises many additional possibilities for strain measurement on structures rather than coupons, and in the presence of vibration.

MECHANICAL LOADING

In addition to thermal strains, harsh environment structures are required to carry loads. This results in mechanical strain. Measuring the mechanical strain is critical to understanding the state of stress at the surface of the component, generally one of the end goals of strain measurement. The EFPI strain sensors have been tested

FIG. 14 Thermal strain on INCONEL beam reported by EFPI sensor and interrogator.



on both ceramic-composite materials and metals at high temperatures. Figure 15 shows a strain trace at 680°C (1250°F) on a ceramic matrix composite (CMC) structural sub-element. The near-zero response for approximately the first 0.45 kN (100 lb) of load was a result of the test article settling into the loading fixture. After this point, increasing loads translate into increasing strain at the measurement location, until a portion of the article fails just below 2.67 kN (600 lb), reducing the stiffness at the gage and leading to an increasing strain rate. A substantial difference is seen between the two strain modes, differing by about 15 %; this was attributed to a software error that has since been corrected, with the absolute mode data found to be correct. This data is from an actual component test, rather than a test contrived for EFPI evaluation.

For mechanical strain on a metal beam with a hardened sensor, testing has been performed strictly for sensor evaluation. Figure 16 shows a loading cycle to

FIG. 15 Mechanical strain in CMC component.

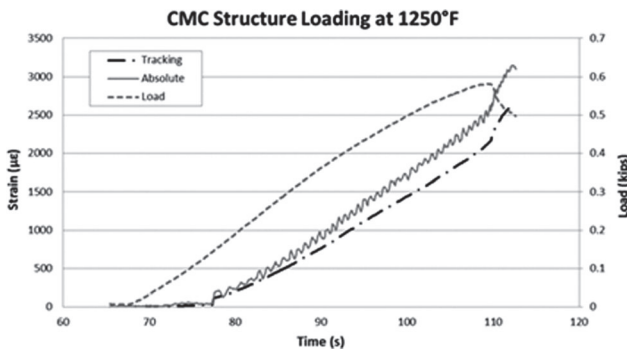
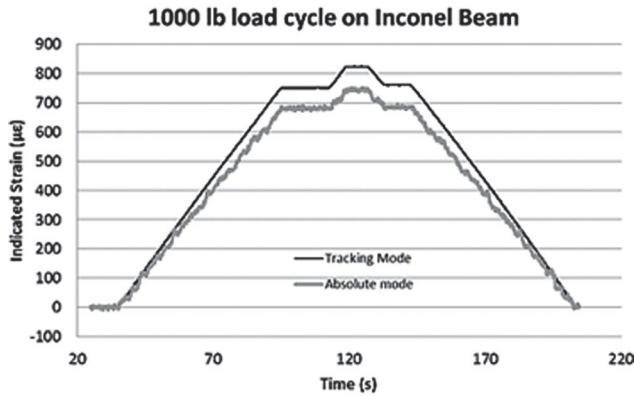


FIG. 16 Mechanical strain on metal beam.



117 MPa (17 ksi) on an INCONEL specimen at room temperature. Once again, there is a difference between the two modes of peak evaluation, which persisted even after the correction noted above. The absolute mode appears to underreport strain with the current hardened gage design for both thermal and mechanical strains. This is logical, since the reported peaks are a function only of EFPI gap, regardless of how the gap is changed. This particular gage was tested extensively and had begun to develop a small amount of hysteresis, evidenced in the slight difference in the starting and ending levels of the minor load cycle at the top of the waveform. Uncertainty in the effective gage length makes it difficult to report strain accuracy for these tests, but fundamentally, the sensor is reporting strain, with the exact calibration yet to be determined. The beam in these tests saw about 575 $\mu\epsilon$, while the values reported by the EFPI were substantially higher.

ACOUSTIC LOADING

The final piece of the measurement puzzle is measurement of strain in the presence of vibration and acoustic excitation. Testing with real-time signal conditioning is underway, with preliminary data presented here showing the basis for how strain measurement will be achieved. The behavior of individual peaks in the interference spectrum determine feasibility and Fig. 17 shows the wavelength reported for two of these peaks during 146 dB acoustic excitation in the 50–500 Hz band. With data collected at 1000 Hz, it was encouraging to see what looks like noise, but is actually a waveform that looks very much like a trace of surface displacement near the gage, acquired with a laser vibrometer. It may therefore be possible to measure dynamic as well as static strains with the EFPI gages within limited frequencies and levels of dynamic strain. However, current needs for dynamic strain measurement are being met by free-filament wire strain gages and the EFPI focus is on static strain measurement.

FIG. 17 EFPI peak motion at 146 dB acoustic excitation.

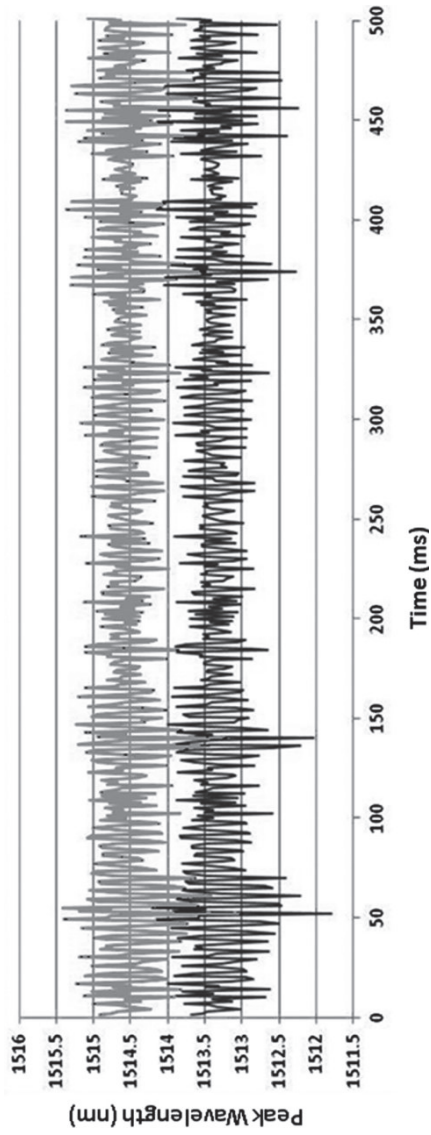
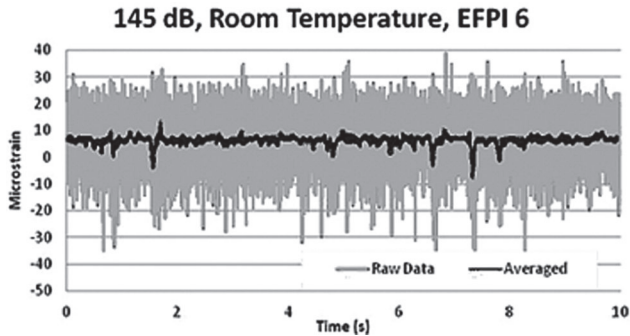
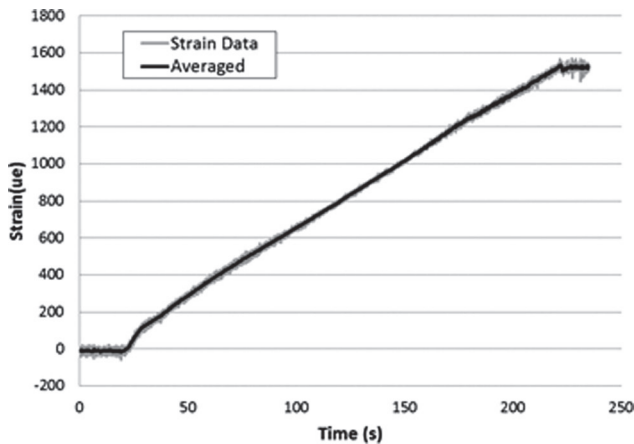


FIG. 18 Strain derived from peak wavelength data during acoustic excitation.



Evaluating over a longer time span, Fig. 18 shows the fringe peaks signals processed into gap and then strain, and the effects of time averaging. This data shows that the data converges, rather than the sensor being completely overwhelmed by the rapidly changing peak wavelengths. Equally important, it provides a stable value without random drift or jumps to different levels. The panel, in this case, was excited acoustically only, so the strain correctly stays near zero. A similar behavior was observed at substantially higher vibration levels, 152 dB. Finally, Fig. 19 shows a longer time span, during which thermal strain was monitored as the panel is heated to 260°C (500°F) during acoustic excitation at 146.5 dB. Both raw data and the

FIG. 19 EFPI strain during thermal ramp combined with acoustic excitation.



results of applying a moving average are shown. The measured strain followed the linear temperature ramp, including the small nonlinearities at the top and bottom of the ramp. Although not reflected in the EFPI data, the panel vibrations were greatest at room temperature and decreased as the panel stiffened in its mounting fixture with increasing temperature. A similar test with earlier instrumentation could not produce data below $\sim 100^{\circ}\text{C}$, as it became overwhelmed by the vibration levels.

Conclusions

In order to fulfill a need for the measurement of static strain on test articles subjected to high temperatures, vibration, and acoustic evaluation, EFPI sensors were chosen as the most promising of several candidate technologies. The existing state-of-the-art EFPI sensors have been improved for increased durability and tested on metal and ceramic-composite materials. Concurrently, signal conditioning instrumentation and software have been developed for reliable measurement at increased data rates. Work continues to improve the gages and signal conditioning with respect to accuracy, repeatability, and reliable calibration and measurement. The demonstration of static strain measurement on complex geometries at temperatures in excess of 650°C (1200°F) will provide a needed measurement capability.

ACKNOWLEDGMENTS

This work was sponsored by the United States Air Force Research Laboratory, AFRL/RQVV, Prime Contract #GS05T10BMC0014, Subcontract SLI-2013-01-009. The support of the United States Air Force and on-site personnel from Sierra Lobo and Booz Allen is gratefully acknowledged. DISTRIBUTION STATEMENT A: Approved for public release; distribution is unlimited, Case RQ-14-262, PA# 88ABW-2014-1943.

References

- [1] Sebastian, J., Boles, W., and Hauber, B., "Strain Sensor Performance at Elevated Temperatures," presented at the *ASTM E08 Workshop on New Sensor Technologies and Issues With Existing Sensor Technologies for Fatigue, Fracture, and Mechanical Testing*, Tampa, FL, Nov 16, 2011, ASTM International, West Conshohocken, PA, -unpublished.
- [2] Lemcoe, M. M., "Performance of High Temperature ($>1100\text{F}$) Strain Gages and Alloys," presented at the *SEM X International Congress & Exposition on Experimental & Applied Mechanics*, June 7-10, 2004, SEM, Bethel, CT, -unpublished.
- [3] Han, M., 2006, "Theoretical and Experimental Study of Low-Finesse Extrinsic Fabry-Perot Interferometric Fiber Optic Sensors," Ph.D. thesis, Virginia Tech, Blacksburg, VA.
- [4] Piazza, A., Hudson, L. D., and Richards, W. L., "Development and Ground-Test Validation of Fiber Optic Sensor Attachment Techniques for Hot Structures Applications,"

presented at the *SensorsGov Expo and Conference*, Hampton, VA, Dec 6–8, 2005, NASA Dryden Flight Research Center, Edwards, CA, -unpublished.

- [5] Banaszak, D. and Kretz, L., “Lab Evaluation of Fiber Optic EFPI Sensors for Extreme Environmental Tests,” Presented at the *JSM 2005*, Minneapolis, MN, Aug 7–11, 2005, American Statistical Association, Alexandria, VA, -unpublished.
- [6] Pinet, É., “Fabry–Pérot Fiber-Optic Sensors for Physical Parameters Measurement in Challenging Conditions,” *Journal of Sensors*, Vol. 2009, Article ID 720980, 9 pages, 2009.

SENSORS FOR ELEVATED TEMPERATURE APPLICATIONS

STP 1584, 2015 / available online at www.astm.org / doi: 10.1520/STP158420140049

P. B. S. Bailey¹

Use of IR Temperature Measurement and Thermography for Control and Monitoring of Fatigue Tests

Reference

Bailey, P. B. S., "Use of IR Temperature Measurement and Thermography for Control and Monitoring of Fatigue Tests," *Evaluation of Existing and New Sensor Technologies for Fatigue, Fracture and Mechanical Testing*, STP 1584, Jidong Kang, David Jablonski, and David Dudzinski, Eds., pp. 169–185, doi:10.1520/STP158420140049, ASTM International, West Conshohocken, PA 2015.²

ABSTRACT

A case study is presented on the practical application of infrared thermography during fatigue testing in the measurement of specimen temperature fluctuations during fatigue of polymer matrix composites. It is demonstrated that such measurements can also be integrated with an outer loop test control, modulating frequency to maintain more consistent specimen conditions throughout the test, and to optimise test speed. Due to the high temperature sensitivity and high specimen variability of structural composites, this approach can simultaneously improve both consistency and time-efficiency in the generation of fatigue-life data for this commercially important family of materials.

Keywords

composite, fatigue, temperature

Manuscript received April 30, 2014; accepted for publication January 29, 2015; published online February 19, 2015.

¹Instron Materials Testing, Instron (A Division of ITW Limited), Coronation Road, High Wycombe, Buckinghamshire, HP12 3SY, UK.

²ASTM Fourth Symposium on the *Evaluation of Existing and New Sensor Technologies for Fatigue, Fracture and Mechanical Testing* on May 7–8, 2014 in Toronto, Canada.

Introduction

Fatigue testing of composite materials has risen rapidly in commercial importance in the space of a little over 5 years, led most noticeably by the wind energy industry. As the adoption of composites has become established in this and now various industries, they are seeking to move from extremely conservative design practices to ever more accurately optimized methods. And while these practices enabled them to bring composite materials into their products quickly, they often failed to take into account factors which present major advantages or savings, but also factors which present significant risk. As we move into an age of composite materials for high strain, long service, and safety critical applications, there is now a commercial need for composites “fatigue” tests (among other methods) to understand and qualify materials in more representative ways.

Extant standards [1,2] are thorough, but not highly prescriptive, embodying conservative recommendations for test frequencies, but a generous ceiling limit on specimen temperature fluctuation. Working at a cyclic loading frequency below 5 Hz results in lengthy tests, during which specimen temperatures can still rise by as much as 20°C. To the laboratory manager, such time is undesirable; to the material scientist, such temperature variation is highly questionable. While any testing standard should be representative, useful, and practically achievable, it is of some concern that more demanding specifications have not yet been placed upon the recording of temperature during fatigue testing of composites.

The purpose of this paper was to assert the importance of measuring temperature appropriately during fatigue testing of composites, and to show the feasibility, benefits, and potential application of non-contact measurement technologies that use the infrared emission from the specimen.

Background

ISSUES OF HEAT GENERATION IN COMPOSITES

It is well-known that the mechanical performance of composites can be affected by test speed, although not all are familiar with the reasons behind this. Ultimately, the reason for the very low strain rates used for pseudo-static testing is to maintain conditions which are as close as possible to isothermal, the importance of which can be condensed into two primary points. The first point is that all processes of deformation and “damage” in polymer matrix composites significantly affect the temperature of the materials, and since the thermal conductivity is relatively low (compared with most metals), localised “hot-spots” dissipate only slowly. Second, the mechanical performance of organic polymers (and therefore composites in which they form the matrix) is significantly temperature sensitive; more so than any other family of materials.

This concern is then exacerbated when we consider a dynamic test, especially

specimen with each cycle of loading and unloading. This paper does not seek to describe or establish in detail the specific nature of this heating effect, but it is reasonable to propose that at any point during a test, there will be a combination of viscous heating through shear of the polymer, and of microscopic fracture and release of strain energy. As already mentioned, the practical outcome of this is that to conduct a high cycle fatigue test at any reasonable test frequency, the specimen will generate a significant amount of heat internally.

Variation Between Specimens

On any particular specimen, the average degree of heating with each cycle will increase with increasing amplitude of the applied load, meaning that when building an S-N curve (Wohler curve) average specimen temperature will increase with applied stress level.

Specimen temperature also fluctuates during the course of a test. The two-stage model of fatigue damage in composites [3] proposes that damage accumulates more rapidly within a composite as the material nears the end of its fatigue life. This certainly agrees with the fact that the rate of heat generation within the specimen often increases towards the end of the test [4].

Furthermore, even the most sophisticated manufacturing methods still result in a significant degree of inherent variability that affects performance at coupon level tests; of particular interest here is the fact that it can also change the rate of heat generation during cyclic loading.

Effects on Mechanical Performance

Many workers in composites research and testing have some awareness or familiarity with the long-established technique of dynamic mechanical thermal analysis, and therefore with the fact that strain rate can affect the apparent stiffness of a material quite radically when it is near its glass transition temperature. Modulus typically drops by between 1 and 3 orders of magnitude between the low elastic (glassy) and high elastic (rubber) states, but the viscoelastic effect is so significant that a major change in strain rate can push the behaviour from one state to the other. However, the operating temperature range is specified well below the onset of glass transition viscoelasticity for a majority of structural composites. This means that moderate variation in strain rate has only a small effect on mechanical behaviour under the majority of intended test conditions. By contrast, the rate of change in elastic modulus with temperature is usually quite significant even well within the glassy region, so a few degrees of variation in test temperature may make a readily measurable difference to its mechanical performance during each individual cycle.

There is some debate, but a number of experimental workers assert strongly that increasing specimen temperature generally decreases fatigue life in structural composites. Regardless of the underlying physics behind these observations, the implication of this would be that temperature variation between specimens will cause increased scatter in fatigue life.

TEMPERATURE PROFILES WITHIN SPECIMENS

Before discussing temperature measurement using infrared emission and contact thermometry, it is necessary to acknowledge the inherent problem of surface temperature measurement. The heating effects discussed above occur throughout the loaded parts of a specimen, but heat is only lost or extracted from the surfaces. This means that there will always be a temperature gradient through the thickness of the specimen; the nature of this gradient will be determined by a combination of factors including the conductivity of matrix and reinforcement, the volume fraction and directionality of the reinforcement in each layer of a laminate, and not least by the overall thickness of the laminate.

It might be argued that the core temperature of the specimen is of equal, if not greater importance to the surface temperature, but at present no transducer is available which can be embedded within a laminate without interfering with its local structure. The primary concern is that the transducer and its connections may act as a stress-raiser or weak interface causing unrepresentative initiation of fibre fracture or delamination. Although several technologies exist which can be embedded (such as very fine thermocouples, or optical fibre Bragg grating based temperature sensors), their size, stiffness, and bonding characteristics are still such that the effect on fatigue performance is significant.

Some specimens will also exhibit gradients along or across their exposed faces, but in this respect multiple measurement locations are obviously possible, as will be discussed later.

Temperature Measurement of Composite Test Specimens

PHYSICAL CONNECTION ISSUES DURING FATIGUE TEST

For many laboratories, thermocouples represent their *de facto* standard method of temperature measurement. However, when applied to specimen temperature measurement during fatigue testing of composites, they can present certain difficulties. The same difficulties would be experienced for other contacting temperature measurement technologies such as platinum resistance wire, or optical fibre transducers.

Firstly, there is the simple issue of reliably attaching a probe to a specimen which may need to survive in excess of 1×10^6 cycles, at significant strain ranges. Even with thorough surface preparation, the use of epoxy resin based adhesives often results in debonding or fracture of the adhesive part way through the test. Adhesive tape often results in poor thermal contact with the specimen surface, while spring mounting systems can lead to abrasion of the surface.

In addition to these purely practical matters, the more serious concern is one of reliable and accurate measurement. Attaching a thermocouple to the specimen

material must be heated. Large wires or springs will tend to extract heat to a greater degree leading to a lower temperature reading, while adhesives and tapes will insulate the surface of the specimen. The measured temperature may or may not be representative of the exposed surface of the specimen, but the area in which it is affixed will definitely be subject to slightly different conditions to the rest of the specimen.

REMOVING TEMPERATURE OFFSET AND TIME LAG USING IR MEASUREMENTS

The result of the poor connection of thermocouples is an inaccurate measurement of surface temperature both in magnitude and time-resolved response. This effect is most clearly demonstrated when a step change in frequency is applied during cyclic loading.

Experimental Set Up

A coupon was prepared and instrumented with two different thermocouples attached with electrical insulating tape, an infrared pyrometer, and an infrared camera. It was loaded using an Instron 8802 load frame with 250 kN load capacity, controlled by an 8800T test controller with 5 kHz loop closure rate and simultaneous 5 kHz data acquisition rate on all analogue input channels. Tests were controlled, data logged and reduced, and live calculations made, using Instron WaveMatrix³ dynamic test control software [5].

The material was a room temperature cured epoxy resin, reinforced with eight plies of (0, 90, 0, and 90°) plain weave, E-glass fabric. The specimen was 2 by 25 mm, with a 150 mm gauge length, plus 50 mm end-tabs in the same material.

The thermocouples were one type K with 0.2 mm wires and a 0.5 mm bead and one type T with 0.5 mm wires and a 1.25 mm bead; both were affixed at the same location on opposite sides of the specimen, 25 mm from the moving grip. The pyrometer was an Optris LT22 thermopile sensor with an 8 to 14 μm spectral range with emissivity set to 0.96, nominal sensitivity of 0.1 K focused on a spot of 10 mm diameter, centered 25 mm from the stationary grip. The camera was an Optris PI450 uncooled bolometer, with a 7.3 to 13 μm spectral range with emissivity set to 0.96, nominal sensitivity of 0.06 K, focused on the whole specimen, giving an output corresponding to the average temperature of one half of the specimen which was not obscured by thermocouples or tape. An additional type K thermocouple, of the same specification, was freely suspended in the air, 20 cm from the specimen.

The nominal response time of the thermopile detector was 150 ms; the camera is capable of 80 Hz frame rate, but the manufacturer does not state a response time. The analogue outputs from the infrared devices were fed into data acquisition channels on the test machine controller. Thermocouple signal conditioning and data acquisition was through a National Instruments NI9211 module connected to

³Instron WaveMatrix is a trademark of Illinois Tool Works Inc., Norwood, MA.

the test control computer by a USB link, and controlled directly by the dynamic test application software (typical polling rate 2 Hz).

Transducer Response to Changes in Internal Heating Generation

The loading regime employed was a peak loading of 60 % of tensile strength, with a loading ratio of 0.1, initially at 3 Hz, then stepped to 6 Hz, then up to 12 Hz, and finally back down to 3 Hz. **Figure 1** shows the specimen temperature recorded by each transducer during the test, plotted with respect to elapsed time.

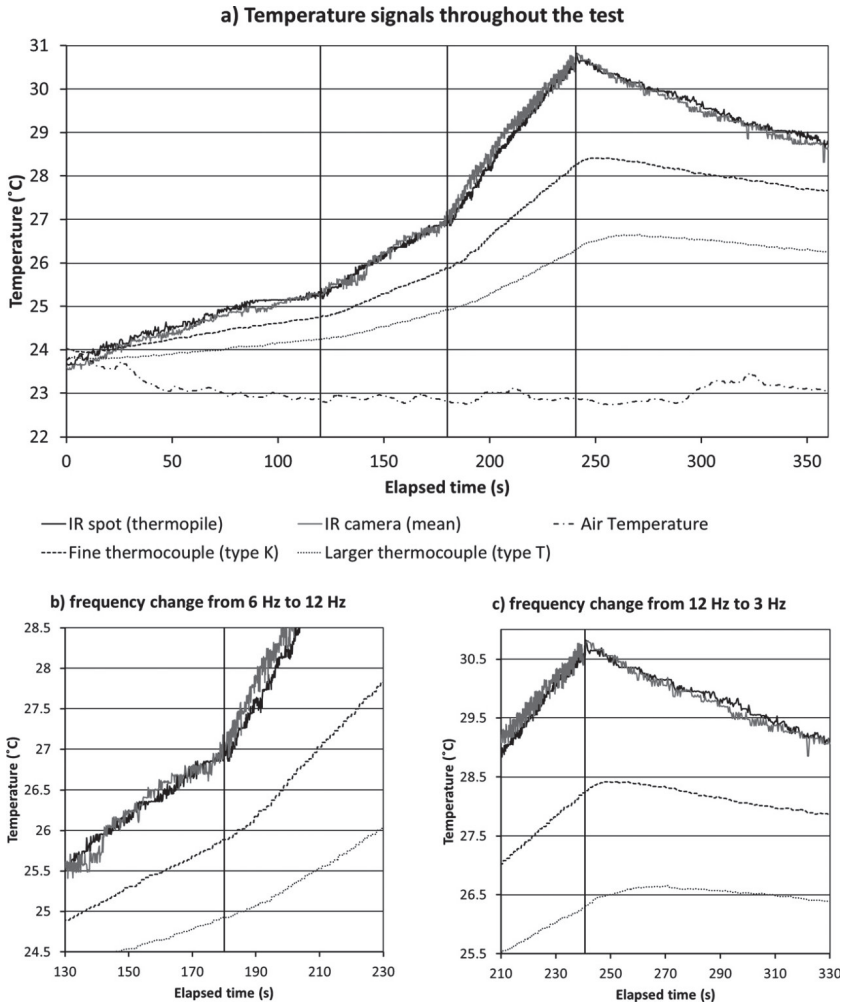
The point which is immediately noticeable is that although all the measurements start within a reasonable level of variation for a simple laboratory demonstration, they then rapidly diverge, with the heavier thermocouple indicating less than half of the temperature increase registered by the two IR devices throughout the test. The lighter thermocouple performed better, but still only registered around 75 % of the temperature increase. Even if the actual emissivity of the specimen is as low as 0.88 (which seems improbable since the initial temperature is in reasonable agreement), then this would not result in more than a 2.2 % over-reading error in the temperature difference. See below for discussion of “Concerns With Using IR Temperature Measurement.”

Figures 1(b) and **1(c)** show the data windowed down to the changes from 6 to 12 Hz, and from 12 back to 3 Hz, respectively. Infrared measurements show that the rate of change in surface temperature is effectively instantaneous, whereas the thermocouples both exhibit a delay of at least 10 s before there is an observed response. For the reduction in frequency, the thermocouple with larger wires and bead shows a greater time lag of 30 s before surface cooling is observed. There is no difference visible above noise level at the change from 3 to 6 Hz. A thermal image of the specimen at the end of the test can be seen in **Fig. 2**. The larger, type T, thermocouple can be seen near the bottom of the frame and appears to have a steep temperature gradient as it moves away from the point of connection. Slight discontinuities can be seen near the top and bottom edges of the tape used to secure the thermocouples.

Concerns With Using IR Temperature Measurement

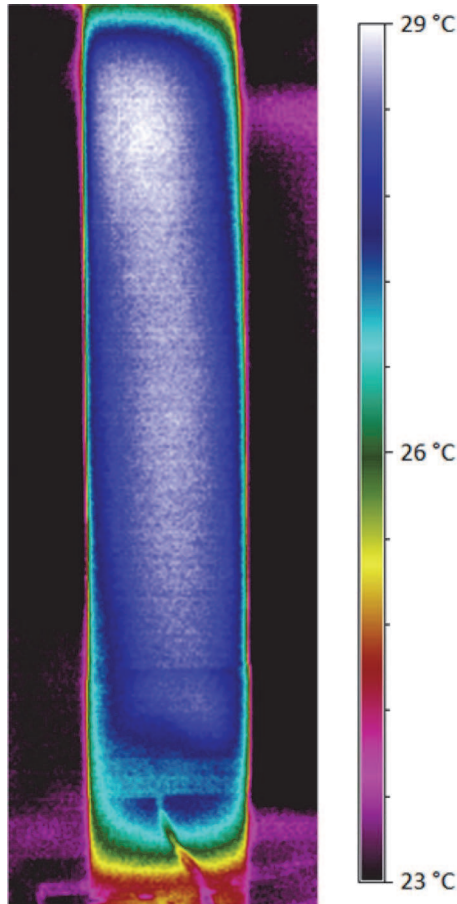
The main concern with employing infrared emission for temperature measurement is that it is intrinsically surface sensitive. Emitted power is dependent upon the emissivity of the surface, which is determined by a combination of its chemistry and topography; thus two visually similar specimens can emit more or less efficiently at a given surface temperature. Furthermore, care must be taken to prevent reflected radiation from the surrounding area causing spurious increases in measured temperature. In a laboratory environment, a standard safety enclosure (including visually transparent polymer shields) would generally suffice for mid-IR measurements, but if working within a convective temperature chamber, then heat-

FIG. 1 Performance of transducers with changing specimen temperature and heating rate.



The effects of emissivity are a serious concern when monitoring metals during prolonged high temperature tests, where oxide layer formation during the test can significantly change the emissivity. However, under fatigue test conditions for polymer matrix composites, the surface will rarely be subject to any chemical or physical change sufficient to alter the emissivity. Operating temperatures for composite materials are necessarily well below those required to cause appreciable oxidation or other chemical reactions; neither would it be expected to work at or near phase transition temperatures.

FIG. 2 Thermal image of specimen at end of test, thermocouple connection near bottom of frame.



A majority of polymers and inorganic fibres (in bulk) have emissivity that lies within a band from 0.88 to 0.96. The Stefan–Boltzmann Law (Eq 1) gives the relationship for the total emitted power with absolute temperature and emissivity.

$$(1) \quad \frac{P}{A} = \varepsilon \cdot \sigma \cdot T^4$$

where:

P = emitted power,

A = emitting area,

ε = emissivity,

σ = the Stefan–Boltzmann constant, and

T = the temperature of the emitting body.

From this it becomes apparent that a small error in the evaluation of emissivity will lead to increasingly significant errors in the temperature or temperature difference determined on a specimen. For example, if the correct emissivity is 0.96, but calculations are based on 0.92, then at exactly 20°C, the temperature will be determined as 23.134°C; if temperature rises by exactly 10°C, then the measured increase will be 10.107°C. Since temperature is raised to the power of 4, then errors increase rapidly as absolute temperature or temperature difference increases. However, as was observed from the data in Fig. 1, significant errors can also arise with thermocouples, which are less predictable, and arguably more difficult to model or correct for in post-test analyses.

There are several mitigating factors for this issue. Firstly, under fatigue conditions, it would be unusual to deliberately allow the specimen temperature to increase greatly beyond 10°C, and temperature variation is the parameter under consideration. Secondly, the error can be expected to remain consistent throughout one sample (batch) of specimens, and usually between batches of material with the same composition and process history. Finally, for almost all applications in polymer matrix composites, the problem can be completely eliminated by the simple expedient of applying a thin coating of known emissivity. Since surface degradation effects would not normally play a part in fatigue phenomena of composites, the requirement for such a coating is simply that it must not affect the mechanical properties of the specimen (for example by solvent swelling or plasticisation of the surface) and must retain intimate contact with the surface throughout the test. A typical choice might be a matt black paint, with low viscosity, and a low volatile organic chemical (VOC) carrier.

Note on High Temperature Solution to Corrected Infrared Temperature Measurement

Although beyond the scope of discussions in this paper, it is important to note that at moderately high temperatures (typically >500°C), “two-colour” pyrometers have been used for some time for more difficult applications. In this case, temperature is determined from the difference in emitted power between two distinct wavebands. As described by Planck Law, radiation from a black body is not constant with wavelength, but rather follows a curve with a steep leading edge at low wavelength, a peak wavelength, and a longer “tail” out into the far infrared. Therefore, provided both measurement bands lie on the same side of the peak wavelength, the gradient between them can then be used to back-calculate the temperature of the emitting body. Some researchers found that this is not completely without issue because the emissivity of a surface does vary with wavelength, according to the chemical composition of the surface and near-surface material. It should be emphasised that Stefan–Boltzmann Law deals with the total radiative flux; therefore using a single average value of emissivity.

Linking Measured Temperature to Test Control

ADAPTIVE FREQUENCY CONTROL

If a reliable, continuous method of temperature control can be fed into the control and data acquisition system for a dynamic test machine, then a range of options become available to control the test, ranging from simply pausing the test at a low load if the specimen exceeds a temperature threshold to automatically modulating the frequency of the test waveform.

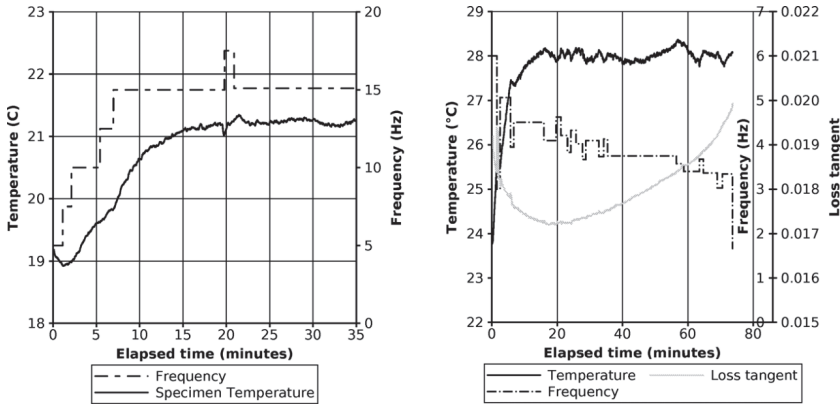
A fatigue test technique has been developed which employs adaptive frequency control in response to specimen temperature. Using a commercial infrared detector to supply a feedback to the control system, frequency control throughout the test can maintain specimen temperature within a tight band. The adaptive frequency control system is effectively an outer loop control algorithm, run by the test software, which adjusts the machine controller parameters to modulate the frequency of the applied load (or displacement) waveform. When implemented as a simple P.I.D. control routine, variation between specimens and materials was found to result in unpredictable overshoot in both frequency and temperature. A number of other approaches were tested, but monitoring the rate of temperature change relative to the target has proven successful, working reliably on any type of composite or polymer material without any need for tuning the frequency control algorithm. Control system algorithms and development cannot be discussed further in this paper due to their commercial sensitivity.

Initial tests were conducted using woven E-glass fibre reinforced composite, with low temperature cured epoxy resin matrix. The tests were conducted using the same type of load frame, controller, and test software as detailed in the previous section of this paper. A Pyris infrared bolometer (also as discussed earlier) with a waveband from 7.3 to 13 μm was used, with temperature readings based on an emissivity of 0.96 for non-contacting temperature measurement, allowing assessment of temperature distribution while simultaneously providing an analogue signal to the control system corresponding to the average specimen temperature. In a more extensive case study, a standard set of load controlled, tension-tension, fatigue tests were conducted to produce an S-N curve for a cross-ply woven-tow carbon fibre reinforced composite, with a mid-temperature cured epoxy resin matrix. Peak stress values between 60 and 80 % of static failure stress were used, with a loading ratio of $R = 0.1$, at a fixed frequency of 4 Hz, with temperature monitored, but not controlled. The complete test regime was then repeated using the adaptive frequency control method to maintain a stable temperature.

Specimens were prepared and tested in accordance with international composites fatigue standards [1,2], with glass fibre reinforced, medium temperature matrix, prepreg material for initial tests, and with carbon fibre reinforced, high performance prepreg material for the full S-N curve.

Figure 3(a) illustrates the start of a typical test, using glass fibre reinforced epoxy
 $R = 0.1$.

FIG. 3 Adaptive frequency control performance on GFRE specimens: (a) (left) Ramping up to optimum frequency for required specimen temperature; (b) (right) Reducing frequency to maintain temperature in late stages of fatigue.



Here, an initial frequency of 5 Hz was set in low ambient temperature ($18 \pm 1^\circ\text{C}$), with a target test temperature of $21.0 \pm 0.5^\circ\text{C}$. Clearly for this loading rate, 5 Hz was not sufficient to cause significant temperature rise, so the system gradually increased this frequency until it stabilized just above 15 Hz, having assessed that target temperature will be achieved within 20 min. It is also interesting to note that at around 20 min into this test, a lab door opening caused a sudden drop in specimen temperature, and thus the system responded by briefly increasing frequency by a small amount to correct this.

Figure 3(b) shows the system reducing the test frequency to prevent overheating. Using the same type of specimen, this time loaded to 60 % of failure stress controlled to $28.0 \pm 0.5^\circ\text{C}$. Having already seen some 50 000 cycles, this is effectively the final part of the test. After an initial settling period commonly observed in composites fatigue, tan delta shows continuous increase as damage accumulation accelerates, as other researchers have observed [4,6,7] in various systems.

Firstly, the starting frequency is quickly reduced to prevent overheating, then gradually adjusted to correct for the increasing energy deposition rate to maintain specimen temperature which would otherwise increase significantly [6].

S-N Curve Generation With Automated Frequency Control Based on Specimen Temperature

Forty-five standard tensile test specimens [1,2] were prepared from a single, flat sheet of thoroughly conditioned epoxy matrix material with woven carbon fibre reinforcement. Following initial measurement of static tensile strength, the remaining specimens were split randomly into two groups. The first group was tested at a

fixed frequency of 4 Hz, in the usual manner used by NCCEF for contract testing of tension–tension fatigue. During these tests, average specimen temperatures varied quite widely, ranging from 26 to 38°C, in a temperature controlled laboratory at $25 \pm 1^\circ\text{C}$

The second group was tested at the same stress ranges, but this time employing the adaptive frequency control method. The control algorithm was given a target temperature of $30.0 \pm 0.5^\circ\text{C}$, and allowed a maximum operating frequency of 15 Hz.

These two datasets are plotted as a standard S–N curve in Fig. 4.

There was no evidence of unusual failure mode for the two outlying points observed at the lowest stress level in the fixed frequency (4 Hz) data. Since the rest of this data set does not show such broad variability, no conclusion can reasonably be drawn on that basis.

Many commercial experimentalists apply a logarithmic fit to the S–N data from composite fatigue testing to facilitate fatigue life prediction. On an empirical basis, this appears a good fit for both sets of data presented; details of the fitting parameters and resultant predictions are tabulated in Table 1.

Whether or not this is the best possible methodology is not the subject of this paper, but it is undeniably a simple extrapolation technique for practically obtainable data; one which will generally give conservative predictions. The range of fatigue resistance and resultant S–N curves for composites are as diverse as those seen for metals (if not more so), so it seems entirely probable that the behavior is not neatly logarithmic, and even a “no fatigue limit” might exist in some cases.

FIG. 4 S–N plot for CFRE (woven prepreg) from fixed frequency and adaptive frequency methods.

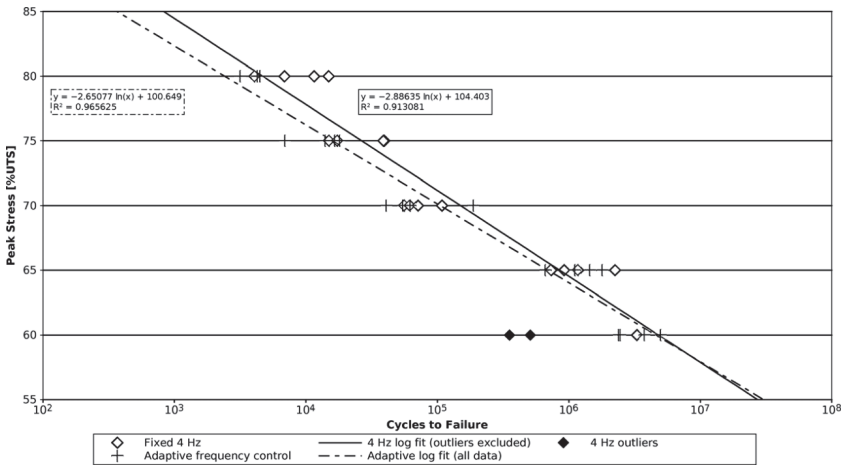


TABLE 1 Comparison of data fitting and prediction.

Logarithmic Fit $\sigma_c = -a \ln(N) + c$	Gradient, a	Intercept, c (% UTS)	Fit Quality (R^2)	Predicted Stress at 10^7 Cycles (%UTS)	Predicted Stress at 10^8 Cycles (%UTS)
4 Hz (all data)	3.156	106.7	0.844	55.9	48.6
4 Hz (exclude outliers)	2.886	104.4	0.931	57.9	51.2
Adaptive frequency	2.651	100.7	0.966	57.9	51.8

Validity of this fitting procedure and rigorous assessment of confidence levels are detailed in relevant international standards for analysis of fatigue life data [8–10].

Examining Fig. 4, there is good congruence of the fitting curves for fixed and adaptive frequency methods. It is interesting to note that both the fit quality (“ R^2 value”) and the intercept (prediction for static failure) show a small improvement for the adaptive frequency data. More importantly, the predicted stress level to achieve specific long fatigue lives (a key criterion for many commercial applications) is extremely similar.

Table 2 gives a comparison of the time reduction and frequency variation resulting from the use of adaptive frequency control for a full set of fatigue tests on this material.

Firstly, from the authors’ viewpoint, the headline figure is that of a 27.5 % reduction in total machine time to produce the data set. On the basis of the NCCEF fixed frequency testing at 4 Hz which took approaching two months of machine time, this represents a significant saving, both in time and power consumption for the laboratory.

Secondly, this time saving is achieved with fairly conservative variation in test frequency. It was proposed that an increase in test frequency of even a whole order of magnitude may have little effect on the fatigue behavior of composite materials

TABLE 2 Comparison of machine time for a fatigue data set.

Frequency Variation	Total Time for S-N Curve	Equivalent Time at 4 Hz	Time Saving Versus 4 Hz
<62 %	40 days	55 days	27.5 %

Load (%UTS)	Specimen Self-Heating Control		Fixed Frequency 4 Hz Equivalent Time Per Specimen (h)
	Frequency Achieved* (Hz)	Time Per Specimen* (h)	
80 %	3.59	0.93	0.84
75 %	4.01	3.9	3.9
70 %	4.64	22	24
65 %	5.03	290	349
60 %	6.49	642	946

* averaged across duration of test ** from cycles to fail

[9,10]. Composite fatigue practitioners frequently mention temperature increases exceeding 20°C in materials with woven reinforcement; clearly this cannot be deemed a well-controlled test, or representative of operating conditions. The authors of this paper propose that automatic frequency modulation offers a valuable and realistic alternative to control the degree of specimen heating [5].

Potential Applications of Thermography for In-Test Analysis

DAMAGE ACCUMULATION

If a fixed frequency is used, then temperature could be used simplistically as a measure of damage accumulation in the same way as damage might. Some workers have previously recorded temperature throughout composites fatigue tests and suggested that it might be useful to infer the rate, type, or severity of damage processes occurring from the specimen temperature [8]. Furthermore, if a simple output of the maximum temperature within the field of view (or a smaller region of interest) is recorded, then localized damage phenomena such as breakage of individual tows could be indicated as brief temperature spikes since they cause transient hot spots at the point of failure due to local release of strain energy. To achieve this, the key technical issue becomes one of selecting a detector in which the temperature resolution and response time are both sufficiently small to resolve these transient changes.

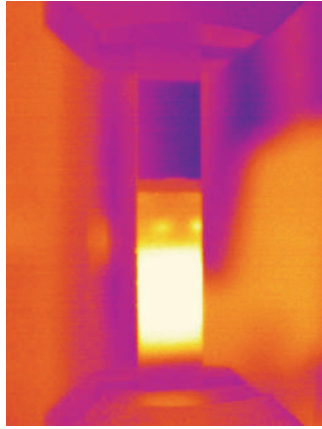
POTENTIAL FULL-FIELD MEASUREMENT

As has just been mentioned, the free commercial availability of infrared imaging has brought about the possibility not only of assessing the temperature of a whole specimen, but to conduct more sophisticated analyses of the damage and failure phenomena during a fatigue test, especially on composite materials. Moderately simple image analysis techniques can be employed to look at features of the specimen.

As a first example of how this might be used, [Fig. 5](#) shows a thermal image taken near the end of a fatigue test on an adhesive lap shear joint between woven carbon fibre reinforced epoxy resin and 2000 series aluminium sheet. The lap joint itself can be identified, as can a growing region of de-bonding, which has resulted in higher surface temperature as less heat is conducted away by the aluminium substrate. Well-established image analysis techniques could be employed to identify the growing region of delamination; it is proposed that with the processing power available in current personal computers, this could be calculated “live” and logged with test data.

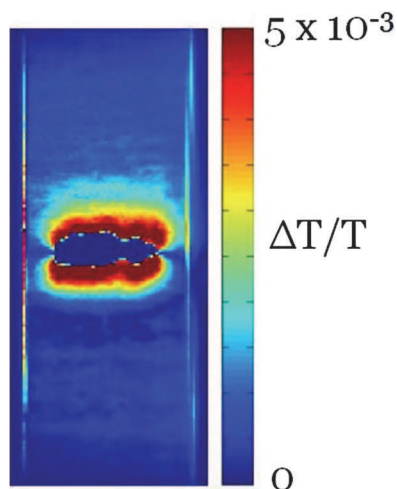
In a more sophisticated example, the technique of thermo-elastic stress analysis has been in development for some years now, and makes use of the fact that an applied elastic stress results in slight change in temperature within a material. The

FIG. 5 Thermal image showing delaminated areas of a lap shear joint during fatigue test.



determination of how the stress is distributed across the test piece [11]. Although the author has not undertaken such work, they are currently collaborating with researchers at The University of Southampton whom have kindly agreed to the reproduction of the image in Fig. 6. Thermo-elastic stress analysis was successfully

FIG. 6 Thermo-elastic stress analysis image showing stress distribution during fatigue test of an impact damaged composite test coupon.



correlated with strain mapping by digital image correlation techniques [12], but the processing requirements are considerably smaller.

Conclusion

The benefits of measuring specimen temperature during fatigue testing of polymer matrix composites using infrared emission based techniques has been discussed and demonstrated, along with the concerns, benefits, and future potential in the context of this area of testing which is rapidly rising in industrial importance.

A case study is presented which shows an integration of this technique with test control that has immediate benefits in overall test time and consistency for generation of S–N curves for composite materials.

References

- [1] ISO 13003:2003: *Fibre-Reinforced Plastics—Determination of Fatigue Properties Under Cyclic Loading Conditions*, ISO, Geneva, Switzerland, 2003.
- [2] ASTM D3479/D3479M-12: Standard Test Method for Tension-Tension Fatigue of Polymer Matrix Composite Materials, ASTM International, West Conshohocken, PA, 2012, www.astm.org.
- [3] Poursartip, A., Ashby, M. F., and Beaumont, P. W. R., “The Fatigue Damage Mechanics of a Carbon Fibre Composite Laminate: I—Development of the Model,” *Compos. Sci. Technol.*, Vol. 25, No. 4, 1986, pp. 193–218.
- [4] Liu, C., Cheng, L., Luan, X., Li, B., and Zhou, J., “Damage Evolution and Real-Time Non-Destructive Evaluation of 2D Carbon-Fiber/SiC-Matrix Composites Under Fatigue Loading,” *Mater. Lett.*, Vol. 62, No. 24, 2008, pp. 3922–3944.
- [5] Illinois Tool Works Inc., 2012, “Material Testing Apparatus and Method,” *International Patent Application No. PCT/US12/69711*.
- [6] Toubal, L., Karama, M., and Lorrain, B., “Damage Evolution and Infrared Thermography in Woven Composite Laminates Under Fatigue Loading,” *Int. J. Fatigue*, Vol. 28, No. 12, 2006, pp. 1867–1872.
- [7] Ogasawara, T., Onta, K., Ogihara, S., Yokozeki, T., and Hara, E., “Torsion Fatigue Behavior of Unidirectional Carbon/Epoxy and Glass/Epoxy Composites,” *Compos. Struct.*, Vol. 90, No. 4, 2009, pp. 482–489.
- [8] ISO 12107:2003: *Metallic Materials. Fatigue Testing. Statistical Planning and Analysis of Data*, ISO, Geneva, Switzerland, 2003.
- [9] ASTM E739-10: Standard Practice for Statistical Analysis of Linear or Linearized Stress-Life (S–N) and Strain-Life (ϵ -N) Fatigue Data, ASTM International, West Conshohocken, PA, 2010, www.astm.org.
- [10] Nijssen, R. L. P. and Cormier, L., “Experiments and Modeling of Influence and Interaction of Temperature and Frequency on Fatigue Life,” *Project UpWind Deliverable D3.1.8 for*

European FP6 Project No. 019945, Knowledge Centre for Wind Turbine Materials and Construction, Wieringerwerf, The Netherlands, 2010.

- [11] Wong, A. K., Sparrow, J. G., and Dunn, S. A., "On the Revised Theory of the Thermoelastic Effect," *J. Phys. Chem. Solids*, Vol. 49, No. 4, 1988, pp. 395-400.
- [12] Crump, D. A., Dulieu-Barton, J. M., Boyd, S. W., Bantams, G. P., and Crammond, G., "High Speed Imaging to Investigate the Failure and Remnant Life of Composite Structure Under Impact," *Eng. Integ.*, No. 35, 2013, pp. 8-11.

STP 1584, 2015 / available online at www.astm.org / doi: 10.1520/STP158420140080

J. P. Jones,¹ S. P. Brookes,² M. T. Whittaker,¹
R. J. Lancaster,¹ and B. Ward³

Assessment of Infrared Thermography for Cyclic High-Temperature Measurement and Control

Reference

Jones, J. P., Brookes, S. P., Whittaker, M. T., Lancaster, R. J., and Ward, B., "Assessment of Infrared Thermography for Cyclic High-Temperature Measurement and Control," *Evaluation of Existing and New Sensor Technologies for Fatigue, Fracture and Mechanical Testing*, STP 1584, Jidong Kang, David Jablonski, and David Dudzinski, Eds., pp. 186–206, doi:10.1520/STP158420140080, ASTM International, West Conshohocken, PA 2015.⁴

ABSTRACT

Infrared thermography (IRT), a non-invasive temperature measurement technique has been investigated and developed for use with cyclic high-temperature loading. The technique utilizes an infrared thermography camera (IRTC) and Rolls-Royce HE23 black thermal paint (TP). The TP is applied to a test-piece surface to provide a stable emissivity value and accurate temperature measurement for the duration of thermal cycling. Spot-welded type N thermocouples (NTCs) are utilized for accuracy validation of the IRTC technique for both temperature monitoring and temperature control. An evaluation of the technique has been employed upon diverse test specimen geometries and alloy compositions at temperatures between 100°C and 700°C. Unfavorable effects during cyclic temperature measurement such as thermocouple shadowing are also highlighted and quantified. In combination with HE23 TP, IRTC control and measurement have proven accurate to within $\pm 2^\circ\text{C}$ NTCs, a validated cyclic high-temperature measurement technique.

Manuscript received July 7, 2014; accepted for publication February 13, 2015; published online March 12, 2015.

¹Institute of Structural Materials, Swansea Univ., Singleton Park, Swansea SA2 8PP, United Kingdom.

²Rolls-Royce, Mechanical Test Operations Centre, GmbH, 15827 Blankenfelde-Mahlow, Germany.

³Rolls-Royce plc, Engineering Rig Test Services, Derby DE24 8BJ, United Kingdom.

⁴ASTM Fourth Symposium on the *Evaluation of Existing and New Sensor Technologies for Fatigue, Fracture and Mechanical Testing* on May 7–8, 2014 in Toronto, Canada.

Keywords

infrared, thermography, cyclic temperature, emissivity, thermal paint, temperature control

Introduction

In recent years, it has become more prevalent to assess aerospace and other high-temperature materials under cyclic temperatures as they are understood to be more damaging than isothermal conditions. The deformation and damage seen in real components is often better represented by these dynamic temperature loading cycles. As an example, cyclic high-temperature testing delivers invaluable insights into the behavior of high-performance aerospace alloys under the extreme conditions typically found inside an aero gas turbine engine. This accurate temperature and loading control during these dynamic cycles is imperative, as they enable the desired phasing between temperature and load, known as the phase angle, to be realized, allowing reliable results to be derived for component lifting interpretation.

The publication of ASTM E2368-10 [1] and, more recently, ISO12111 [2] strain-controlled thermo-mechanical fatigue standards, emphasizes the significance of dynamic temperature effects on material fatigue behavior. However, uncertainty still remains with regard to how accurately temperature can be measured and controlled. When considering data scatter, it is critical not to neglect temperature accuracy [3–7]. Reliable test results can only be accomplished provided that temperature has been kept to within good temperature tolerances ($\pm 5^\circ\text{C}$ or $\pm 1\%$ ΔT circumferentially at the center gauge location and $\pm 10^\circ\text{C}$ or $\pm 2\%$ ΔT axially) as recommended and emphasized by these standards [2].

The desired thermal response during standard tests under isothermal fatigue (IF) can be achieved using a conventional resistance furnace controlled and monitored by thermocouples (TCs). This technique, however, is not appropriate for rapid dynamic thermal cycles, as the heating and cooling rates generated by the furnace are too slow to cope with the dynamic temperature rates required.

In the aerospace industry, temperature ramp rates for dynamic cycles are often based on an engine flight cycle, combining takeoff, climb, cruise, and descent in a single test cycle. The test cycle is accelerated so that testing ramp rates in real time may exceed $\pm 10^\circ\text{C/s}$. The rapid temperatures necessary for these tests requires a special type of furnace to be employed, such as RLFs or induction coil systems (ICS), which offer this capability. RLF and ICS heat sources are attractive as they can be easily adapted to fit to the frame of existing test machines; therefore, they enable the use of established fixtures and specimen geometries, leading to direct comparisons with previous isothermal tests. ICS heating offers a far cheaper and more reliable solution; however, a downside to the technique is the homogeneity of the applied temperature, which is often far less uniform than in a conventional radiant furnace.

Additional complications arise when considering the traditional methods by which temperature is measured and usually controlled under dynamic

high-temperature cycles. A recommendation is that temperature control may be carried out using spot-welded TCs at the specimen shoulder (or still in the parallel length, but outside the gauge section) for heating and cooling rates up to 10°C/s [2]. The authors have found the accuracy and practicality of such a technique under rapid dynamic thermal cycles to be questionable, particularly in specimens with a long parallel gauge section, where large distances exist between the material under investigation (between the extensometer arms in a strain controlled tests) and the TC location on the test-piece shoulder.

Thermocouples have known limitations; the correct type must be selected according to the temperature range under investigation to ensure accuracy [3,8]. Temperature errors can also arise from increasing absorption coefficients of the oxidizing test piece, and via heat conduction through the TC wires giving rise to cold spots [3,9]. Cracks are known to initiate from the TC contact point, especially if the TC has been spot welded to the specimen surface [2]. The spot weld essentially acts as a surface defect, which in turn acts as a stress raiser resulting in crack initiation [10,11].

Ensuring that the TC wire diameter is as small as possible, using individual and not beaded TCs, and providing additional thermal contact by wrapping TC wire around the test piece are measures that can be taken to minimize the severity of the technique [9]. However, despite all of these measures, spot-welded TCs will induce a cold spot, hence, a surface defect and a resulting crack initiation site [3]. It is, therefore, not recommended that TCs be spot welded in the test-piece gauge section [2].

Direct temperature measurement or control can be achieved from the test-piece gauge section without inducing surface defects using ribbon type TCs. However, if this technique is to be employed, then adequate thermal contact between the test piece and TC must be maintained throughout the entire test. Additionally, caution must be taken to ensure that the contact does not degrade during cycling as a result of oxidation and/or surface roughening [3,8,9].

Another alternative approach is co-axial TCs. This style of TC arrangement requires holes to be machined into the test-piece surface to allow insertion of the TC. Dynamic temperature accuracy is dependent on the machined hole diameter, as the closer the TC diameter is to that of the hole, the more accurate the reading will become [9]. However, despite the utmost diligence, this technique still proves challenging [8]. A further method of TC control involves spot-welding TCs to the adjacent shoulders of the specimen provided the heating and cooling rates are $\leq 10^{\circ}\text{C/s}$ [2,3,8,9], reducing the applicability of the technique for cyclic high-temperature testing.

An alternative approach is the use of pyrometers. Pyrometers provide a completely non-invasive method for measuring and/or controlling the temperature of a test piece by measuring the amount of thermal radiation emitted from the surface of the material. Accuracy of the temperature measurement is related to the spot size

required to obtain the most accurate temperature measurements, because any angular deflection of the beam from the surface of the specimen may result in measurement inaccuracy. Additionally, the spectral range of the pyrometer must surpass the T_{\min} and T_{\max} of the desired temperatures, as inaccuracies become apparent within close proximity to the pyrometer's temperature range capabilities [8].

Pyrometers and TCs share a similar limitation. Both techniques can only measure the small area they encompass, typically around 2 mm^2 . In addition, pyrometers require thermal profiling using TCs; hence, despite being a non-invasive technique and avoiding complications with TC shadowing (discussed further below) during testing, inherent temperature errors have already been brought forward from the thermal profiling procedure using TCs.

However, the use of pyrometers for dynamic temperature control is not recommended by the relevant standards involved with cyclic high-temperature testing [2] as they are sensitive to progressive oxidation causing changes to the surface condition [9]. Depending on the specific temperature and wavelength, the energy radiated by a metallic surface is highly sensitive to any change in the surface condition and, therefore, is directly proportional to the spectral emissivity of the object [3]. Without a stable emissivity value, it is extremely difficult to achieve accurate temperature measurement with a non-invasive technique such as a pyrometer [9,12].

A solution to this is to pre-oxidize the specimen to produce a stable oxide layer and, hence, stable surface emissivity [13]. However, pre-heat treatments and, thus, consistent oxide formation has previously been found to lack repeatability. Previous work has found that the surface emissivity evolution with temperature is dependent on the material, surface preparation, thermal treatment, and the chemical reactions on the surface [14]. Further work suggests that there is no conclusive trend of emissivity observed as a function of oxidation time ($15 \pm 60 \text{ min}$) at a given oxidation temperature [15].

However, provided a stable oxide layer and, thus, a constant surface emissivity can be achieved, the high-temperature pre-exposure and the resultant oxide formation can influence the fatigue life of the test piece [16]. A reduction in fatigue life occurs for some alloys subjected to pre-test temperatures $\geq 500^\circ\text{C}$ [17]. The reductions in fatigue life can be a direct result of surface oxide scale cracking in combination with increased crack growth rates resulting from an enhanced susceptibility to intergranular cracking [17,18]. This effect was investigated on two Ni-base superalloys in the temperature range $650\text{--}704^\circ\text{C}$ for exposures of 100 to $\geq 1000 \text{ h}$ [17]. The investigation concluded that pre exposure increased scatter in the results and reduced fatigue life by up to 70 % compared to unexposed specimens.

In summary, an entirely new non-invasive technique is required that encompasses the complete test setup from thermal profiling to the actual test, that can be used with rapid dynamic temperature cycling for measurement and control purposes. The technique must avoid complications with emissivity inconsistencies and TC shadowing while acquiring temperature readings from the specimen gauge section with the utmost accuracy. Additional desirable benefits include an

all-encompassing gauge section profiling ability at a less arduous and time-consuming pace than currently employed profiling techniques.

An infrared thermography camera (IRTC) has the ability to monitor and control temperature over the entire test piece, rather than a small single spot, such as a pyrometer or TC. The current paper seeks to document attempts to implement the IRTC technique for temperature monitoring and control purposes. The technique is used in combination with Rolls-Royce HE23 thermal paint (TP) to stabilize emissivity and highlight the benefits of both a known emissivity and accurate control of temperature over a larger region of the test piece.

Description of Apparatus

In this investigation, two separate testing systems have been utilized. The first system consists of an MTS 250 kN Landmark servo-hydraulic load frame, where heat is applied via a radiant lamp furnace (RLF), modified and supplied by Severn Thermal Solutions. The second system is comprised of an MTS 100 kN Landmark servo-hydraulic load frame, on which an induction coil (IC) was mounted to apply heating. Test-piece temperature is initially measured via type N thermocouples (NTCs) providing a feedback signal to a PID Eurotherm temperature controller. Test-piece temperature is monitored and compared using an IRTC. Temperature measurement was then reversed, using the IRTC as the control providing a feedback signal and monitored by the type N thermocouples. The testing systems are shown in [Fig. 1](#), and described in additional detail in the following sections.

HEATING SYSTEMS

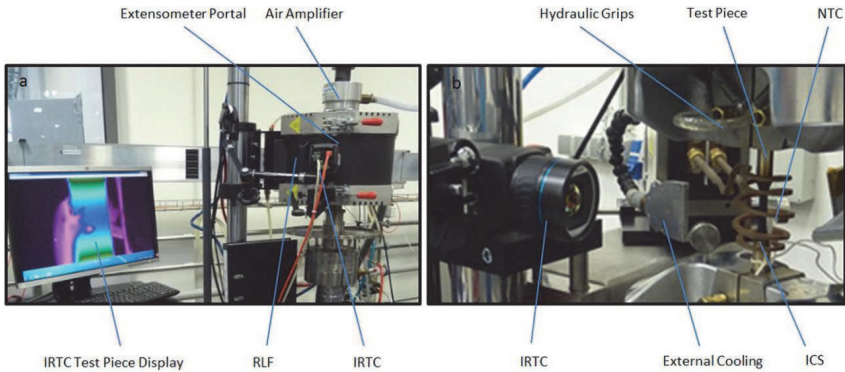
The 12 kW RLF (model number RHS2117) has been tailored for this application and supplied by Severn Thermal Solutions. The furnace comprises of two longitudinally divided half cylinders hinged at the center, with each half containing six lamps. The 12 high-power, vertically mounted quartz lamps heat the specimen to the test temperature. Behind each lamp is a parabolic reflector, which focuses the radiant light toward the center of the furnace. The IRTC was mounted on the front of the RLF, positioned to image the specimen through the extensometer portal ([Fig. 1\(a\)](#)).

Induction heating allows for rapid heating and cooling rates and can be used with a range of specimen designs and materials. A Trueheat 10-kW IC heater delivers an effective method of heating the test specimen to temperatures up to 1200°C, depending on the material and specimen geometry. Metallic materials are heated directly with accurate tailored design of the ICS ensuring localized and uniform heating over the entire gauge section of the test piece. This system enabled an IRTC to be mounted in various positions around the test piece to enable a 360° view of both heating and cooling effects upon the test piece ([Fig. 1\(b\)](#)).

MEASUREMENT AND CONTROL

Test-piece temperature is measured by three NTCs along the gauge section ensur-

FIG. 1 The two temperature measurement and furnace configurations used: (a) RLF with the Flir 655C IRTC, and (b) ICS with the Flir 655C IRTC.



chosen as a baseline temperature reading based on low cost and simplicity of use as well as being the most widely accepted measurement method in most mechanical testing standards. Furthermore, the use of thermocouples does not require the spectral emissivity of test materials to be defined. The NTCs are used to measure temperature at the test-piece surface from the upper, lower, and center locations of the gauge section. These temperatures are used to validate measurements taken from a FLIR SC655 IRTC at the same locations upon the test piece (discussed in further detail below).

TEST SPECIMENS

Various test specimens were used in this investigation totaling four specimen geometry and alloy combinations. This included the nickel-base alloys, Nimonic 90 and Udimet 720, because these are the most widely available alloys for components used for high-temperature applications. Titanium 6/4 and stainless steel alloys were also considered. An abundance of archived test data is available for these alloys, enabling a comparison of the results with previously used temperature-control techniques. Examples of the different specimen geometries used to explore the flexibility of the IRTC and its ability to cope with variations in specimen area, shape, and any reflection caused by the features within are shown in Fig. 2.

Each of the specimens used in the investigation was prepared identically. One side of the specimen remained in the as-received condition referred to as “front,” while the opposing back face, or “back,” was coated with HE23 TP. The HE23 TP was applied to maintain a stable surface emissivity upon the specimen surface for the duration of testing and is described in more detail in the next section.

Prior to coating with TP, some of the specimen surfaces were lightly grit blasted with 120/220 grit to slightly roughen the surface to improve the bond between the

FIG. 2 The different test-piece geometries used in the investigation coated with HE23 TP.



specimen surface and the TP as described in previous work [19]. A conventional air spray gun was used to apply the paint to a thickness of approximately 20–25 μm . The paint was then air dried and cured in a furnace at 300°C for 1 h. A scanning electron microscope (SEM) image of the thickness of the HE23 TP coating on the surface of a test piece is given in Fig. 3.

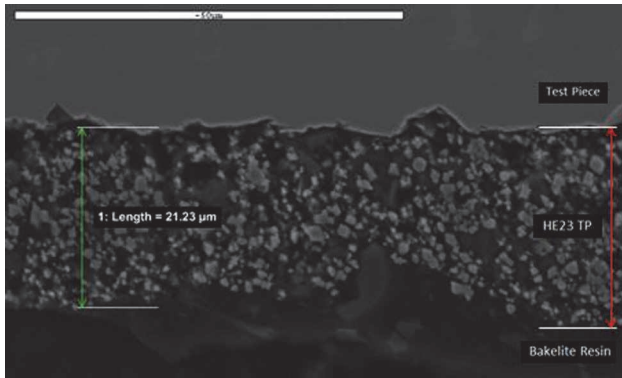
HE23 THERMAL PAINT

As previously mentioned, the principal uncertainty within non-invasive temperature-measurement techniques, such as a pyrometer or IRTC, is the emissivity input value to be used from which the temperature can be measured. Techniques used to measure, correct, and reduce the influence of emissivity values such as TPs are described in previous work [19].

These paints can be applied to encompass the entire specimen surface as a permanent coating. Alternatively, the paint can be applied in a single smaller location or a small spot to determine the emissivity by comparing the measured radiance temperature of this spot with that of the uncoated surface [19]. To avoid complications and inaccuracies with respect to radiation from nearby heat sources, such TPs should yield as high an emissivity value as possible, close to the emissivity of a black body, which is rated with a value of 1 [8].

Rolls-Royce plc has developed a variety of exclusive thermal indicating paints

FIG. 3 An SEM image of the HE23 TP coating thickness upon a test-piece surface.



These indicating paints display an array of permanent color changes in proportion with the temperature they are exposed to, and typically encompass a temperature range of 140°C–1330°C [19]. A description of the practical measurement of reference paint emissivity is also provided [20].

The emissivity of the HE23 TP was found to be stable over a wide temperature range up to 1300°C using pyrometers (Fig. 4). This consistency persists over a range of incidence angles as a result of its high stability and lower angular dependency on emissivity [19]. In summary, HE23 TP can deliver an effectively constant, very high emissivity value across an extremely wide temperature range. The paint has the potential to prove invaluable, delivering accurate temperature measurement over an extensive range of both high and low temperatures under non-invasive techniques [19].

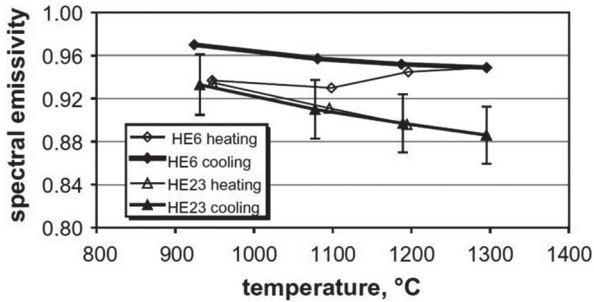
The HE23 TP has proven to be effective for applications such as reference coatings, to measure temperature with a radiation thermometer of surfaces with unknown emissivity [19]. The HE23 TP is used in combination with the non-invasive IRTC technique, and is described in this paper to investigate the stability, accuracy, and repeatability of the temperature measurement and control in comparison to NTCs.

Experimental Procedure

THERMAL CYCLES

An RLF and an ICS heat source were both used to employ isothermal and cyclic temperature cycles, for the purposes of this work, called dynamic dwell and dynamic (Fig. 5). The dynamic dwell cycle ramps from 100°C to 600°C to 100°C, holding the temperature at every 100°C interval for 3 min, then ramping up to the

FIG. 4 Normal spectral emissivity of TP HE6 and HE23 measured during first heating and cooling run [19].



next temperature interval. The dynamic thermal cycle used represents a typical gas turbine flight cycle, commonly utilized to test components under cyclic temperature loading. The dynamic cycle employs a 300°C–615°C temperature range over a 4 min period. Throughout all of the dynamic thermal cycles, the response from the IRTC technique was compared to reference NTCs at the same location on the test-piece gauge section.

TEMPERATURE COMPARISON

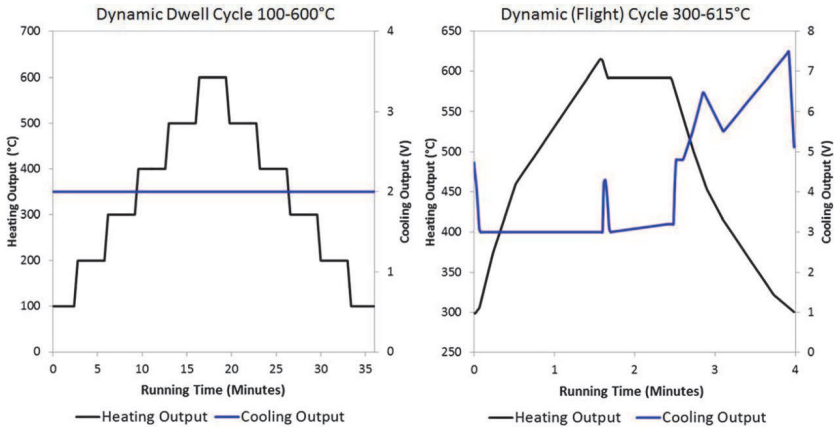
To determine the ease of use, accuracy, stability, and other benefits of the IRTC technique, temperature comparisons were made by an N-type thermocouple (NTC), a known validated temperature-measurement technique enabling validation of the results. Temperature comparisons between the techniques were made on a point-to-point basis; areas of the specimens measured by the non-invasive technique were coated in TP enabling a stable emissivity of the specimen surface to be maintained, while NTCs were attached to uncoated areas of the specimen.

Using both techniques to control and monitor temperature alternatively, comparisons could be made between the responses of each. Under the ICS temperature, readings were taken from each technique at the center test-piece gauge location (Sp1/TC1), outlined in Fig. 6. Using the RLF measurement, comparisons were taken at the upper (Sp2/TC2), center (Sp1/TC1), and lower (SP3/TC3) test-piece gauge section locations, as well as the average temperature of the entire gauge section area, Ar1, as shown in Fig. 7.

During initial trials, significant reflection errors were observed using the IRTC under both ICS and RLF heating methods, despite a built-in variable input to compensate for the effects. The degree of the inaccuracy caused was found to be dependent on the amount and severity of reflective material within view of the device, typically around 15°C. This was solved by coating the reflective panels inside the RLF

(Fig. 7) and hanging a thick black rubber sheet behind the ICS.

FIG. 5 Thermal cycles used in the investigation for comparisons of temperature-measurement techniques.



Results and Discussion

EMISSIVITY STABILITY OF HE23 THERMAL PAINT

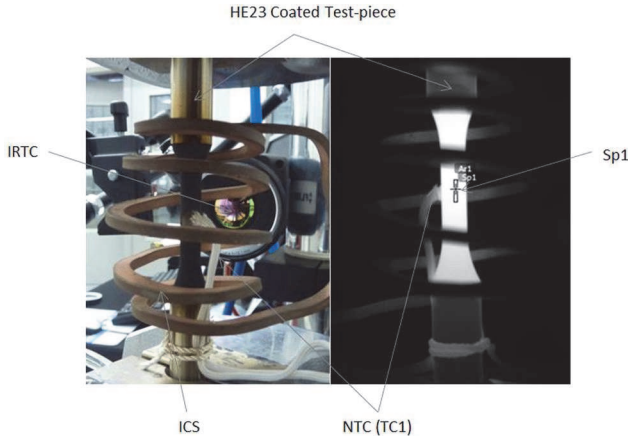
Isothermal tests were performed to study the accuracy and time-dependent effects on the indicated temperature of the IRTC in comparison to NTC control. The investigation was conducted at 50°C intervals between 400°C and 600°C on a Nimonic 90 test piece with no prior oxidation. Specimens were held at each temperature interval for 5 min before values were recorded.

The emissivity input value of the IRTC focused on the test piece was adjusted to ensure that the same temperature reading was retrieved in comparison to the NTC control, within a tolerance of within $\pm 2^\circ\text{C}$. To maintain the same temperature reading as the NTC control, the emissivity input value required reducing as the temperature and resultant oxide formation increased with time upon the specimen surface (Fig. 8). These results are consistent with those gained by Roebuck et al. [12], where large temperature differences were observed between TCs and pyrometers when compared on non-oxidized metal surfaces.

Identically repeating the test with specimens coated with HE23 TP, the emissivity value remained constant throughout the temperature range under ICS and RLF heat sources. The IRTC maintained accuracy to within $\pm 2^\circ\text{C}$ at all temperatures using a constant emissivity input value of 1 (Fig. 8).

To investigate the time-dependent effects of degradation at temperature upon the accuracy of the IRTC, a 15-h 400°C isothermal test was performed on a Nimonic 90 test piece coated in HE23 TP. Measured values from the IRTC were compared to the NTC control at the upper (Sp2/TC1), center (Sp1/TC1), and lower (Sp3/TC3) locations of the test-piece gauge section (previously defined).

FIG. 6 The temperature measurement comparison setup, under an ICS heat source, between an NTC and an IRTC.



Accuracy was found to be within $\pm 2^{\circ}\text{C}$ of the NTCs at each location for the duration of the test, with no indication of any adverse effects on the HE23 TP coating or accuracy of the non-invasive technique from oxidation. A repeat test was performed for 3 h to confirm these results post-heat treatment. Again, measured values from the IRTC aimed at the test piece coated in HE23 TP were accurate to within $\pm 2^{\circ}\text{C}$ of the NTCs.

IRTC TEMPERATURE-MONITORING ACCURACY

The IRTC temperature-monitoring technique using HE23 TP coated test pieces proved to be accurate to within $\pm 2^{\circ}\text{C}$ of control NTCs under isothermal

FIG. 7 The temperature measurement comparison setup, under a RLF heat source, between NTCs and an IRTC.

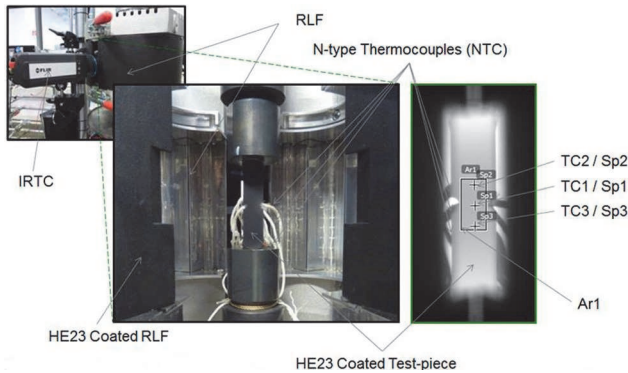
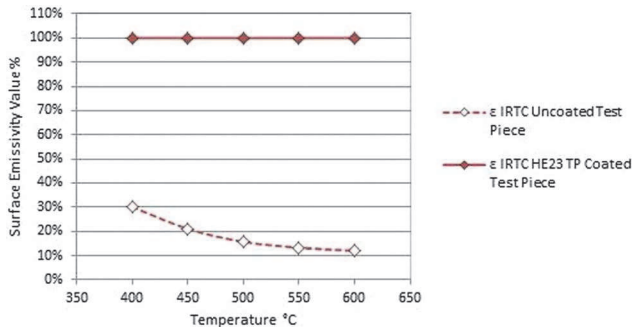


FIG. 8 Emissivity input required to maintain isothermal temperature accuracy under an ICS heat source to within $\pm 2^\circ\text{C}$ of a control NTC when monitoring temperature using an IRTC aimed at HE23 coated and uncoated test pieces.



conditions. Following these successful trials, several dynamic dwell and dynamic thermal cycles (defined earlier) were performed to test the dynamic cycle accuracy. In a similar manner to the isothermal performance, the results prove that the IRTC technique is accurate to within $\pm 2^\circ\text{C}$ of the control NTCs during dynamic thermal cycling.

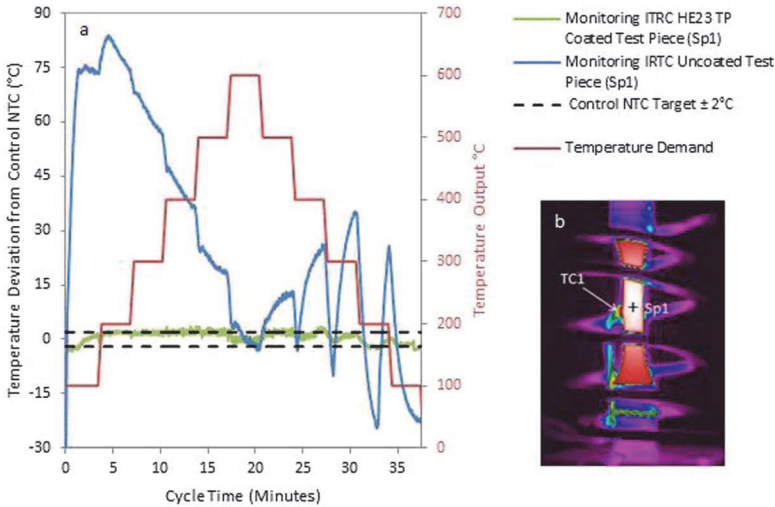
Using HE23 TP-coated test pieces, the accuracy of the IRTC under both ICS and RLF heat sources is almost identical to the NTC control during the heating, cooling, and dwell periods of the thermal cycles. When measuring the temperature of non-coated test pieces, the accuracy of the IRTC technique reduces considerably because of the absence of the coating. Temperature measurements only remain accurate compared to the NTC control at the temperature at which the emissivity input was calculated, in this case 600°C , outlining the need for the TP coating to maintain a stable emissivity, avoiding fatigue life limiting pre-test heat treatments.

A typical response of the IRTC using both TP coated and uncoated test pieces under an ICS heat source during a dynamic 300°C – 615°C thermal cycle in comparison to NTC control is shown in Fig. 9. The emissivity input values used for the IRTC with the uncoated test piece was 0.16, calibrated during the dwell period of the thermal cycle at the peak temperature of 600°C . The emissivity input value of the IRTC with the HE23 TP coated specimen was 1.

IRTC TEMPERATURE-CONTROL ACCURACY

The IRTC was directly connected to the furnace controller input channel forming a closed loop control. The IRTC technique allows multiple methods of temperature control to be used, such as single-point and area-based control coupled with maximum, minimum, and average temperature outputs. To optimize the technique, each of these IRTC control method combinations was utilized and compared to the

FIG. 9 (a) Degree of temperature deviation away from NTC temperature control of a monitoring IRTC with both HE23 TP coated and uncoated test-pieces. Comparison is made during a dynamic dwell cycle, under an ICS heat source. The graph includes $\pm 2^\circ\text{C}$ target margins away from the control NTC. (b) The corresponding location upon the test-piece gauge section at which the comparison was made (Sp1/TC1), center of the test-piece gauge section.



monitoring NTCs for various alloy and geometry test pieces to find the optimum control method.

Controlling temperature using the single-point method, typically from the center gauge location (Sp1), showed accuracy to within $\pm 2^\circ\text{C}$ of the monitoring NTC during dwell periods of the thermal cycle. This response was also seen when using the area control method, which averages the temperature of the entire test-piece gauge section Ar1. The area-control method encompassed all three NTCs (TC1, TC2, and TC3) spot welded on the test piece as well as the three IRTC single-point measurements (Sp1, Sp2, and Sp3) in the same location. Using this method, the entire gauge section was not more than $\pm 2^\circ\text{C}$ of the control NTC during the dwell periods of the dynamic thermal cycles (Fig. 10). Using this method, the entire test-piece gauge section is controlled while specific user-defined areas and single points can be monitored (Sp1/Sp2/Sp3). Moreover, the feedback from the IRTC allows the entire field of view to be analyzed during the test and later for post-test analysis.

However, despite the excellent accuracy in comparison to the monitoring NTCs during dwell periods of the cycle, for the dynamic cycle, NTC monitoring temperatures deviated by as much as 22°C during cooling stages and up to 10°C

(Fig. 10).

IRTC CONTROL VERSUS NTC CONTROL

When controlling temperatures using the NTC, the measured response from the IRTC in combination with the HE23 TP coating was accurate to that measured by the NTC throughout the duration of testing. This was observed with both dynamic and dynamic dwell cycles, using both ICS and RLF heating. Temperature deviations remained below $\pm 2^{\circ}\text{C}$ for the majority of the test (Fig. 11(a)).

Utilizing the IRTC as the temperature control method in combination with the HE23 TP-coated specimen generated contrasting results in comparison to the NTC monitor. Accuracy to within $\pm 2^{\circ}\text{C}$ was achieved for the majority of the tests between the IRTC Ar1 control and monitoring NTCs, during both dynamic and dynamic dwell cycles. These results were consistent under the ICS and RLF heat sources. Deviations of up to 10°C were found between temperatures recorded during the heating and cooling stages of the dynamic dwell cycle (Fig. 11(b)). The NTC monitor overshoot the IRTC control temperature throughout the heating stages of the thermal cycles. A similar trend was found during the cooling stages as the NTC monitor reacts more dramatically to the cooling air, resulting in an increased cooling rate compared to that of the IRTC control. These temperature differences were enhanced during the dynamic cycles with minimum temperatures observed by the NTC monitor of up to 20°C lower during cooling than that of the IRTC control (Fig. 10(a)).

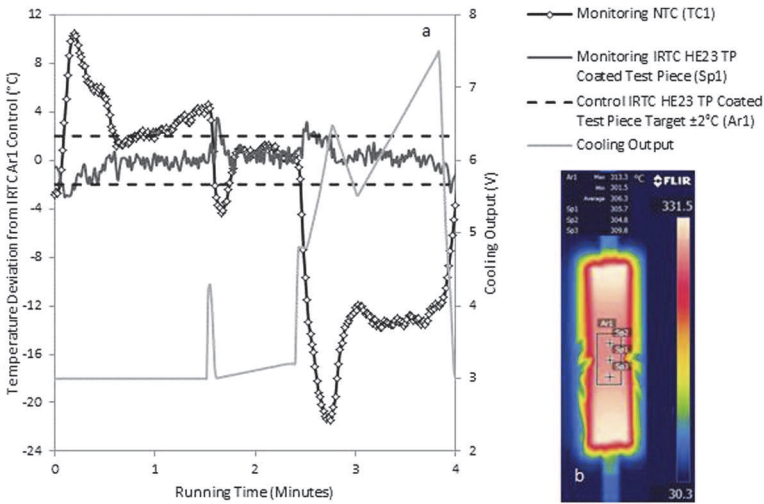
In summary, the IRTC can monitor the temperature governed by the NTC control through all stages of thermal cycling. However, the same response is not observed when monitoring temperature with the NTC with the IRTC controlling the temperature. The NTC absorbs heat energy during the heating and sheds heat during the cooling stages of the thermal cycle giving rise to different ramp rates and, directly compared to the IRTC, inaccurate temperature readings. The small mass of the thermocouples gives rise to rapid temperature changes, however, in Fig. 11(a), the response time of the controlling furnace is slower than the time it takes for consistency to be achieved, and, hence, no deviation is observed.

THERMOCOUPLE SHADOWING EFFECTS

Any object that is close or attached to the surface of the test piece will affect the way it is heated and cooled, this can be termed as “shadowing” the test piece. Thermocouples with their insulation sleeving shield the test piece from cooling air and trap-radiated heat. Cooling air is impeded by the TC reducing its effectiveness in the specific location while generating air turbulence around the TC, giving rise to pockets of warmer or cooler air near the specimen surface. These effects can be amplified when using larger diameter TC wires and heavier sheathing.

During thermal profiling of a test piece prior to testing, the majority of the test-piece gauge section contains spot-welded TCs. For this study, the TCs are applied to the specimen gauge section to establish an accurate thermal response in accordance with governing standards [1,2]. Furnace or coil positions are accurately adjusted, as are the external cooling air jets, to generate the precise thermal profile

FIG. 10 (a) Degree of temperature deviation away from the IRTC average Ar1 temperature control with a HE23 TP coated test piece of monitoring NTCs at the TC1/Sp1 location. The comparison is made during a dynamic cycle, under an RLF heat source. The graph includes $\pm 2^\circ\text{C}$ target margins away from the IRTC average Ar1 control. (b) The corresponding location upon the test-piece gauge section at which the comparison was made (Sp1/TC1), centre of the test-piece gauge section.

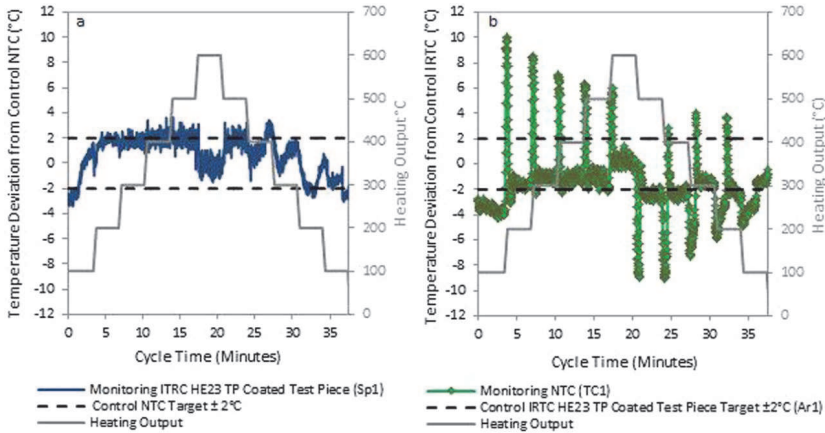


required [8]. However, because of the effects of TC shadowing, the generated thermal profile will be significantly altered once a test piece, with a reduced number of TCs, eventually replaces the dummy profile specimen. Without TCs on the specimen gauge section, the effects of heating and cooling will be more direct to the specimen surface.

A flat test piece coated in HE23 TP together with the IRTC was used to quantify the extent of the error that can be generated by TC shadowing. Utilizing an ICS heat source, the test piece was heated from 100°C to 600°C at 100°C intervals, holding the temperature at each interval for 5 min. External cooling air was then aimed at the test piece from two opposing directions at approximately 180° from each other one with and one without TCs impeding the cooling airflow. Comparisons of the thermal response upon the breadth of the specimen gauge section with and without TCs impeding the external cooling air were made using linear line profiles and point measurements by the IRTC at each 100°C temperature interval.

Similar responses and trends were found at each temperature interval, an example at the 500°C interval is shown in Fig. 12(a), with the corresponding measurement Fig. 12(b). Cooling of the specimen was significantly hindered by

FIG. 11 (a) Temperature monitoring response of the IRTC at Sp1 during NTC temperature control from TC1 under a dynamic dwell thermal cycle using RLF heating. (b) Temperature monitoring response of an NTC at TC1 during IRTC temperature control over Ar1 under a dynamic dwell thermal cycle using RLF heating. Depicted in both graphs by hashed lines are $\pm 2^\circ\text{C}$ target margins away from the governing control method.



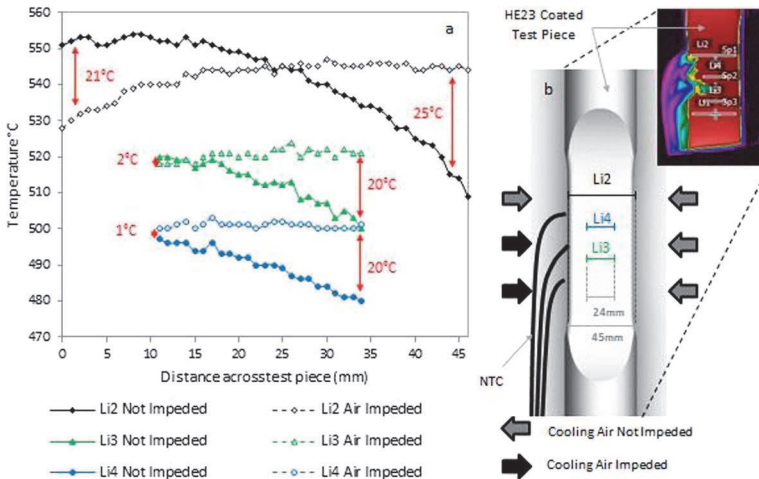
the insulated TCs. Results show there is no influence of the cooling air on the temperatures of the gauge section when TCs are present (linear line profiles Li3 and Li4; Fig. 12). The temperature of the gauge section was reduced significantly when cooling air was directed from the opposing direction without TCs impeding the air-flow. A substantial decrease in temperature of over 20°C was achieved for both linear profiles Li3 and Li4 (Fig. 12). The effect of cooling air from both sides and without TCs is shown in line profile Li2 (Fig. 12)

IRTC TEMPERATURE CONTROL LCF TEST VALIDATION

Investigating the capabilities of the IRTC Ar1 area temperature control technique further, a generic 300°C isothermal 40 kN trapezoidal low cycle fatigue (LCF) test, termed a “fair test,” was carried out under RLF heating to examine any adverse effects of loading on the temperature-control method (Fig. 13(a)). A titanium 6/4 fair test specimen was coated in HE23 TP, and the temperature control was governed by the average temperature throughout the specimen gauge section area, Ar1. The area allotted for temperature control was a thin rectangle, vertically aligned along the center gauge section of the cylindrical specimen.

The results showed no detrimental effects of loading on the temperature accuracy during the test (Fig. 13(b)). Moreover, utilizing the averaging control method balanced the temperature of the specimen faster and more accurately than observed

FIG. 12 (a) Comparisons of the thermal response across the breadth of the specimen gauge section under ICS heating, measured using the IRTC HE23 TP technique. (b) Line profile measurement locations and cooling air flow paths.



with TCs. The satisfactory quality of the test result was based on the number of cycles to failure, compared to the scatter of previously performed fair tests (Fig. 13(c)) under the same test conditions.

A repeat test was performed to investigate the effects of shot blasting prior to the application of HE23 TP, to enable enhanced adhesion between the TP coating and the specimen. Again, the temperature accuracy and control during the test did not deviate by more than $\pm 2^\circ\text{C}$ over the entire specimen gauge section. However, the resulting life of the specimen was reduced compared to the previous test but still fell within scatter of previous TC controlled fair tests. Fractographic analysis showed that shot blasting did, however, generate defects on the material surface enabling cracks to initiate easily and frequently leading to additional initiation sites and a premature failure life compared to non-shot blasted specimens.

Electron backscatter diffraction (EBSD), an SEM-based microstructural-crystallographic technique, was used to examine the HE23 TP-coated fair test specimen post-test. Analysis focused on any indications of adverse effects of the TP coating on the microstructure. Orientation, texture, internal strain, and grain size were quantified and compared between the bulk and surface of the material coated in HE23 TP. No significant variations were found between the two locations, as shown in Fig. 14.

EDX analysis was performed on a test piece that had been coated in HE23 TP and subjected to numerous thermal cycles in the temperature range 100°C – 700°C .

FIG. 13 (a) Trapezoidal load waveform and temperature profile used during the LCF fair test. (b) Temperature response of the monitoring IRTC Sp1, Sp2, Sp3, and Ar1 locations upon an HE23 TP-coated test piece during IRTC average Ar1 area control. (c) A scatter plot comparison of all thermocouple temperature controlled Ti6/4 LCF fair tests at Rolls-Royce MTOC, with thermography controlled tests displayed as filled and unfilled circles. Values are compared through standard deviation against the mean value, in this case set to zero.

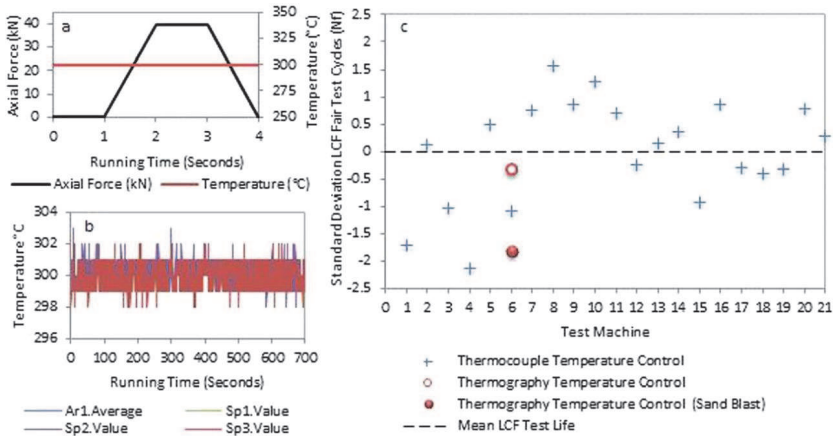


FIG. 14 Macro images of the LCF Ti6/4 fair test specimen fracture surface, failed under IRTC temperature control with no prior shot blasting. Shown are EBSD orientation and internal strain maps of the surface of the test piece and in the bulk of the material.

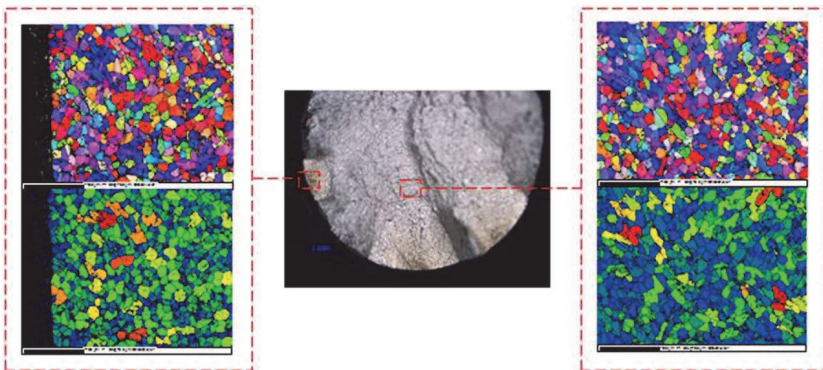
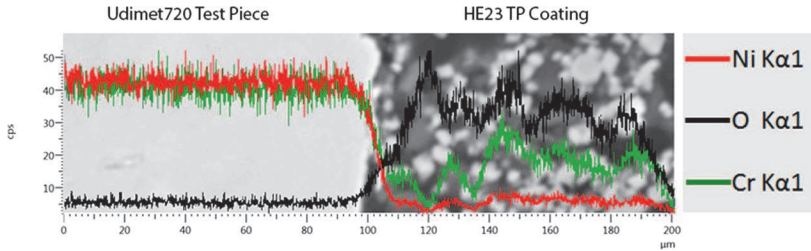


FIG. 15 EDX elemental line scan analysis of the interface between the HE23 TP coating and Udimet720 test-piece surface, subjected to thermal cycles a 100°C–700°C temperature range.



piece surface show no decline of nickel or increase in oxygen at the surface of the specimen, indicating no diffusion had taken place (Fig. 15). The paint appears to be acting as an oxidation barrier preventing the test piece from oxidizing. Further work is planned to investigate this in more depth.

Conclusions

Numerous complications and inaccuracies can be associated with TCs when using rapid heating and cooling rates. Because of this, new technology in the form of an IRTC was considered that would be non-invasive, and offers the option to not only monitor temperature but also to control it. The work undertaken in this study has shown that:

- Pyrometers have proven accurate for temperature control and monitoring purposes, provided specimens are heat treated prior to testing to enable the generation of a stable emissivity value of the test-piece surface within the experimental study and previous work [13]. Without a stable surface, emissivity results can prove inaccurate as the specimen oxidizes and its emissivity alters accordingly [9,12].
- Despite the effectiveness of pre-heat treating to generate a stable emissivity and, hence, oxide layer [13], the effect of this high-temperature pre-exposure and resulting oxide formation on the specimens can be detrimental to the fatigue life of Ni alloys at temperatures $\geq 500^\circ\text{C}$, deeming the technique undesirable in some cases [17].
- Emissivity readings are the primary cause of inaccuracy when using non-invasive temperature techniques on uncoated test-piece surfaces. The HE23 TP provides a stable value of emissivity with both pyrometry and IRTC temperature measurement and control purposes using both ICS and RLF heat sources. Results have shown consistent accuracies to within $\pm 2^\circ\text{C}$ of the NTCs when using the HE23 TP coating in combination with an IRTC or pyrometer. No prior high-temperature heat treatment of the specimen is required before the tests can begin.

- The results obtained prove that the IRTC is a very promising method for measuring and controlling temperature under both ICS and RLF heat sources. This study has generated significant results when controlling temperature using the IRTC, highlighting inaccuracies associated with TCs, such as exceeding cycle maxima and minima.
- TCs have shown to be sensitive to cooling air and as a result display faster cooling rates and apparent lower temperatures than those observed using the IRTC. The TC not only measures the heat from the specimen but also absorbs heat energy heated during the test. As a result faster heating rates are observed with peak temperatures exceeding the target temperature by as much as 10°C. As the IRTC is completely non-invasive and is not affected by the cooling or heating, it has proved an extremely accurate and reliable temperature measurement technique when used in combination with the HE23 TP coating.
- The IRTC can control temperature over the entire test-piece gauge section area, rather than a single point, which is the only option when using TCs and pyrometers. Averaging the temperature over the entire gauge section generated stable and accurate results from all regions of the gauge section in comparison to monitoring TCs.

In summary, the IRTC can accurately measure temperatures when using HE23 TP-coated materials. The IRTC is not affected by cooling air or heating devices and does not cause shadowing effects. Profiling and control can be achieved within a rapid setup time and encompasses the entire gauge section generating a significant volume of data that can be analyzed live or post-testing.

ACKNOWLEDGMENTS

The writers acknowledge the EPSRC Rolls-Royce Strategic Partnership in Structural Metals for Gas Turbines (EP/H500375/1 and EP/H022309/1) for support of this work and provision of materials.

References

- [1] ASTM E2368-10: Standard Practice for Strain Controlled Thermomechanical Fatigue Testing, ASTM International, West Conshohocken, PA, 2010, www.astm.org.
- [2] ISO 12111, "BSI Standards Publication Metallic Materials—Fatigue Testing—Strain-Controlled Thermomechanical Fatigue Testing Method," British Standards Institution, London, 2011.
- [3] Hahner, P., Rinaldi, C., Bicego, V., Affeldt, E., Brendel, T., Andersson, H., Beck, T., Klingel-hoffer, H., Kuhn, H., and Koster, A., "Research and Development into a European Code-of-Practice for Strain-Controlled Thermo-Mechanical Fatigue Testing," *Int. J. Fatigue*, Vol. 30, No. 2, 2008, pp. 372–381.
- [4] Kuhn, H., Kahlcke, O., and Brookes, S., "A Practicable Nominal Temperature Tolerance for TMF-Tests," *Int. J. Fatigue*, Vol. 30, No. 2, 2008, pp. 277–285.

- [5] Brendel, T., Affeldt, E., Hammer, J., and Rummel, C., "Temperature Gradients in TMF Specimens. Measurement and Influence on TMF Life," *Int. J. Fatigue*, Vol. 30, No. 2, 2008, pp. 234–240.
- [6] Beck, T., Hähner, P., Kühn, H.-J., Rae, C., Affeldt, E., Andersson, H., Köster, A., and Marchionni, M., "Thermo-Mechanical Fatigue—The Route to Standardisation ('TMF-Standard' Project)," *Mater. Corros.*, Vol. 57, No. 1, 2006, pp. 53–59.
- [7] Andersson, H. and Sjoström, E., "Thermal Gradients in Round TMF Specimens," *Int. J. Fatigue*, Vol. 30, No. 2, 2008, pp. 391–396.
- [8] Hähner, P., Affeldt, E., Beck, T., Klingelhöffer, H., Loveday, M., and Rinaldi, C., "Validated Code-of-Practice for Thermo-Mechanical Fatigue Testing," *EUR 22281 EN*, Office for Official Publications of the European Communities, Luxembourg, 2006.
- [9] Beck, T. and Rau, K., "Temperature Measurement and Control Methods in TMF Testing—A Comparison and Evaluation," *Int. J. Fatigue*, Vol. 30, No. 2, 2008, pp. 226–233.
- [10] Brookes, S. P., "Thermo-Mechanical Fatigue Behaviour of the Near- γ -Titanium Aluminide TNB-V5 Under Uniaxial and Multiaxial Loading," BAM-Dissertationsreihe, Berlin, 2009.
- [11] Brookes, S. P., Kühn, H.-J., Skrotzki, B., Klingelhöffer, H., Sievert, R., Pfetzinger, J., Peter, D., and Eggeler, G., "Axial-Torsional Thermomechanical Fatigue of a Near- γ TiAl-Alloy," *Mater. Sci. Eng. A*, Vol. 527, Nos. 16–17, 2010, pp. 3829–3839.
- [12] Roebuck, B., Edwards, G., and Gee, M. G., "Characterisation of Oxidising Metal Surfaces With a Two Colour Pyrometer," *Mater. Sci. Technol.*, Vol. 21, No. 7, 2005, pp. 831–840.
- [13] Lancaster, R. J., Whittaker, M. T., and Williams, S. J., "A Review of Thermo-Mechanical Fatigue Behaviour in Polycrystalline Nickel Superalloys for Turbine Disc Applications," *Mater. High Temp.*, Vol. 30, No. 1, 2013, pp. 2–12.
- [14] Neuer, G., "Spectral and Total Emissivity of High-Temperature," *Int. J. Thermophys.*, Vol. 19, No. 3, 1998, pp. 917–929.
- [15] Greene, G., Finrock, C., and Irvine, T., "Total Hemispherical Emissivity of Oxidized Inconel 718 in the Temperature Range 300–1000°C," *Exp. Therm. Fluid Sci.*, Vol. 22, Nos. 3–4, 2000, pp. 145–153.
- [16] Encinas-Oropesa, A., Drew, G. L., Hardy, M. C., Leggett, A. J., Nicholls, J. R., and Simms, N. J., "Effects of Oxidation and Hot Corrosion in a Nickel Disc Alloy," *Superalloys 2008, Eleventh International Symposium*, Pennsylvania, USA, Sept 14–18, 2008, pp. 609–618.
- [17] Gabb, T. P., Telesman, J., Kantzos, P. T., Smith, J. W., and Browning, P. F., "Effects of High Temperature Exposures on Fatigue Life of Disk Superalloys," NASA Glenn Research Center, Cleveland, OH, 2004, pp. 3–6.
- [18] Pineau, A., "High Temperature Fatigue of Ni-Base Superalloys: Microstructural and Environmental Effects," *Engineering Against Fatigue*, University of Sheffield, Sheffield, UK, 1999, pp. 557–565.
- [19] Brandt, R., Bird, C., and Neuer, G., "Emissivity Reference Paints for High Temperature Applications," *Measurement*, Vol. 41, No. 7, 2008, pp. 731–736.
- [20] Bird, R., Mutton, C., and Shepherd, J., "Surface Temperature Measurement in Turbines," *AGARD Conference Proceedings 598*, Brussels, Belgium, Oct 20–24, 1998, pp. 21.4–21.10.

ASTM INTERNATIONAL
Helping our world work better

ISBN: 978-0-8031-7613-3
Stock #: STP1584

www.astm.org